Photophysical properties of [Cr(ox)3]3- : influence of the chemical environment, external pressure and electromagnetic radiation

Milos, Mia

UNIVERSITÉ DE GENÈVE
FACULTÉ DES SCIENCES
Section de chimie et biochimie
Département de chimie physique
Professeur Andreas Hauser

Photophysical properties of $[Cr(ox)_3]^{3-}$: influence of the chemical environment, external pressure and electromagnetic radiation

THÈSE

présentée à la Faculté des sciences de l'Université de Genève
pour obtenir le grade de Docteur ès sciences, mention chimie

par

Mia MILOS
de Croatie

À mes parents, à ma sœur

« On ne voit bien qu'avec le coeur. L'essentiel est invisible pour les yeux »
Antoine de Saint-Exupéry

Remerciements

Ce travail a été effectué dans le département de chimie physique de l'Université de Genève, sous la direction du Professeur Andreas Hauser de mai 2006 à juin 2010. Je le remercie tout d'abord pour m'avoir accueillie au sein de son groupe. Je le remercie particulièrement pour les conversations scientifiques que nous avons eues, non seulement pour m'avoir clarifié les projets, mais aussi pour m'avoir permis de développer mes idées, construire un raisonnement et l'approfondir. Je le remercie également pour sa présence pendant ces quatre années et pour la bonne ambiance qu'il a su instaurer dans son groupe.

Je tiens à remercier les Professeurs Hans Bill, Christian Reber et Hans A. Riesen pour l'honneur qu'ils me font d'avoir accepté d'évaluer cette thèse.

Mes remerciements vont également aux membres du groupe, sans ordre particulier, Sébastien, Tiphaine, Kevin, Max, Will, Nathalie, Pradip, Prodipta, Enza, Hans and Itana. J'ai beaucoup apprécié l'ambiance ainsi que les discussions scientifiques et moins scientifiques que nous avons pu échanger. Et je leur suis notamment reconnaissante pour l'épaulement au cours de la dernière année de ma thèse. Je remercie Dominique Lovy qui a su résoudre tous mes problèmes informatiques et électroniques, je remercie Nahid Amstutz pour son aide au niveau des synthèses inorganiques, Isabelle Garin pour tout le côté administratif et Patrick Barman qui fait un travail technique exceptionnel et pour qui rien est impossible.

Un merci à mes ami(e)s proches qui ont très bien réussi à me changer les idées dans les moments difficiles et qui sont toujours partants pour des activité sportives et loisirs.

J'aimerais particulièrement remercier mes parents et ma sœur pour m'avoir soutenue et encouragée durant toute la vie et en particulier pendant les moments les plus difficiles.

Résumé

Les processus de transfert d'énergie d'excitation, impliquant un donneur et un accepteur jouent un rôle important dans diverses applications technologiques telles que les lasers solides [1], les lampes fluorescentes [2], les cellules de conversion d'énergie solaire [3], mais aussi dans les domaines des sciences de la vie et de la terre telles que la respiration cellulaire et la photosynthèse [4]. Ainsi, il est primordial de comprendre les mécanismes de transfert d'énergie d'excitation pour pouvoir les exploiter. Durant cette thèse, le transfert d'énergie d'excitation a été étudié sur le complexe de tris-oxalates de chrome, $[Cr(ox)_3]^{3-}$, dans deux différentes matrices: soit dans les réseaux tridimensionnels formés par les oxalates et les ions sodium formant une cavité qui est stabilisée par un cation sous forme d'un complexe tris-bipyridine [5], $[M^{II}(bpy)_3][NaCr(ox)_3]$ avec $M^{II} = Ru^{2+}$, Zn^{2+} et $[M^{III}(bpy)_3][NaCr(ox)_3]ClO_4$ avec $M^{III} = Rh^{3+}$, Cr^{3+}, soit en tant que dopant dans les cristaux du type $NaMgAl(ox)_3{\cdot}9(H_2O/D_2O):Cr^{3+}$ [6]. Sur les composés tridimensionnels, trois types de transfert d'énergie d'excitation ont été établis. Le transfert d'énergie résonant entre les membres de la largeur inhomogène séparés par la valeur de la levée de dégénérescence en champ nul (ZFS), le transfert d'énergie assisté par phonon devenant dominant au-dessus de 4 K, ainsi que le transfert dit quasi-résonant qui se manifeste comme une diffusion spectrale des raies individuelles d'un spectre de rétrécissement de raie de fluorescence (FLN) et qui est dû a l'interaction dipolaire électrique d'un chromophore donné avec tous ses voisins spectraux [7]. Un modèle simplifié se basant sur des équations différentielles décrivant la désactivation temporelle d'un état excité a été développée afin de mieux comprendre l'influence de différents paramètres sur le transfert d'énergie même. La Figure 1 montre la manifestation spectrale des trois types de transfert d'énergie, tandis que la Figure 2 représente un schéma décrivant les origines des 3 types de transfert d'énergie d'excitation.

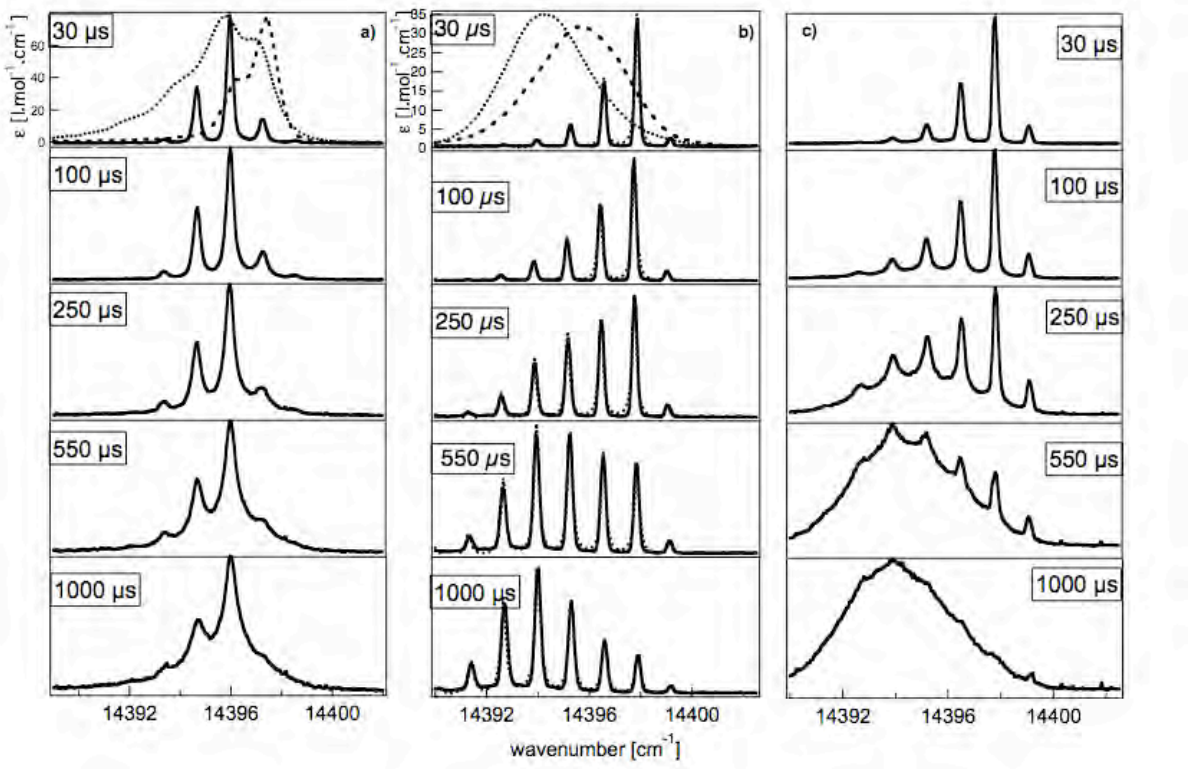

Figure 1. a) Spectres FLN dépendant du temps de $[Ru(bpy)_3][NaCr(ox)_3]$ à 1.4 K suivant une excitation de 14396.0 cm^{-1}, b) spectres FLN dépendant du temps de $[Rh(bpy)_3][NaCr(ox)_3]ClO_4$ à 1.4 K suivant une excitation de 14397.8 cm^{-1} et c) spectres FLN dépendant du temps de $[Rh(bpy)_3][NaCr(ox)_3]ClO_4$ à 3.2 K suivant la même excitation.

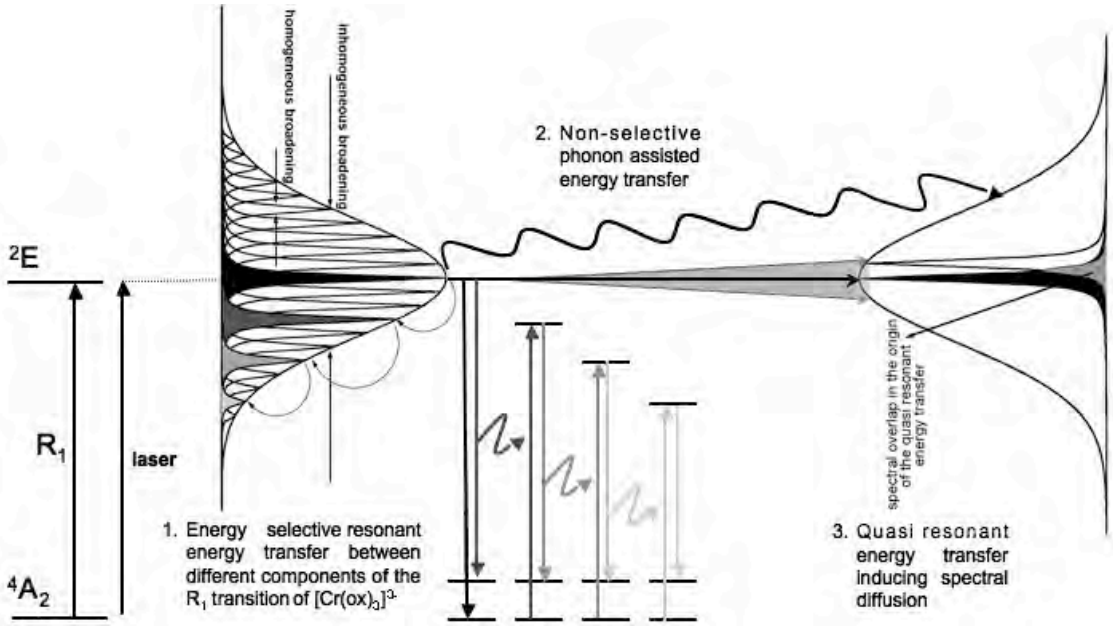

Figure 2. Schéma regroupant les trois mécanismes de transfert d'énergie.

Une étude spectroscopique sur une série de réseaux tridimensionnels du type $[Zn_{1-x}Ru_x(bpy)_3][NaCr(ox)_3]$ a permis de mettre le lien entre la structure électronique et la géométrie du composé modèle [8]. La Figure 3 représente schématiquement les sept voisins métalliques les plus proches d'un ion Cr^{3+} dont les ligands des quatre premiers, soit à 6.2 et 8.6 Å, ont des recouvrements optimaux avec les oxalates du Cr^{3+} central.

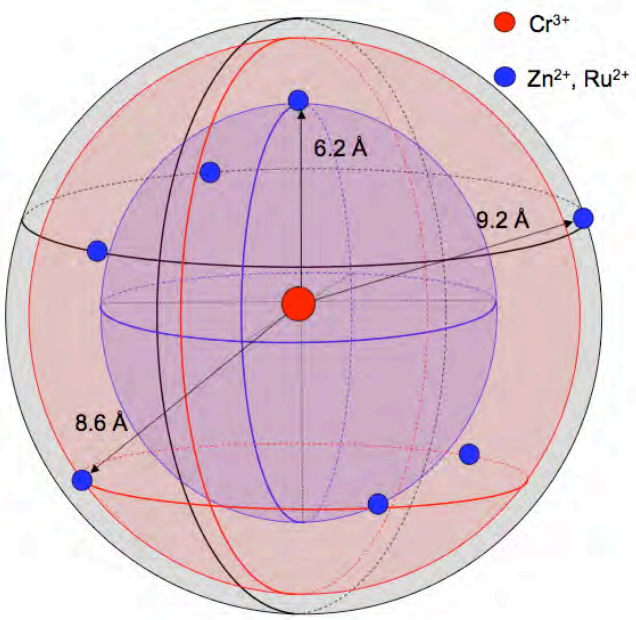

Figure 3. Schéma des 7 voisins métalliques les plus proche d'un ion Cr^{3+} donné.

En effet, la distribution des deux différents ions métalliques Zn^{2+} et Ru^{2+} sur ces 4 positions spécifiques, crée cinq sites spécifiques du Cr^{3+} qui sont résolus dans les spectres d'absorption, Figure 4. Grâce aux spectres d'absorption à haute résolution et aux expériences sous haute pression, un modèle simulant les absorptions de chaque site spécifique pour une fraction molaire de Ru^{2+} donnée a pu être développé. L'intensité des absorptions des différents sites à été modélisée par la distribution binomiale, tandis que l'énergie exacte pour chaque site a été obtenue par régression linéaire suite à une pression chimique ressentie. En effet, les deux ion Ru^{2+} et Zn^{2+}, n'ayant pas la même taille, n'appliquent pas la même pression chimique sur l'ion Cr^{3+}.

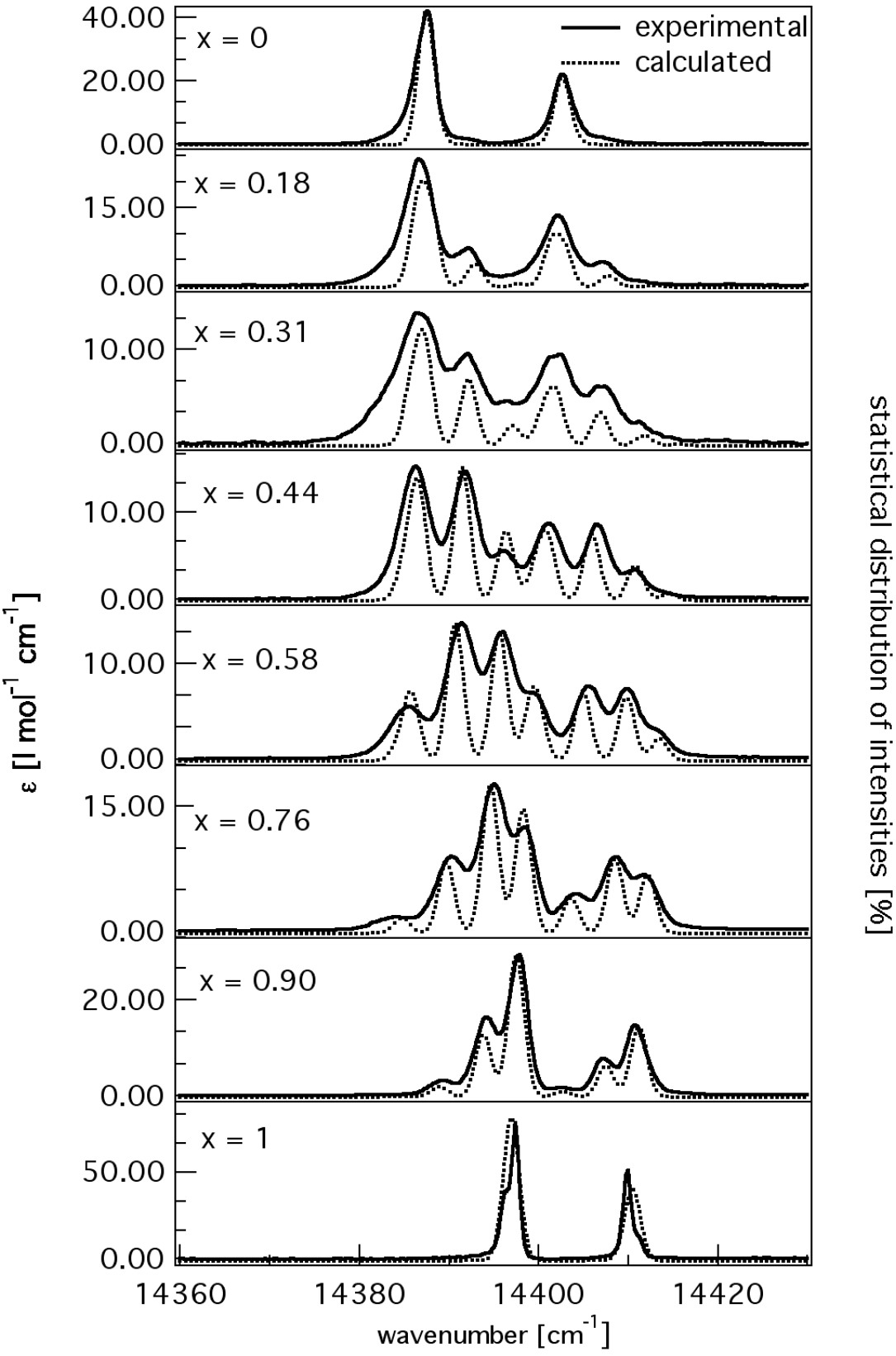

Figure 4. Spectres d'absorption de la série des composés du type $[Zn_{1-x}Ru_x(bpy)_3][NaCr(ox)_3]$ à 10 K, (—) données expérimentales, (·····) spectres calculées.

Toujours dans les mêmes réseaux tridimensionnels d'oxalates mais cette fois-ci avec les ions métalliques suivants $[Rh_{1-x}Cr_x(bpy)_3][NaM^{III}_{1-y}Cr_y(ox)_3]ClO_4$, avec M^{III} = Rh^{3+}, Al^{3+} et x = 3.5 mole% et y = 1 mole%, le transfert d'énergie d'excitation du $[Cr(ox)_3]^{3-}$ vers $[Cr(bpy)_3]^{3+}$ sous pression physique a pu être établi [9]. L'étude est basée sur le fait que les donneurs et accepteurs ne dépendent pas de la même façon de la pression et ainsi le recouvrement spectral entre les deux change en augmentant la pression physique. Grâce à cette étude-là, nous avons démontré qu'il est possible de dissocier les deux contributions au transfert d'énergie qui a lieu dans ce composé, soit la contribution rapide basée sur le couplage super-échange et la contribution plus lente basée sur le couplage dipolaire entre l'accepteur et le donneur. La Figure 5 montre la variation du recouvrement spectral lorsque la pression physique est augmentée pour les deux composés étudiés.

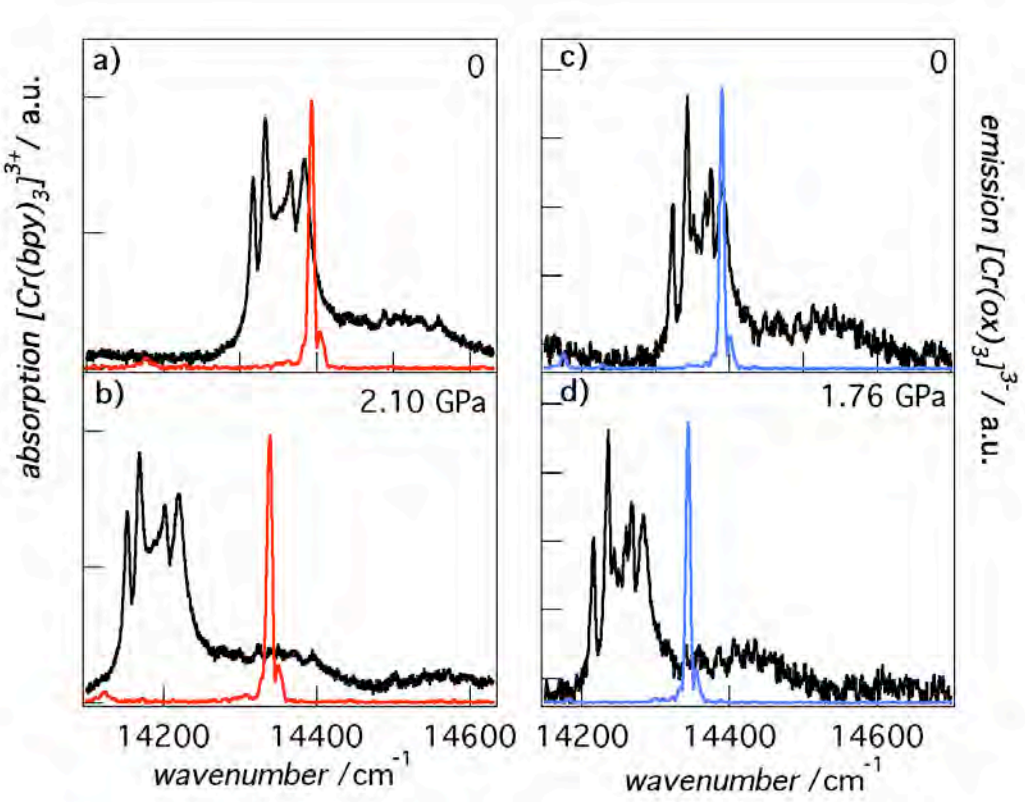

Figure 5. Absorption extrapolée de la transition $^4A_2 \rightarrow {}^2T_1$ de $[Cr(bpy)_3]^{3+}$ et émission expérimentale de la transition $^2E \rightarrow {}^4A_2$ de $[Cr(ox)_3]^{3-}$ à 10 K dans $[Rh_{1-x}Cr_x(bpy)_3][NaAl_{1-y}Cr_y(ox)_3]ClO_4$ pour deux pression différentes, a) 0 GPa et b) 2.10 GPa et dans $[Rh_{1-x}Cr_x(bpy)_3][NaRh_{1-y}Cr_y(ox)_3]ClO_4$ pour les pressions c) 0 GPa et d) 1.76 GPa.

Dans le composé $NaMgAl(ox)_3{\cdot}9(H_2O/D_2O)$ dopé avec 1% Cr^{3+} , il est possible de creuser efficacement des trous persistants et transitoires. En augmentant la concentration de Cr^{3+} à 20% on observe un transfert d'énergie résonant dans les spectres FLN, se manifestant avec six membres de rétrécissement du spectre de fluorescence. En combinant les deux propriétés physiques du $[Cr(ox)_3]^{3-}$ dans le composé donné, nous avons démontré expérimentalement qu'il est possible de creuser des trous persistants par transfert d'énergie [10]. La Figure 6 montre les résultats expérimentaux où les trous issus d'un transfert d'énergie peuvent être identifiés.

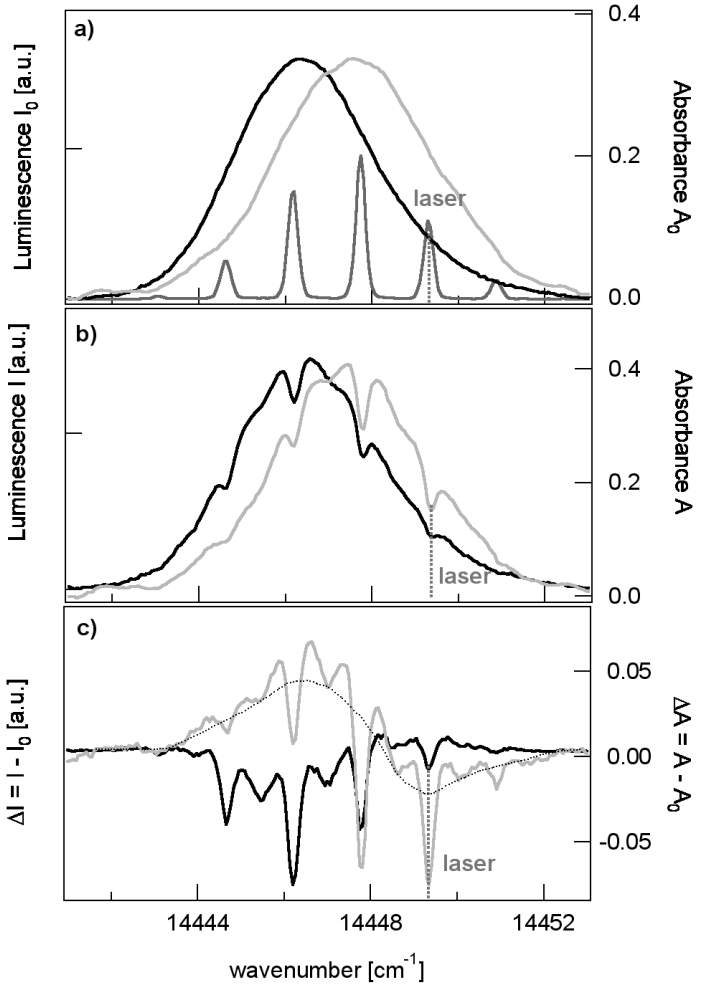

Figure 6. a) Absorption (—), luminescence non sélective avant le creusement de trous spectraux (—) et spectre FLN (—) de la transition R_1 de Cr^{3+} dans $NaMg[Al_{0.8}Cr_{0.2}(ox)_3]{\cdot}9(H_2O/D_2O)$ à 1.4 K. L'excitation sélective est à 14449.3 cm^{-1}. b) Spectres de la luminescence non sélective (—) et de l'absorption (—) après le creusement de trous spectraux à 14449.3 cm^{-1}. c) La différence des spectres de luminescence (—) et d'absorption (—) avant et après le creusement des trous spectraux à 14449.3 cm^{-1}.

Références :

[1] M.M. Feyer, H. Injeyan, U. Keller: Trends in optics and photonics, Washington DC, 1999.

[2] T. Justel, H. Nikol, C. Ronda, Angewandte Chemie-International Edition 37 (1998) 3085.

[3] M. Grätzel, Nature 414 (2001) 338.

[4] J.M. Berg, J.L. Tymoczko, L. Stryer: Biochemistry, W. H. Freeman; 6th Edition, 2006.

[5] S. Decurtins, H.W. Schmalle, R. Pellaux, P. Schneuwly, A. Hauser, Inorg. Chem. 35 (1996) 1451.

[6] H. Riesen, A.D. Rae, Dalton Trans. (2008) 4717.

[7] M. Milos, S. Kairouani, S. Rabaste, A. Hauser, Coord. Chem. Rev. 252 (2008) 2540.

[8] M. Milos, A. Hauser, Inorg. Chem. 49 (2010) 3402.

[9] M. Milos, P. Pal, A. Hauser, ChemPhysChem to be published (2010).

[10] M. Milos, A. Hauser, J. Phys. Chem. A 114 (2010) 4169.

TABLE OF CONTENTS

1. Introduction

Spectroscopy concerns the investigation of physical systems with the help of electromagnetic radiation. Optical spectroscopy involves ultraviolet, visible or infrared electromagnetic radiations. In certain types of optical spectroscopy, the radiation originates from an external source such as a lamp or a laser and is modified by the system, whereas in other types, the radiation originates within the system itself. Interaction of light with a system can induce photochemical reactions or photophysical processes. In a photochemical reaction the energy of the absorbed radiation offers the advantage over thermal methods of forming thermodynamically unfavourable products or overcoming large activation barriers in a short period of time. Photophysical processes involve the production of an excited state and subsequent relaxation events, which lead from one state of a molecular entity to another through radiation and radiationless processes finally restoring the system in its initial ground state. Thus during purely photophysical processes, no chemical reaction takes place. This thesis will be focused on photophysical processes of complexes of one particular transition metal ion, that is Cr^{3+}, in several different crystal lattices, such as $[M^{II}(bpy)_3][NaCr(ox)_3]$ with $M^{II} = Zn^{2+}$, Ru^{2+}, $[M^{III}(bpy)_3][NaCr(ox)_3]ClO_4$ with $M^{III} = Rh^{3+}$, Cr^{3+}, and $NaMgCr(ox)_3{\cdot}9H_2O$ ($ox = C_2O_4^{2-}$, bpy = 2,2'-bipyridine). Several aspects will be presented such as the different energy migration and energy transfer mechanisms that can be observed in those systems and the influence of the local environment on the electronic structure of the $3d^3$ ion in addition to the common contributions to the Hamiltonian of the free ion. It will also be shown that it is possible to burn persistent spectral holes, not only by direct excitation, but also by resonant energy transfer based on dipole-dipole interaction. It will be presented how it is possible to distinguish and separate the two contributions to the resonant energy transfer between $[Cr(ox)_3]^{3-}$ and $[Cr(bpy)_3]^{3+}$ by investigating the effect of external pressure. Finally, a model for simulating resonant and quasi-resonant energy transfer leading to fast spectral diffusion within the ^2E state of Cr^{3+} ion will be presented. Before presenting and discussing the corresponding experimental results in Chapters 3 to 8, Chapter 1 will introduce the subject more thoroughly by giving an overview of the theory required for understanding the

photophysical processes, and Chapter 2 will describe the experimental methods used in this thesis.

1.1 Electronic structure and spectroscopy of $3d^3$ ions

Transition metal ions are very interesting to photophysicists and photochemists because of their optical properties. They are frequently used as optically active dopants in commercial phosphors [1] and in tuneable solid-state lasers [2] and their complexes find use as photosensitisers in solar cells [3]. They owe their versatility to the partially filled valence d-shell, giving rise to spectroscopic transitions of different character, namely metal-to-ligand or ligand-to-metal charge transfer transitions and metal-centred d-d transitions involving the non-bonding and anti-bonding d-orbitals of the metal ion. In this thesis we are mostly interested in the latter. Those transitions mainly require energies in the visible domain of the electromagnetic radiation.

The electronic structure of transition metal ions is strongly influenced by the ligands that coordinate the central transition metal ion [4]. The Hamiltonian for impurity ions is given by:

$$H = H_0 + H_{e-e} + H_{LF} + H_{SO} \qquad (1)$$

Where H_0 represents the central potential of the free ion, $H_{e\text{-}e}$ is the electrostatic interaction between electrons, H_{SO} represents the contribution of the spin-orbit coupling and H_{LF} incorporates the ligand field interaction between the central ion and its ligands. The electron-electron interaction, $H_{e\text{-}e}$, determines the free ion states of the transition metal ions. Those states are labelled $^{2S+1}$L according to the Russel-Saunders coupling scheme [5], where S is the total spin and L is the total angular momentum. Each electron has a spin of ½. Depending on the number of d-electrons in the system and obeying the Pauli principle, one can determine all the possibilities of the multiplicity of the system. On the other hand for each multiplicity, one can obtain all the possibilities of the projection in the space that correspond to the total angular momentum. L can take values 0, 1, 2, 3, 4, … whose attributes are S, P, D, F, G,… respectively. According to Hund's rule, the ground state is the state with the highest spin-multiplicity, and in the case that two states have the same highest spin-

multiplicity, the one with the highest total angular momentum represents the ground state. The energy separation between the various ^{2S+1}L states is usually given in terms of Racah parameters A, B, and C [6]. These parameters describe the strength of the electrostatic repulsion between the electrons. For 3d transition metal ions, the ligand field Hamiltonian, H_{LF}, is dominant over the spin-orbit interaction. The various ^{2S+1}L states are consequently split by the ligand field [4,7]. The split states are identified by the irreducible representations of the point group of the coordination sphere [8]. Regarding the symmetry around the central ion, different point groups can be defined such as the octahedral group O_h, or subgroups thereof for distorted geometries as for instance D_3 for tris-chelate complexes. The point groups are formed according to the symmetry properties of the coordination sphere, and each point group has a number of irreducible representations that are labelled A, B, E, T. A and B are used for one-dimensional representations, E for two-dimensional representations, and T for three-dimensional representations. Each point group has a character table that displays the characters of the different irreducible representations. Finally, the last contribution to the total Hamiltonian is the spin-orbit coupling. Splittings due to the spin-orbit coupling can be equally investigated with group-theoretical techniques. If one takes the example of Cr^{3+}, it is a 3d ion with 3 electrons in the d orbitals. The three electrons give two possibilities for the total spin, S = 1/2 and S = 3/2 leading to multiplicities of 2 and 4, respectively. On the other hand, the electrons can be spatially arranged in such a way as to give rise to the term symbols ^4F, ^4P, ^2G, and ^2F. When a 3d ion is surrounded by an octahedral crystal field, some of the free ion states are split. Thus, the ground state ^4F splits into three energy levels, the $^4A_{2g}$ ground level and $^4T_{2g}$ and $^4T_{1g}$ excited levels. The ^2G state is split into ^2E_g, $^2T_{1g}$, $^2T_{2g}$, and $^2A_{1g}$, while the ^4P term symbol becomes $^4T_{1g}$ and ^2F becomes $^2A_{2g}$, $^2T_{2g}$ and $^2T_{1g}$ in the octahedral field. The spin functions are unaffected by the ligand field. Sugano and Tanabe have calculated the energy of the states for the $3d^n$ ions as a function of the octahedral crystal field strength [9]. Figure 1.1 shows the Tanabe-Sugano diagram for $3d^3$ ions.

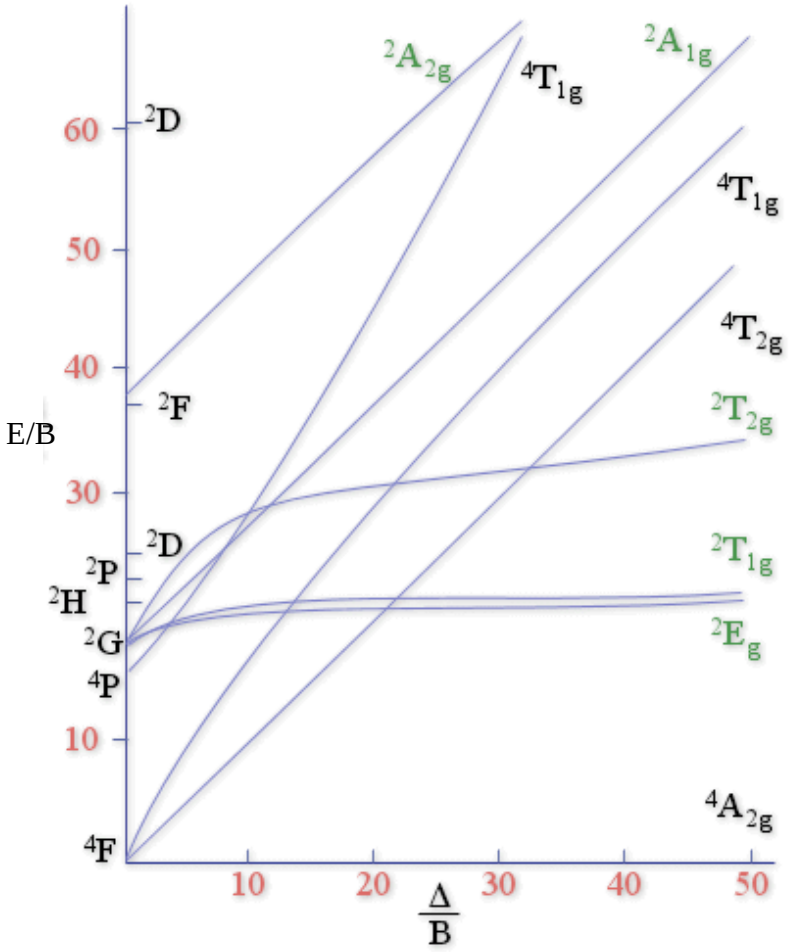

Figure 1.1. Tanabe-Sugano diagram for $3d^3$ ions in an octahedral crystal field [10].

Finally, the lifting of the degeneracy due to the spin-orbit coupling of all crystal field levels can be calculated. For instance, the $^4T_2$ level of Cr^{3+} splits into four levels, while the ^2E and $^4A_2$ of Cr^{3+} in a perfect octahedral field don't split under spin-orbit coupling. However, in slightly distorted octahedral systems, such is commonly seen for Cr^{3+} complexes, the ^2E and $^4A_2$ states are split. This lift of degeneracy in the last case is due to the combined effect of spin-orbit coupling and lower symmetry fields. This splitting is termed zero field splitting (ZFS) and will be used several times in this thesis. Figure 1.2 shows the electronic structure of the $3d^3$ ions including the lifting of the degeneracy due to the electron-electron repulsion, ligand field strength and spin-orbit coupling in an octahedral field and in a distorted trigonal field.

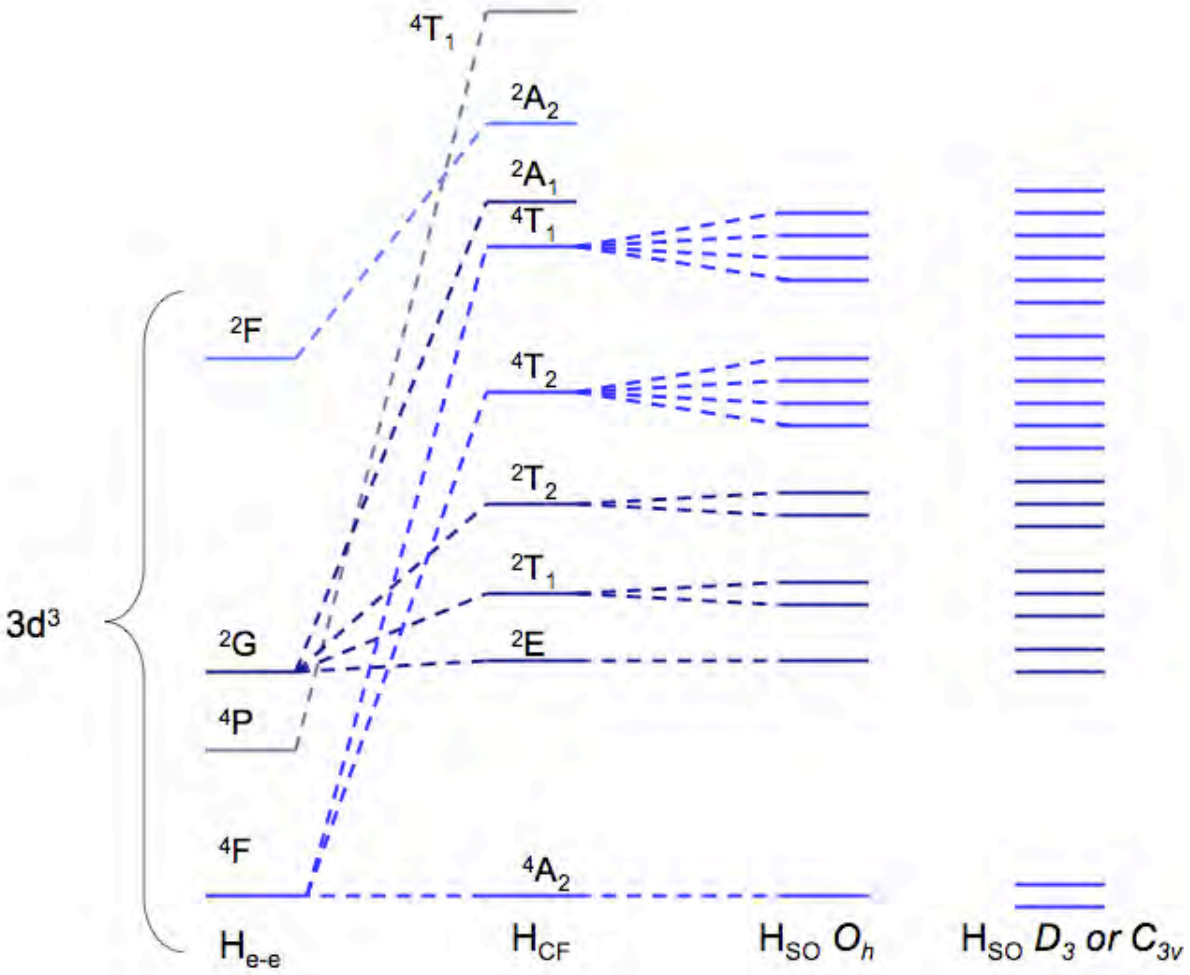

Figure 1.2. Electronic structure of the $3d^3$ in an octahedral crystal field and with a trigonal distortion.

1.2 Photophysical processes

The energetically lowest electronic state of a molecule is the ground state, and at low temperatures mainly all the population is in the electronic ground state. It is possible to excite molecules from their ground state to excited states with an electromagnetic wave such as light [7,11]. The electronic transitions require energies in the UV, visible region or IR of the electromagnetic radiation. Once a complex absorbs light, it is in an excited state. There are several pathways for deactivation back to the ground state. The radiative pathways are fluorescence and/or phosphorescence. Fluorescence corresponds to the emission from the lowest vibrational state of the excited state having the same spin-multiplicity as the ground state, while the

phosphorescence is the luminescence involving a change in spin-multiplicity. The lifetime for the later is longer. The non-radiative pathways are vibrational relaxation, internal conversion and intersystem crossing. Internal conversion is an isoenergetic radiationless transition between two electronic states of the same spin-multiplicity, while intersystem crossing is an isoenergetic radiationless transition between two electronic states having different spin-multiplicities. Both often result in a vibrationally excited molecular entity in the lower electronic state, which then usually deactivates to its lowest vibrational level by heat dissipation.

All the photophysical processes mentioned above are presented in Figure 1.3. An excited state can also deactivate via energy transfer or energy migration. Those processes will be discussed in Section 1.4.

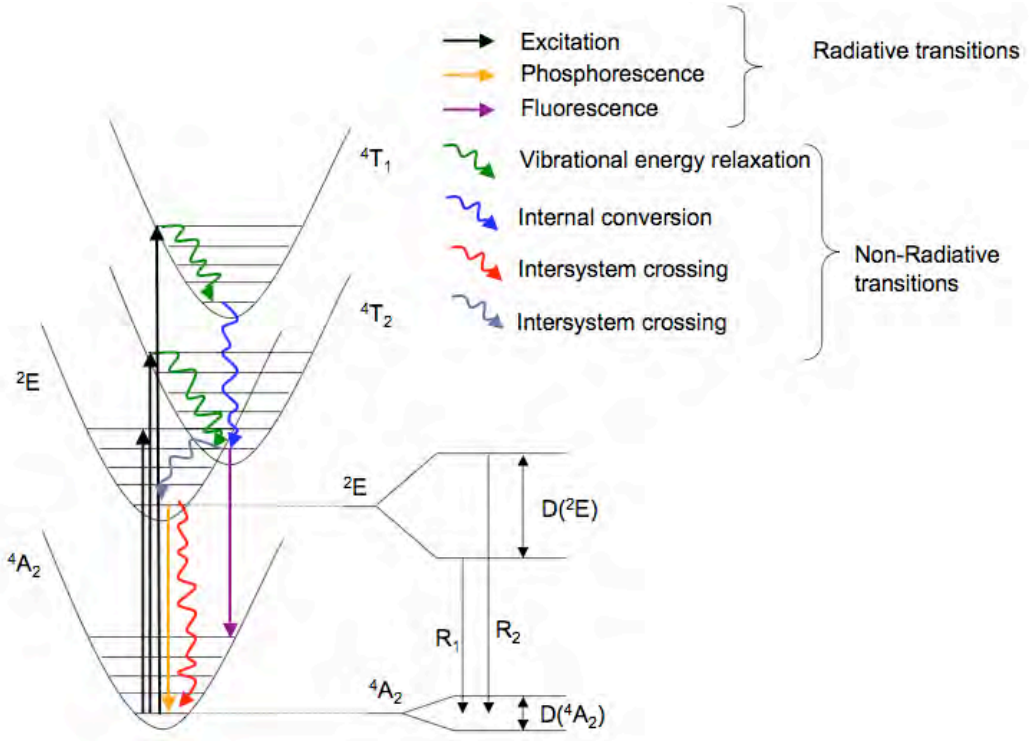

Figure 1.3. Photophysical processes involved in the electronic structure of transition metal ions as for instance in an octahedral complex of Cr^{3+}.

An excited state can be characterised by its lifetime and its luminescence quantum yield. The observed lifetime is defined as the reciprocal of the total relaxation rate constant:

$$\tau_{obs} = k_{tot}^{-1} \tag{2}$$

The total relaxation rate constant is given by the sum of the radiative and the non-radiative rate constants:

$$k_{tot} = k_{rad} + k_{nr} \tag{3}$$

Where the radiative rate constant is related to the refraction index of the sample, *n*, the transition frequency, $\tilde{\nu}_0$, and the oscillator strength of the corresponding transition, *f*, according to:

$$k_{rad} \approx \frac{n\left[\frac{1}{3}\left(n^2+2\right)\right]^2 \tilde{\nu}_0^2 f}{1.5} \tag{4}$$

The oscillator strength can be calculated from the absorption spectrum of the chromophore with:

$$f = 4.32 \cdot 10^{-9} \int \varepsilon(\tilde{\nu}) d\tilde{\nu} \tag{5}$$

Where ε is the molar extinction coefficient of the chromophore. The total non-radiative rate constant is the sum of the rate constants of all the individual non-radiative processes leading from this state:

$$k_{nr} = k_{IC} + k_{ISC} + k_{ET} + ... \tag{6}$$

Where k_{IC} is the internal conversion rate, k_{ISC} is the intersystem crossing rate, and k_{ET} is the energy transfer rate. The luminescence quantum yield is defined as the number of emitted photons relative to the total number of deactivated molecules via radiative and non radiative ways:

$$\eta_{lum} = \frac{k_{rad}}{k_{rad} + k_{nr}} = \frac{\tau_{obs}}{\tau_{rad}} \tag{7}$$

Chapter 6 will show an application of the former, where the energy transfer quantum yield will be calculated according to:

$$\eta_{ET} = \frac{I_A}{I_D + I_A} \tag{8}$$

Where I_A and I_D are the luminescence intensities of the acceptor and donor, respectively.

1.3 Homogeneous and Inhomogeneous line width

An optical absorption (or emission) band contains important information about the interactions between the electromagnetic radiation and the system [11,12]. The homogeneous line width of the electronic origin, the transition between the zero-point energy of the ground state and the zero-point energy in the excited state, is governed by the lifetime of the excited state, T_1, and the pure dephasing time T_2^*. These two times are often combined in an effective dephasing time T_2:

$$\frac{1}{T_2} = \frac{1}{2T_1} + \frac{1}{T_2^*} \tag{9}$$

Using the effective dephasing time the homogeneous line width of an electronic origin between the two electronic levels is described by Equation (10), where $\omega_1 = \vec{\mu}_1 \cdot \vec{E}_0 / \hbar$ denotes the Rabi frequency, and $\omega_1^2 T_1 T_2$ describes the power broadening by the probing laser.

$$\Gamma_{hom} = \frac{1}{\pi T_2}\sqrt{1+\omega_1^2 T_1 T_2} \tag{10}$$

Consequently, if the laser power is very low, the homogeneous line width will be approximately given by:

$$\Gamma_{hom} \approx \frac{1}{\pi T_2} \tag{11}$$

Dephasing processes that are included in T_2^* can be due to electron-phonon interactions or electron-spin-electron-spin and electron-spin-nuclear-spin interactions. The finite width of the electronic transition is a direct manifestation of Heisenberg's uncertainty principle, $\Delta\nu\Delta t \geq 1/2\pi$, $\Delta\nu = \Gamma_{hom}$ being the full frequency width at half maximum of the transition and $\Delta t = \frac{1}{2} T_2$ ($\approx T_1$ if $T_2^* >> T_1$) the time available to measure the frequency of the transition. This broadening mechanism leads to the Lorentzian profile (Figure 1.4) given as normalised line shape function:

$$g(\nu) = \frac{\Gamma_{hom}/2\pi}{(\nu-\nu_0)^2 + (\Gamma_{hom}/2)^2} \tag{12}$$

In very weakly doped ruby (Al_2O_3:Cr^{3+}) the residual homogeneous line width of the R_1 line at 2 K is a low as 20 kHz [13]. In the systems to be studied here, it is around 20 MHz at 1.5 K for low doping levels and increases to 600 MHz for higher doping levels

due to spin-spin relaxation processes [14]. Homogeneous line widths typically increase rapidly with increasing temperature due to phonon assisted relaxation processes.

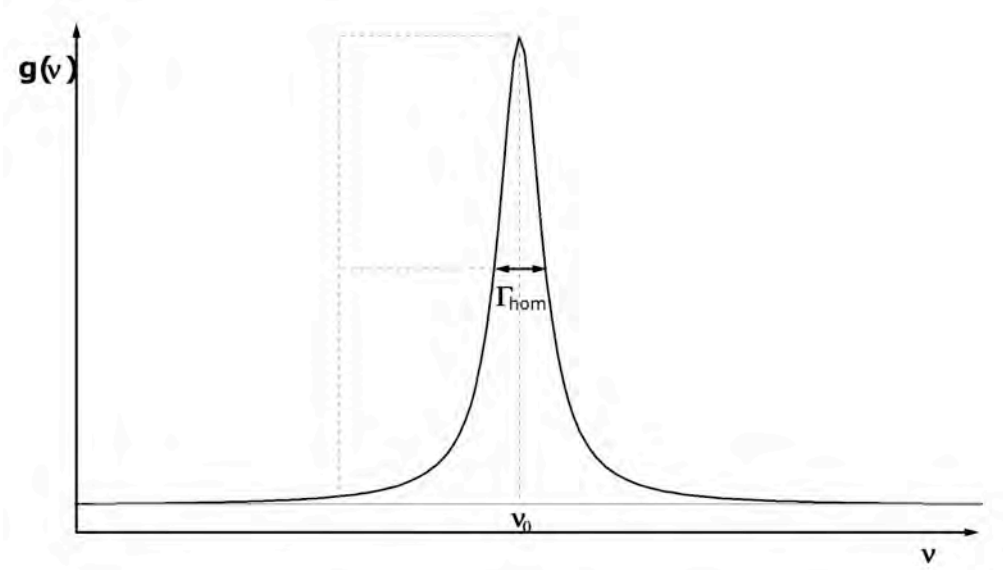

Figure 1.4. Homogeneous line width obtained from a Lorentzian line shape function.

The natural broadening is a type of *homogeneous broadening*, in which all the absorbing chromophores are assumed to be identical and then to contribute with identical line-shape functions to the spectrum. As a rule, the different absorbing centres have slightly different resonant frequencies due to slightly different environments, so that the line shape results from the convolution of the line shapes of the different centres, weighted by their corresponding concentrations. This type of broadening is called *inhomogeneous broadening*, and, often, it leads to a Gaussian line shape (Figure 1.5) given by:

$$g(\nu) = \frac{1}{\sqrt{2\pi}\sigma} e^{-\frac{(\nu-\nu_0)^2}{2\sigma^2}} \tag{13}$$

Where the standard deviation σ is related to the inhomogeneous line width Γ_{inh}, that is, the full width at half maximum:

$$\Gamma_{inh} = 2\sigma\sqrt{2\,ln\,2} = 2.35\sigma \tag{14}$$

Inhomogeneous broadening in solids occurs as a result of non-equivalent static distortions in the environment of an optically active centre, dislocations in the crystal or inhomogeneous isotope distribution. In amorphous matrices, the inhomogeneous may be quite large, but even in well crystallised compounds it dominates the

homogeneous width of electronic origins at low temperatures because the crystal lattice is not perfect due to impurities and defects. As a result there is a distribution of crystalline environments for the absorbing centres, and consequently a distribution of resonance frequencies (Figure 1.5). Again in well-annealed and lightly doped ruby, the inhomogeneous line width of the R lines may be as low as 0.1 cm^{-1} or lower [13]. In our systems with metal-organic complexes, it will typically be somewhat larger, that is, between 1 and 5 cm^{-1}.

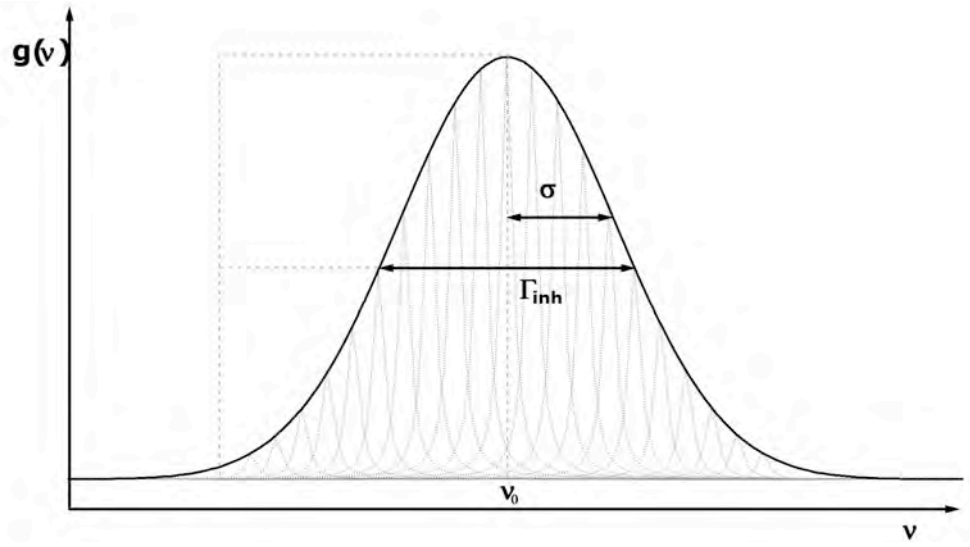

Figure 1.5. Inhomogeneous line width obtained from a Gaussian line shape function.

1.4 Energy transfer processes

As mentioned earlier, an excited state can be deactivated via energy transfer processes. Energy transfer processes require a donor in an excited state at a given energy and an acceptor that can accept this energy [7,15]. A particular case where the donor and the acceptor are chemically identical chromophores is called energy migration. Figure 1.6 shows a common application of energy migration within a donor band. The selectively excited subset of chromophores within the inhomogeneous emission band are not directly resonant with the absorption of an acceptor in the sample and are spatially too far away for a direct process. However, several steps of energy migration within the emission band of the donor can increase the probability of transferring energy to the acceptor by increasing the spectral overlap.

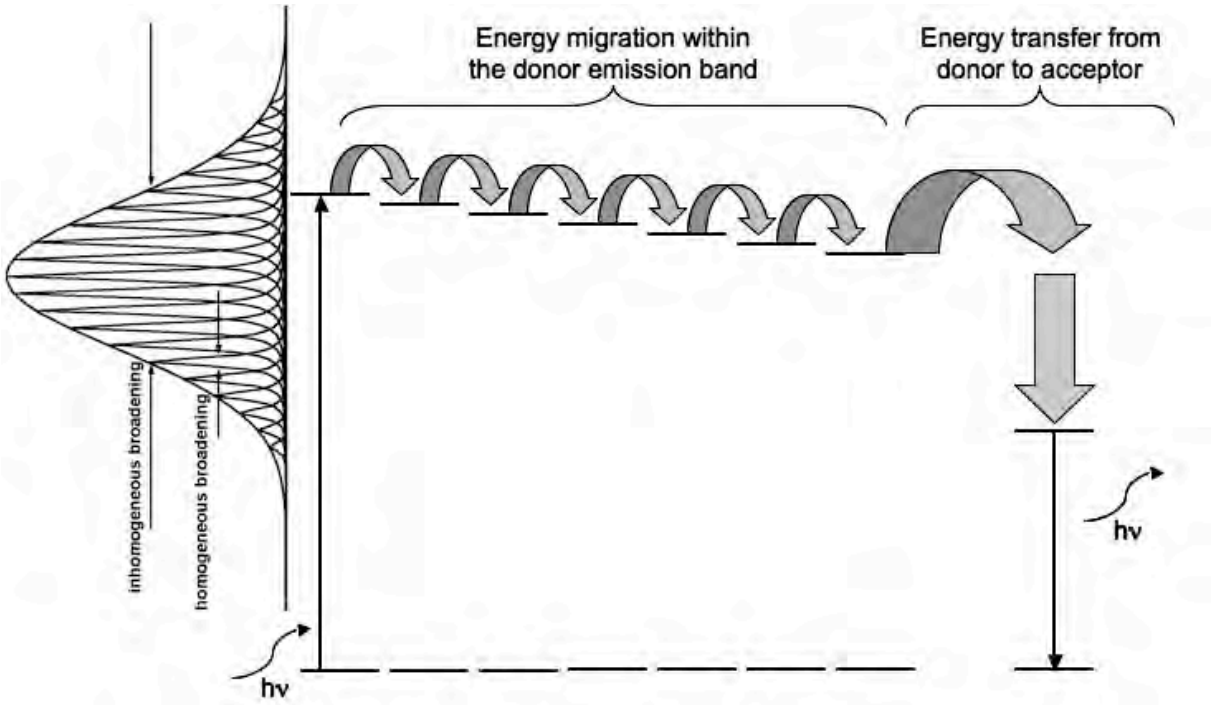

Figure 1.6. Scheme of energy migration within the emission band of the donor followed by energy transfer from the final donor to final acceptor.

For both, energy migration and energy transfer, the same laws govern the processes. The energy can be transferred or migrated resonantly or non-resonantly. Non-resonant energy transfer is most often phonon assisted. The surplus energy in this case is dissipated non-selectively into the environment, that is, into the vibrations of the lattice. Phonon assisted energy transfer or migration becomes dominant at higher temperatures. On the other hand, the resonant energy transfer or migration is based on specific interactions between the donor and the acceptor and require a spectral overlap between the emission of the donor and the absorption of the acceptor. The probability w_{AD} for a resonant energy transfer process from the initially excited donor D* to the acceptor A is given by Equation (15) according to Fermi's Golden Rule.

$$w_{DA} = \frac{2\pi}{\hbar}\left|\left\langle DA^* \left| H' \right| D^* A \right\rangle\right|^2 \Omega_{DA} \qquad (15)$$

In Equation (15), $\left\langle DA^* \left| H' \right| D^* A \right\rangle$ is the electronic coupling matrix element. There are several types of interactions between donors and acceptors. In this thesis, the energy transfer based on super-exchange coupling and dipole-dipole interaction will be mainly discussed. The energy transfer probability for both types of energy transfer is

proportional to the spectral overlap integral Ω_{DA}, between the donor emission and acceptor absorption, which takes care of the energy conservation. The spectral overlap Ω_{DA} is the integral of the normalised line shape functions of the donor emission, g_D, and the acceptor absorption, g_A, and is given by:

$$\Omega_{DA} = \int g_A(\tilde{\nu})\, g_D(\tilde{\nu})\, d\tilde{\nu} \tag{16}$$

The interaction Hamiltonian for the exchange coupling is given by:

$$H'_{ex} = -2\sum_{i,j} J_{ij} s_i^a s_j^b \tag{17}$$

Where J_{ij} is the exchange integral corresponding to an interaction between two electrons on centres *a* and *b*, and s_i^a and s_j^b are spin angular momentum operators for the electrons.

The rate constant for the Förster type energy transfer [16] is given by Equation (18) (in SI units)

$$w_{DA} = \left(\frac{1}{4\pi\varepsilon_0}\right)^2 \left(\frac{3\hbar e^4}{4\pi n^4 m^2}\right) \times \frac{\kappa^2 f_D f_A \Omega_{DA}}{R_{DA}^6 \nu_{DA}^2} = \frac{1}{\tau_D}\left(\frac{R_c}{R_{DA}}\right)^6 \tag{18}$$

Where τ_D is the intrinsic luminescence lifetime of the donor in the absence of any acceptor chromophores, R_{DA} is the donor-acceptor separation, and R_c is the critical radius given by:

$$R_c = \left(Const \times \frac{\kappa^2 f_A \Omega_{DA} \eta_D^r}{\tilde{\nu}_{DA}^4}\right)^{1/6} \tag{19}$$

In Equation (19), f_A is the dimensionless oscillator strength of the acceptor transition, η_D^r is the luminescence quantum efficiency of the donor transition, $\tilde{\nu}_{DA}$ is the mean energy at which the transfer takes place, and κ is a geometrical factor, which averaged over all possible orientations, takes on a value of 2/3.

Equation (20) presents the general formulation for modelling the time deactivation of a given initially excited state.

$$\frac{dN_{ei}}{dt} = -\left(k_D + k_{ET}\sum_j \Omega_{i,j} N_{gj}\right) N_{ei} + k_{ET}\sum_j \Omega_{j,i} N_{gi} N_{ej} \qquad \text{i = 1, 2, ..., n} \tag{20}$$

N_{ei} and N_{ej} are the numbers of centres of the i^{th} and j^{th} set in the excited state which are interacting via the dipole dipole interaction and have a spectral overlap different from zero, N_{gi} and N_{gj} are the corresponding ground state populations, k_D is the total

constant rate of the radiative deactivation of the excited state to the ground state, k_{ET} is related to the energy transfer probability, and the $\Omega_{i,j}$ describe all possible spectral overlap integrals according to Equation (21).

$$\Omega_{DA} = \frac{1}{\pi} \frac{\Gamma_{hom}}{\Gamma_{hom}^2 + \left(\tilde{\nu}_D - \tilde{\nu}_A\right)^2} \tag{21}$$

Figure 1.7 shows a scheme supporting the model developed for the energy migration. In this figure, all the parameters involved in the model are schematically presented. It is important to notice that energy transfer is a reversible process, thus for modelling the deactivation of an excited state with time, one should include the repopulation of the initially excited chromophore via the back energy transfer from the neighbour acceptor.

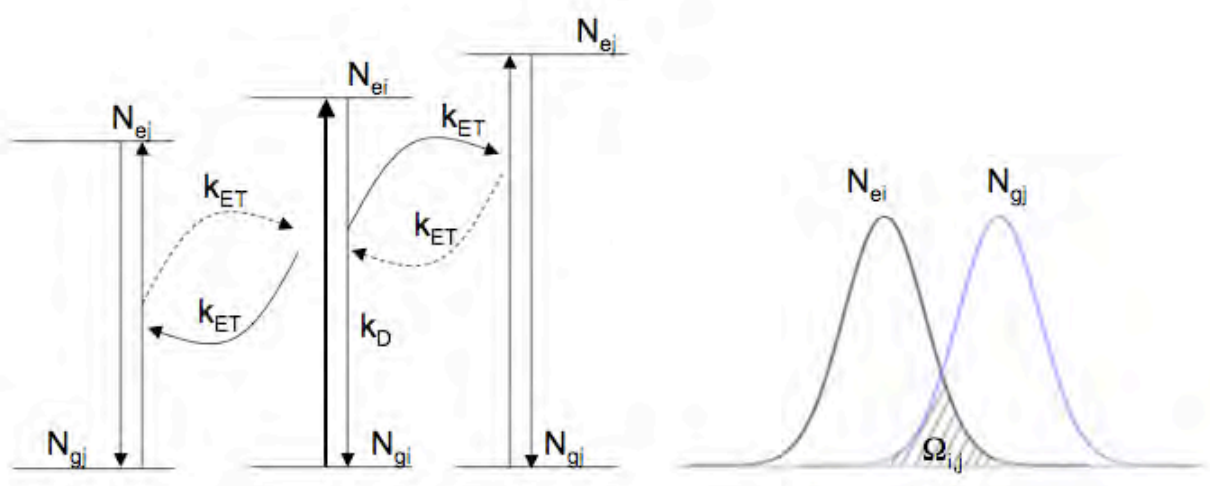

Figure 1.7. Schematic representation of all the processes that are involved when a given state such as the ^{2}E state of Cr^{3+} deactivate to its ground state.

For weak excitation, such as $N_{ei} << N_{gi}$, the N_{gi} are constant and are given by the inhomogeneous Gaussian distribution function. In this case, the set of differential equations becomes linear and can be solved numerically for $N_{ei}(t)$ using the starting condition that at $t = 0$, $N_{ei \neq i_0} = 0$ and $N_{ei_0} = N_0$.

1.5 Influence of external pressure on the electronic structure

From thermodynamic laws one learn that for a given macroscopic system, the volume of a material must decrease upon isothermal compression [17] according to

$$\left(\frac{\partial V}{\partial P}\right)_T < 0 \tag{22}$$

In microscopic systems, the same law holds, however the precise manner in which a material reduces its volume under an applied pressure is unspecified by thermodynamic laws and requires considerations at a molecular level. Bond lengths, bond angles, covalency, coordination number, and intermolecular forces can be influenced by pressure. The optical properties that carry information on electronic energy levels are strongly dependent on the variation of the parameters mentioned above. Consequently, high-pressure experiments are a nice tool showing the relationship of local structure and bonding to electronic energy levels and optical properties. The bulk modulus, *K*, gives an indication of the sensitivity of a system to pressure [18]:

$$\frac{1}{K} = -\frac{1}{V}\left(\frac{\partial V}{\partial P}\right)_T \tag{23}$$

Systems with large bulk modulus such as ruby (253 GPa, [19]), have small compressibility, and consequently show small volume decrease with pressure and thus small changes in optical properties. On the other hand, systems with small bulk moduli show large compressibility leading to significant changes in optical and structural properties with increasing pressure. However, the magnitude of pressure-induced effects is not only related to the stiffness of a material but also to the nature of the electronic state. The nature of a state determines the interaction of the state with the lattice: the stronger is the interaction, the greater is the pressure effect on the optical properties [20,21]. For example, in d-d transitions, where the ground and excited states do not involve the same d-orbital occupancy, the strength of lattice interaction changes as one goes from the excited state back to the ground state. Thus, spin allowed d-d transitions are strongly influenced by the pressure. On the other hand, 4f orbitals of lanthanides that are shielded by 5d and 6s orbitals and interact only weakly with surrounding ligands, are only weakly influenced by the applied pressure. Spin flip d-d transitions are closer to the f-f transitions in character

since the excited and the ground state in a spin flip d-d transition involve the same strong field electronic configuration and thus very similar strengths of the lattice interaction.

Figure 1.8 shows a scheme of the single configuration coordinate model, with the excited and ground state that are involved in a pressure experiment. Pressure can potentially influence E_0, the electronic origin energy difference between the excited state and the ground state, and S, the Huang-Rhys factor. The value of S is a measure of the strength of coupling of the luminescent centre to the surrounding environment. Changes in E_0 may lead to a red or blue shift of the energy difference depending upon the nature of the electronic states involved in the transition, while changes in S leads to changes in the optical line width. Depending upon the nature of states involved, one can have one or the other of the two limiting cases, or a combination of two effects may occur.

The pressure experiments involved in this thesis will mainly focus on the influence on E_0. The parameter that is obtained from pressure experiments is the shift rate. An ion that undergoes a spin flip d-d transition in a high bulk modulus host will have a small shift rate. The classic example is the $^2E \rightarrow {}^4A_2$ spin-flip phosphorescence in ruby ($Al_2O_3:Cr^{3+}$, K = 253 GPa), with a shift rate of -7.6 cm^{-1}/GPa at RT [22-24]. For the same bulk modulus but a spin allowed transition such as the $^4T_2 \rightarrow {}^4A_2$ fluorescence, the shift rate is 84 cm^{-1}/GPa [25]. The red shift of the former is due to the dominant contribution of the increase in the nephelauxetic effect [26] with decreasing metal-ligand bond length. For the blue shift of the latter, the concomitant increase in ligand-field strength is responsible. Examples of lattices with a low bulk modulus are the halide lattices such as Cs_2NaYCl_6, with K = 49.5 GPa [27]. The shift rates of Cr^{3+} doped in this halide lattice are -37 cm^{-1}/GPa and 257 cm^{-1}/GPa for the spin-flip and spin allowed transition, respectively [27]. Finally, an example for f-f transitions is taken form Sm^{2+}:BaFCl, where the shift rate is -20 cm^{-1}/GPa [28].

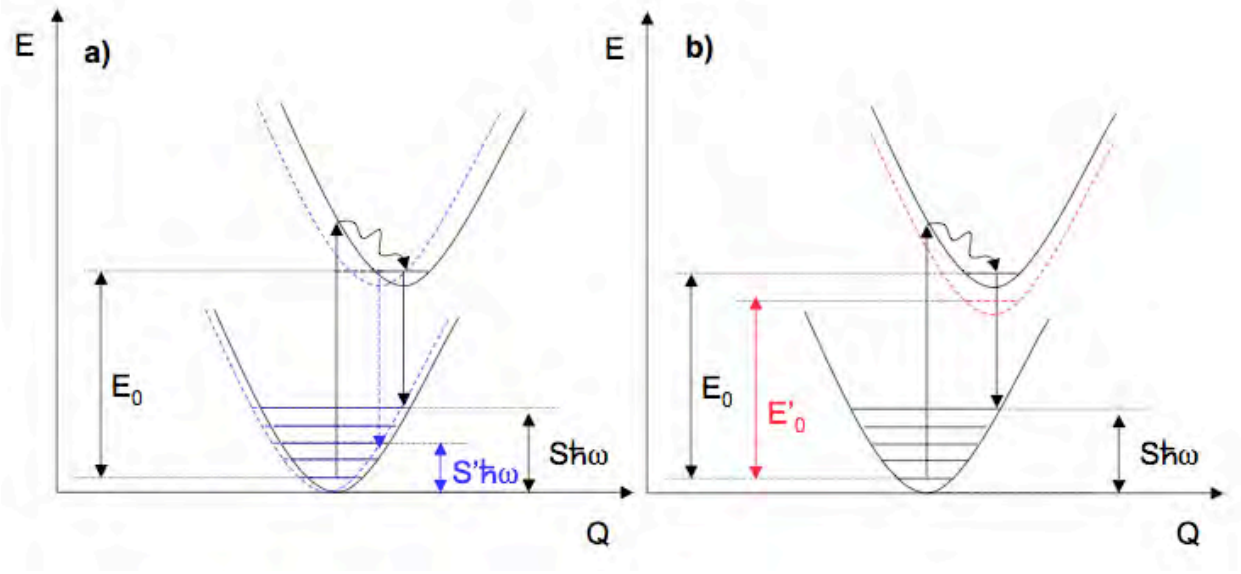

Figure 1.8. The single configuration coordinate model. The excited and the ground state of a probe are presented. a) The blue dotted line correspond to the potential wells of the ground and excited states when the pressure is applied and has an influence on the Huang-Rhys factor S, while b) the red dotted line correspond to the excited state potential well when pressure is applied and has an influence on the electronic origin energy difference.

1.6 Outline

The theme of this thesis is focussed on the photophysical properties of the Cr^{3+} in trigonally distorted octahedral crystal fields. In Chapter 2, the synthetic procedures and the experimental methods needed for the various processes to be studied are described. In addition to standard absorption and emission experiments at cryogenic temperatures, this comprises notably time resolved high-resolution laser spectroscopy such as fluorescence line narrowing and spectral-hole burning. Results, that were published in Coordination Chemistry Reviews [29] in 2008 on the subject of different mechanisms and manifestations of energy migration within the ^2E state of Cr^{3+} in three-dimensional oxalate networks are presented in Chapter 3. More specifically, the rates of resonant energy migration between $[Ru(bpy)_3][NaCr(ox)_3]$ and $[Rh(bpy)_3][NaCr(ox)_3]ClO_4$ are compared and discussed. Chapter 4 presents results that were published in Inorganic Chemistry in 2010 [30]. They concern a study of mixed crystals of general composition $[Zn_{1-x}Ru_x(bpy)_3][NaCr(ox)_3]$ with x = 0, 0.18, 0.31, 0.44, 0.58, 0.76, 0.90, and 1. Changing apparently inert ions in the near environment of the active chromophore $[Cr(ox)_3]^{3-}$ creates specific sites rather than

just increasing the inhomogeneous line width of the chromophore. Moreover, it was possible to model the populations of each specific site by a simple binomial distribution for a given concentration of the substituting ion, in this case Ru^{2+}. Finally, using the results of high-pressure experiments, it was also possible to model the shift of the absorption bands of each specific site as the molar fraction of Ru^{2+} increases. With this study, we point out that the nephelauxetic effect that influence the electronic energy of the ^2E depends not only on the Cr-O bond length, but also on the distance between the oxalate and bypiridine planes in $[Zn_{1-x}Ru_x(bpy)_3][NaCr(ox)_3]$ and the ensuing π-interactions. Results that were published in The Journal of Physical Chemistry A in 2010 [31] are presented in Chapter 5. This project is based on Riesen's discovery of efficient persistent spectral hole burning in $NaMgAl_{1-x}Cr_x(ox)_3{\cdot}9H_2O/D_2O$ [32]. We extended this work by optimising the sample in order to burn a series of persistent spectral side-holes holes by resonant energy transfer. Chapter 6 shows results that are accepted to ChemPhysChem in 2010 [33]. The work is based on tuning energy transfer with external pressure in co-doped systems $[Rh_{1-x}Cr_x(bpy)_3][NaAl_{1-y}Cr_y(ox)_3]ClO_4$ and $[Rh_{1-x}Cr_x(bpy)_3][NaRh_{1-y}Cr_y(ox)_3]ClO_4$. The energy is transferred resonantly from $[Cr(ox)_3]^{3-}$ to $[Cr(bpy)_3]^{3+}$ with two different mechanisms, super-exchange interaction and dipole-dipole interaction between the respective transition electric dipole moments. With increasing pressure, the spectral overlap between the donor emission and the acceptor absorption is modified and consequently the energy transfer rate changes as well. Chapter 7 shows the model for simulating energy transfer and the resulting spectral diffusion within the ^2E state of Cr^{3+} in $[Ru(bpy)_3][NaCr(ox)_3]$ that was published in The Journal of Luminescence in 2009 [34]. Finally in Chapter 8 the results of a full study and the application of the model for spectral diffusion by comparing the different energy transfer processes in $[Ru(bpy)_3][NaCr(ox)_3]$, $[Zn(bpy)_3][NaCr(ox)_3]$ and $[Rh(bpy)_3][NaCr(ox)_3]ClO_4$ are summarized. At the end, a conclusion will follow, as well as some suggestions for further work.

References

[1] T. Justel, H. Nikol, C. Ronda, Angew. Chem. 37 (1998) 3085.

[2] M.M. Feyer, H. Injeyan, U. Keller: Trends in optics and photonics, Washington DC, 1999.

[3] M. Grätzel, Nature 414 (2001) 338.

[4] B. Henderson, G.F. Imbusch: Optical Spectroscopy of inorganic solids, Clarendon Press, Oxford, 1989.

[5] H.N. Russell, F.A. Saunders, Astrophys. J. 61 (1925) 38.

[6] G. Racah, Phys. Rev. 62 (1942) 438.

[7] E.I. Solomon, A.B.P. Lever: Inorganic electronic structure and spectroscopy, John Wiley & Sons, New York, 1999.

[8] F.A. Cotton: Chemical applications of group theory, Wiley-Interscience, New York, 1971.

[9] Y. Tanabe, S. Sugano, J. Phys. Soc. Jpn. 11 (1956) 864.

[10] www.uel.education.fr/consultation/reference/chimie/elementsd1/apprendre/gcb.eld.fa.301.a2/content/access.htm.

[11] J. Garcia Solé, L.E. Bausa, D. Jaque: An Introduction to the Optical Spectroscopy of Inorganic Solids, John Wiley & Sons, Ltd, 2005.

[12] H. Riesen, Coord. Chem. Rev. 250 (2006) 1737.

[13] A. Szabo, R. Kaarli, Phys. Rev. B 44 (1991) 12307.

[14] A. Hauser, M.E. von Arx, V.S. Langford, U. Oetliker, S. Kairouani, A. Pillonnet, Top. Curr. Chem. 241 (2004) 65.

[15] B. DiBartolo, X. Chen: Advances in Energy Transfer Processes, World Scientific, New Jersey, 2001.

[16] T. Förster, Annal. Der Phys. 2 (1948) 55.

[17] P. Atkins, J.D. Paola: Physical Chemistry, Oxford University Press.

[18] C. Kittel: Introduction to Solid State Physics, John Wiley & Sons, 2005.

[19] M.L. Cohen, Phys. Rev. B 32 (1985) 7988.

[20] K.L. Bray, Top. Curr. Chem. 213 (2001) 1.

[21] C. Reber, J.K. Grey, E. Lanthier, K.A. Frantzen, Comm. Inorg. Chem. 26 (2005) 233.

[22] G.J. Piermarini, S. Block, J.D. Barnett, R.A. Forman, J. Appl. Phys. 46 (1975) 2774.

[23] K. Syassen, High Press. Res. 28 (2008) 75.

[24] K. Nakano, Y. Akahama, Y. Ohishi, H. Kawamura, Jap. J. of App. Phys. 39 (2000) 1249.

[25] S.J. Duclos, Y.K. Vohra, A.L. Ruoff, Phys. Rev. B 41 (1990) 5372.

[26] C.K. Jørgensen, Discuss. Farad. Soc (1958) 110.

[27] A.G. Rinzler, J.F. Dolan, L.A. Kappers, D.S. Hamilton, R.H. Bartram, J. Phys. and Chem. Solid. 54 (1993) 89.

[28] T. Penhouet, H. Hagemann, J. Alloy. Comp. 451 (2008) 74.

[29] M. Milos, S. Kairouani, S. Rabaste, A. Hauser, Coord. Chem. Rev. 252 (2008) 2540.

[30] M. Milos, A. Hauser, Inorg. Chem. 49 (2010) 3402.

[31] M. Milos, A. Hauser, J. Phys. Chem. A 114 (2010) 4169.

[32] H. Riesen, J.L. Hughes, Chem. Phys. Lett. 372 (2003) 563.

[33] M. Milos, P. Pal, A. Hauser, ChemPhysChem, accepted (2010).

[34] M. Milos, A. Hauser, J. Lumin. 129 (2009) 1901.

2. Experimental part

2.1 Synthesis and Structures

2.1.1 The three-dimensional oxalate networks

The synthesis of the three-dimensional oxalate networks $[M^{II}(bpy)_3][NaM^{III}(ox)_3]$ and $[M^{III'}(bpy)_3][NaM^{III}(ox)_3]ClO_4$ (M^{II} = Ru^{2+}, Zn^{2+}, Fe^{2+}, ...; M^{III} = Al^{3+}, Cr^{3+}, Rh^{3+}, ...; $M^{III'}$ = Cr^{3+}, Rh^{3+}, ox = $C_2O_4^{2-}$, bpy = 2,2'-bipyridine) was developed by Decurtins et al. [1,2] The M^{III}-tris-oxalate complexes are bridged by sodium ions forming a cavity into which a tris-bipyridine complex perfectly fits. The size of the cavity selectively embed the tris-bipyridine complexes leading to optimal π-π interactions between the oxalate and the bipyridine ligands such that auto-assembly between the reactants takes place after adding NaCl as “molecular glue” according to the equation:

$$3[M^{II}(bpy)_3]Cl_2 \cdot 6H_2O + 3K_3[Cr(ox)_3] \cdot 3H_2O + 3NaCl \rightarrow 3[M^{II}(bpy)_3][NaCr(ox)_3] + 9KCl$$

An additional counter ion is required for the tri-valent tris-bipyridine complex sitting in the cavity, which is taken into account by using the perchlorate salt of the tris-bipyridine complex as starting material:

$$3[M^{III}(bpy)_3](ClO_4)_3 \cdot 3H_2O + 3K_3[Cr(ox)_3] \cdot 3H_2O + 3NaCl \rightarrow 3[M^{II}(bpy)_3][NaCr(ox)_3]ClO_4 + 9KCl$$

Figure 2.1 shows separately the $[Cr(ox)_3]^{3-}$ and $[Cr(bpy)_3]^{3+}$ complexes and the space-filling model of the three-dimensional oxalate network encapsulating the tris-bipyridine complex.

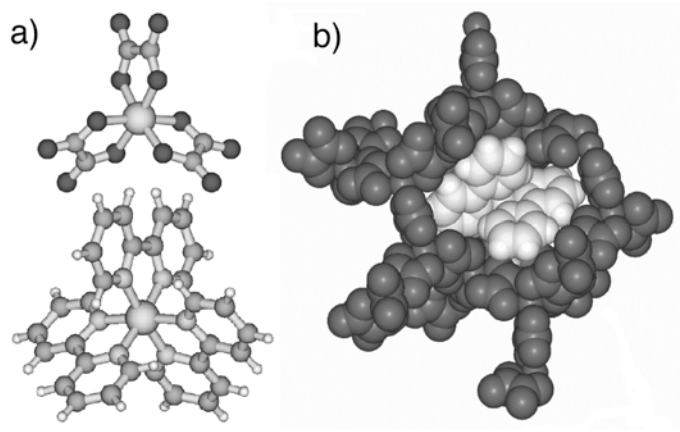

Figure 2.1. a) The building blocks $[M(bpy)_3]^{2+/3+}$ and $[M'(ox)_3]^{3-}$. b) The three-dimensional oxalate network formed by the addition of NaCl.

During this thesis, several projects were performed with different compositions of three-dimensional oxalate network compounds. The study on energy migration within the ^2E state of Cr^{3+} and the comparison of the different manifestations published in Coordination Chemistry Reviews [3] was performed on neat $[Ru(bpy)_3][NaCr(ox)_3]$ and $[Rh(bpy)_3][NaCr(ox)_3]ClO_4$ synthesised according to standard procedures [2].

The study of the electronic and structural properties of the mixed crystals, published in Inorganic Chemistry [4] was done on a series of compounds of general composition $[Zn_{1-x}Ru_x(bpy)_3][NaCr(ox)_3]$. The starting materials are $K_3[Cr(ox)_3]\cdot 3H_2O$ (0.4874 g), $[Ru(bpy)_3]Cl_2\cdot 6H_2O$ (0.7486 g), $[Zn(bpy)_3]Cl_2\cdot 6H_2O$ (0.7129 g), $[Rh(bpy)_3](ClO_4)_3\cdot 3H_2O$ (0.9234 g), and NaCl (0.1169 g). The corresponding masses are dissolved in 100 ml of water in order to obtain aqueous solution with 0.01 M concentration for all the complexes and 0.02 M for NaCl. The volumes of solutions that were used for the synthesis of the compounds of general composition $[Zn_{1-x}Ru_x(bpy)_3][NaCr(ox)_3]$ with x = 0, 0.05, 0.1, 0.2, 0.4, 0.6, 0.8, and 1 are summarized in Table 2.1. Powders and monocrystals were synthesised. In both cases the complexes are mixed first and at the end NaCl solution is added. For obtaining the powders, the mixture is stirred at room temperature. Powder, that is formed after few minutes, is filtered and put in an oven at 80°C overnight in order to dry. For obtaining the monocrystals, the mixture is put in the fridge, and after 3 days, very well developed tetrahedral crystals were obtained. The nominal concentrations differ from

the effective concentrations. The latter are obtained by ICP-MS giving for powders x = 0, 0.23, 0.39, 0.56, 0.78, 0.89, 0.96, 1 and for monocrystals 0, 0.18, 0.31, 0.44, 0.58, 0.76, 0.90, and 1.

Table 2.1. The volumes of the solutions used in the synthesis of $[Zn_{1-x}Ru_x(bpy)_3][NaCr(ox)_3]$ are in ml. The reactants were $K_3[Cr(ox)_3]\cdot 3H_2O$, $[Ru(bpy)_3]Cl_2\cdot 6H_2O$, $[Zn(bpy)_3]Cl_2\cdot 6H_2O$, and NaCl and the concentrations of aqueous solutions were 0.01 M, except for NaCl, where the concentration was 0.02 M.

x	0	0.05	0.1	0.2	0.4	0.6	0.8	1
$[Cr(ox)_3]^{3-}$	30	30	30	30	30	30	30	30
$[Ru(bpy)_3]^{2+}$	0	1.5	3	6	12	18	24	30
$[Zn(bpy)_3]^{2+}$	30	28.5	27	24	18	12	6	0
NaCl	15	15	15	15	15	15	15	15

In the study of energy transfer between $[Cr(ox)_3]^{3-}$ and $[Cr(bpy)_3]^{3+}$ under external pressure submitted to ChemPhysChem [5] the co-doped compounds used were $[M^{III}_{1-x}Cr_x(bpy)_3][NaM'^{III}_{1-y}Cr_y(ox)_3]ClO_4$ with $M^{III} = Rh^{3+}$ and $M'^{III} = Al^{3+}$ and Rh^{3+}.

Table 2.2. The volumes of the solutions used in the synthesis of $[M^{III}_{1-x}Cr_x(bpy)_3][NaM'^{III}_{1-y}Cr_y(ox)_3]ClO_4$ are in ml. The reactants were $K_3Cr(ox)_3\cdot 3H_2O$, $K_3Rh(ox)_3\cdot 4.5H_2O$, $[Rh(bpy)_3](ClO_4)_3\cdot 3H_2O$, $[Cr(bpy)_3](ClO_4)_3\cdot Hbpy\cdot ClO_4$, and NaCl and the concentrations of aqueous solutions were 0.01 M, except for NaCl, where the concentration was 0.02 M.

	$M^{III} = Rh^{3+}$ $M'^{III}=Al^{3+}$		$M^{III} = Rh^{3+}$ $M'^{III}=Rh^{3+}$				
	x = 0.07 y = 0.01	x = 1 y = 0	x = 0.07 y = 0.01	x = 1 y = 0	x = 0.5 y = 0	x = 0 y = 1	x = 0 y = 0.5
$[Cr(bpy)_3]^{3+}$	0.7	10	0.7	10	5	0	0
$[Rh(bpy)_3]^{3+}$	9.3	0	9.3	0	5	10	10
$[Cr(ox)_3]^{3-}$	0.1	0	0.1	0	0	10	5
$[Rh(ox)_3]^{3-}$	---	---	9.9	10	10	0	5
$[Al(ox)_3]^{3-}$	9.9	10	---	---	---	---	---
NaCl	5	5	5	5	5	5	5

The starting materials for this project are $K_3[Cr(ox)_3]\cdot 3H_2O$ (0.4874 g), $K_3[Al(ox)_3]\cdot 3H_2O$ (0.4624 g), $K_3[Rh(ox)_3]\cdot 4.5H_2O$ (0.5653 g), $[Rh(bpy)_3](ClO_4)_3\cdot 3H_2O$ (0.9238 g), $[Cr(bpy)_3](ClO_4)_3\cdot Hbpy\cdot ClO_4$ (1.0756 g), and NaCl (0.1169 g). The corresponding masses are dissolved in 100 ml of water in order to obtain aqueous solution with 0.01 M concentration for all the complexes and 0.02 M for NaCl. The molar fractions studied for this project, as well as the volumes of the solutions used for obtaining single crystals are given in Table 2.2. The monocrystals are obtained, as described previously.

2.1.2 $NaMgAl(ox)_3\cdot 9(H_2O/D_2O):Cr^{3+}$

The crystals of $NaMgAl(ox)_3\cdot 9(H_2O/D_2O):Cr^{3+}$ with 1%, 10%, 20% and 30% of Cr^{3+} were synthesised following literature procedures [6,7]. Solutions for crystal growth were prepared accordingly. The equation of the chemical reaction is:

$$(1\text{-}x)Al_2(SO_4)_3 + xCr_2(SO_4)_3 + 2MgO + 6H_2C_2O_4 + 2NaOH + 3Ba(OH)_2 \rightarrow 2\ NaMg[Al_{1-x}Cr_x(C_2O_4)_3] + 3BaSO_4 \downarrow$$

With x = 0.01, 0.1, 0.2, and 0.3. All the solutions were prepared in warm mixed water, that is 50% H_2O and 50% D_2O. All the quantities are calculated in order to react with 0.005 mol of the total metal concentration. According to the desired doping level and as detailed in Table 2.3, the required quantities of $Al_2(SO_4)_3$ and $Cr_2(SO_4)_3$ were dissolved in 10 ml of the H_2O/D_2O water mixture, giving a total metal concentration of 0.5 M. Then, stoichiometric quantities of solid MgO and of a 3 M solution of $H_2C_2O_4$ were added. Once the dissolution was complete, the stoichiometric quantities of 18.45 M NaOH in D_2O and a hot 1.5 M solution of $Ba(OH)_2$ were added to the mixture, which was stirred for 3 h. The $BaSO_4$ precipitate was filtered, and the remaining solution was concentrated by evaporation of 2/3 of the solvent. The crystals were grown by slow evaporation at room temperature in the dark. All the quantities in grams for preparing the solutions of the chemicals involved in the

synthesis are given in Table 2.3. The solutions were made in 10 ml of the solvent except for the NaOH where the total volume of the solution is 1 ml.

Table 2.3. The quantities of the chemicals for preparing the solutions used in the synthesis of $NaMgAl(ox)_3{\cdot}9(H_2O/D_2O):Cr^{3+}$ are in grams. All the solutions are made in 10 ml of mixed H_2O/D_2O except for NaOH where the total volume of the solution was 1 ml.

	$Al_2(SO_4)_3$	$Cr_2(SO_4)_3$	MgO	$H_2C_2O_4$	NaOH	$Ba(OH)_2$
1%	3.1204	0.0196	0.403	3.783	0.58	4.7325
10%	2.8368	0.1961	idem			
20%	2.5216	0.3922				
30%	2.2064	0.5883				

2.2 Conventional absorption and emission spectroscopy

Electronic absorption spectra were obtained on single crystals using a Fourier-transform spectrometer equipped for measuring in the infrared and visible spectral range (Bruker IFS66/S). The absorption spectra were collected at a spectral resolution of 0.5 cm^{-1}. The light source is a tungsten lamp. For absorption measurements crystals with one corner of the tetrahedron polished down to a thickness of ~60 μm were mounted on copper apertures, placed in a closed cycle cryostat (Oxford Instruments CCC1204), and collected at 10 K in an atmosphere of He exchange gas.

For non-selective luminescence spectra, samples were excited at 532 nm, that is into the $^4A_2 \rightarrow {}^4T_2$ transition of Cr^{3+}, from an intracavity frequency doubled Nd:YAG laser (ILEE VA-I-N-532). The resulting emission was analysed using a double monochromator (SPEX 1403) and a CCD camera (Roper Instruments), giving a spectral resolution of 0.25 cm^{-1}, or the above-mentioned FT instrument using a PM tube for detection (Hamamatsu R928).

2.3 Fluorescence Line Narrowing

Fluorescence Line Narrowing (FLN) is, in general, an energy selective technique and, in case of crystalline systems, may become site selective spectroscopy. The first FLN spectrum in the solid state was performed by Szabo on ruby using a ruby laser [8]. The principle of the experiment is to excite a subset of chromophores within an inhomogeneously broadened transition of a given absorption spectrum, usually an electronic origin. In this thesis, the FLN spectra were recorded exclusively within the R_1 line of the $^2E \rightarrow {}^4A_2$ emission of Cr^{3+} in distorted octahedral fields. As detailed in Section 1.1, Cr^{3+} in a trigonally distorted octahedral field exhibits zero field splittings (ZFS) of both the ^2E and the $^4A_2$ states. Figure 2.2 shows a scheme representing the principle of FLN spectroscopy, together with the mechanism for resonant energy transfer discussed in detail in Chapter 3.

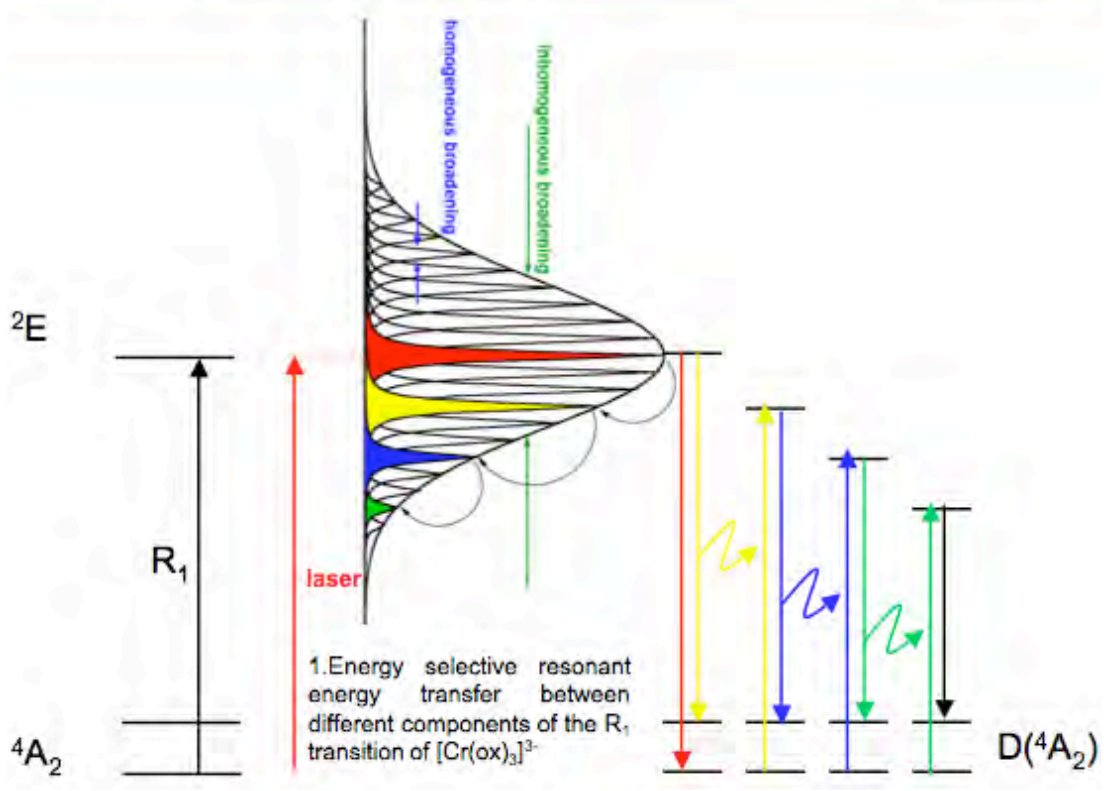

Figure 2.2. Principle of the FLN spectroscopy and resonant energy migration within the ^3E line of trigonally distorted octahedral Cr^{3+}.

After selective excitation of a subset of chromophores within the inhomogeneous distribution, here with a single frequency red laser, the excited chromophores can

deactivate to the lower or the upper level of the ground state. If they do so by simple emission, this results in two sharp lines with theoretical line widths equal to the homogenous line width. Since at low temperatures the homogeneous line width is often much smaller than the inhomogeneous broadening, the thus narrowed luminescence spectrum can resolve the small ZFS of the ground state. In concentrated samples, the energy coming from the deactivation can also be transferred non-radiatively to another chromophore requiring the same energy for excitation. If this energy transfer is phonon-assisted, then all narrowing is lost into the appearance of the inhomogeneous line width of the non-selectively excited luminescence. However, if this occurs resonantly, then this will result on the one hand in a broadening of the sharp lines with time, known as spectral diffusion, or if the energy available from the transition to the upper level of the ground state is sufficient to excite a chromophore of another set from its lower level, one can observe multi-line patterns for the FLN spectra as will be detailed in the experimental chapters. Those multi-line patterns have peaks separated by the ZFS of Cr^{3+} in the given lattice, and represent the resonant energy transfer within the absorption band. FLN spectroscopy thus constitutes an excellent diagnostic tool for differentiating energy migration types at high concentrations of chromophores. Figure 2.3 shows a picture from the laboratory presenting the optical table with the FLN experiment set-up. FLN spectra were obtained by selective excitation using a single frequency Ti:Sapphire laser (Coherent 899, 2 GHz bandwidth) pumped by a 5 W diode-pumped, frequency-doubled Nd:YVO_4 laser (Coherent Verdi) at around 14450 cm^{-1}, that is, within the R_1 electronic origin of Cr^{3+}. The collected emission was dispersed by a double monochromator (SPEX 1403) and recorded with a CCD camera (Roper Instruments), giving a spectral resolution of 0.25 cm^{-1}. Sample temperatures between 1.5 and 4.2 K with the sample sitting in liquid helium were achieved in a pumped He bath cryostat (Cryoindustries, 800, 2623). In order to avoid laser signal during the detection, both the laser and the resulting luminescence of the sample pass through a chopper with a phase-shift.

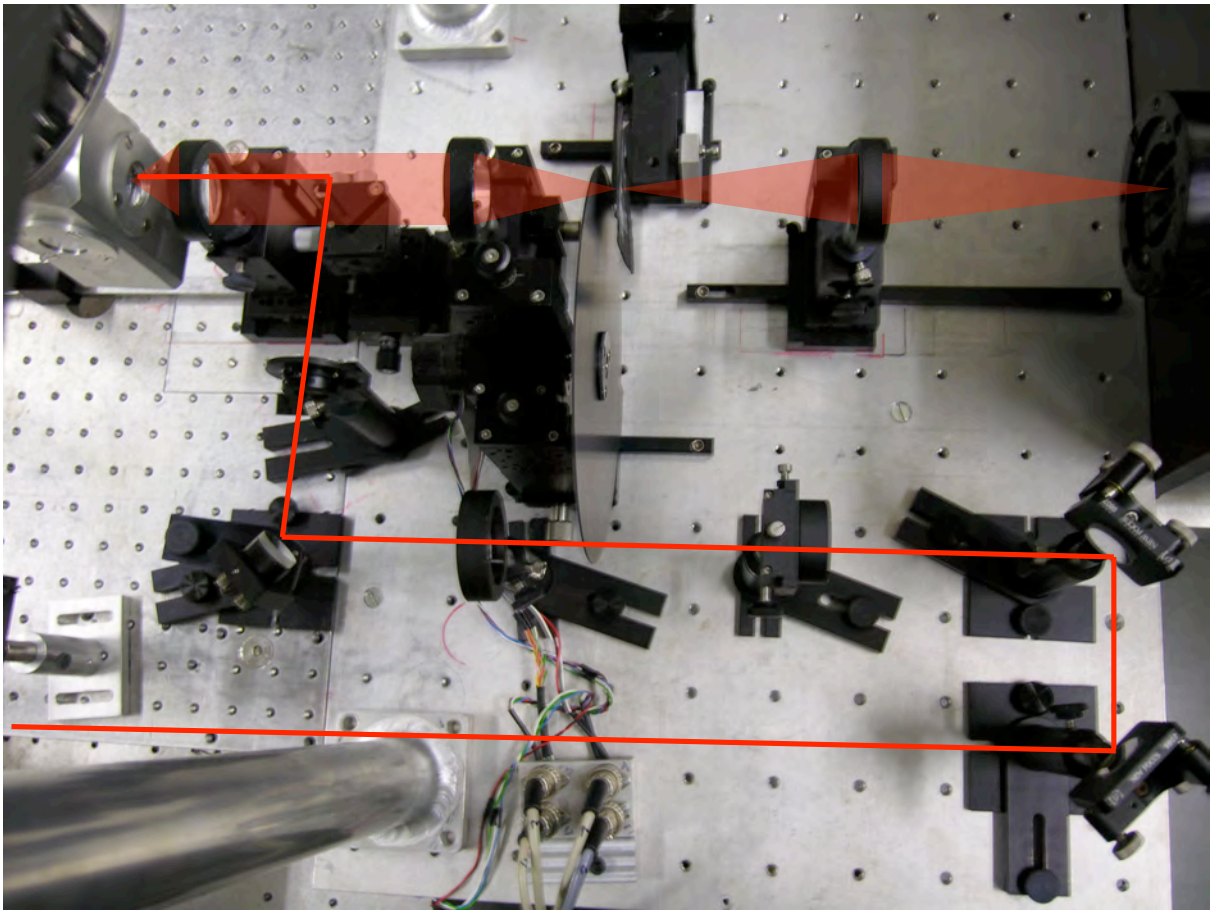

Figure 2.3. The FLN set up as used in our laboratory. The red line shows the path of the excitation laser through the alternating chopper through which also the collected luminescence from the sample is passed. The alternating chopper and the pinhole at the focal point of the collection optics are crucial for an efficient elimination of the excitation laser light from the detection set-up.

Consequently, the light coming from the laser is cut during the detection of the luminescence coming from the sample. Special discs for the chopper, built in this laboratory and shown in the Figure 2.4, allow recording time resolved FLN spectra.

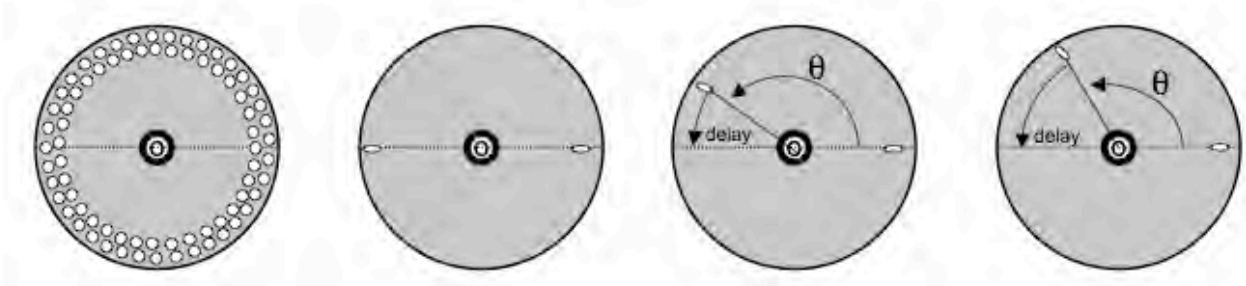

Figure 2.4. Discs for steady state and the time resolved FLN experiments.

There are two holes in the discs, one letting through the laser for the excitation and the other letting through the sample emission for the detection. The slit widths are such that excitation pulses down to 10 μs can be achieved. The angle between the two holes on the chopper determines the delay between the excitation and detection of the luminescence. Table 2.4 shows the delays for each angle at 8000 rpm.

Table 2.4. The delays for the corresponding angles on the discs for the time-resolved FLN spectra at 8000 rpm.

Angles θ (degree)	Delay (μs)
179.52	10
178.56	30
175.20	100
168.00	250
153.60	550
132.00	1000
103.20	1600
67.20	2350
24	3250

The optical table is aligned using a standard polished ruby sample. The aligning experiment was done at room temperature using the steady state disc, with 56 mW laser excitation at 14396.4 cm^{-1} (694.62 nm), 0.5 s acquisition time on the CCD and 40 μm slits on the monochromator. The resulting spectrum for the optimally aligned table is shown in Figure 2.5.

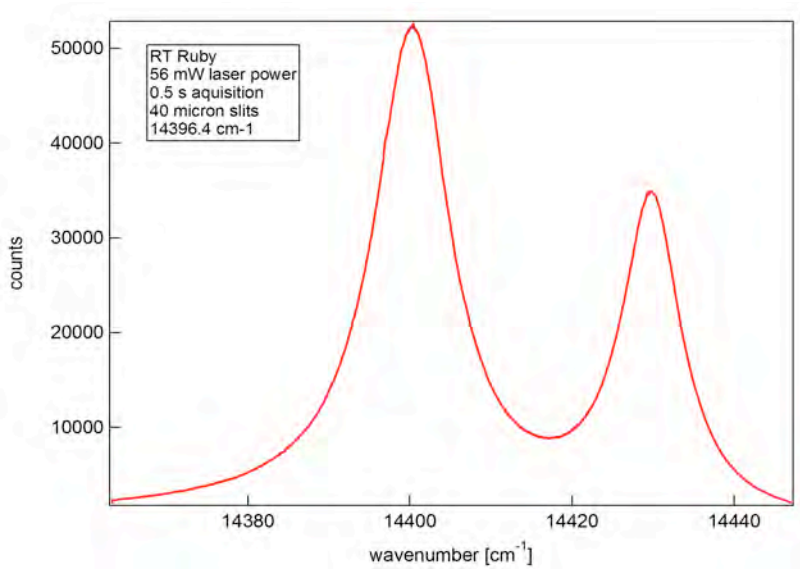

Figure 2.5. The R lines of ruby as measured using the FLN set-up serve to optimise the optical paths on the table.

2.4 Persistent spectral Hole Burning

Spectral hole burning is likewise an energy selective technique, which consists of exciting a subset of chromophores within an inhomogeneously broadened absorption band with a narrow band laser and afterwards recording the remaining absorption [9]. There are two different types of spectral hole burning: transient [10] and persistent [11,12] spectral hole burning. Transient spectral hole burning is a universal phenomenon. Upon selective excitation of a subset of chromophores a depletion of the ground state occurs at the laser frequency. This depletion, which manifests itself as a spectral hole in the inhomogeneous absorption spectrum, lasts as long as the system takes to relax back to the initial ground state level. Thus it is obvious that it is much easier to perform experiments on long-lived excited states. On the other hand, persistent spectral hole burning gives rise to long-lived holes in the absorption bands and involves a photochemical [13] or photophysical [14,15] reaction of the subset of chromophores under irradiation. In this thesis, an example of persistent photophysical spectral hole burning will be shown. In contrast to the high-resolution work of Riesen et al. [16,17], the phenomenon to be studied here requires only comparatively low resolution provided by the above-mentioned double

monochromator. Figure 2.6 shows the corresponding scheme of the set-up for the persistent spectral hole burning with which spectral holes can be detected both in emission and in absorption. It is basically the same set up as for FLN experiments; the difference is the second laser for non-selective excitation that joins the path of the first red laser through a beam splitter. Thus, one can be sure that the laser which burns the hole, and the laser for non-selective excitation hit the sample at exactly the same spot. The lasers used for the persistent hole burning are the above mentioned Ti:sapphire laser (Coherent 899, 2 GHz bandwidth) pumped by a 5 W diode-pumped, frequency-doubled Nd:YVO_4 laser (Coherent Verdi) for the burning part, and the intracavity frequency doubled 532 nm Nd:YAG laser (ILEE VA-I-N-532) for the excitation after burning the hole. For detecting the spectral holes in a conventional transmission experiment a tungsten halogen lamp in conjunction with a narrow band pass filter were used. The three optical paths are shown in the scheme of Figure 2.6.

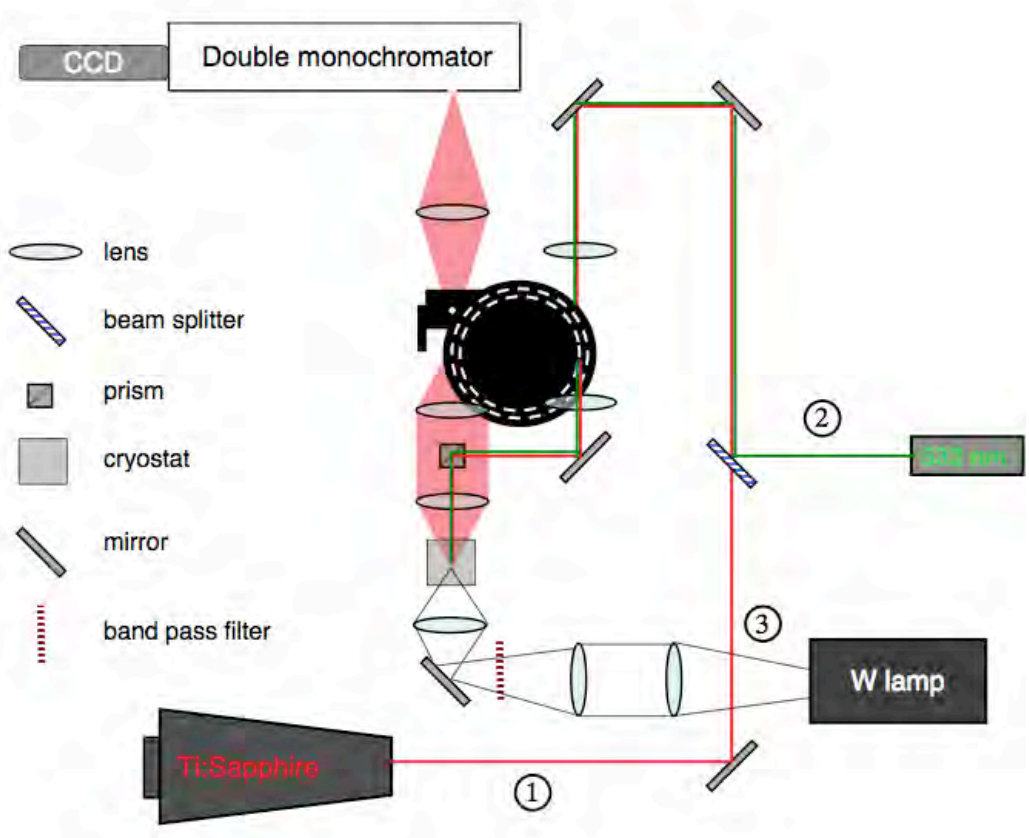

Figure 2.6. Optical set-up for FLN, Hole Burning spectroscopy, and conventional absorption and luminescence spectroscopy.

2.5 High pressure experiments

The high-pressure experiments were realised in a Diamond Anvil cell (MiniDAC of D'Anvils Ltd). It consists of two diamonds separated by a metal gasket. The advantage of the diamond is its resistance to compressibility and its transparency to the optical part of the electromagnetic radiation. The diameter of the polished side of the diamonds is 700 µm, and with applying a pressure between the two diamonds with the metal gasket in between, an indentation is made of the same diameter, 700 µm, as shown in Figure 2.7 [18]. The last step, for preparing the Diamond Anvil cell ready for the experiments, is to make a hole within the indentation in the metal gasket, in which later, the sample and the pressure sensor will be put. In our experiments the holes have a diameter of 200-300 µm.

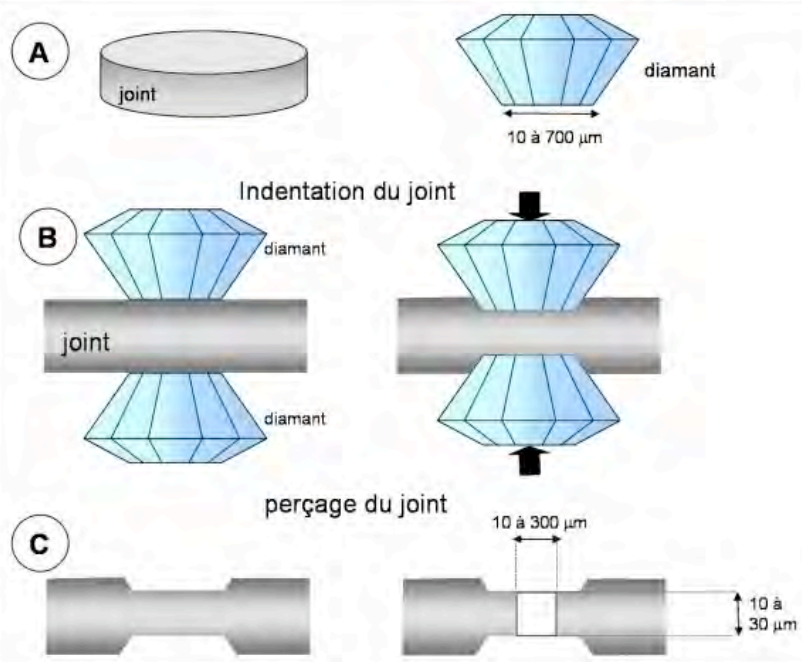

Figure 2.7. The conception and construction of the diamond anvil cell. In our experiments the diameter of the polished side of the diamond is 700 µm and the hole where the sample is put is 200-300 µm [18].

Once the cell is prepared, the sample and the pressure sensor are put into the sample chamber. A pressure transmitter is required in order to have a homogeneous pressure in the entire sample chamber. The pressure transmitter can be a gas, or a mixture of methanol/ethanol or silicon oil, depending on the pressure range to be applied and on the sample to be studied as well. In our experiments, we mainly used

a silicon oil, polydimethylsiloxane, trimethylsiloxy terminated. Finally the cell is closed with the other diamond, paying attention to avoid any gas bubbles that could remain in the sample chamber and would influence the experimental results. All the steps are shown in the Figure 2.8. The pressure sensor must be a sample whose shift rate as a function of pressure is well known and established. The commonly used ruby cannot be used in the present case, as its R lines overlap with the R lines of the $[Cr(ox)_3]^{3+}$. Thus in a first step, we determined the shift rate of the $^5D_0 \rightarrow {}^7F_0$ transition of Sm^{2+}:BaFCl using ruby as pressure sensor. This system was then used as reference to determine the shift rate of $[Cr(ox)_3]^{3-}$ in the networks. And last but not least, the shift rate of the latter was used as reference for the project on energy transfer under external pressure. In this case, the pressure sensor was within the sample $[Cr(bpy)_3][NaCr(ox)_3]ClO_4$ itself. Once the Diamond Anvil cell with the sample is ready for the measurements, it is placed in a closed cycle cryostat (Oxford Instruments CCC1204), and spectra could be collected down to 10 K.

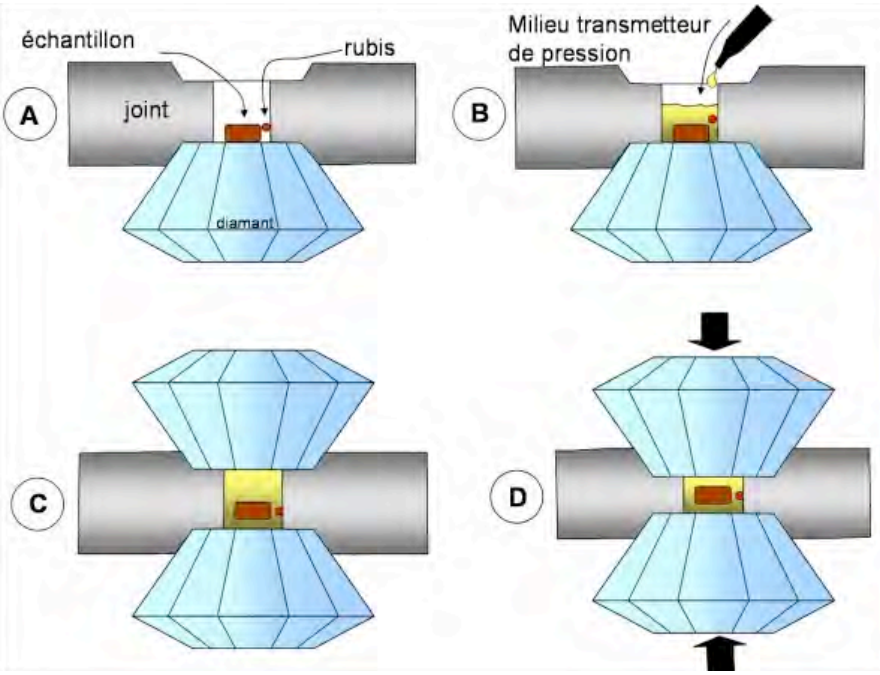

Figure 2.8. The different steps of preparing the Diamond Anvil cell with the sample ready for the high-pressure measurements [18].

References

[1] S. Decurtins, H.W. Schmalle, P. Schneuwly, J. Ensling, P. Gütlich, J. Am. Chem. Soc. 116 (1994) 9521.

[2] S. Decurtins, H.W. Schmalle, R. Pellaux, P. Schneuwly, A. Hauser, Inorg. Chem. 35 (1996) 1451.

[3] M. Milos, S. Kairouani, S. Rabaste, A. Hauser, Coord. Chem. Rev. 252 (2008) 2540.

[4] M. Milos, A. Hauser, Inorg. Chem. 49 (2010) 3402.

[5] M. Milos, P. Pal, A. Hauser, ChemPhysChem, accepted (2010).

[6] T.S. Piper, R.L. Carlin, J. Chem. Phys. 35 (1961) 1809.

[7] J. Lipkowski, J. Herbich, Roczn. Chem. 49 (1975) 853.

[8] A. Szabo, Phys. Rev. Lett. 25 (1970) 924.

[9] B.M. Kharlamov, L.A. Bykovskaya, R.I. Personov, Chem. Phys. Lett. 50 (1977) 407.

[10] H. Riesen, Coord. Chem. Rev. 250 (2006) 1737.

[11] W. Moerner, Proceedings of SPIE, International Society for Optical Engineering 541 (1985) 60.

[12] W.E. Moerner, in W.E. Moerner (Ed.), Top. Curr. Phys. Springer-Verlag, Berlin, 1988.

[13] J. Friedrich, D. Haarer, Angew. Chem. 23 (1984) 113.

[14] M.L. Lewis, H. Riesen, Phys. Chem. Comm 26 (2001) 1.

[15] T. Monks-Corrigan, H. Riesen, Chem. Phys. Lett. 419 (2006) 321.

[16] M.L. Lewis, H. Riesen, J. Phys. Chem. A 106 (2002) 8039.

[17] H. Riesen, J.L. Hughes, Chem. Phys. Lett. 372 (2003) 563.

[18] http://planet-terre.ens-lyon.fr/planetterre/XML/db/planetterre/metadata/LOM-cellule-diamant.xml.

3. Energy Migration within the ^2E state of Cr^{3+}

*Published in Coordination Chemistry Review, 252, **2008**, 2540*

Mia Milos, Sélim Kairouani, Sébastien Rabaste, Andreas Hauser*

Contents

Abstract

Excitation energy migration is an important phenomenon at high concentration of luminescent chromophores. In crystalline solids it results in a quenching of the intrinsic luminescence of the chromophore as the excitation energy migrates to impurity centres or other forms of trap sites. As concluded from the extensively studied systems where Cr^{3+} is doped as the active chromophore into inert host lattices, energy migration in crystalline solids is usually a phonon-assisted process, in which the simultaneous creation or annihilation of phonons helps to bridge the energy miss-match in the energy levels of two neighbouring chromophores within a inhomogeneously broadened absorption band. However, in the three-dimensional network systems $[Ru(bpy)_3][NaCr(ox)_3]$ and $[Rh(bpy)_3][NaCr(ox)_3]ClO_4$, it proved possible to unambiguously identify three different mechanisms for energy migration within the R_1 line of the $^4A_2 \rightarrow {}^2E$ transition of Cr^{3+}. In addition to the common temperature dependant phonon-assisted process, a resonant process between the zero-field split components of the $^4A_2$ ground state leading to a multi-line pattern in a Fluorescence Line Narrowing spectrum and quasi-resonant process within the same component leading to fast spectral diffusion can be identified at very low temperature. The parameters governing these processes are discussed and the behaviour of the model systems is compared to more conventional doped oxides and related systems.

Keywords: resonant and phonon-assisted excitation energy migration; $[Cr(ox)_3]^{3-}$; fluorescence line narrowing; spectral diffusion

3.1 Introduction

Excitation energy transfer processes are subject of continuing attention since they play an important role in many areas of physics, chemistry and biology. In such a process, the excitation energy is transferred from an initially excited chromophore, the donor, to a nearby chromophore, the acceptor. Excitation energy transfer processes are important for solid state lasers [1], fluorescent lamps and displays [2], solar energy conversion cells [3], conformational analyses of proteins and investigations on the folding dynamics of DNA [4], and many other areas of current research. For high chromophore concentrations, the excitation energy can be transferred over longer distances in a sequence of transfer steps in which donor and acceptor are chemically identical and in which the acceptor in one step becomes the donor for the next step. This is generally referred to as energy migration [5].

Excitation energy can be transferred from the initially excited donor to an acceptor via radiative and non-radiative processes [6]. Radiative energy transfer is a sequential process in which the donor emits a photon, which, in turn, is reabsorbed by the acceptor. The probability of a radiative energy transfer process is proportional to the concentration of the acceptor, the spectral overlap integral between the emission of the donor and the absorption of the acceptor, and it depends on the shape and size of the sample, but it does not require any explicit interaction between donor and acceptor and is therefore of long-range nature. Radiative processes may become important in large samples such as laser crystals. With regard to energy migration, they result in an apparent increase of the observed luminescence lifetime, a phenomenon referred to as photon trapping [7]. For instance, the observed lifetime of the $^2F_{5/2} \rightarrow {}^2F_{7/2}$ emission in YAG:Yb^{3+} increases from the intrinsic value of 0.95 ms in a diluted and optically thin sample to around 1.3 ms for larger crystals [8]. Likewise, in Al_2O_3:Cr^{3+} (ruby) the apparent lifetime of the R-line emission may increase from the intrinsic value of 3.8 ms up to 12 ms [7].

In a non-radiative energy transfer process, the deactivation of the donor and the excitation of the acceptor take place simultaneously and thus requires an electronic interaction between the two. In 1949, Förster [9] proposed the first mechanism for non-radiative energy transfer based on electric-dipole–electric-dipole interaction

between the donor and the acceptor transition dipole moments of the respective excitations. As dipole-dipole interactions fall off as R^{-3}, they are of comparatively long-range nature. Dexter [10] extended the work of Förster to include higher order multipole interactions and magnetic dipole interactions as well as exchange interactions. The latter may become dominant if the two chromophores are in close contact with each other, for instance two metal centres via a common bridging ligand or organic chromophores via π-π stacking. If such is the case, super-exchange may substantially enhance the interaction at short distances, and if sufficiently strong, the energy transfer may occur as excitonic motion [11] rather than as simple hopping. Both mechanisms consider the energy transfer to be a resonant process, that is, the energy provided by the donor is entirely transferred to the acceptor. Thus, the absorption of the acceptor transition must energetically match the emission of the donor transition. If such is not the case, an eventual energy mismatch can be bridged by the creation or annihilation of vibrational energy in a so-called phonon-assisted process [12]. Phonon-assisted energy transfer and energy migration is a common phenomenon in systems having narrow absorption and emission lines with generally small or no spectral overlap such as f-f transitions in lanthanide containing systems or spin-flip transitions in transition metal ions [13]. Phonon-assisted energy transfer is strongly temperature dependent and usually freezes in at low temperatures.

One of the model systems for studying energy migration in inorganic solids is provided by the spin-forbidden $^4A_2 \rightarrow {}^2E$ transition of Cr^{3+} [14] in octahedral coordination in a moderate to strong ligand field. In Section 3.2, the relevant physical parameters are discussed and the corresponding literature is briefly reviewed. In Section 3.3, the theoretical concepts for excitation energy transfer, with emphasis on energy migration at high chromophore concentration, are introduced. As discussed in detail in Section 3.4, the three-dimensional oxalate networks of compositions $[Ru(bpy)_3][NaCr(ox)_3]$ and $[Rh(bpy)_3][NaCr(ox)_3]ClO_4$ serve as model compounds for the unambiguous identification of the different mechanisms of energy migration within the ^2E state of the $[Cr(ox)_3]^{3-}$ chromophore [15].

3.2 The $^4A_2 \rightarrow {}^2E$ transition of Cr^{3+} in pseudo-octahedral coordination

The Cr^{3+} ($3d^3$) ion in octahedral or close to octahedral coordination, particularly in doped materials such as ruby, has been extensively studied by spectroscopists for over a hundred years and has played an important role in the development of ligand-field theory [16]. Thus, for weak ligand fields, the lowest excited state is a $^4T_2(t_{2g}{}^2e_g{}^1)$ state having the same spin multiplicity as the $^4A_2(t_{2g}{}^3)$ ground state, whereas for moderate to strong ligand fields the lowest excited state is the $^2E(t_{2g}{}^3)$ state having a different spin multiplicity but the same orbital occupancy as the ground state. In addition there are higher lying doublet and quartet ligand-field states. As a result the Cr^{3+} ion has comparatively strong visible absorption bands corresponding to spin-allowed ligand-field transitions from the $^4A_2(t_{2g}{}^3)$ ground state to the $^4T_2(t_{2g}{}^2e_g{}^1)$, $^4T_1(t_{2g}{}^2e_g{}^1)$ and $^4T_1(t_{2g}{}^1e_g{}^2)$ excited states and additional weak but sharp features at the edge to the near infrared corresponding to the multiplet of the $^4A_2(t_{2g}{}^3) \rightarrow {}^2E(t_{2g}{}^3)$ transition as well as to other doublet states at higher energies. For the $^4A_2 \rightarrow {}^4T_2$ transition, one electron is promoted to the anti-bonding e_g orbitals resulting in a marked elongation of the metal-ligand bond-length. On the other hand, the $^4A_2 \rightarrow {}^2E$ transition is a spin-flip transition, and consequently there are no important geometrical changes in the ^2E state with respect to the ground state, as is schematically shown in the configurational coordinate diagram in Figure 3.1.

Upon excitation, deactivation may occur via different channels depending upon the ligand-field strength as well as the excitation energy [17]. Excitation into the higher-lying spin-allowed bands mainly results in rapid non-radiative deactivation to the $^4T_2$ state. In turn, the $^4T_2$ state can undergo a radiationless intersystem crossing process to the ^2E state if the latter is the lowest excited state, or it can undergo a radiative or non-radiative transition down to the ground state if it is the lowest excited state. Finally for complexes in solution it can be involved in excited state chemical reactions, such as for instance photo-induced ligand exchange [17]. If the ^2E state is the lowest excited state, $^2E \rightarrow {}^4A_2$ luminescence is generally observed, at least at low temperatures. For small $^4T_2 - {}^2E$ energy gaps, this luminescence may be quenched via thermal population of the $^4T_2$ state [17, 18].

In this study, emphasis will be on the $^4A_2 \rightarrow {}^2E$ transition and in particular on different mechanisms of non-radiative energy transfer processes that take place within this transition for chromium(III) in an oxygen environment. The excited-state dynamics of such systems have been studied in detail by Forster [18]. In ruby each Cr^{3+} is surrounded by a trigonally distorted (C_{3v}) octahedron of six nearest neighbour oxygen atoms. All sites are crystallographically equivalent, $^4T_2$ is above ^2E and the gap $^4T_2 - {}^2E$ is quite large. As a result the $^2E \rightarrow {}^4A_2$ phosphorescence dominates up to 400 K. In emerald ($Be_3Al_2(SiO_3)_6:Cr^{3+}$) the $^4T_2 - {}^2E$ gap is smaller and consequently the phosphorescence is only observed up to 77 K. Above that temperature the broad fluorescence from the $^4T_2 \rightarrow {}^4A_2$ grows in intensity and dominates at 300 K.

In lower than octahedral symmetry, as for instance in the C_3 site symmetry of Cr^{3+} in ruby, both the $^4A_2$ ground state as well as the ^2E excited state are split by the combined effects of the lower symmetry and spin-orbit coupling, as schematically shown in Figure 3.1. In ruby the zero-splitting splitting (ZFS) of the ^2E state is 29 cm^{-1} and easily resolved optically in both absorption and emission spectra, giving rise to the two R-lines. The ground state ZFS of 0.39 cm^{-1} is not so easily resolved in simple luminescence spectra. It can be determined by EPR spectroscopy [19] or by more sophisticated techniques such as Fluorescence Line Narrowing spectroscopy [20-22] or Spectral Hole Burning [21-23].

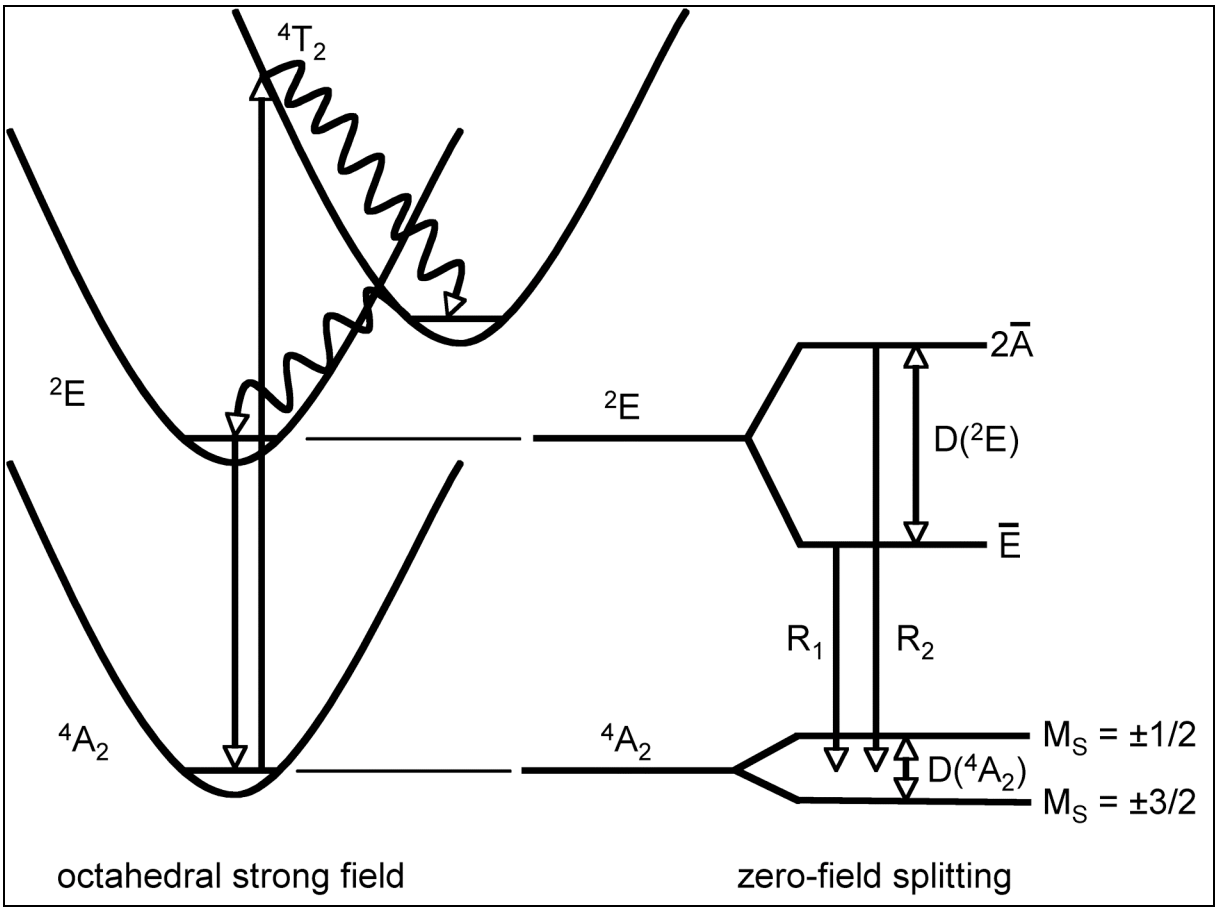

Figure 3.1. Scheme of the ground state and the lowest excited ligand-field states of Cr^{3+} in a moderate to strong octahedral ligand field (left) and the zero-field splittings resulting from a trigonal distortion and spin-orbit coupling (right).

3.3 The model systems $[Ru(bpy)_3][NaCr(ox)_3]$ and $[Rh(bpy)_3][NaCr(ox)_3]ClO_4$

The $[Cr(ox)_3]^{3-}$ complex may be considered as chemist's version of ruby, with six-fold oxygen coordination and the tris-chelate complex having D_3 point group symmetry. As shown below, its spectroscopic properties are very similar to those of Cr^{3+} in ruby. However, as molecular unit, it can be incorporated into stoechiometric compounds, for instance in the three-dimensional networks as model systems for studying different mechanisms of energy migration.

3.3.1 The crystal structure

The three-dimensional networks of the compounds $[Ru(bpy)_3][NaCr(ox)_3]$ and $[Rh(bpy)_3][NaCr(ox)_3]ClO_4$ crystallise in the cubic and chiral space group $P2_13$ with Z = 4 [24]. The site symmetry of all metal centres is C_3, that is, in the crystal structure the three-fold molecular axis of the tris-chelate complex is retained. As shown in Figure 3.2, the three-dimensional network is formed by the $[Cr(ox)_3]^{3-}$ complexes bridged by the Na^+ ions, and it provides perfect cavities for the size and the geometry of the $[M^{II/III}(bpy)_3]^{2+}$ complexes. The structure of the oxalate network is effectively stabilised by the templating effect of the tris-bipyridine complexes through electrostatic interactions as well as $\pi\pi$ interactions between the oxalate and the bipyridine ligands. The chromium and the sodium ions are perfectly organised in an alternating fashion throughout the oxalate network. Thus, the chromium ions are never connected to each other directly by an oxalate bridge, and therefore super-exchange interactions between them are virtually non-existent [25]. This will have important consequences for energy migration.

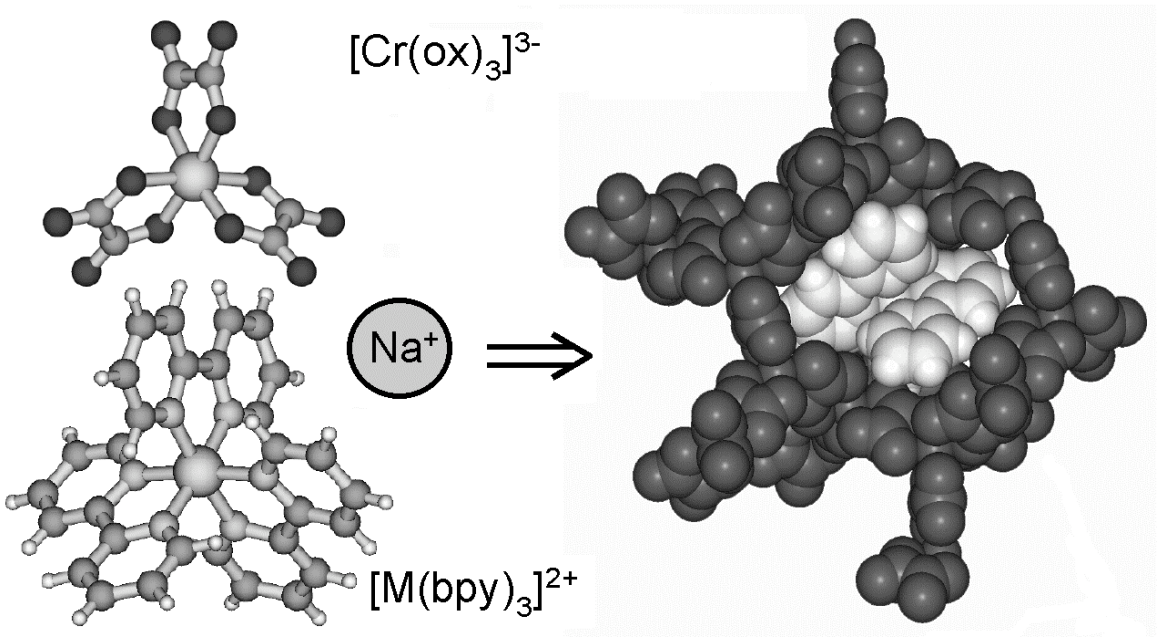

Figure 3.2. The complexes $[Cr(ox)_3]^{3-}$ and $[M(bpy)_3]^{2+}$, and the three-dimensional oxalate network (black) encapsulating the tri-bipyridine cation (white) in $[M(bpy)_3][NaCr(ox)_3]$ (adapted from Ref. [15a]).

3.3.2 Absorption and emission spectra

Figure 3.3 shows the single crystal absorption spectrum of $[Zn(bpy)_3][NaCr(ox)_3]$ in the region of the ligand-field bands. It is essentially identical to the spectrum of $[Cr(ox)_3]^{3-}$ reported by Schmitdke et al. [26a] and Mortensen [26b]. The broad bands centred at 18000 cm^{-1} and at 25400 cm^{-1} are readily attributed to the spin-allowed $^4A_2 \rightarrow {}^4T_2$ and $^4A_2 \rightarrow {}^4T_1$ transitions, respectively. The weak and sharp features at 14400, 14800 and 21000 cm^{-1} are attributed to the spin-flip transitions $^4A_2 \rightarrow {}^2E$, $^4A_2 \rightarrow {}^2T_1$ and $^4A_2 \rightarrow {}^2T_2$, respectively, which have their intensity concentrated in the electronic origins.

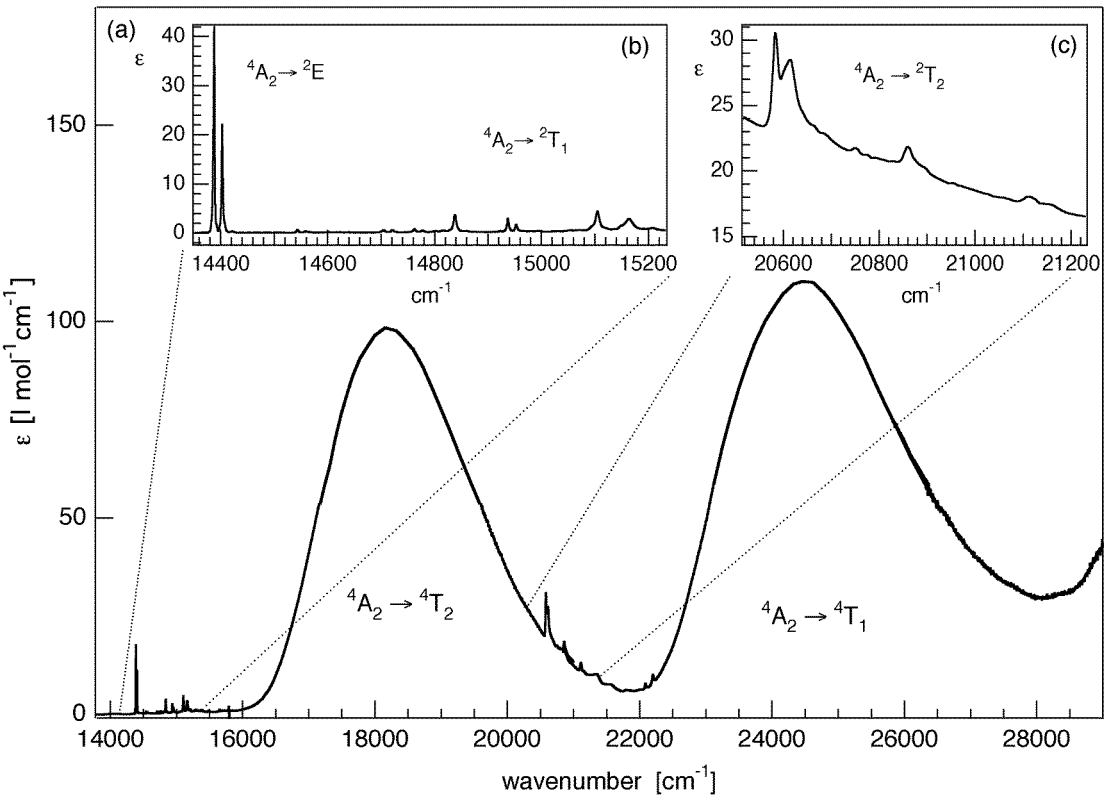

Figure 3.3. Single crystal absorption spectrum of $[Zn(bpy)_3][NaCr(ox)_3]$ at 10.4 K; a) full spectrum, b) the $^4A_2 \rightarrow {}^2E$ and $^4A_2 \rightarrow {}^2T_1$ transitions, and c) the $^4A_2 \rightarrow {}^2T_2$ transition.

Figure 3.4 shows the enlarged region of the electronic origins of the $^4A_2 \rightarrow {}^2E$ transition, that is, the R_1 and the R_2 lines, in absorption at 10.4 K for $[Rh(bpy)_3][NaCr(ox)_3]ClO_4$ and $[Ru(bpy)_3][NaCr(ox)_3]$, respectively. For the former, the

ZFS of the ^2E state is 13.1 cm^{-1}, for the latter it is 13.7 cm^{-1}. The key difference between the spectra of the two compounds lies in the inhomogeneous line width resulting from non-equivalent static distortions in the crystalline environment of the chromophores. Whereas for $[Rh(bpy)_3][NaCr(ox)_3]ClO_4$ it is approximately 4.3 cm^{-1}, it is considerably smaller for $[Ru(bpy)_3][NaCr(ox)_3]$. The oscillator strengths, however, are identical, and for R_1 a value of $6x10^{-7}$ can be derived from standard theory [27]. The shoulders in both R lines of the ruthenium(II) compound indicate that for this compound the ZFS of the $^4A_2$ ground state is on the verge of being resolved. A least squares fit with a sum of two Gaussians to both R lines give a value of 1.29(7) cm^{-1} for the ground state ZFS and a inhomogeneous line width of 1.1(1) cm^{-1}. This value of the ZFS is in line with values determined by EPR spectroscopy [28] and high-resolution optical methods [29], which also identified the Ms = ±3/2 component of the $^4A_2$ multiplet as the ground state.

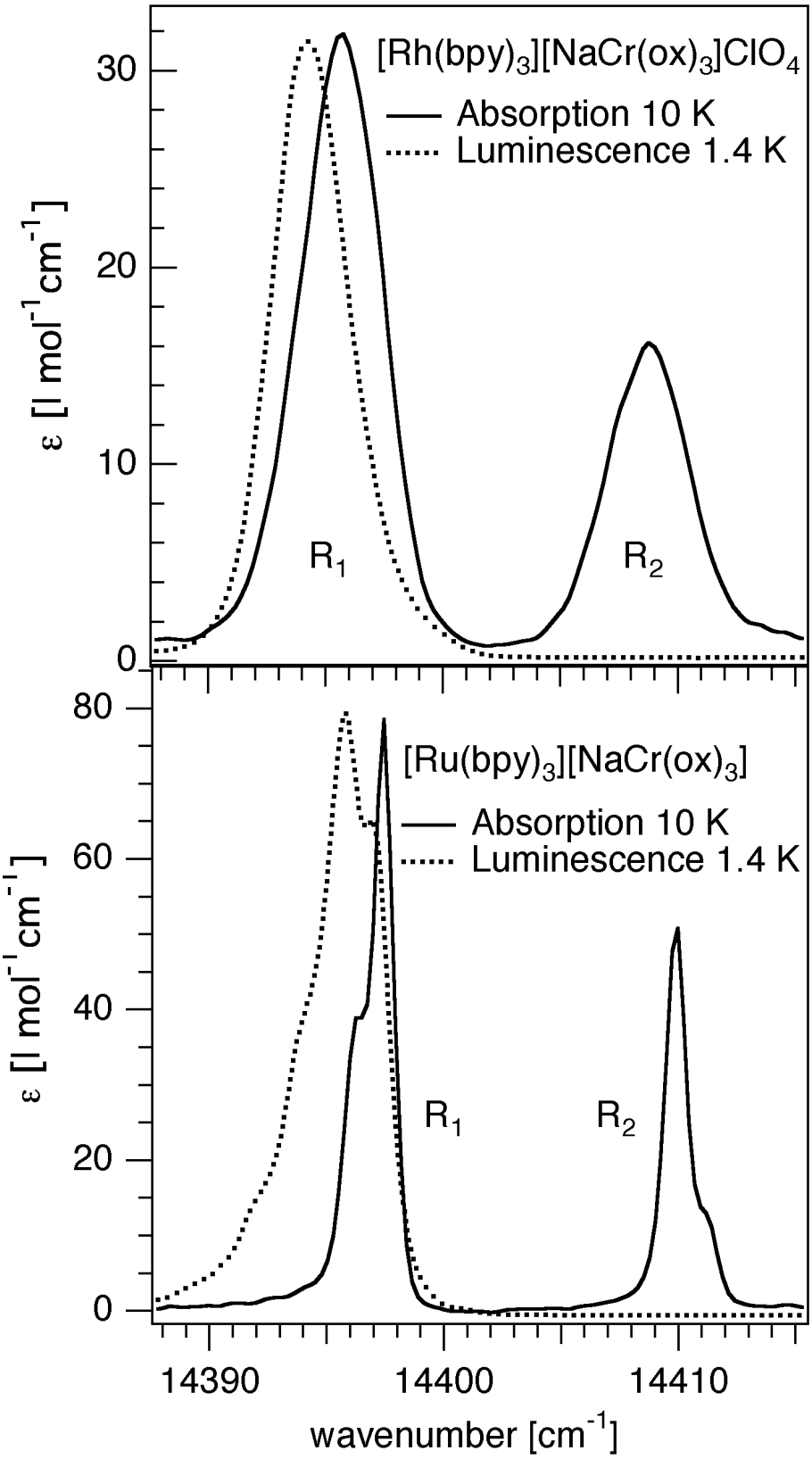

Figure 3.4. The $^4A_2 \rightarrow {}^2E$ transition in absorption at 10.4 K (——) and in emission at 1.4 K (····) for $[Rh(bpy)_3][NaCr(ox)_3]ClO_4$ (top) and $[Ru(bpy)_3][NaCr(ox)_3]$ (bottom) single crystals. For the latter, the fit of two Gaussians to the R lines in absorption is included.

Figure 3.4 includes the luminescence observed at 1.4 K upon non-selective excitation into the $^4T_2$ absorption band of the $[Cr(ox)_3]^{3-}$ chromophore at 18416 cm^{-1} (543 nm). The narrow band luminescence is assigned to the $^2E \rightarrow {}^4A_2$ transition and is fed via efficient intersystem crossing from the $^4T_2$ state. At 1.4 K only the lower component of the ^2E state is populated and therefore only the R_1 line is observed. For both compounds and in contrast to diluted systems, the luminescence is slightly shifted to lower energies with respect to the absorption. This gives a first indication that in these highly concentrated systems energy migration is indeed important. In addition, the emission from $[Ru(bpy)_3][NaCr(ox)_3]$ shows a weak structure with multiple spacings corresponding to the ZFS of the ground state.

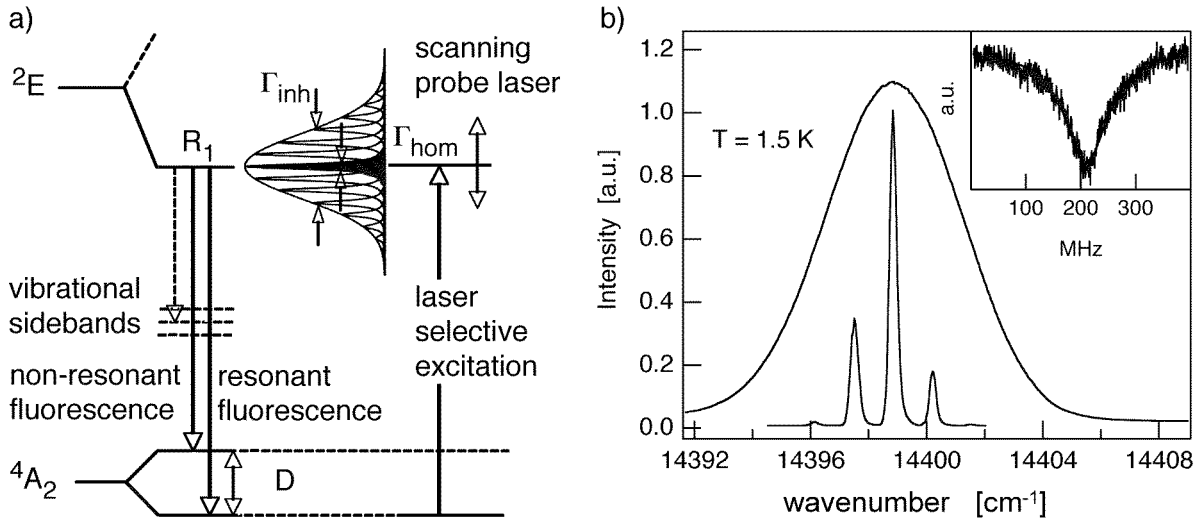

Figure 3.5. a) The principle of fluorescence line narrowing using laser selective excitation exciting a subset of complexes within the inhomogeneously broadened electronic origin. In order to prevent laser light from the excitation source from entering the detection system, the excitation source is chopped at a comparatively high frequency and the luminescence light is only collected during the dark time of the excitation source. For transient spectral hole burning, a single frequency pump laser is kept at a fixed frequency keeping up a steady state population in the excited state. This spectral hole is probed by a second single frequency laser, which is scanned across the corresponding spectral range. Detection can be either done by direct transmission or in an excitation type configuration using the vibrational side bands of the emission. b) Non-selective luminescence and FLN spectrum at 1.5 K of $[Rh(bpy)_3][NaAl(ox)_3]ClO_4$ doped with 0.5% Cr^{3+}. Inset: transient spectral hole of the resonant line.

In contrast to ruby for which the luminescence quantum efficiency is close to unity from cryogenic temperatures all the way up to room temperature, this is not the case for the oxalate networks. Even when doped into inert host lattices such as $[Rh(bpy)_3][NaAl(ox)_3]ClO_4$ where Cr^{3+} substitutes for Al^{3+}, the luminescence is quenched at T > 100 K. This is due to rapid non-radiative multiphonon relaxation via thermally activated back-intersystem crossing to the $^4T_2$ state [30]. Nevertheless, at T < 50 K, the luminescence quantum efficiency in such dilute systems approaches unity as borne out by the observed luminescence lifetime in diluted systems of 1.3 ms [15], that is, close to the radiative lifetime estimated from the oscillator strength, again according to standard theory [27]. In the concentrated oxalate networks, the luminescence intensity decreases rapidly above 4.2 K, another indication for rapid energy migration and quenching by killer traps present at low concentrations even if ultra pure chemicals are used in the synthesis.

3.4 Electronic origins, homogeneous line widths and inhomogeneous broadening

The ultimate line width called the homogenous line width Γ_{hom} of an electronic origin having a Lorentzian lineshape is given by its total dephasing time T_2 according to

$$\Gamma_{hom} = \frac{1}{\pi T_2} = \frac{1}{\pi}\left(\frac{1}{2T_1} + \frac{1}{T_2^*}\right) \qquad (1)$$

where T_2^* is the pure dephasing time and T_1 is the lifetime of the excited state level. T_1 contains all processes affecting the lifetimes of the levels in question and should not be confused with the observed luminescence lifetime. For a comprehensive discussion of the different contributions to T_2^* with special emphasis on transition metal complexes, the reader is referred to the excellent reviews by Riesen [32], who states that at low temperatures in diamagnetic systems, T_2^* is usually quite large and can thus be neglected as contribution to Γ_{hom}, but in paramagnetic systems electron-spin–electron-spin and electron-spin–nuclear spin interactions substantially shorten T_2^* and thus contribute to the residual homogeneous line width at low temperatures.

At temperatures above ~6 K, dephasing due to electron-phonon interactions become the dominant contribution to Γ_{hom} [6].

For most Cr^{3+} chromophores it is difficult to accurately determine the ZFS by conventional optical spectroscopy because at low temperatures the inhomogeneous distribution even in high quality crystals is often not only much larger than the homogeneous line width, it is also larger than the ZFS. As mentioned above, an alternative to EPR spectroscopy is provided by Fluorescence Line Narrowing (FLN) spectroscopy [18-22, 31]. The principle is shown schematically in Figure 3.5. A narrow band laser, tuned to the electronic origin of interest, selectively excites only a subset of chromophores within the inhomogeneously broadened band. For the $^4A_2 \rightarrow {}^2E$ transition in the absence of energy transfer processes, a typical three-line spectrum is observed as for instance in the FLN spectrum of $[Cr(ox)_3]^{3-}$ doped into $[Rh(bpy)_3][NaAl(ox)_3]ClO_4$ included in Figure 3.5. The central line is the resonant line and corresponds to the emission of the selectively excited chromophores back to the ground state component from which they were excited. The two satellites are non-resonant lines and are shifted to lower and higher energy by the ground state ZFS, the latter being a hot band resulting from the excitation from the Ms = ±1/2 component of the $^4A_2$ state. Indeed, the FLN spectrum confirms the ZFS of 1.3 cm^{-1} as determined above for $[Ru(bpy)_3][NaCr(ox)_3]$ by conventional spectroscopy.

In the above FLN spectra, the spectral resolution is limited to 0.25 cm^{-1} (8 GHz) by the ¾ m double monochromator used for light-dispersion. This is several orders of magnitude larger than the homogeneous line width. A versatile technique for determining homogeneous line widths is spectral hole burning [21-23, 31]. In spectral hole burning a subset of chromophore is depleted in the ground state upon selective laser excitation, resulting in a persistent or transient dip in the absorption or excitation spectrum. A transient ground state depletion can be monitored with a second laser, which is scanned at lower power across the wavelength of the pump beam. The inset of Figure 3.5 shows such a spectral hole recorded in excitation mode under continuous irradiation by the pump beam into the R_1 line of $[Rh(bpy)_3][NaAl(ox)_3]ClO_4$ doped with 0.5% Cr^{3+} at 1.5 K. The line shape is close to Lorentzian with an observed line width Γ_{obs} of 40 MHz. Spectral hole burning is a sequential two photon process: the first photon is used to burn the hole, the second photon is used in the readout

process. Therefore the homogenous line width Γ_{hom} corresponds to $\Gamma_{obs}/2$. Thus, in the lightly doped oxalate network at low concentration the homogeneous line width is 20 MHz at 1.5 K. This is in line with the value determined for the $NaMg[Al(ox)_3]\cdot 9H_2O$ host lattice doped with 1% Cr^{3+} by Riesen et al. [29], who also used hole burning spectroscopy in weak magnetic fields to unambiguously show that the Ms = ±3/2 component of the $^4A_2$ state is the true ground state of $[Cr(ox)_3]^{3-}$ and to determine ground and excited state g-values to high precision [32]. Riesen et al. also showed that the residual homogeneous line width of the R_1 becomes orders of magnitude smaller in a magnetic field due to the reduction in electron-spin–electron-spin relaxation, which is the main dephasing mechanism at low temperatures even in comparatively lightly doped materials [32], since spin-lattice relaxation times within the components of the $^4A_2$ ground state are of the order of milliseconds at low temperatures [33].

Accordingly, in more concentrated systems, homogeneous line widths are larger than in diluted system due to spin-spin relaxation. As shown in Figure 3.6 for T = 1.5 K, Γ_{hom} increases in a sigmoidal fashion from the initial 20 MHz (~0.0007 cm^{-1}) at x = 0.5% to a limiting value of ~600 MHz (~0.02 cm^{-1}) at x = 100%. The latter value may be considered as upper limit as it probably overestimates the true value since at high concentrations resonant energy migration (see below) within one subset may result in additional broadening of the observed line width in the hole burning experiment.

As likewise shown in Figure 3.6, the homogeneous line width is temperature dependent, increasing rapidly above 4.2 K, in particular for the diluted system. This is due to phonon-assisted relaxation processes such as direct absorption or emission of phonons, and Raman and Orbach processes [6] basically within the two components of ^2E state. As shown by Riesen, for $[Cr(ox)_3]^{3-}$ [29] and similar chromium(III) complexes [34], both the direct process as well as Raman processes contribute to the homogeneous line width above 4.2 K. In contrast, for ruby Raman processes dominate at higher temperatures [35, 22]. The key difference between the otherwise very similar chromophores lies in the density of phonon states at the energies of the ^2E ZFS, which is much higher for the softer oxalate systems with a Debye temperature of around 50 K [36] as compared to 950 K for ruby [37]. The fact that in the dilute oxalate network the homogeneous line width increases more rapidly than in

the $NaMgAl(ox)_3 \cdot 9H_2O$ host investigated by Riesen et al. [29] is due to the smaller ZFS of 13.2 cm^{-1} as compared to 20 cm^{-1} for the latter. For a comprehensive discussion of the homogeneous line width as a function of temperature the reader is referred to Ref. [31]. For the present discussion it is important to note that for the concentrated oxalate network the homogeneous line width is dominated by spin-spin relaxation up to ~5 K and is thus almost constant below that temperature.

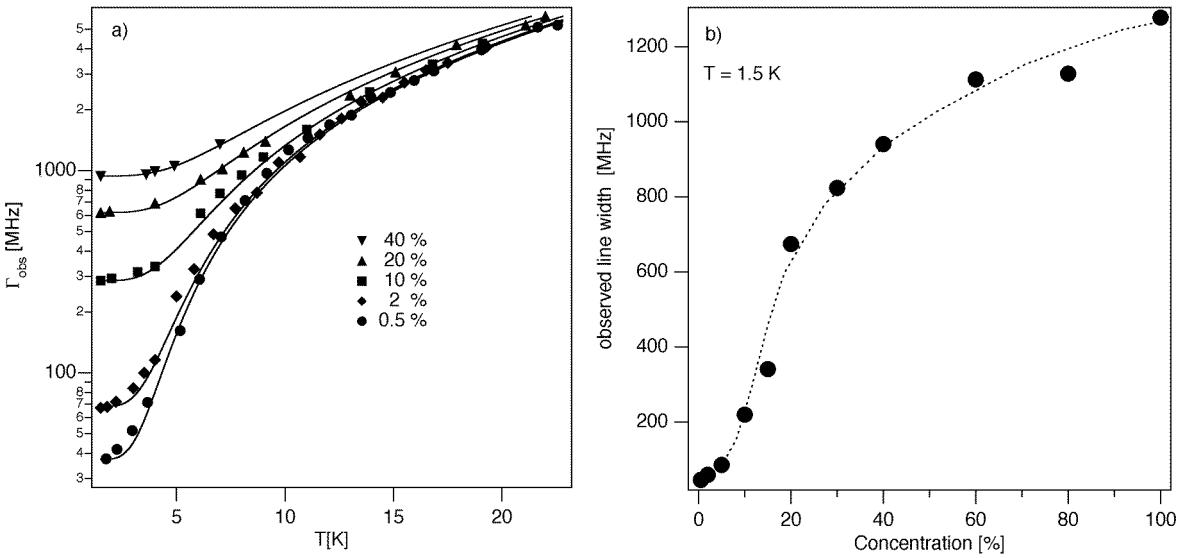

Figure 3.6. a) The observed line width $\Gamma_{obs} = 2\Gamma_{hom}$ in transient hole-burning under steady state excitation as a function of temperature for the mixed crystals $[Rh(bpy)_3][NaAl_{1-x}Cr_x(ox)_3]ClO_4$ (x = 0.005, 0.2, 0.1, 0.2 and 0.4). b) The observed line width Γ_{obs} as a function of the mole fraction x at 1.5 K.

3.5 Theoretical aspects of energy migration

As discussed above, at low temperatures the homogeneous line width of electronic origins is usually several orders of magnitude smaller than the inhomogeneous distribution even in high-quality crystalline materials and at high chromophore concentrations. Thus the question to be asked is, is the energy migration a truly resonant process, with the initially excited chromophore looking for a partner with which it is electronically resonant within one homogeneous line width, or is the energy transferred to the nearest neighbour, with which it is not necessarily resonant, and the energy mismatch is made up by the creation or annihilation of phonons as

schematically shown in Figure 3.7. Even though energy migration in crystalline materials with high dopant concentrations was found to be dominated by phonon-assisted processes in a majority of cases, the following discussion begins with the resonant process, this in view of the extraordinary behaviour of the model systems to be discussed in Section 3.6.2.

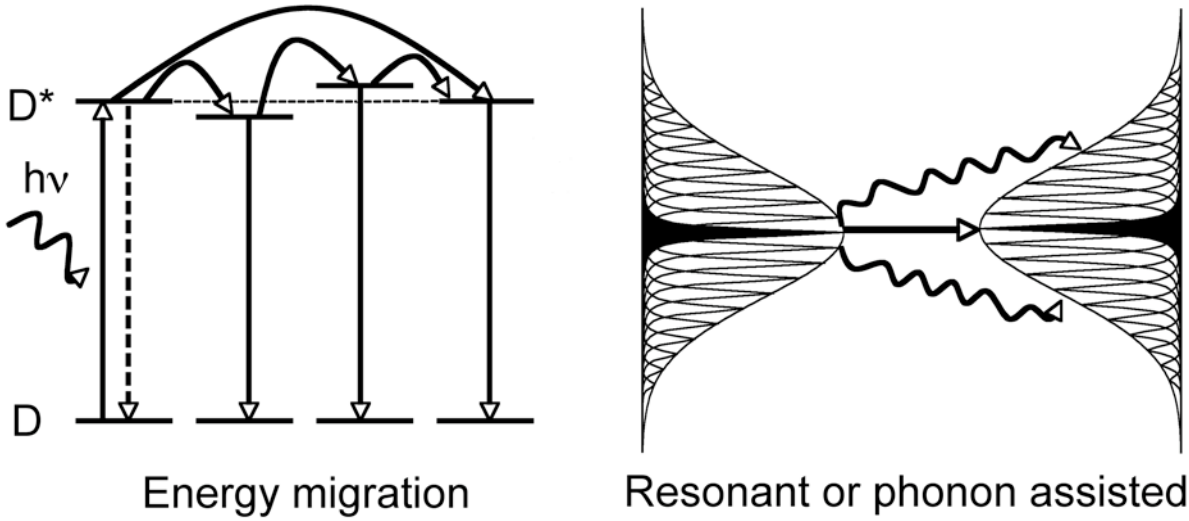

Figure 3.7. Schematic representation of excitation energy migration at high chromophore concentration: as a result of the inhomogeneous distribution, the transfer to nearest neighbours is not resonant and requires the creation or annihilation of phonons to bridge the energy mismatch. Resonant transfer is only possible between truly resonant chromophores within the inhomogeneous distribution and these are not usually nearest neighbours.

3.5.1 Resonant energy transfer

The dominant contribution to the electronic interaction for resonant energy transfer is most often the electric-dipole–electric-dipole interaction between the respective transition dipole moments. The corresponding rate constant can be cast in the well-known form (in SI units) [6]

$$w_{DA} = \left(\frac{1}{4\pi\varepsilon_0}\right)^2\left(\frac{3\hbar e^4}{4\pi n^4 m^2}\right)\times\frac{\kappa^2 f_D f_A \Omega_{DA}}{R_{DA}^6 \nu_{DA}^2} = \frac{1}{\tau_D}\left(\frac{R_c}{R_{DA}}\right)^6 \qquad (2)$$

where τ_D is the intrinsic luminescence lifetime of the donor in the absence of any acceptor chromophores, R_{DA} is the donor-acceptor separation, and R_c is the critical radius given by

$$R_c = \left(Const \times \frac{\kappa^2 f_A \, \Omega_{DA} \, \eta_D^r}{\tilde{\nu}_{DA}^4} \right)^{1/6} \qquad (3)$$

In Equation (3), f_A is the dimensionless oscillator strength of the acceptor transition, η_D^r is the luminescence quantum efficiency of the donor transition, $\tilde{\nu}_{DA}$ is the mean energy at which the transfer takes place, and κ^2 is a geometrical factor, which averaged over all possible orientations takes on a value of 2/3. Ω_{DA} is the spectral overlap integral of the normalised line shape functions of the donor emission, g_D, and the acceptor absorption, g_A, and is given by

$$\Omega_{DA} = \int g_A(\tilde{\nu}) g_D(\tilde{\nu}) d\tilde{\nu} \qquad (4)$$

It takes care of energy conservation. *Const* regroups all the fundamental quantities, including the ones appearing upon substitution of the oscillator strength of the donor transition by the proportionality $f_D \sim 1/\tau_D^r = \eta_D^r / \tau_D$ [27]. For $\tilde{\nu}_{DA}$ in wavenumbers, a typical value for the index of refraction n = 1.7 for the compounds in question, and R_c in Å, *Const* $\approx 10^{31}$. The physical significance of the critical radius is that at an effective donor-acceptor separation $R_{DA} = R_c$, the probability for excitation energy transfer is equal to the probability of luminescence of the donor, that is, the quantum efficiency for energy transfer $\eta_{DA}^{et} = 0.5$.

With respect to energy migration, the spectral overlap is restricted to the electronic origin of the corresponding transition. Thus efficient resonant energy migration is only to be expected for systems with small Stokes' shifts and Huang-Rhys factors close to zero. The $^4A_2 \rightarrow {}^2E$ spin-flip transition of Cr^{3+} should thus be ideally suited for energy migration studies. However, at low temperatures the homogeneous line width of the electronic origins is much smaller than the inhomogeneous distribution. Thus, only those chromophores within a homogenous line width of each other inside the inhomogeneous distribution can transfer the energy resonantly. For such truly resonant chromophores, the maximum spectral overlap integral can be expressed as

$$\Omega_{DA} = \int \left[g(\tilde{\nu}) \right]^2 d\tilde{\nu} = \frac{1}{\pi \Gamma_{hom}} \qquad (5)$$

where g(ν) is the Lorentzian lineshape function with the corresponding homogeneous line width Γ_{hom}. Using the value for the homogeneous line width of concentrated materials of the order of $\Gamma_{hom} \leq 0.02$ cm^{-1} (600 MHz) at 1.5 K, and an oscillator strength of the spin and parity forbidden $^4A_2 \rightarrow {}^2E$ transition of ~6x10^{-7}, Ω_{DA} and R_c take on values of 16 cm and 34 Å, respectively. It is interesting to note that the value for R_c is of the order of the values found for the best donor-acceptor pairs used in FRET studies with organic dyes [38] despite the fact that the $^4A_2 \rightarrow {}^2E$ transition is both parity as well as spin-forbidden. This is due to the much larger value of the spectral overlap integral as compared to the one found for the large absorption and emission bands of the organic dyes, which counteracts the small value of the oscillator strength of the acceptor.

In order for energy migration to proceed via such a resonant process the concentration of chromophores, which are resonant within one homogenous line width inside the inhomogeneous distribution must be sufficiently large. At the centre of the inhomogeneous distribution, this concentration is simply given by the ratio of the homogenous to the inhomogeneous line width according to

$$N_{res} = \frac{2\Gamma_{hom}}{\Gamma_{inh}} N_{tot} \qquad (6)$$

Where N_{tot} is the total concentration of chromophores and the factor of 2 takes into account the partial spectral overlap between spectral neighbours within the inhomogeneous distribution. With this the mean number of resonant or quasi-resonant chromophores, n_m, within a sphere of radius R_c can be estimated as a function of both Γ_{hom} and Γ_{inh}

$$n_m = \frac{2\Gamma_{hom}}{\Gamma_{inh}} N_{tot} \cdot \frac{4\pi}{3} R_c^3 \qquad (7)$$

In which R_c is a function of Γ_{hom} according to equations (3) and (5), and thus $n_m \sim \sqrt{\Gamma_{hom}}/\Gamma_{inh}$. Figure 3.8 shows the mean number of resonant chromophores at the centre of the inhomogeneous distribution as function of the homogeneous line width with the inhomogeneous line width as parameter and taking $N_{tot} = 10^{21}$ cm^{-3}, which corresponds to the concentration of the neat model compounds or a 1% Cr^{3+} doped ruby. For a homogeneous line width of 0.02 cm^{-1}, the critical inhomogeneous width is

around 4 cm^{-1}. For larger inhomogeneous distributions, the concentration of resonant species becomes too small, and the resonant process cannot be efficient, for narrower distributions, it can, in principle, become very efficient as on average there are more than two resonant species within a sphere of R_c. As will become evident in the discussion on energy migration in the model compounds, namely the three-dimensional oxalate networks, the above is of utmost importance. In contrast, in the much-studied doped oxides, resonant processes are of lesser importance.

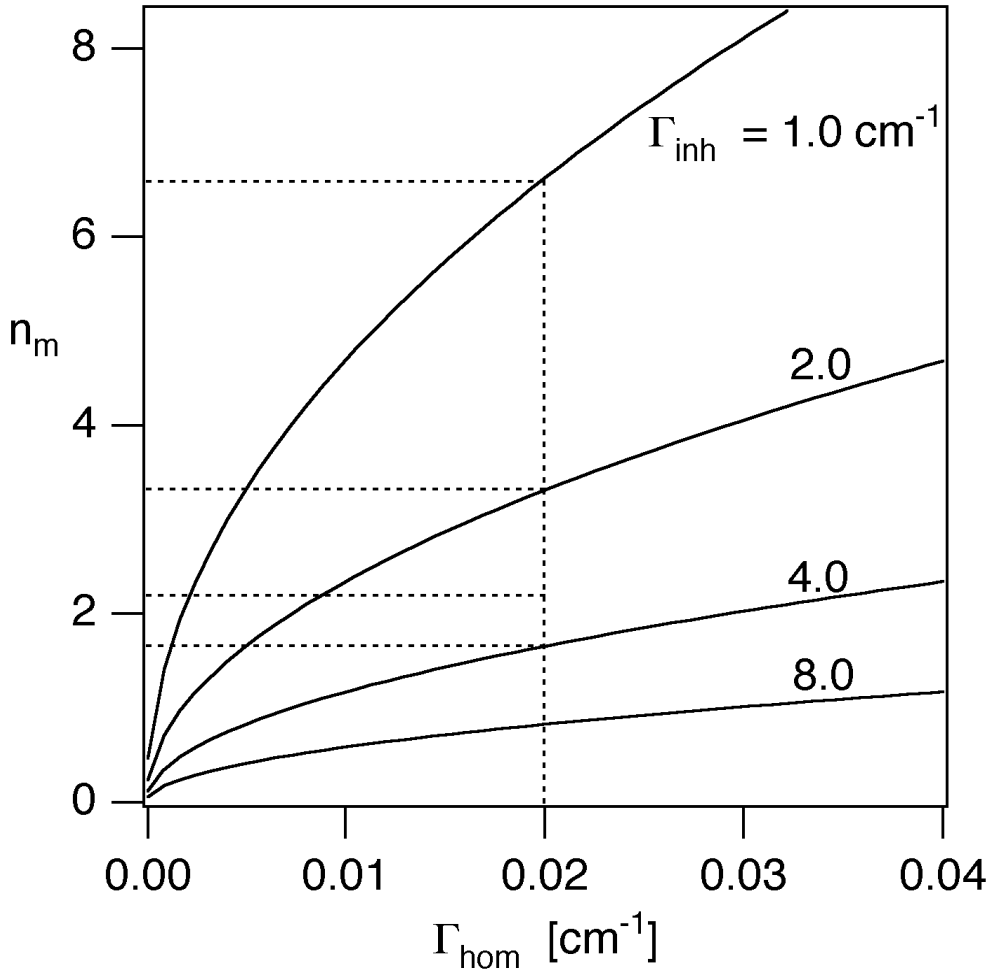

Figure 3.8. Mean number of resonant chromophores at the centre of the inhomogeneous distribution as a function of the homogeneous line width Γ_{hom} for different values of the inhomogeneous line width Γ_{inh}.

3.5.2 Phonon-assisted energy transfer

As mentioned above, at low temperature two spatially nearest neighbour chromophores are not necessarily spectral neighbours within the inhomogeneously broadened band. As a result, the spectral overlap integral is usually very small and resonant energy migration between nearest neighbours does not occur. However, the small energy mismatch can be made up by the creation and annihilation of phonons in phonon-assisted processes. Similar to the processes responsible for the increase in homogeneous line width at higher temperatures, these can occur in a direct process with the annihilation or creation of a single phonon, or in Orbach and Raman processes which are two-phonon processes. In view of the small energy mismatch of $\sim\Gamma_{inh}$ to be bridged by the phonon-assisted process, the latter two are more likely [12]. Irrespective of the mechanism, phonon-assisted energy migration is strongly temperature dependent and usually freezes below ~10 K.

3.6 Energy migration within the $^2E \rightarrow {}^4A_2$ transition

3.6.1 $Al_2O_3:Cr^{3+}$ and other doped systems

The $^2E \rightarrow {}^4A_2$ transition Cr^{3+} in ruby is probably the most studied transition of any transition metal ion of the periodic table, and a large number of fundamental phenomena were discovered using ruby. Among these, excitation energy transfer and migration and the discussion of the possible mechanisms play a key role [14]. The luminescence spectrum of ruby is dominated by the two R-lines corresponding to emission from isolated Cr^{3+} centres, but already at comparatively low Cr^{3+} concentrations additional lines, the so-called N-lines appear at lower energies. These have been attributed to exchange coupled pairs of Cr^{3+} ions [39] with different bridging geometries. Thus, a number of different energy transfer processes have to be considered: the energy migration within the ^2E state of the isolated Cr^{3+} centres, and the transfer from isolated centres to the different exchange coupled pairs as final acceptors [14, 40]. As the relative concentration of exchange coupled pairs and the

homogeneous as well as the inhomogeneous line widths of the single ions all vary with the Cr^{3+} concentration, and as the inhomogeneous line width furthermore depends upon the crystal quality and the homogeneous line width upon temperature, the problem of energy migration in ruby becomes a multi-parameter problem. Indeed, the discussion on the mechanisms of the various energy transfer processes has been controversial. Time-resolved FLN experiments show that above ~10 K, energy migration is dominated by phonon-assisted processes [41]. However, the nature of the processes could not be answered unambiguously. More importantly, the initially postulated fast resonant energy migration between resonant single ions at low temperatures [40, 42] was later shown to be incorrect by Jessop and Szabo [43] and Chu et al. [44], who showed it to occur on a millisecond timescale. Indeed, according to the above arguments, a Cr^{3+} concentration of >1 mole% would be required to achieve a sufficient concentration of resonant species. However at such concentrations, the concentration of exchange coupled pairs becomes so high that the energy is quickly transferred to these, where it remains trapped.

As another example of a doped oxide, emerald ($Be_3Al_2(SiO_3)_6:Cr^{3+}$) has been studied by Hasan et al. [45]. Emerald has the beryl structure, the site symmetry of Cr^{3+} is D_3. In emerald, the nearest-neighbour Al^{3+} sites are 4.6 Å apart whereas in ruby the distance is only 2.65 Å. Exchange interactions are thus negligible. In contrast to ruby, the energy transfer in emerald has been clearly established to be two-phonon-assisted and dipole-dipole in nature, in line with a number of other materials [46] as well as with theoretical considerations [12].

3.6.2 With $[Cr(ox)_3]^{3-}$ as chromophore in three-dimensional oxalate networks

The steady state FLN spectra at 1.4 K for excitation into the R_1 line of the $^4A_2 \rightarrow {}^2E$ transition of both $[Rh(bpy)_3][NaCr(ox)_3]ClO_4$ and $[Ru(bpy)_3][NaCr(ox)_3]$ are shown in Figure 3.9 together with the non-selective R_1 emission and absorption. For the former, the excitation wavelength for FLN was tuned to slightly higher energy than the maximum of the absorption, for the latter to slightly lower energy. For $[Rh(bpy)_3][NaCr(ox)_3]ClO_4$, the FLN spectrum consists of more lines than the simple

three-line spectrum spaced by the ground state ZFS. Indeed, up to eight narrowed lines with spacings between adjacent lines corresponding to D = 1.3 cm^{-1} are observed [15]. Thus even though more than the expected three lines are observed, some energy selectivity is preserved in this compound at 1.4 K. For $[Ru(bpy)_3][NaCr(ox)_3]$ on the other hand, the selectivity seems to be lost to a large extent. The FLN spectrum is much more similar to the broadened emission spectrum with non-selective excitation. At elevated temperature any energy selectivity in the FLN spectrum is likewise lost even for $[Rh(bpy)_3][NaCr(ox)_3]ClO_4$, as demonstrated by the steady state FLN spectra recorded at 4.2 K included in Figure 3.9. This behaviour is characteristic for energy non-selective phonon-assisted energy migration.

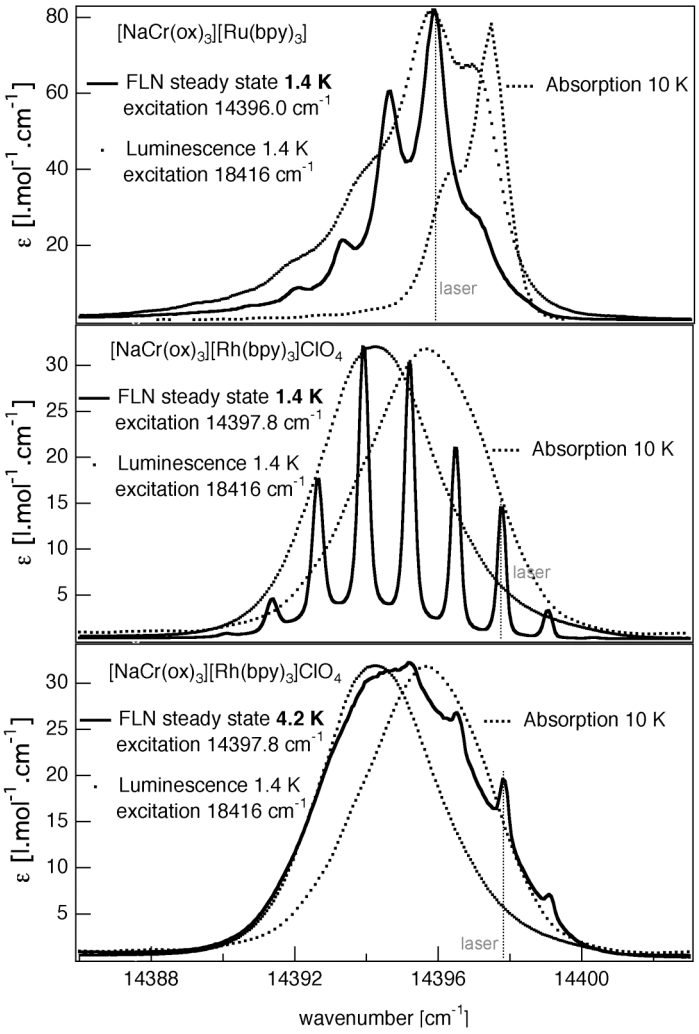

Figure 3.9. Steady state FLN spectra of the R_1 line of the $^4A_2 \rightarrow {}^2E$ transition of (top) $[Ru(bpy)_3][NaCr(ox)_3]$ at 1.4 K, (middle) of $[Rh(bpy)_3][NaCr(ox)_3]ClO_4$ at 1.4 K, and (bottom) at 4.2 K. The R_1 absorption and the non-selective emission spectra are included for direct comparison.

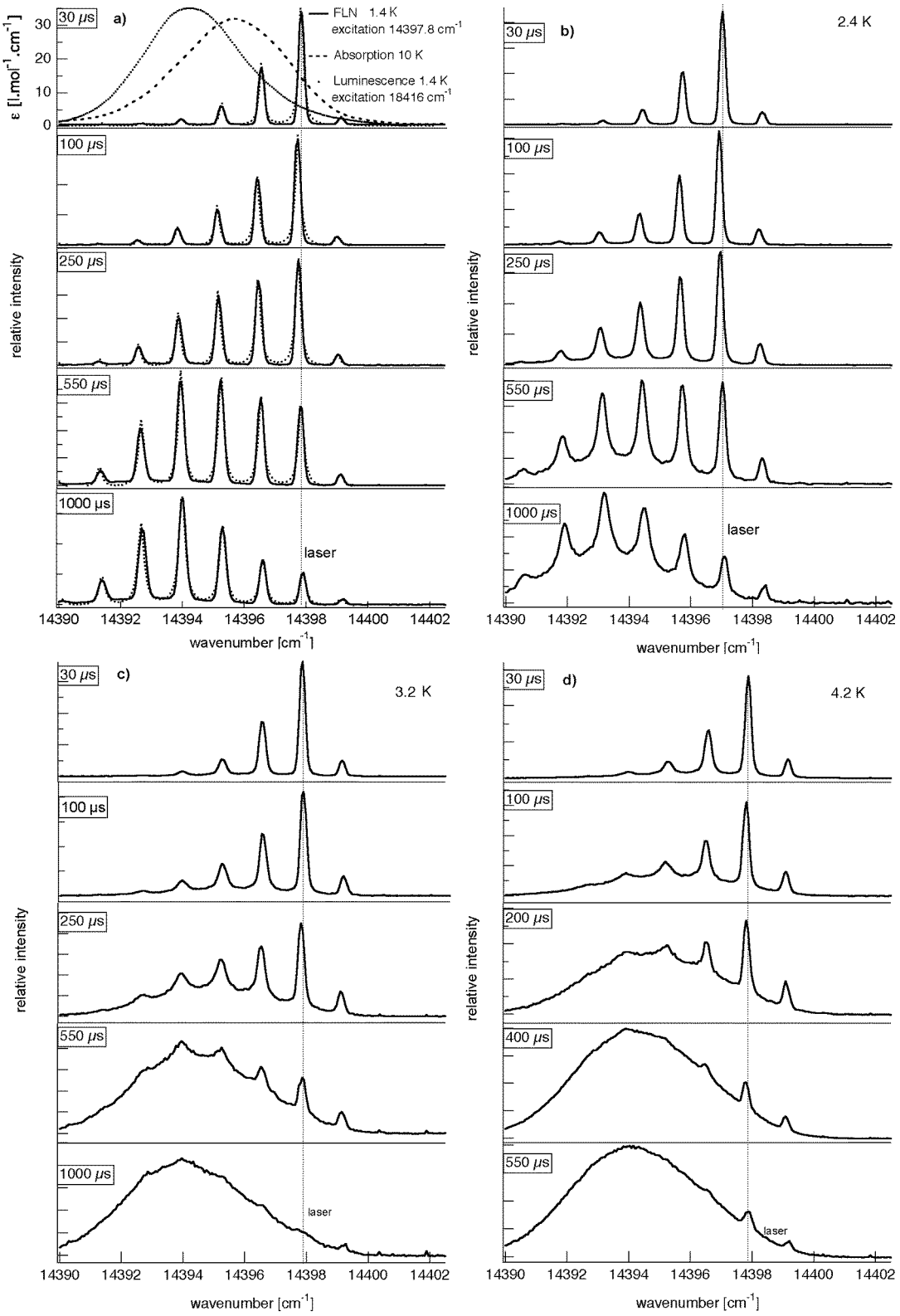

Figure 3.10. Time-resolved FLN spectra of the R_1 line of the $^4A_2 \rightarrow {}^2E$ transition of $[Rh(bpy)_3][NaCr(ox)_3]ClO_4$ at different temperatures, a) 1.4 K, b) 2.4 K, c) 3.2 K, and d) 4.2 K. The steady state FLN spectra as well as absorption and the non-selective emission spectra are included.

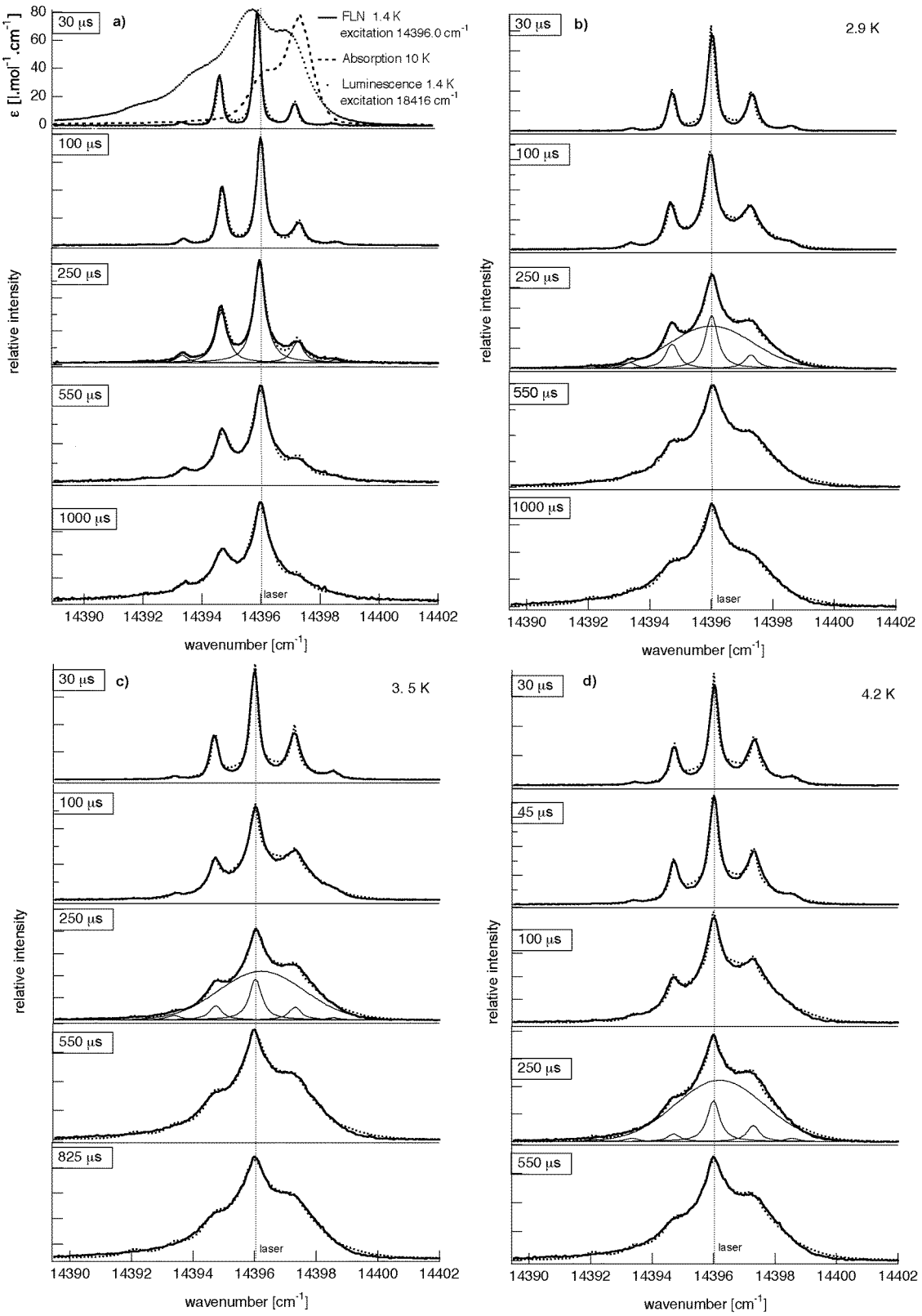

Figure 3.11. Time resolved FLN spectra of the R_1 line of the $^4A_2 \rightarrow {}^2E$ transition of $[Ru(bpy)_3][NaCr(ox)_3]$ at different temperatures, a) 1.4 K, b) 2.9 K, c) 3.5 K, and d) 4.2 K. The steady state FLN spectra as well as absorption and the non-selective emission spectra are included.

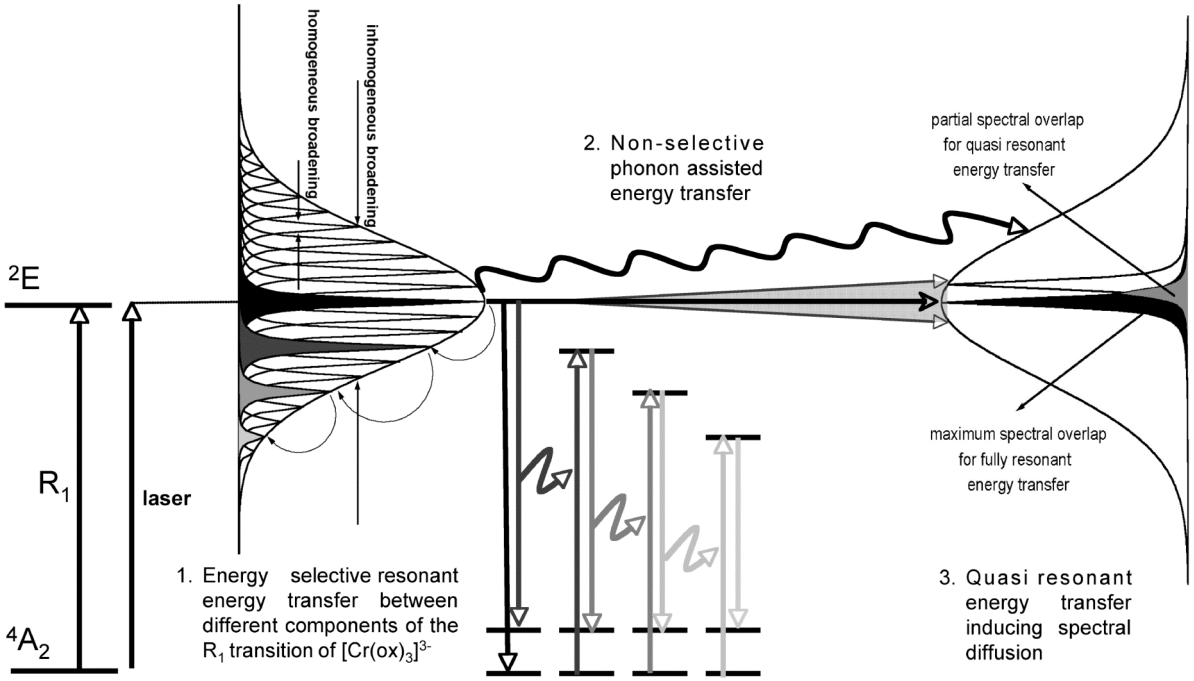

Figure 3.12. Schematic presentation of the three mechanisms for energy migration in the three-dimensional oxalate networks. 1. Resonant energy transfer between different components of the ground state giving rise to a multi-line spectrum with spacings corresponding to the ground state ZFS. 2. Non-energy selective phonon-assisted energy migration between spatial neighbours at elevated temperature resulting in a growing inhomogeneous back-ground spectrum. 3. Quasi-resonant energy migration between spectral neighbours resulting in spectral diffusion around the resonant line.

But how is the very different low-temperature behaviour of the two compounds to be explained? Further experimental evidence is provided by time-resolved FLN spectra following pulsed excitation shown in Figures 3.10 and 3.11. For $[Rh(bpy)_3][NaCr(ox)_3]ClO_4$ the 1.4 K spectrum at the shortest delay of 30 µs is very close to the three-line spectrum for isolated chromophores. The additional lines appear sequentially at longer delays. As schematically shown in Figure 3.12, this is explained by energy transfer in which the initially excited chromophore as donor gives the energy of its transition from the excited state to the upper component, that is, the M_S = ±1/2 component of the ground state, to an acceptor within the inhomogeneous distribution for which the transition from the M_S = ±3/2 component to the excited state is resonant. In turn the acceptor becomes the donor for the next step in handing the energy down the ladder spaced by the ZFS of the ground state.

For $[Ru(bpy)_3][NaCr(ox)_3]$ the 1.4 K spectrum at the shortest delay of 30 µs is likewise very close to the three-line spectrum for isolated chromophores, and at longer delays some additional lines appear, however the total number is lower. This is to be expected, as the inhomogeneous line width of the ruthenium(II) containing compound is only 1.1 cm^{-1} as compared to 4.4 cm^{-1} for the rhodium(III) compound, and thus less multiples of the ground state ZFS can be accommodated within the inhomogeneously broadened band. The important difference is that in addition to the appearance of new lines, the initially sharp lines broaden out rapidly for longer delays. This is not due to phonon-assisted energy migration. The phonon-assisted process being totally frozen in at 1.4 K for the rhodium(III) compound, there is no reason as to why it should be so much faster in the ruthenium(II) compound. Indeed, the narrower inhomogeneous distribution would slow it down rather than accelerate it. Additionally, the evolution of the band shape is very much different from the one typical for the phonon-assisted process observed at higher temperature. As shown in Figure 3.10, the non-energy selective phonon-assisted process in the rhodium(III) compound manifests itself as an increasingly rapid growing in of the full inhomogeneously broadened band without affecting the band width or the temporal evolution of the sharp bands, whereas in the ruthenium(II) compound at l.4 K the individual sharp line broadens out. This broadening has its origin in quasi-resonant energy migration between spectral neighbours due to partial overlap between the respective Lorentzians as schematically shown in Figure 3.12. Curve fitting of the multi-line spectra with a set of Lorentzians spaced by 1.3 cm^{-1} results in the evolution of the line width as function of delay time displayed in Figure 3.13 for both compounds. Whereas the line width of the individual sharp lines for $[Rh(bpy)_3][NaCr(ox)_3]ClO_4$ stays almost constant at the value of the spectral resolution of the spectrometer of 0.2 cm^{-1}, for $[Ru(bpy)_3][NaCr(ox)_3]$ it increases rapidly from that value to reach almost the limiting value of 1.1 cm^{-1} of the inhomogeneous line width for this compound. The question remains, why is the behaviour of the two compounds at 1.4 K so very different. As noted before, the key difference lies in their inhomogeneous line width. With reference to Figure 3.8, at a homogenous line width of 0.02 cm^{-1}, for $[Rh(bpy)_3][NaCr(ox)_3]ClO_4$ there are approximately 1.5 acceptors available for either the stepwise resonant or the quasi-resonant energy migration within the same

component of the ground state. For $[Ru(bpy)_3][NaCr(ox)_3]$ there are more than 6, provided the homogeneous line widths in the two compounds are similar. In the present case and according to the Inokuti and Hirayama equation [47], an increase in the concentration of potential acceptors of a factor of four results in an increase of the energy transfer efficiency of at least an order of magnitude. Whereas for $[Rh(bpy)_3][NaCr(ox)_3]ClO_4$, a pseudo first order rate constant for the resonant energy transfer process of $k_{et}^{r} \approx 10^4\ s^{-1}$ had been estimated [15], this must therefore be of the order of $10^5\ s^{-1}$ for $[Ru(bpy)_3][NaCr(ox)_3]$. Or in other words, on average the energy is transferred ~100 times before radiative decay. With each step adding approximately $\Gamma_{hom} \approx 0.02\ cm^{-1}$ to the observed line width in the FLN spectrum, this explains the evolution of the observed line width from 0.2 cm^{-1} at 30 µs delay all the way to the full inhomogeneous width of 1.1 cm^{-1} at longer delays $[Ru(bpy)_3][NaCr(ox)_3]$, as well as the negligible increase for $[Rh(bpy)_3][NaCr(ox)_3]ClO_4$, for which the observed line width is limited by the spectral resolution of the monochromator.

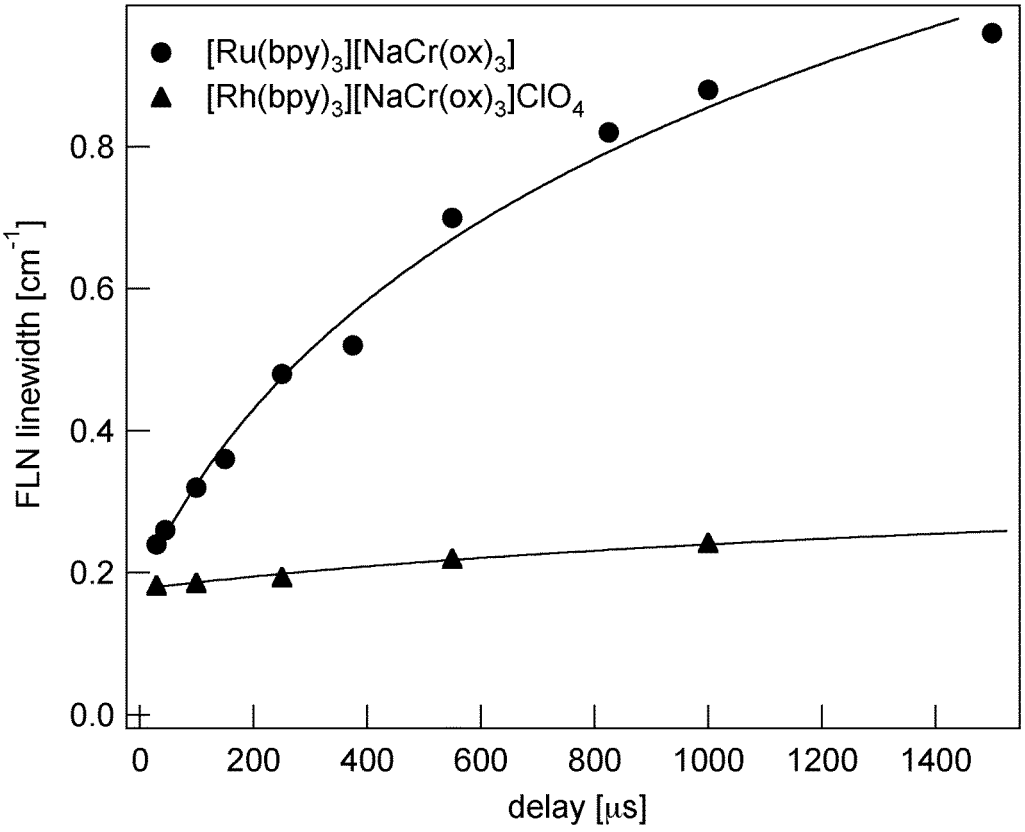

Figure 3.13. Evolution of the line width as a function of delay time for of the sharp lines in the FLN spectra at 1.4 K of $[Rh(bpy)_3][NaCr(ox)_3]ClO_4$ (▲) and $[Ru(bpy)_3][NaCr(ox)_3]$ (●).

Within the temperature interval of 1.4 to 4.2 K, the resonant processes are independent of temperature, as born out by the time-resolved FLN spectra at higher temperatures included in Figures 3.10 and 3.11 At the higher temperatures there is merely a growing in of the inhomogeneous background, the evolution of the sharp lines themselves is identical to the one at 1.4 K. This is to be expected, as in the concentrated systems, the homogeneous line width as the crucial parameter does not vary much within this temperature interval. However, at 4.2 K the phonon-assisted process becomes dominant, all narrowed features being lost after 500 µs following the excitation. For $[Rh(bpy)_3][NaCr(ox)_3]ClO_4$, the hopping rate for the phonon-assisted process at 4.2 K can be estimated from the time-resolved spectra in Figure 3.10 In the spectrum at a delay of ~100 µs the integrated intensity of the phonon-assisted background is almost identical to the integrated intensity of the sharp features, and therefore the hopping rate must also be of the order of $k_{et}^{ph} \approx 10^4$ s^{-1} at this temperature. Due to the higher density of low frequency phonons as compared to ruby and the somewhat larger ground state ZFS, phonon assisted processes set in a lower temperature in the oxalate networks.

3.7 Conclusions

The very specific crystal structure of the model compounds with a strictly alternating sequence of sodium and chromium ions in the oxalate backbone ensures that exchange interactions between chromium ions are negligible, and that therefore the interaction between the chromophores is restricted to multipole-multipole interactions. As a result, three different mechanisms of non-radiative energy migration within the electronic origin of the $R_1(^4A_2 \rightarrow {}^2E)$ transition of $[Cr(ox)]^{3-}$ could be identified in the three-dimensional network compound. In addition to the common energy non-selective phonon-assisted process, previously observed in a number Cr^{3+} doped oxides, two different resonant and thus energy selective processes can be observed down to 1.4 K. The first one occurs between different ground state components. It is dominant if the inhomogeneous line width is substantially larger than the ground state

ZFS, and it gives rise to a multi-line pattern in FLN spectra with spacings equal to the ground state ZFS of D = 1.3 cm^{-1}. The second one occurs between the same components of the ground state and in an FLN spectrum gives rise to spectral diffusion of the initially sharp lines. It is dominant for small inhomogeneous distributions, which result in a higher concentration of species resonant within one homogeneous line width.

Whereas the inhomogeneous line width as well as the ground state ZFS are comparatively easy to determine experimentally, the third crucial parameter, the homogeneous line width is much more difficult to determine. The value obtained in the steady state transient hole-burning experiment does not necessarily correspond to the correct value as it might already show some broadening through energy migration and power broadening. Even though in the discussion equal values for the homogeneous line width in the systems were assumed, this is by no means certain and will have to be ascertained. Both problems can and will be addressed with time-resolved hole-burning.

The surprisingly large value of R_c for Förster-type energy transfer is due to the small homogeneous line width of the purely electronic transition at low temperatures, which counteracts the small oscillator strength of the formally symmetry and spin-forbidden transition. In $[Rh(bpy)_3][NaCr(ox)_3]ClO_4$, the resonant energy migration goes on average over at least 5 steps down the ladder and probably also over an equal number of quasi-resonant steps. At more than 20 Å per step, the energy migrates up to 200 Å on average. As mentioned above, in $[Ru(bpy)_3][NaCr(ox)_3]$ the resonant or quasi-resonant process is as much as 10 times faster, and therefore the energy could migrate up to 2000 Å. In contrast, phonon-assisted migration is a hopping process between nearest neighbours and thus is limited to 9.4 Å only per step.

Finally, the effect of applying an external magnetic field could give some further insight into the role of the homogeneous line width for the resonant energy transfer process, because an external magnetic field reduces the electron-spin–electron-spin relaxation and thus the homogeneous line width substantially. Another intriguing question to ask and indeed to be addressed is, is it possible to burn persistent side-holes via resonant energy transfer in a system, which shows persistent hole burning

such as the $NaMg[Al(ox)_3]x9H_2O$ system studied by Riesen et al. [48] and the step-wise energy migration of the oxalate networks simultaneously.

Acknowledgements

We thank the Swiss National Science Foundation for financial support of this work.

References

[1] M. M. Fejer, H. Injeyan, U. Keller (eds), Advanced solid state lasers, in OSA trends in optics and photonics, vol. 26, Optical Society of America, Washington 1999.

[2] T. Justel, H. Nikol, C. Ronda, Angew. Chem. Int. Ed 37 (1998) 3084.

[3] M. Grätzel, Nature, 414, (2001), 338.

[4] a) R. M. Clegg (ed), Rev. Mol. Biotechnol. 82 (2002) 177, b) D. L. Andrews, A. A. Demidov (eds), Resonance energy transfer, Wiley, Chichester, 1999.

[5] a) G. Blasse, K. C. Powell, Structure and Bonding 42, Springer, Heidelberg, 1980, b) Energy Transfer Processes in Condensed Matter, NATO ASI Series B 114, B. DiBartolo (ed.) Plenum, New York, 1985, c) Advances in Energy transfer processes, B. DiBartolo, X. Chen (eds), World Scientific, New Jersey, 2001.

[6] B. Henderson, G. F. Imbusch, Optical Spectroscopy of Inorganic Solids, Clarendon Press, Oxford, 1989.

[7] a) F. Auzel, G. Baldacchini, J. Lumin 125 (2007) 25, b) F. Auzel, F. Bonfigli, S. Gagliari, G. Baldacchini, J. Lumin. 94–95 (2001) 293.

[8] M. Hehlen, Journal of the Optical Society of America B 14 (1997) 1312.

[9] T. Förster, Ann. Phys. 2 (1948) 55.

[10] D. L. Dexter, J. Chem. Phys. 21 (1953) 836.

[11] C. B. Harris, D. A. Zwemer, Annual Review of Physical Chemistry 29 (1978) 473.

[12] a) T. Holstein, S. K. Lyo, R. Orbach, Phys. Rev. Lett. 36 (1976) 891, b) T. Holstein, S. K. Lyo, R. Orbach in: W. M Yen, P. M. Selzer (eds), "Laser

Spectroscopy of Solids", Topics in Applied Physics 49, Springer, Berlin, 1981, p. 39.

[13] a) S. Xia, P. A. Tanner, Phys. Rev. B 66 (2002) 214305, b) P. A. Tanner in: H. Yersin (ed.), Topics in Current Chemistry 241, Springer, Berlin, 2004, p. 167.

[14] G. F Imbusch and W. H. Yen in: W. M. Yen and M. D. Levenson (eds), Lasers, spectroscopy and new ideas, Springer, Optical Series, Vol. 54, Berlin, 1987, p. 248.

[15] a) A. Hauser, M. E. von Arx, V. S. Langford, S. Kairouani, U. Oetliker, A. Pillonnet in: H. Yersin (Ed.), Topics in Current Chemistry 241, Springer, Berlin, 2004, p. 65, b) M. E. von Arx, V. S. Langford, U. Oetliker, A. Hauser, J. Phys. Chem A 106 (2002) 7099, c) M. E. von Arx, A. Hauser, H. Riesen, R. Pellaux, S. Decurtins, Phys. Rev. B54 (1996) 15800.

[16] S. Sugano, Y. Tanabe, H. Kamimura, Pure and Applied Physics 33, Academic press, New York, 1970.

[17] a) A. W. Adamson, W. L. Waltz, E. Zinato, D. W. Watts, P. D. Fleischauer, R. D. Lindholm, Chem. Revs 68 (1968) 541, b) A. W. Adamson, Coord. Chem. Rev. 3 (1968) 169, c) G. Irwin, A. D. Kirk, Coord. Chem. Rev. 211 (2001) 25, d) E. Zinato, P. Riccieri, Coord. Chem. Rev. 211 (2001) 5, e) A. Derwahl, F. Wasgestian, D. A. House, W. T. Robinson, Coord. Chem. Rev. 211 (2001) 45.

[18] L. S. Forster, Coord. Chem. Rev. 248 (2004) 261.

[19] L. E. Collins, M. A. Morrison, P. L. Donoho, Amer. J. Phys. 42 (1974) 560.

[20] A. Szabo, Phys. Rev. Lett. 25 (1970) 924.

[21] P. M. Selzer in: W. M Yen, P. M. Selzer (eds), "Laser Spectroscopy of Solids", Topics in Applied Physics 49, Springer, Berlin, 1981, p. 113.

[22] W. M. Yen, P. M. Selzer in: W. M Yen, P. M. Selzer (eds), "Laser Spectroscopy of Solids", Topics in Applied Physics 49, Springer, Berlin, 1981, p. 141.

[23] a) A. Szabo, Phys. Rev. B 11 (1975) 4512, b) T. Muramoto, S. Nakamishi, T. Hashi, Opt. Comm. 21 (1977) 139.

[24] S. Decurtins, H. W. Schmalle, R. Pellaux, P. Schneuwly, A. Hauser, Inorg. Chem. 35 (1996) 1451.

[25] a) S. Decurtins, R. Pellaux, Comments on Inorganic Chemistry 20 (1998) 143, b) S. Decurtins, R. Pellaux, G. Antorrena, F. Pallacio, Coord. Chem. Rev. 192 (1999) 841, c) E. Coronado, J. R. Galan-Mascaros, C. J. Gomez-Garcia, J. M. Martinez-Agudo, Inorg. Chem. 40 (2001) 113.

[26] a) T. Schönherr, J. Spanier, H. H. Schmidtke, J. Phys. Chem. 93 (1989) 5969, b) O. S. Mortensen, J. Chem. Phys. 47 (1969) 4215.

[27] T. Brunold, H. U. Güdel in: “Inorganic Electronic Structures and Spectroscopy”, Vol. 1 (E. I. Solomon and A. B. P. Lever, eds) Wiley, New York, 1999.

[28] S. Lahity, R. Kakkar, Chem. Phys. Lett. 88 (1982) 499.

[29] M. L. Lewis, H. Riesen, J. Phys. Chem. A 106 (2002) 8039.

[30] a) L. S. Forster, Coord. Chem. Rev. 227 (2002) 59, b) M. Yamaga, B. Henderson, K. P. O’Donnell, J. Phys.: Condens.Matter 1 (1989) 9175, c) N. J. Linck, S. J. Berens, D. Madge, R. G. Linck, J. Phys. Chem 87 (1983) 1733.

[31] a) H. Riesen, Structure and Bonding 107 (2004) 179, b) H. Riesen, Coord. Chem. Rev. 250 (2006) 1737.

[32] a) J. L. Hughes, H. Riesen, J. Phys. Chem. A 107 (2003) 35, b) H. Riesen, J. L. Hughes, Chem. Phys. Lett. 370 (2003) 26.

[33] C. A. Bates, J. P. Bentley, R. A. Lees, W. S. Moore, J. Phys. C 2 (1969) 1970.

[34] a) L. M. Lewis, H. Riesen, PCCP 4 (2002) 4845, b) H. Riesen, E. Krausz, J. Chem. Phys. 97 (1992) 7902.

[35] G. F. Imbusch, W. M. Yen, A. L. Schawlow, D. E. McCumber, M. D. Sturge, Phys. Rev. 133 (1964) A1029.

[36] C. Ecolivet, S. Rabaste, A. Hauser, results from Brillouin scattering, unpublished.

[37] M. Lucht, M. Lerche, H.-C. Wille, Yu. V. Shvyd'ko, H. D. Rüter, E. Gerdau, P. Becker, J. Appl. Cryst. 36 (2003) 1075-1081.

[38] J. R. Lakowicz, Principles of Fluorescence Spectroscopy, 3rd ed., Springer, Berlin, 2006.

[39] S. A. Basun, R. S. Meltzer, G. F. Imbusch, J. Lumin. 125 (2007) 31.

[40] G. F. Imbusch, Phys. Rev. 153 (1967) 326,

[41] a) P. M. Selzer, D. S. Hamilton, W. M. Yen, Phys. Rev. Lett. 38 (1977) 858, b) P. M. Selzer, D. L- Huber, B. B. Barnett, W. M. Yen, Phys. Rev. B. 17 (1978) 4979.

[42] A. Monteil, E. Duval, J. Phys. C 12 (1979) L416.

[43] P. E. Jessop, A. Szabo, Phys. Rev. Lett. 45 (1980) 1712,

[44] S. Chu, H. M. Gibbs, S. L. Call, A. Passner, Phys. Rev. Lett. 45 (1980) 1715.

[45] Z. Hasan, S. T. Keany, N. B. Manson, J. Phys. C 19 (1986) 6381.

[46] a) P. M. Selzer, D. S. Hamilton, R. Flach, W. M. Yen, J. Lumin. 12-13 (1976) 737, b) P. Avouris, A. Campion, M. A. El-Sayed, Chem. Phys. Lett. 50 (1977) 9, c) I. Y. Chan, B. L. Goldenberg, J. Chem. Phys. 79 (1983) 3711, d) R. Balda, J. Fernandez, J. L. Adam, M. A. Arriandiaga, Phys. Rev. B 54 (1996) 12076.

[47] M. Inokuti, F. Hirayama, J. Chem. Phys. 43 (1965)1978.

[48] H. Riesen, J. L. Hughes, Chem. Phys. Lett. 372 (2003) 563.

4. Structural study of mixed crystals of $[Zn_{1-x}Ru_x(bpy)_3][NaCr(ox)_3]$ probed by high-resolution absorption spectroscopy and high-pressure experiments

*Published in Inorganic Chemistry, 49, **2010**, 3402.*

Mia Milos, Tiphaine Penhouët, Prodipta Pal, Andreas Hauser*

Contents

Abstract

In the mixed crystal series of the cubic three dimensional networks of composition $[Zn_{1-x}Ru_x(bpy)_3][NaCr(ox)_3]$ ($0 \leq x \leq 1$, ox = $C_2O_4^{2-}$, bpy = 2,2'-bipyridine) high-resolution absorption spectroscopy in the region of the $^4A_2 \rightarrow {}^2E$ transition (R-lines) reveals the creation of five specific spectroscopic sites for the $[Cr(ox)_3]^{3-}$ complex. The concentration of these spectroscopic sites follows a binomial distribution of $[Zn(bpy)_3]^{2+}$ and $[Ru(bpy)_3]^{2+}$ among the four nearest neighbors of a given $[Cr(ox)_3]^{3-}$ complex within the network. The tris-bipyridine complexes occupying those positions have an optimal π-π interaction with the oxalate ligands of the tris-oxalate chromophore. The energy of each spectroscopic $[Cr(ox)_3]^{3-}$ site depends on the total concentration of $[Ru(bpy)_3]^{2+}$ in the mixed crystal and on its specific distribution among the four nearest neighbors. Single crystal X-ray diffraction indicates a reduction of the unit cell volume when $[Zn(bpy)_3]^{2+}$ (a = 15.6365(18) Å) is substituted by $[Ru(bpy)_3]^{2+}$ (a = 15.5098(6) Å). This alone would lead to a red-shift of the R lines in analogy to the red-shift of 25.2 cm^{-1}/GPa due to the decrease of the metal ligand Cr–O bond length as observed in high-pressure luminescence experiments. However, specific π-π interactions with the nearest neighbors have the opposite effect and shift the transition in discrete jumps to higher energies with increasing $[Ru(bpy)_3]^{2+}$ mole fraction.

4.1 Introduction

Three dimensional oxalate networks of general composition $[M^{II}(bpy)_3][M^{I}M^{III}(ox)_3]$, $[M'^{III}(bpy)_3][M^{II}M^{III}(ox)_3]$ and $[M'^{III}(bpy)_3][M^{I}M^{III}(ox)_3]ClO_4$ (ox = $C_2O_4^{2-}$; bpy = 2,2'-bipyridine; M^{I} = Li, Na; M^{II} = Ru, Zn, Co, Fe, Mn ... ; M^{III} = Al, Cr, Rh, ...; M'^{III} = Rh, Cr) were first synthesized by Decurtins et al. [1,2]. In this class of compounds, the tris-bipyridine cation tightly fits into the cavities provided by the three dimensional polymeric anionic $[M^{I}M^{III}(ox)_3]_\infty$ network. They are of interest because of their magnetic properties,[3] such as ferro- and antiferromagnetic order [4] or the incorporation of a spin-crossover function [5]. Likewise, they posses unique photophysical properties as exemplified by several energy transfer studies with the $[Cr(ox)_3]^{3-}$ complex as the active chromophore [6]. The lowest excited state of $[Cr(ox)_3]^{3-}$ is the ^2E state, and it is spectroscopically accessible via the spin-forbidden $^4A_2 \rightarrow {}^2E$ spin-flip transition in the form of a sharp doublet (R-lines) due to the zero-field splitting of the ^2E state. This feature makes the $[Cr(ox)_3]^{3-}$ complex a very interesting chromophore, since small variations in the local geometry around the chromophore affect absorption as well as luminescence spectra. For instance, in mixed crystals of composition $[Rh(bpy)_3][NaAl_xCr_{1-x}(ox)_3]ClO_4$, increasing the Cr^{3+} concentration leads to a decrease of the inhomogeneous broadening of the R lines from initially 5.9 cm^{-1} at $x < 0.1$ to 3.8 cm^{-1} at $x > 0.9$, and is accompanied by a shift to higher energy of 1.7 cm^{-1} [6].

In this article, we present a series of mixed crystals of composition $[Zn_{1-x}Ru_x(bpy)_3][NaCr(ox)_3]$, where the mole fraction of the $[Cr(ox)_3]^{3-}$ chromophore is kept at 100%, and we investigate the influence of the complexes sitting in the cavity of the oxalate network on the $^4A_2 \rightarrow {}^2E$ transition as function of the $[Ru(bpy)_3]^{2+}$ mole fraction. We will show that rather than just create disorder resulting in non-specific inhomogeneous broadening of the R-lines, we create specific spectroscopic sites for $[Cr(ox)_3]^{3-}$, which manifest themselves in additional splittings and concentration dependant shifts. In order to fully understand the different effects, we also investigate the shift of the R-lines as a function of external pressure. Finally, we propose a model which for a given mole fraction of $[Ru(bpy)_3]^{2+}$ gives the population distribution and energy of each individual specific site.

4.2 Experimental methods

4.2.1 Materials

The starting materials, $K_3Cr(ox)_3 \cdot 3H_2O$ and $[Ru(bpy)_3]Cl_2 \cdot 6H_2O$, were synthesized according to literature procedures [7,8]. $[Zn(bpy)_3]Cl_2 \cdot 6H_2O$ was prepared by adding $ZnCl_2$ to 3 equivalents of 2,2'-bipyridine in boiling water followed by slow evaporation of the solvent. The following chemicals were used as received: $RuCl_3$·hydrate, purum (Fluka); 2,2'-bipyridine, puriss. (Fluka); $ZnCl_2$ anhydrous, purum (Fluka); $K_2(ox) \cdot H_2O$, purum (Fluka); $H_2C_2O_4 \cdot 2H_2O$, ultra (Fluka); $K_2Cr_2O_7$ (Aldrich), NaCl (Aldrich).

4.2.2 Synthesis of mixed crystals of composition $[Zn_{1-x}Ru_x(bpy)_3][NaCr(ox)_3]$, $0 \leq x \leq 1$

The neat compounds (x = 0 and 1) were prepared according to the literature method of Decurtins and coworkers [2]. Accordingly, 10^{-2} M aqueous solutions of $K_3Cr(ox)_3$, $[Ru(bpy)_3]Cl_2 \cdot 6H_2O$, $[Zn(bpy)_3]Cl \cdot 6H_2O_2$ and NaCl were prepared. To obtain $[Zn(bpy)_3][NaCr(ox)_3]$ and $[Ru(bpy)_3][NaCr(ox)_3]$, 20 ml of the $K_3Cr(ox)_3$ and NaCl solutions were added to the same volumes of $[Zn(bpy)_3]^{2+}$ or $[Ru(bpy)_3]^{2+}$ solutions, respectively. Single crystals of the neat compounds in the form of perfect tetrahedra of 0.5 mm edge were obtained by slow evaporation of the solutions stored at 5 °C in a refrigerator.

The series of $[Zn_{1-x}Ru_x(bpy)_3][NaCr(ox)_3]$ mixed crystals were obtained by adding different volumes of the $[Zn(bpy)_3]^{2+}$ and $[Ru(bpy)_3]^{2+}$ solutions in order to have the nominal values of x = 0, 0.05, 0.1, 0.2, 0.4, 0.6, 0.8, and 1. Crystals were obtained of the mixed compounds in the same way as for the neat compounds. The effective Zn^{2+} and Ru^{2+} concentrations were determined by inductively coupled plasma-mass spectrometry (ICP-MS) and resulted in effective x values of 0, 0.18, 0.31, 0.44, 0.58, 0.76, 0.90, and 1, respectively. Powder samples were prepared by quick precipitation while stirring the mixture. For the same nominal ratios, the ICP-MS analysis gave real x values of 0, 0.23, 0.39, 0.56, 0.78, 0.89, 0.96, and 1, respectively.

4.2.3 X-ray diffraction

A crystal of size 0.2 x 0.1 x 0.04 mm was selected and mounted on a glass fiber. Data were collected on a STOE IPDS II image plate diffractometer using Mo Kα radiation at 293K. Integration of the data and absorption correction were done in the X-area software [9]. The structure was solved using the charge flipping method in the program Superflip [10] and refined by full matrix least-squares procedures on F^2 using Crystals [11]. H atoms positions could be located on Fourier difference maps but were recalculated geometrically. They were refined with strong restrains for a few cycles and then were allowed to ride on their parent atoms during the rest of the refinement. CRYSTALLOGRAPHIC DATA: formula $C_6CrNaO_{12}.C_{30}H_{24}N_6Ru$, Space-group $P2_13$, Z = 4, a = 15.5098 (6) Å, 32468 reflections measured, face-indexed absorption correction Tmin = 0.89 Tmax = 0.97, 3349 independent reflections (Rint = 0.097) of which 2442 with resolution larger than 0.81 Å were used in the least-square refinement, 172 parameters, R = 0.0492, wR = 0.0662, S = 0.8736, min and max residual peak density -0.54/0.63 $e \cdot Å^{-3}$, Flack parameter 0.01(4). X-ray powder diffraction diagrams of mixed $[Zn_{1-x}Ru_x(bpy)_3][NaCr(ox)_3]$, $0 \leq x \leq 1$, at room temperature were obtained on a Bruker Advanced D8 diffractometer using Bragg-Brentano geometry in reflection mode, monochromatic $CuK_{\alpha 1}$ radiation and a PSD detector. The powder diffraction patterns were fitted by profile matching with the FullProf software [12] within space group $P2_13$, using initial the parameters for neat $[Zn(bpy)_3][NaCr(ox)_3]$ and the lattice constant *a* as the only free parameter [13].

4.2.4 High-resolution absorption spectroscopy

Electronic absorption spectra were obtained on single crystals using a Fourier-transform spectrometer equipped for measuring in the infrared and visible spectral range (Bruker IFS66/S). The absorption spectra were collected at a spectral resolution of 0.5 cm^{-1}. For absorption measurements crystals with one corner of the tetrahedron polished down to a thickness of ~60 µm were mounted on copper

apertures, placed in a closed cycle cryostat (Oxford Instruments CCC1204), and collected at 10 K in an atmosphere of He exchange gas.

4.2.5 High-pressure luminescence measurements

Luminescence measurements were performed at 10 K using the same closed cycle cryostat and the FT spectrometer as for the absorption measurements. High pressures were achieved using a diamond anvil cell (MiniDAC of D'Anvils Ltd.). The sample chamber consisted of a hole with a diameter of 400 µm drilled into a pre-indented metal gasket. A single crystal of neat $[M(bpy)_3][NaCr(ox)_3]$ (M = Zn or Ru) was placed in the sample chamber with a crystal of Sm^{2+}:BaFCl used to calibrate the pressure inside the DAC (note: ruby cannot be used as it's R-lines are at exactly the same energy as those of $[Cr(ox)_3]^{3-}$). A 4:1 methanol:ethanol mixture was used as the pressure-transmitting medium. The crystals were excited at 532 nm and 405 nm (<10 mW) using laser diodes in order to selectively obtain the luminescence from the $[Cr(ox)_3]^{3-}$ and Sm^{2+} chromophores, respectively. The $^5D_0 \rightarrow {}^7F_0$ transition of Sm^{2+} is centered at 14531 cm^{-1} and is not split further by spin-orbit coupling. The shift rate of the $^5D_0 \rightarrow {}^7F_0$ transition of Sm^{2+} is -21 cm^{-1}/GPa [14]. The exact position of the $^5D_0 \rightarrow {}^7F_0$ luminescence band was determined with a Gaussian fit, and using the above shift rate, the pressure within the DAC was established for each experiment.

4.3 Results

4.3.1 Crystal structure of $[Zn_{1-x}Ru_x(bpy)_3][NaCr(ox)_3]$, $0 \leq x \leq 1$

The three-dimensional networks of the neat compounds $[Zn(bpy)_3][NaCr(ox)_3]$ and $[Ru(bpy)_3][NaCr(ox)_3]$ crystallize in the cubic and chiral space group $P2_13$ with Z = 4 [13]. The single crystal structure of $[Zn(bpy)_3][NaCr(ox)_3]$ has been reported previously [13]. Details of the single crystal structure determination of $[Ru(bpy)_3][NaCr(ox)_3]$ are given in the supporting information. The site symmetry of all metal centers is C_3. The three-dimensional network is formed by the $[Cr(ox)_3]^{3-}$ complexes bridged by the Na^+ ions, and it provides perfect cavities for the size and

the geometry of the $[M^{II}(bpy)_3]^{2+}$ complexes. The structure of the oxalate network is stabilized by the templating effect of the tris-bipyridine complexes through electrostatic interactions as well as π-π interactions between the oxalate and the bipyridine ligands. Table 4.1 reports structural parameters obtained from single crystals of the neat compounds, which will be relevant for the discussion of the spectroscopic properties. In addition to the lattice parameters, the unit cell volumes, Cr-O and Na-O bond lengths, and the interplane distances between oxalate ligands and the nearest and next-nearest neighbor bipyridine ligands are given.

Table 4.1. Lattice constant *a*, average Cr-O bond lengths, Cr-M^{2+} distance between a given Cr^{3+} and the seven M^{2+} ions of the nearest neighbor shell, and interplane distance between oxalate ligands and the bipyridine ligands of the next and next-nearest neighbors for $[Zn(bpy)_3][NaCr(ox)_3]$ and $[Ru(bpy)_3][NaCr(ox)_3]$ single crystals at room temperature.

	a [Å]	Cr–O [Å]	Na–O [Å]	Cr–M^{2+} (1^{st}) [Å]	Cr–M^{2+} (2^{nd}) [Å]	Cr–M^{2+} (3^{rd}) [Å]	p(bpy)-p(ox) (1^{st}) [Å]	p(bpy)-p(ox) (2^{nd}) [Å]
$[Zn(bpy)_3]$ $[NaCr(ox)_3]$	15.6365(18)	1.9695(2)	2.371(3)	6.1712(7)	8.586(1)	9.236(1)	3.634	3.623
$[Ru(bpy)_3]$ $[NaCr(ox)_3]$	15.5098(6)	1.9685(3)	2.339(3)	6.1501(8)	8.5150(9)	9.1453(9)	3.755	3.730

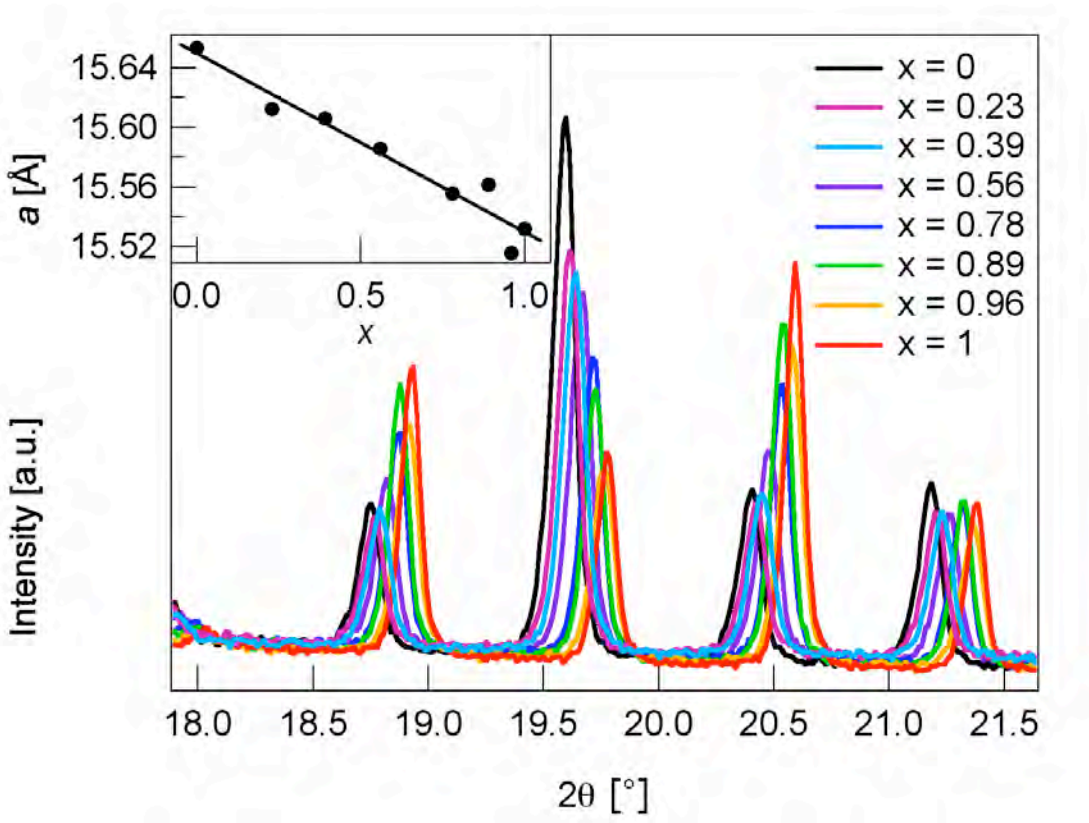

Figure 4.1. Powder diffraction patterns of $[Zn_{1-x}Ru_x(bpy)_3][NaCr(ox)_3]$, with x = 0, 0.23, 0.39, 0.56, 0.78, 0.89, 0.96, 1 at room temperature. The inset shows the evolution of the lattice parameter a as a function of the mole fraction x of $[Ru(bpy)_3]^{2+}$ as obtained from profile matching using the FullProf software.[12]

X-ray powder diffraction patterns were recorded for the series of mixed crystals with composition $[Zn_{1-x}Ru_x(bpy)_3][NaCr(ox)_3]$ synthesized as described in Section 4.2. Figure 4.1 shows an enlarged part of the diffraction patterns in the range of $17.9^o \leq 2\theta \leq 21.7^o$. The lattice parameter a was obtained by profile matching after entering the space group, the fractional coordinates of all atoms for the neat $[Zn(bpy][NaCr(ox)_3]$ from literature [13], and the approximate lattice parameter a as starting value. a is shown as function of the effective $[Ru(bpy)_3]^{2+}$ mole fraction x as determined by ICP-MS in the inset of Figure 4.1. It decreases linearly with increasing $[Ru(bpy)_3]^{2+}$ mole fraction, going from 15.6531 Å to 15.5318 Å for x from 0 to 1, thus obeying Vegard's law[15]. The corresponding unit cell volume decreases from 3835.3 to 3746.8 $Å^3$, that is, by 92.2 $Å^3$ or 2.4%. The small apparent difference between the lattice parameters obtained from powder and single crystals of the same compound is probably due to a small shift of the origin for the former. Thus, the difference is not

related to the structure of the oxalate network, and for the discussion the lattice parameters obtained from the single crystal determinations will be used.

4.3.2 Electronic absorption spectroscopy

Figure 4.2 shows the single crystal absorption spectrum of $[Zn(bpy)_3][NaCr(ox)_3]$ from 14000 to 29000 cm^{-1}. In accordance with previously published spectra of compounds with $[Cr(ox)_3]^{3-}$ as chromophore [16-18], the broad bands centered at 17889 cm^{-1} and 24270 cm^{-1} are readily attributed to the spin-allowed $^4A_2 \rightarrow {}^4T_2$ and $^4A_2 \rightarrow {}^4T_1$ transitions, respectively. The weak and sharp features at 14400, 14800 and 20580 cm^{-1} are assigned to the spin-flip transitions $^4A_2 \rightarrow {}^2E$, $^4A_2 \rightarrow {}^2T_1$ and $^4A_2 \rightarrow {}^2T_2$, respectively. Ligand field parameters can be estimated using the energies of $^4A_2 \rightarrow {}^4T_2$, $^4A_2 \rightarrow {}^4T_1$ and $^4A_2 \rightarrow {}^2E$ transitions and the Tanabe and Sugano energy matrices [19]. Hence, the ligand field parameters are 10Dq ≈ 17889 cm^{-1}, B ≈ 617 cm^{-1} and C ≈ 3249 cm^{-1}. Those parameters are close to the ones obtained for ruby [20,21], 10Dq ≈ 18100 cm^{-1}, B ≈ 650 cm^{-1} and C ≈ 3200 cm^{-1}.

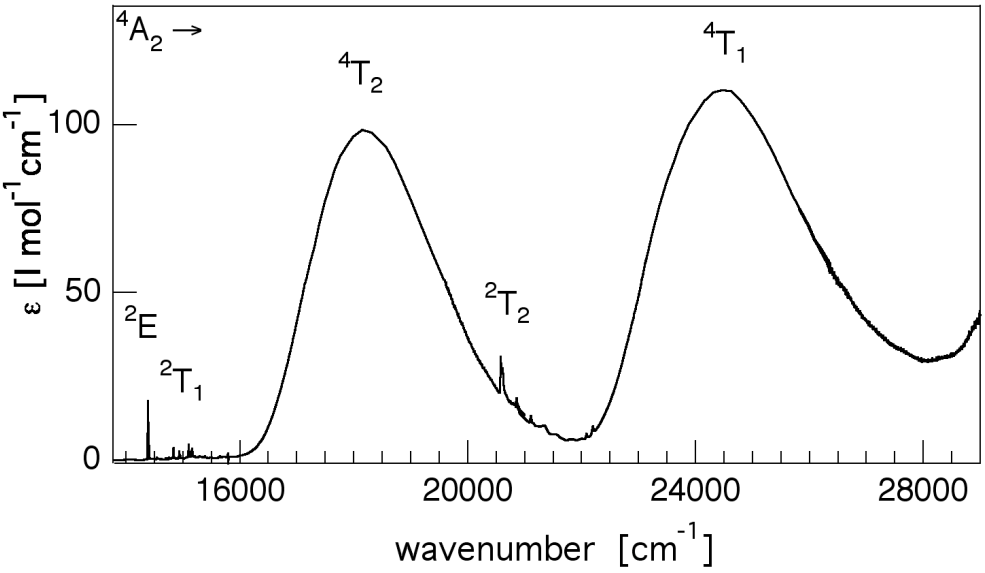

Figure 4.2. Single crystal absorption spectrum of $[Zn(bpy)_3][NaCr(ox)_3]$ at 10 K and 2.0 cm^{-1} spectral resolution.

As mentioned above, the lowest energy transition of Cr^{3+} in $[Cr(ox)_3]^{3-}$ in a strong ligand field is the spin-forbidden $^4A_2 \rightarrow {}^2E$ spin-flip transition of a d^3 ion. At 10 K, it

appears as two sharp zero-phonon lines (R-lines) with relatively small inhomogeneous line widths and relatively large extinction coefficients. These characteristics make it ideal for studying the structural homogeneity around the Cr^{3+} ions. A minor change in the local environment can be followed by the evolution of the $^4A_2 \rightarrow {}^2E$ band shape. Consequently, local structural information on $[Zn_{1-x}Ru_x(bpy)_3][NaCr(ox)_3]$ mixed crystals can be obtained by analyzing the $^4A_2 \rightarrow {}^2E$ transition as a function of *x*. Figure 4.3 shows the single crystal absorption spectra at 0.5 cm^{-1} spectral resolution in the region of the R-lines for x = 0, 0.18, 0.31, 0.44, 0.58, 0.76, 0.90, and 1, respectively. The spectrum of the neat compound $[Zn(bpy)_3][NaCr(ox)_3]$ consists of two Gaussian bands corresponding to the R_1 and R_2 lines. A zero-field splitting (ZFS) of the ^2E level of 15.2 cm^{-1} and an inhomogeneous line width of 2.1 cm^{-1} is obtained from a least squares fit to a Gaussian profile. This is in accordance with values observed for $[Cr(ox)_3]^{3-}$ in other hosts and matrices [6,16,22]. The ZFS of the $^4A_2$ ground state is not resolved. The origin of the ZFS of the $^4A_2$ and ^2E levels is the trigonal distortion (C_3 site symmetry [13]) and the spin-orbit coupling of the d^3 ion. For $[Ru(bpy)_3][NaCr(ox)_3]$, the inhomogeneous line width is somewhat smaller, and the ZFS of the $^4A_2$ ground state is resolved in the absorption spectrum of both R lines. Fitting each R-line with two Gaussians results in an inhomogeneous line width of 1.1 cm^{-1} and a ZFS of the $^4A_2$ ground state of 1.3 cm^{-1}, which is likewise in the range observed for this compound [16,17,22]. As compared to the neat $[Zn(bpy)_3]^{2+}$ compound, the ZFS of the ^2E state has decreased to 12.5 cm^{-1}, and the R-lines appear shifted to higher energies by ~10 cm^{-1}.

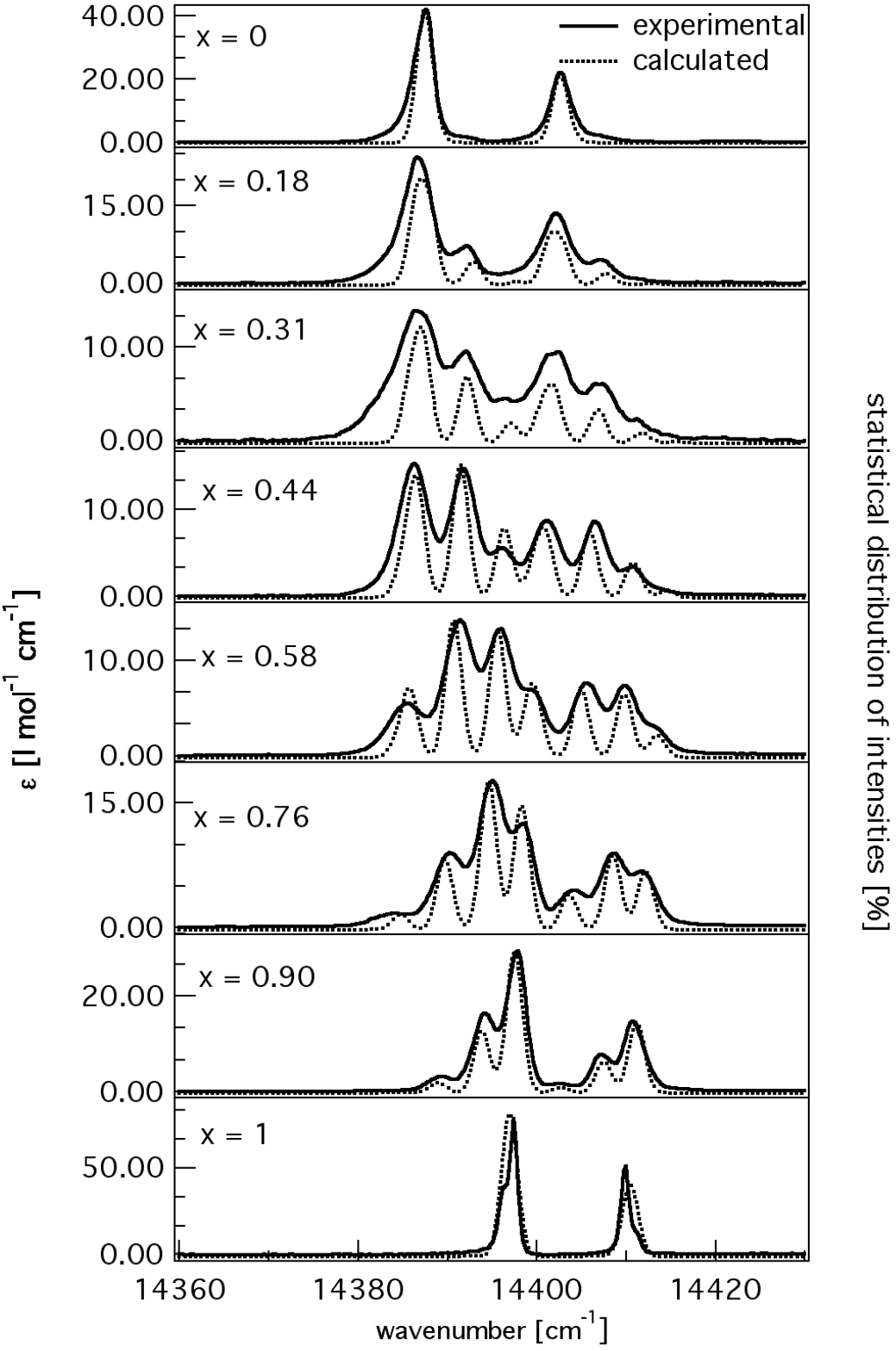

Figure 4.3. Single crystal absorption spectra of $[Zn_{1-x}Ru_x(bpy)_3][NaCr(ox)_3]$ at 10 K in the region of the $^4A_2 \rightarrow {}^2E$ transition, (—) experimental, (···) simulated as described in the text.

The absorption spectra of the mixed crystals do not at all show the initially expected smooth transition from the spectrum of one of the neat compounds to the spectrum of the other one, with at most an increase in the inhomogeneous line width for a certain range of *x*. Instead they show additional and distinct splittings of the R lines. These splittings and the relative intensities of the resulting multi-line spectrum can be quantitatively modeled (for a discussion see Section 4.4) on the basis of five distinct spectroscopic sites, which appear with different concentrations as function of the Ru^{2+} mole fraction across the series. On the basis of this observation, the ZFS of the ^2E state can be simply obtained by taking the energy difference between corresponding R lines. The analysis reveals that the ZFS of the ^2E state is within experimental accuracy independent of the specific site and only depends on the given Ru^{2+} mole fraction.

4.2.5 High-pressure luminescence experiments

Figures 4.4a and b show the luminescence of the R lines of $[Ru(bpy)_3][NaCr(ox)_3]$ and $[Zn(bpy)_3][NaCr(ox)_3]$, respectively, at different pressures going from 0 to 1.2 GPa and at 10 K. Even in the neat compounds the luminescence of the spin-flip transitions shifts to lower energies by about 1.5 cm^{-1} as compared to the absorption because of efficient energy migration within the ^2E state [23]. The insets of Figures 4a and b show the shift of the R_1 line as a function of external pressure as determined from Gaussian fits to the emission bands. The shift is linear and identical for both compounds for pressures up to 1 GPa with a shift rate of -25.2 ± 1.2 cm^{-1}/GPa. This is more than three times greater than shift rate of the R_1 line of Cr^{3+} in ruby, the latter being -7.59 cm^{-1}/GPa [23]. It is due to the higher compressibility of the three-dimensional oxalate network compounds compared to ruby. As will be discussed in more detail in Section 4.4, in the softer material there is a more pronounced increase of the nephelauxetic effect with applied pressure, for which both a shortening of the Cr–O bond lengths and increasing π-π interactions between oxalate and bipyridine ligands are responsible. Above ~1 GPa a doubling of the R-lines in $[Zn(bpy)_3][NaCr(ox)_3]$ indicates a pressure-induced crystallographic phase transition.

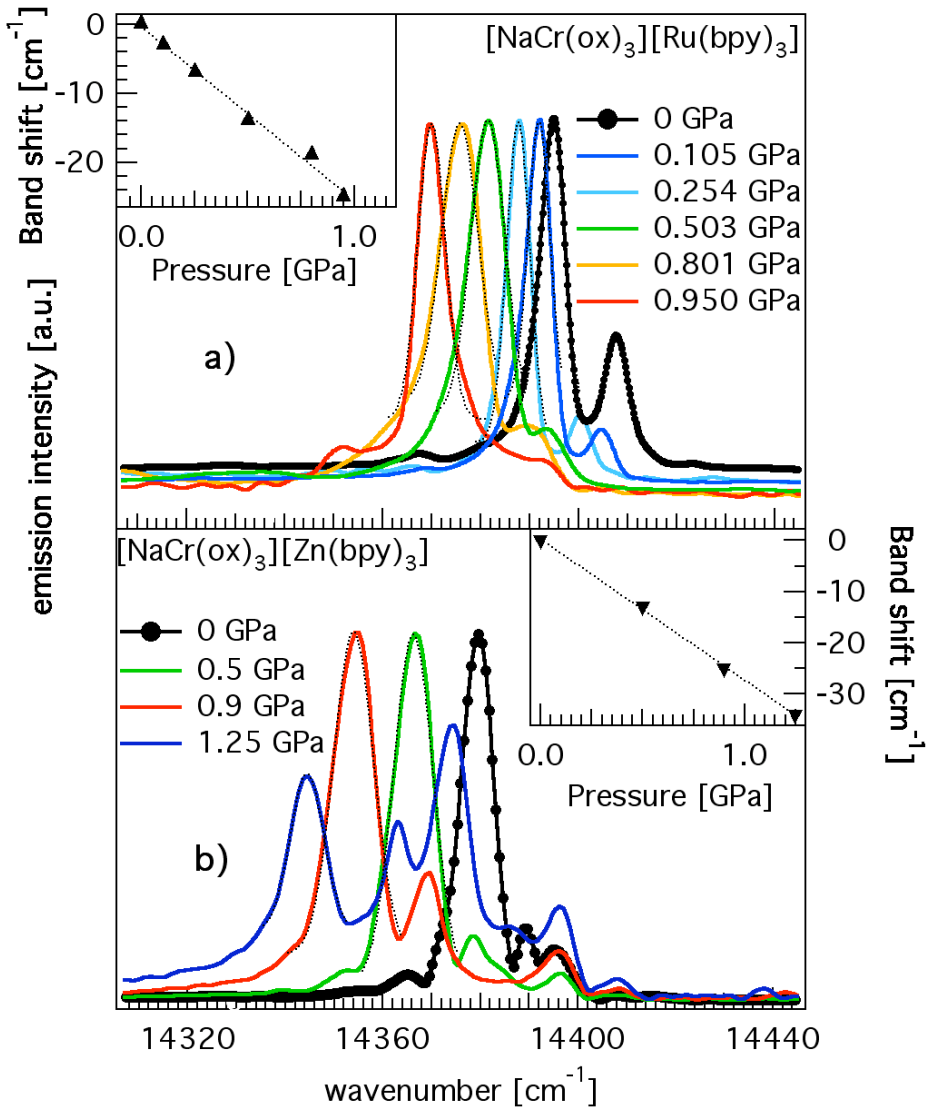

Figure 4.4. a) Luminescence spectra of $[Ru(bpy)_3][NaCr(ox)_3]$ (●) under atmospheric pressure and under different external pressures up to 1 GPa (—) at 10 K. The inset shows the dependence of the R_1 line with external pressure. b) Luminescence spectra of $[Zn(bpy)_3][NaCr(ox)_3]$ at 10 K under atmospheric pressure (●) and after applying different external pressures. The inset shows the dependence of the R_1 band shift with pressure.

4.4 Discussion

4.4.1 Absorption spectroscopy and specific spectroscopic sites

Within the three-dimensional network, the chromium oxalates are bridged by sodium ions making cavities in which the tris-bipyridine complexes are embedded. The three-dimensional structure can be simplified by considering a given Cr^{3+} ion and the neighboring M^{2+} ions. As schematically shown in Figure 4.5, the closest M^{2+} ion sits

on the threefold axis of the central ion at a distance of 6.2 Å. Three other M^{2+} ions are found at a distance of 8.6 Å, and the next three at 9.2 Å. These seven M^{2+} ions make up the nearest neighbor shell around a given Cr^{3+} ion. The closest M^{2+} neighbor to the Cr^{3+} has all three bipyridine ligands interacting with each oxalate ligand of the Cr^{3+} via a very good π-π overlap. The next three M^{2+} ions, sitting at 8.6 Å, have one of their three bipyridines that have an optimal overlap with on of the oxalates of the Cr^{3+}. The other two bipyridine ligands interact with the next Cr^{3+} ions in the lattice. For the last three, the π-π interactions between oxalate and bipyridine ligands are weak since the ligand planes are orthogonal to each other [24,25]. The origin of the 5 specific experimentally observed spectroscopic sites in the mixed crystal series $[Zn_{1-x}Ru_x(bpy)_3][NaCr(ox)_3]$ can thus be explained by considering the distribution of Zn^{2+} and Ru^{2+} among the four nearest $[M(bpy)_3]^{2+}$ neighbors of a given $[Cr(ox)_3]^{3-}$ complex for which non-negligible π-π interactions occur. A given Cr^{3+} ion can be surrounded by four Zn^{2+} ions. Such a site will be labeled (4,0). A Cr^{3+} surrounded by three Zn^{2+} and one Ru^{2+} ion will be labeled (3,1). Accordingly, the three other sites are labeled (2,2) and (1,3) for two or one Zn^{2+} and two or three Ru^{2+} ions, respectively, and (0,4) when all four positions are occupied by Ru^{2+}. Sites (3,1), (2,2), and (1,3) each have two sub-sites with different weights due to the fact that the four nearest M^{2+} neighbors are not at the same distance from the central ion, one being 2.3 Å closer than the other three. In Figure 4.3, the sub-sites are not resolved spectroscopically and will thus be neglected in the following. However, it is possible that they give rise to a somewhat larger inhomogeneous broadening of the corresponding absorption bands.

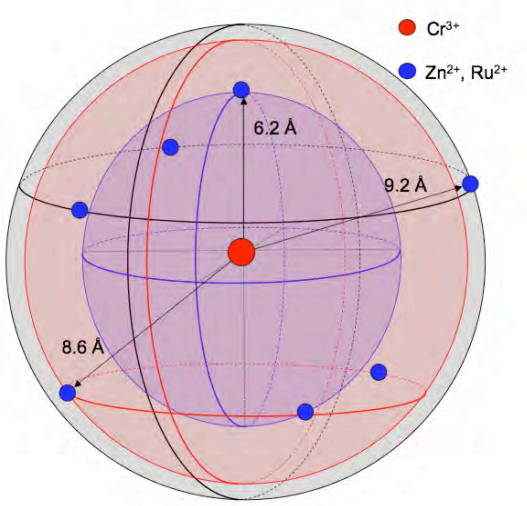

Figure 4.5. Schematic representation of the nearest-neighbor shell around a given Cr^{3+} ion.

The population of the 5 spectroscopic sites depends on the relative concentrations of Ru^{2+} and Zn^{2+}. For x = 0 and 1, only sites (4,0) and (0,4), respectively are populated. For arbitrary values of x the population of site (*N-n, n*) is given by a binomial distribution

$$p_n(x) = \binom{N}{n} \cdot (1-x)^{N-n} \cdot x^n \qquad N = 4, \text{ and } n = 0, 1, 2, 3, 4 \qquad (4.1)$$

The exact energy of the R-lines is modeled to depend upon x taking into account the global variation of the lattice constant on the one hand, and upon the specific environment according to the binomial distribution on the other hand. For the former we expect a linear red shift with increasing value of x due to the fact that for the neat Ru compound the lattice parameter a is smaller than for the neat Zn compound, which directly results in a reduction of the average Cr-O bond length, which, in turn, results in a reduction of the electronic repulsion due to an increasing electronic delocalization towards the ligands (nephelauxetic effect) [26,27]. The latter results in a step-wise shift to higher energies with an increasing number of Ru^{2+} ions in the nearest neighbor shell. This is due to the decreasing π-π interaction between oxalate and bipyridines and thus a decreasing nephelauxetic effect, because replacing Zn^{2+} with Ru^{2+} results in an increasing distance between bipyridine and oxalate ligand planes (see Table 4.1). Thus, the positions of the R_1 and R_2-lines for each of the five sites and as a function of x may be described by

$$\nu_{ni}(x) = \nu_{ni}^0 - b_i x \qquad i = 1, 2 \qquad (4.2)$$

Where ν_{ni}^{0} are the positions of R-lines of the site with *n* nearest neighbor Ru^{2+} ions extrapolated to *x* = 0 and *b* takes into account the global effect of an increasing Ru^{2+} concentration. With relative oscillator strengths of the R-lines to be f_1:f_2 = 2:1 taken directly from the spectrum at *x* = 0, and neglecting the variation in the inhomogeneous band width by assuming an average value of 2 cm^{-1} full width at half maximum, the absorption spectrum is given by a sum of Gaussians for each R-line according to

$$A_i(\tilde{\nu}) \sim f_i \sum_n \left(\binom{N}{n} \cdot (1-x)^{N-n} \cdot x^n \right) \cdot exp\left(-\frac{\left(\tilde{\nu} - (\tilde{\nu}_{ni}^{0} - b_i x)\right)^2}{2\sigma^2} \right) \qquad \text{i = 1, 2} \quad (4.3)$$

There are 4 fitting parameters in Equation 4.3, namely $\tilde{\nu}_{1,1}^{0}, \tilde{\nu}_{2,1}^{0}, \tilde{\nu}_{3,1}^{0}$ and b_1. The other constants such as $\tilde{\nu}_{0,1}^{0}$, $\tilde{\nu}_{4,1}^{0}$, all the $\tilde{\nu}_{n,2}^{0}$ of the R_2 line and b_2 can either be obtained directly from the experiment at *x* = 0 and 1, or they can be expressed as functions of the first four fitting parameters. Thus, $\tilde{\nu}_{4,1}^{0} = \tilde{\nu}_{4,1}^{1} + b_1$, $\tilde{\nu}_{n,2}^{0} = \tilde{\nu}_{n,1}^{0} + D(^2E)_4^0$, where $D(^2E)_4^0$ is the ZFS of the ^2E state of the site (4,0) for *x* = 0, and $b_2 = \tilde{\nu}_{4,1}^{1} - \tilde{\nu}_{4,2}^{1} + D(^2E)_4^0 + b_1$, where the superscript refers to *x* = 1. The simultaneous best fit of Equation 4.3 to all the experimental spectra of Figure 4.3 gives initial positions at 14387.5, 14389.0, 14393.9, 14398.8, and 14402.5 cm^{-1} for the R_1-line of the sites (4,0), (3,1), (2,2), (1,3), and (0,4) respectively, and b_1 = 5.5 cm^{-1}, and 14402.7, 14404.2, 14409.1, 14414.0, and 14417.7cm^{-1} for the R_2-line and b_2 = 7.2 cm^{-1}. Figure 4.3 includes the calculated absorption spectra using the above parameters. The overall agreement between experimental and calculated spectra across the series is good. The biggest deviations are due the variation in the inhomogeneous broadening, which is larger for the distributions with high concentrations of sub-sites and which are not resolved spectroscopically. In order to further illustrate this, Figure 4.6 indicates the positions of the five individual sites for three different compositions. The model developed in this paper shows clearly that several sites are hidden within the same band. For example, the band at 14399 cm^{-1} of the compound with *x* = 0.58 is composed of three sites, R_1(0,4), R_2(3,1) and R_2(4,0). This is the principle reason why it's difficult to extract the ZFS of individual sites for the different concentrations directly from the experimental data. In this multi-site system, neither FLN nor hole burning spectroscopy on the individual sites are possible, the former due to efficient excitation

energy transfer [16], and the latter due to the fact that in the very well crystallized three-dimensional oxalate network, persistent hole burning is not observed.

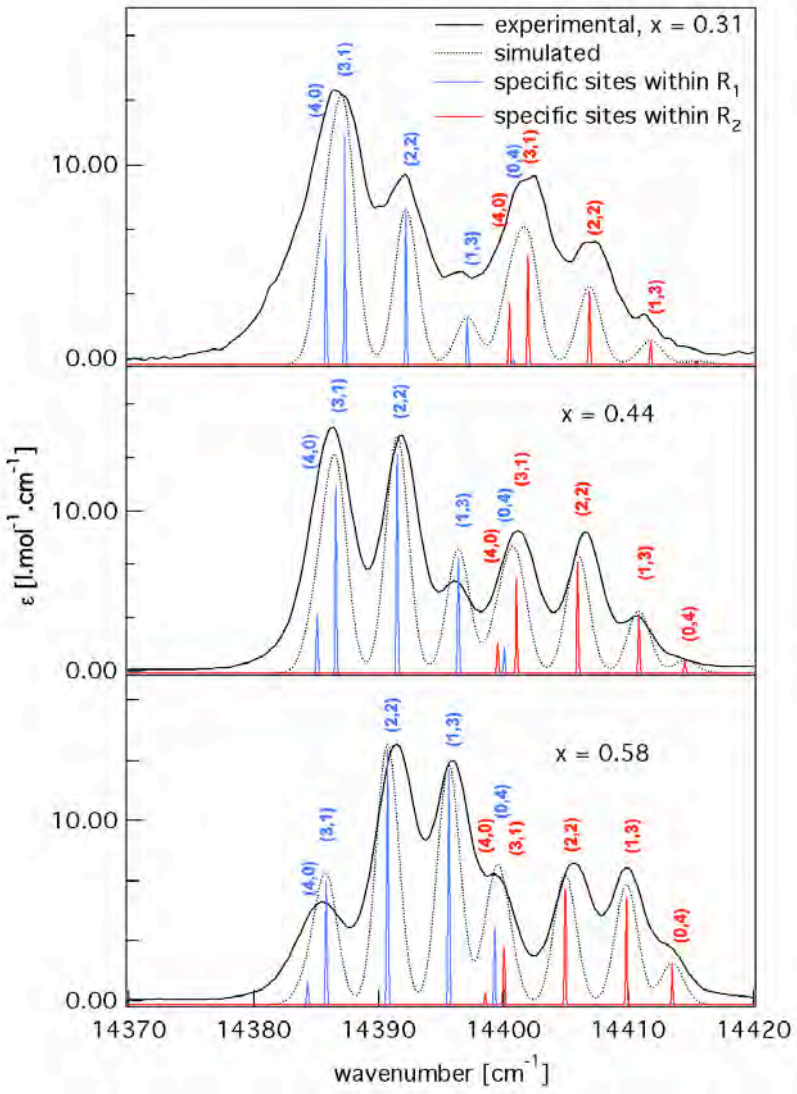

Figure 4.6. The energies of the individual sites for Ru^{2+} mole fraction x = 0.31, 0.44 and 0.58 in the mixed crystal series $[Zn_{1-x}Ru_x(bpy)_3][NaCr(ox)_3]$ at 10 K.

4.4.2 Chemical and physical pressure on $[Cr(ox)_3]^{3-}$

The basic effect of pressure on any molecular solid is to decrease its volume. As a result, not only structural parameters such as bond angles and bond lengths but also intra- and intermolecular interactions change, thus affecting chemical, electrical, optical, and magnetic properties of the material. With regard to optical properties, absorption and emission bands shift with pressure either to higher or lower energies depending upon the nature of the states involved. Materials with high bulk moduli are

more difficult to compress, and thus exhibit small volume changes per unit pressure, and generally show smaller pressure shifts of electronic states in comparison to systems with low bulk moduli. An example of a hard material is ruby with a bulk modulus of 253 GPa [28,29] and a shift of -7.59 cm^{-1}/GPa, that is to lower energies[30], for the $^4A_2 \rightarrow {}^2E$ transition. The isothermal compressibility κ is the inverse of the bulk modulus K and gives an indication of the sensitivity of a system to pressure[31,32]

$$\kappa = -\frac{1}{V}\left(\frac{\partial V}{\partial P}\right)_T = \frac{1}{K} \qquad (4.4)$$

Brillouin scattering experiments on the related system $[Rh(bpy)_3][NaCr(ox)_3]ClO_4$,[33] gave a value for K of ~10 GPa.

When applying pressure on $[M^{II}(bpy)_3][NaCr(ox)_3]$ two important geometrical parameters are influenced: the Cr-O bond length decreases and the interplane separation between oxalate and bipyridine ligands decreases likewise. Both effects contribute to the observed red shift. When the Cr-O bond length decreases, the Racah parameters B and C decrease as well because of increased delocalization of electrons onto the oxalate ligands. When the interplane separation between the oxalates and the bipyridines decreases, π-π interactions increase, leading to a further delocalization of electron density from the oxalate ligands to the bipyridines and amplifying the nephelauxetic effect. With -25.2 $cm^{-1}GPa^{-1}$, the resulting shift rate of the $^4A_2 \rightarrow {}^2E$ transition is thus quite large compared to ruby [23] and other Cr^{3+} doped lattices [34-36].

The lattice parameters *a* as obtained for $[Zn(bpy)_3][NaCr(ox)_3]$ and $[Ru(bpy)_3][NaCr(ox)_3]$ from X-ray diffraction are 15.6365 Å and 15.5098 Å, respectively. Thus, replacing Zn^{2+} with Ru^{2+} decreases the unit cell volume by 92.2 $Å^3$ or 2.4%. For a bulk modulus of 10 GPa, the same decrease in volume requires an external pressure of ~0.24 GPa. Thus, for an external pressure of 0.24 GPa, which reduces the volume of $[Zn(bpy)_3][NaCr(ox)_3]$ to that of $[Ru(bpy)_3][NaCr(ox)_3]$ at ambient pressure, the R_1-line shifts by approximately 6.0 cm^{-1} to lower energy. This value has to be compared to the b_i (i = 1, 2) parameters of the model described in 4.1. It is indeed very close to the average value of 6.5 cm^{-1} obtained from the fit for the latter. Hence, the b_i parameters have a physical significance, and correspond to

the energy shift of the luminescence band solely due to the volume contraction on going from $[Zn(bpy)_3][NaCr(ox)_3]$ to $[Ru(bpy)_3][NaCr(ox)_3]$ while keeping the immediate chemical environment of a given site unchanged.

The crystallographic data given in Table 4.1 shows that when replacing $[Zn(bpy)_3]^{2+}$ with $[Ru(bpy)_3]^{2+}$, the Cr-O distance decreases only very slightly from 1.970 Å to 1.969 Å, while the distance between the oxalate and bipyridine planes increases more significantly, that is, from 3.634 Å to 3.755 Å for the nearest-neighbor pair. As for external pressure, the Cr-O bond length decreases upon reduction of the unit cell parameter, but in contrast to external pressure, the substitution of Zn^{2+} by the smaller Ru^{2+} results in a reduced π-π interaction. Thus, in contrast to external pressure, the relevant geometric changes upon substitution work in opposite directions. With regard to the oxalate network the reduction in the size of the $[M(bpy)_3]^{2+}$ ion is absorbed by the Na-O bond rather than by the Cr-O bond and therefore overall, the effect of the change in π-π interaction dominates. Thus for the neat compounds, $[Zn(bpy)_3][NaCr(ox)_3]$ and $[Ru(bpy)_3][NaCr(ox)_3]$ with only one specific site, (4,0) and (0,4), respectively, the R-lines shift to higher energies by ~10 cm^{-1} despite the decrease in Cr-O bond length. Within the mixed crystal series the decrease of the π-π interaction strength when substituting the Zn^{2+} with Ru^{2+} sequentially around a given Cr^{3+} is responsible for the discrete shifts to higher energies, while the small decrease of the Cr-O bond length with increasing $[Ru(bpy)_3]^{2+}$ mole fraction is responsible for the small shift to lower energies of each individual specific site.

4.5 Conclusions

In the series of mixed crystals with composition $[Zn_{1-x}Ru_x(bpy)_3][NaCr(ox)_3]$, distinct sites are created for each Cr^{3+} ion. High-resolution absorption spectroscopy, high-pressure luminescence experiments and crystallographic data allowed some clear-cut conclusions about the relation between the geometric and electronic structure of Cr^{3+} in the three-dimensional oxalate network lattices. The specific sites arise according to the distribution of the four closest M^{2+} positions around the Cr^{3+}. Thus, five specific sites are resolved spectroscopically. Each individual site shifts to lower energy when the mole fraction of $[Ru(bpy)_3]^{2+}$ is increased. This is due to the

shortening of the Cr-O bond length, and thus decreasing Racah parameters. On the other hand, the energies of each specific site increase with an increasing number of $[Ru(bpy)_3]^{2+}$ on the four specific positions around a given Cr^{3+}. This is due to the decrease of the π-π interaction when a smaller $[M(bpy)_3]^{2+}$ complex is sitting in the oxalate cavity. Thus, the nephelauxetic effect decreases and the R_1 and R_2 of each site discretely shift to higher energies. In this paper, we developed a simple model that nicely fits the absorption spectra of the mixed crystal series. The population of each site was modeled with a statistical binomial distribution, while the energy of the ^2E transition of each site and its dependence on the $[Ru(bpy)_3]^{2+}$ mole fraction was modeled with reference to high-pressure experiments on the neat $[Ru(bpy)_3][NaCr(ox)_3]$ compound. With our results we demonstrate the importance of π-π interactions in the second coordination shell even for the photophysical properties of involving metal centered d-d transitions.

Acknowledgments

The authors thank the Swiss National Science Foundation (grant number 200020-125175) for funding, C. Besnard for the crystal structure of the ruthenium compound, F. Kubel for advice regarding the evaluation of the powder diffraction data, N. Amstutz for her help in the preperation of the samples, and H. Hagemann for his help with the pressure experiments.

References

[1] S. Decurtins, H.W. Schmalle, P. Schneuwly, J. Ensling, P. Gutlich, J. Am. Chem. Soc. 116 (1994) 9521.

[2] S. Decurtins, H.W. Schmalle, R. Pellaux, P. Schneuwly, A. Hauser, Inorg. Chem. 35 (1996) 1451.

[3] F. Pointillart, C. Train, M. Gruselle, F. Villain, H.W. Schmalle, D. Talbot, P. Gredin, S. Decurtins, M. Verdaguer, Chem. Mater. 16 (2004) 832.

[4] E. Coronado, J.R. Galan-Mascaros, C.J. Gomez-Garcia, E. Martinez-Ferrero, M. Almeida, J.C. Waerenborgh, Eur. J. Inorg. Chem. (2005) 2064.

[5] M. Zerara, A. Hauser, ChemPhysChem 5 (2004) 395.

[6] M.E. von Arx, V.S. Langford, U. Oetliker, A. Hauser, J. Phys. Chem. A 106 (2002) 7099.

[7] G.M. Booth H.S., Inorg. Synth. 1 (1939) 35.

[8] R.A. Palmer, T.S. Piper, Inorg. Chem. 5 (1966) 864.

[9] Stoe & Cie (2005). X-AREA. Stoe & Cie GmbH, Darmstadt, Germany.

[10] L. Palatinus, G. Chapuis, J. Appl. Cryst. 40 (2007) 786.

[11] P.W. Betteridge, J.R. Carruthers, R.I. Cooper, K. Prout, D.J. Watkin, J. Appl. Cryst. 36 (2003) 1487.

[12] J. Rodriguez-Caravajal, Physica B 192 (1993) 55.

[13] R. Sieber, S. Decurtins, H. Stoeckli-Evans, C. Wilson, D. Yufit, J.A.K. Howard, S.C. Capelli, A. Hauser, Chem-Eur J 6 (2000) 361.

[14] Y.R. Shen, W.B. Holzapfel, Phys. Rev. B 52 (1995) 12618.

[15] L. Vegard, Z Phys 5 (1921) 17.

[16] T. Schönherr, J. Spanier, H.H. Schmidtke, J. Phys. Chem. 93 (1989) 5969.

[17] M. Milos, S. Kairouani, S. Rabaste, A. Hauser, Coord. Chem. Rev. 252 (2008) 2540.

[18] T.S. Piper, R.L. Carlin, J. Chem. Phys. 35 (1961) 1809.

[19] Y. Tanabe, S. Sugano, J. Phys. Soc. Jpn. 9 (1954) 753.

[20] R.G. Munro, J. Chem. Phys. 67 (1977) 3146.

[21] Y. Tanabe, S. Sugano, J. Phys. Soc. Jpn. 11 (1956) 864.

[22] H. Riesen, Coord. Chem. Rev. 250 (2006) 1737.

[23] K.L. Bray, Top. Curr. Chem. 213 (2001) 1.

[24] V.S. Langford, M.E. von Arx, A. Hauser, J. Phys. Chem. A 103 (1999) 7161.

[25] A. Hauser, M.E. von Arx, V.S. Langford, U. Oetliker, S. Kairouani, A. Pillonnet, Top. Curr. Chem. 241 (2004) 65.

[26] C.E. Schaffer, C.K. Jorgensen, J. Inorg. & Nucl. Chem. 8 (1958) 143.

[27] C.K. Jorgensen, Discuss. Farad. Soc (1958) 110.

[28] A.P. Jephcoat, R.J. Hemley, H.K. Mao, R.E. Cohen, M.J. Mehl, Phys. Rev. B 37 (1988) 4727.

[29] P. Richet, J.A. Xu, H.K. Mao, Phys. Chem. Miner. 16 (1988) 207.

[30] G.J. Piermarini, S. Block, J.D. Barnett, R.A. Forman, J. Appl. Phys. 46 (1975) 2774.

[31] C. Kittel: Introduction to Solid State Physics, John Wiley & Sons, 2005.

[32] M.L. Cohen, Phys. Rev. B 32 (1985) 7988.

[33] C. Ecolivet, S. Rabaste, unpublished results.

[34] Y.R. Shen, T. Riedener, K.L. Bray, Phys. Rev. B 61 (2000) 11460.

[35] P.R. Wamsley, K.L. Bray, J. Lumin. 63 (1995) 31.

[36] M. Grinberg, A. Suchocki, J. Lumin. 125 (2007) 97.

5. Persistent spectral hole-burning in the R_1 line of Cr^{3+} doped $NaMg[Al(oxalate)_3]\cdot 9(H_2O/D_2O)$ induced by resonant energy transfer

*Published in Journal of Physical Chemistry A, 114, **2010**, 4169.*

Mia Milos, Andreas Hauser*

Contents

Abstract

In the three-dimensional network $[Rh(bpy)_3][NaCr(ox)_3]ClO_4$ (ox = oxalate, bpy = 2,2'-bipyridine) phonon-assisted as well as resonant energy migration within the R_1 line of the $^4A_2 \rightarrow {}^2E$ transition of Cr^{3+} has been identified. The latter is dominant below 4.2 K, and in a fluorescence line narrowing spectrum it manifests itself in a multi-line pattern across the inhomogeneous line width with spacings corresponding to the zero-field splitting of the $^4A_2$ ground state [M. Milos, S. Kairouani, S. Rabaste, A. Hauser, Coord. Chem. Rev. 252 (2008) 2540]. On the other hand, H. Riesen demonstrated very efficient spectral hole burning within the R_1 line of Cr^{3+} doped at very low concentrations into partially deuterated $NaMg[Al(ox)_3]\cdot 9H_2O$ [H. Riesen, Coord. Chem. Rev. 250 (2006) 1737]. Here, we show that at higher Cr^{3+} concentrations in the same host, both phenomena can be observed simultaneously, the resonant energy migration thus creating an additional series of persistent side holes.

Keywords:

Persistent spectral hole burning; energy migration; fluorescence line narrowing; $[Cr(ox)_3]^{3-}$.

5.1 Introduction

Spectral hole burning is a high-resolution site selective spectroscopy that can overcome some aspects of the inhomogeneous broadening, which obscures information regarding the electronic structure. Three different mechanisms of hole burning have been established to date [1]: photochemical hole burning, photophysical hole burning and transient hole burning. The first mechanism involves a photochemical reaction upon the excitation of a subset of chromophores, and at the same time as the spectral hole is burnt, a photoproduct appears at quite different energy than the initially excited chromophore. Photophysical hole burning involves a rearrangement of host-guest interactions, and as a consequence, the initially excited subset of chromophores absorbs at slightly different energy but still within the inhomogeneous line width. Those two mechanisms result in persistent holes. The third mechanism is, in principle, universal. Upon selective excitation of a subset of chromophores, a depletion of the ground state occurs at the laser frequency. This depletion lasts as long as the system takes to relax back to the initial ground state.

Persistent photophysical hole burning is rather common in amorphous systems at low temperatures [2], but there are a few reports on photophysical hole burning in crystalline systems [3,4]. One of the crystalline systems that exhibits persistent photophysical hole burning is Cr^{3+} doped $NaMg[Al(ox)_3]\cdot 9H_2O$, ox = oxalate [5], in which Cr^{3+} substitutes for Al^{3+}. The photophysical and structural properties of this system have been studied extensively in the past [6-11]. The crystal structure and in particular the number of water molecules in the lattice are crucial and have been well established [11]. Persistent photophysical holes can be burnt within the R_1 line of the $^4A_2 \rightarrow {}^2E$ transition of Cr^{3+}. At a concentration of 1 mole%, the width of these holes in the absence of an external magnetic field is 20 MHz at 2.8 K and corresponds to the residual homogeneous line width limited by spin-spin relaxation [9]. Partial deuteration of the water molecules increases the spectral hole burning efficiency by a factor of 1000 and leads to holes that are stable up to 100 K [11]. The proposed mechanism is based on the rotational reorientation of water molecules of crystallisation hydrogen bonded to oxalate around their pseudo C_2 axes. When the DHO molecules undergo a 180° flip motion, the difference in the zero-point energies

of the excited and ground state, and hence the transition frequency, changes. Thus, each photoinduced flip of a DHO molecules results in spectral hole-burning [10].

Excitation energy transfer or energy migration within the R_1 line of the $^4A_2 \rightarrow {}^2E$ transition of Cr^{3+} has been observed in a series of chromium tris-oxalate compounds [12-14], namely in $[Rh(bpy)_3][NaCr(ox)_3]ClO_4$, bpy = 2,2'-bipyridine. In addition to the common temperature dependant phonon-assisted process, a resonant process between the zero-field split components of the $^4A_2$ ground state has been identified. The latter is dominant below 4.2 K, and in a fluorescence line narrowing (FLN) spectrum it leads to a multi-line pattern of sharp peaks spaced by the ground state zero-field splitting (ZFS) across the inhomogeneous line width of the R_1 line. In contrast to Cr^{3+} doped $NaMg[Al(ox)_3]\cdot 9H_2O$, the rigid oxalate networks show no persistent spectral hole burning.

In this letter, we will show that at higher concentrations of Cr^{3+} in partially deuterated mixed crystals of $NaMg[Al_{1-x}Cr_x(ox)_3]\cdot 9H_2O$ it is possible to simultaneously burn persistent holes and to observe resonant energy transfer, the latter in fact resulting in a series of additional persitant side holes.

5.2 Experiment

$NaMg[Al(ox)_3]\cdot 9H_2O$ and $NaMg[Cr(ox)_3]\cdot 9H_2O$ were prepared as described in the literature [15]. Mixed crystals of $NaMg[Al_{1-x}Cr_x(ox)_3]\cdot 9H_2O$ were grown by slow evaporation from aqueous solutions containing given fractions of $[Al(ox)_3]^{3-}$ and $[Cr(ox)_3]^{3-}$. The effective Cr^{3+} concentrations in the crystals were determined from single crystal absorption spectra. Partially deuterated crystals were grown from solutions containing the desired ratio of H_2O/D_2O. Crystals of the following compositions were used in the present study: protonated $NaMg[Al_{0.99}Cr_{0.01}(ox)_3]\cdot 9H_2O$, partially deuterated $NaMg[Al_{0.99}Cr_{0.01}(ox)_3]\cdot 9(H_2O/D_2O)$ and $NaMg[Al_{0.8}Cr_{0.2}(ox)_3]\cdot 9(H_2O/D_2O)$, the latter both with H_2O/D_2O ratio of 1.

The samples were cooled to 1.4 K in a helium bath cryostat (Cryo Industries). Conventional transmission spectra were measured by passing white light from a

tungsten lamp through a band pass filter and analysing the transmitted light using a double monochromator (SPEX 1403) and a CCD camera (Roper Instruments), giving a spectral resolution of 0.25 cm^{-1}. For non-selective luminescence spectra samples were excited at 532 nm, that is into the $^4A_2 \rightarrow {}^4T_2$ transition of Cr^{3+}, from an intracavity frequency doubled Nd:YAG laser (10650). FLN spectra were obtained by selective excitation using a Ti:Saphire laser (Coherent 699) at around 14450 cm^{-1}, that is within the R_1 electronic origin of Cr^{3+}. The collected emission was dispersed by the same monochromator and detected by the same CCD camera as above. Persistent photophysical holes were burnt with the same Ti:Saphire laser for 40 min and with a laser power of 5mW/mm^2. The spectral holes were observed in absorption and luminescence spectra using the same detection setup, and in both cases the irradiation power was reduced with grey filters to avoid heating of the sample and reduce photophysical hole filling.

5.3 Results and discussion

Figures 5.1a and 5.1b show the absorption and non-selectively excited luminescence spectra in the region of the R_1 line of the $^4A_2 \rightarrow {}^2E$ transition at 1.4 K for the dilute samples of this study, namely the $NaMg[Al_{0.99}Cr_{0.01}(ox)_3]\cdot 9H_2O$, and the partially deuterated $NaMg[Al_{0.99}Cr_{0.01}(ox)_3]\cdot 9(H_2O/D_2O)$. In the fully protonated system the inhomogeneous line widths of the two components are ~ 0.8 cm^{-1}, and the ground state ZFS of D = 1.6 cm^{-1} is fully resolved and in agreement with EPR and FLN spectroscopy [5,6].

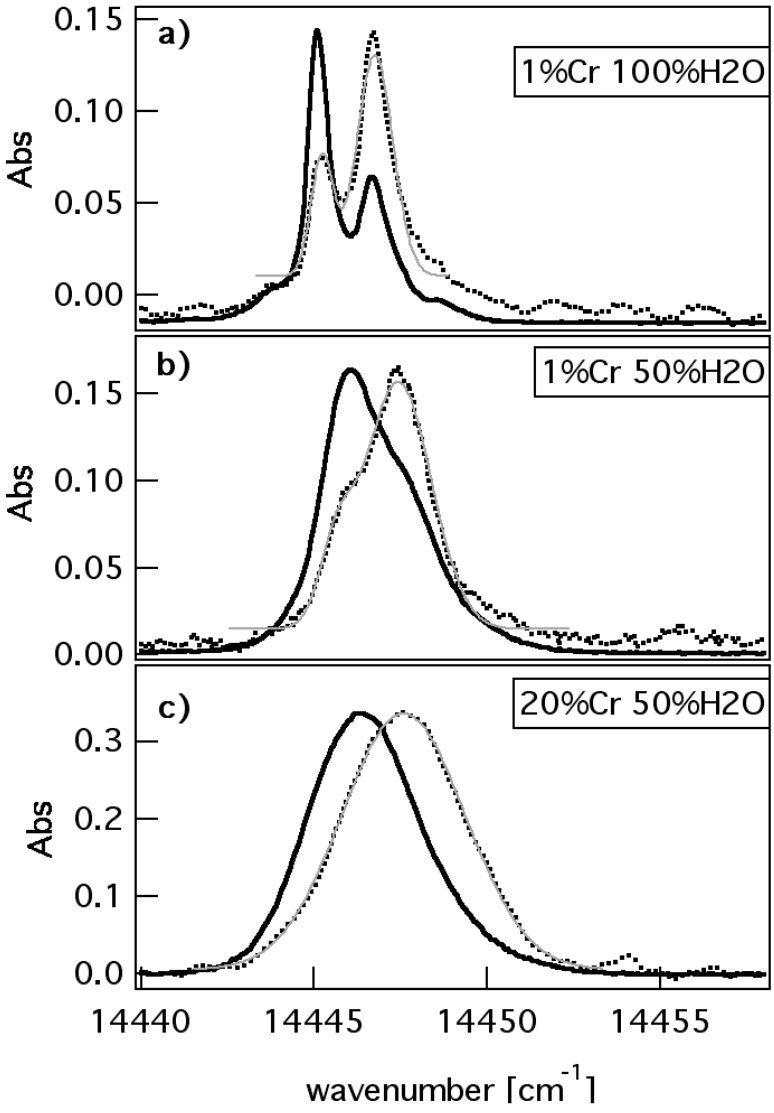

Figure 5.1. Absorption (·····) and luminescence (—) in the region of the R_1 lines of the $^4A_2 \rightarrow {}^2E$ transition of $[Cr(ox)_3]^{3-}$ in different lattices at 1.4 K: a) $NaMg[Al_{0.99}Cr_{0.01}(ox)_3]\cdot 9H_2O$, b) $NaMg[Al_{0.99}Cr_{0.01}(ox)_3]\cdot 9(H_2O/D_2O)$, and c) $NaMg[Al_{0.8}Cr_{0.2}(ox)_3]\cdot 9(H_2O/D_2O)$.

Partially deuterating the system broadens both components of the R_1 line and consequently the inhomogeneous line widths is ~ 1.7 cm^{-1}. The ground state ZFS is barely discernable as shoulder in both absorption and emission spectra. The intensity ratios of the zero-field split components in absorption and emission for both samples are in agreement with the ±3/2 component of the $^4A_2$ state being below the ±1/2 component [16,17]. Figure 5.1c shows the absorption and non-selectively excited luminescence spectra at 1.4 K of the more concentrated system of this study, namely $NaMg[Al_{0.8}Cr_{0.2}(ox)_3]\cdot 9(H_2O/D_2O)$. With ~ 4.2 cm^{-1}, the inhomogeneous broadening of

the ±3/2 and ±1/2 components of the R_1 line of this sample is large enough such that the ground-state ZFS is not resolved. There is, however, another difference compared to the more dilute samples: whereas the Stokes shift for the compounds containing 1% of Cr^{3+} is close to zero, the Stokes shift for the sample containing 20% Cr^{3+} is ~2 cm^{-1}, as a first indication for energy migration at high Cr^{3+} concentrations.

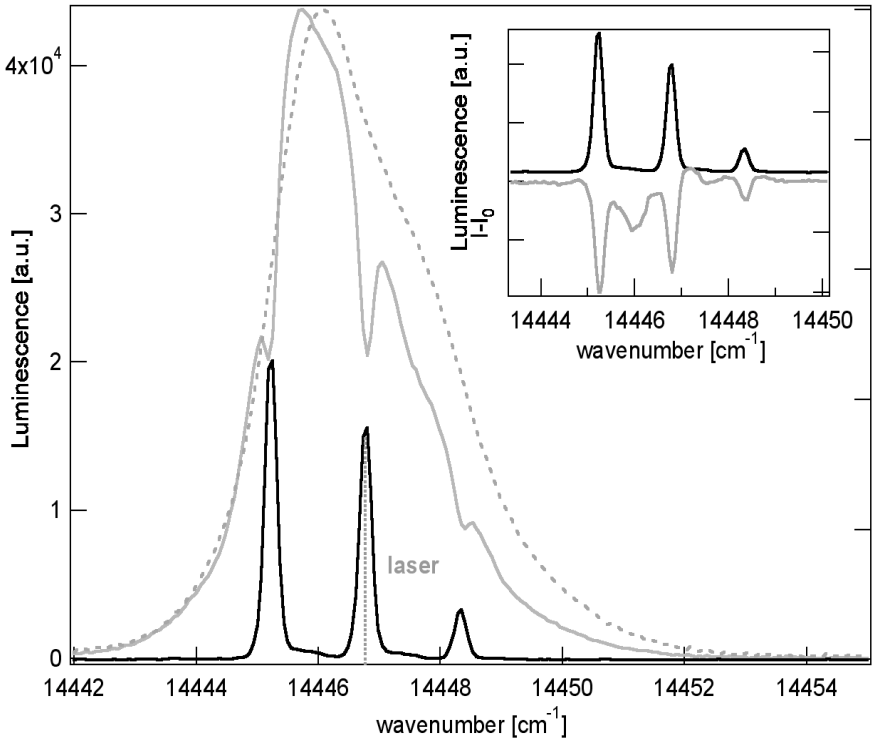

Figure 5.2. FLN spectrum (—) and non-selectively excited luminescence spectrum before (----) and after spectral hole burning (—) of $NaMg[Al_{0.99}Cr_{0.01}(ox)_3]\cdot 9(H_2O/D_2O)$ at 1.4 K. Inset: difference in non-selectively excited luminescence before (I_0) and after hole burning (I) together with the FLN spectrum.

The FLN spectrum presented in Figure 5.2 on dilute but partially deuterated $NaMg[Al_{0.99}Cr_{0.01}(ox)_3]\cdot 9(H_2O/D_2O)$ shows the typical three-line spectrum characteristic for isolated Cr^{3+} chromophores, with the central line at the laser frequency of 14446.8 cm^{-1} and the satellite lines at ±D from the resonant line [13]. In accordance with Ref. [5] persistent holes were burnt in this system by selectively irradiating at 14446.8 cm^{-1} for 40 minutes and with 5 mW/mm^2 laser power. As expected and shown in Figure 5.2, three holes are observed in the subsequently recorded non-selectively excited luminescence spectrum, that is, the resonant hole at 14446.8 cm^{-1} and the side holes

at ±D. Since the excitation takes place in the middle of the absorption band, there are less chromophores that contribute to the luminescence spectrum. This explains the difference between non-selectively excites luminescence spectra before and after spectral hole burning at the red wing of the band. It should be noted that in Figure 5.2 the hole width is limited by the spectral resolution of the monochromator of 0.25 cm^{-1}. This is several orders of magnitude larger than the 20 MHz of the homogeneous line width as determined by Riesen et al. [9]. However, in the context of the present study this is not important.

For the more concentrated sample, $NaMg[Al_{0.8}Cr_{0.2}(ox)_3]\cdot 9(H_2O/D_2O)$, both FLN and spectral hole burning give very different results compared to the diluted systems. In addition to the absorption and non-selectively excited luminescence, Figure 5.3a shows the FLN spectrum of $NaMg[Al_{0.8}Cr_{0.2}(ox)_3]\cdot 9(H_2O/D_2O)$ upon excitation at 14449.3 cm^{-1} with low laser power. Instead of the three lines, the FLN spectrum consists of six lines separated by the ground state ZFS. As for the diluted sample, the laser excites a subset of chromophores inside the inhomogeneously broadened R_1 line of the $^4A_2 \rightarrow {}^2E$ transition having a transition energy within a homogeneous line width around the excitation energy. In addition to returning back to the ground state by luminescence and as schematically shown in Figure 5.4, in the more concentrated sample the initially excited chromophore can transfer its energy resonantly to a subset of chromophores within the R_1 line that are separated by the ground state ZFS. The thus excited chromophore will, in turn, emit at -D and -2D from the laser line or transfer its energy resonantly to a subsequent chromophore again at -D lower in energy. Repetitive resonant energy transfer thus results in the observed multi-line pattern. The fact that the line resonant with the laser line carries only about 15% of the total luminescence intensity indicates that the energy transfer rate constant is 5 to 10 times larger than the radiative decay rate constant of $k_r = 700\ s^{-1}$ ($\tau_r = 1.3$ ms) [13].

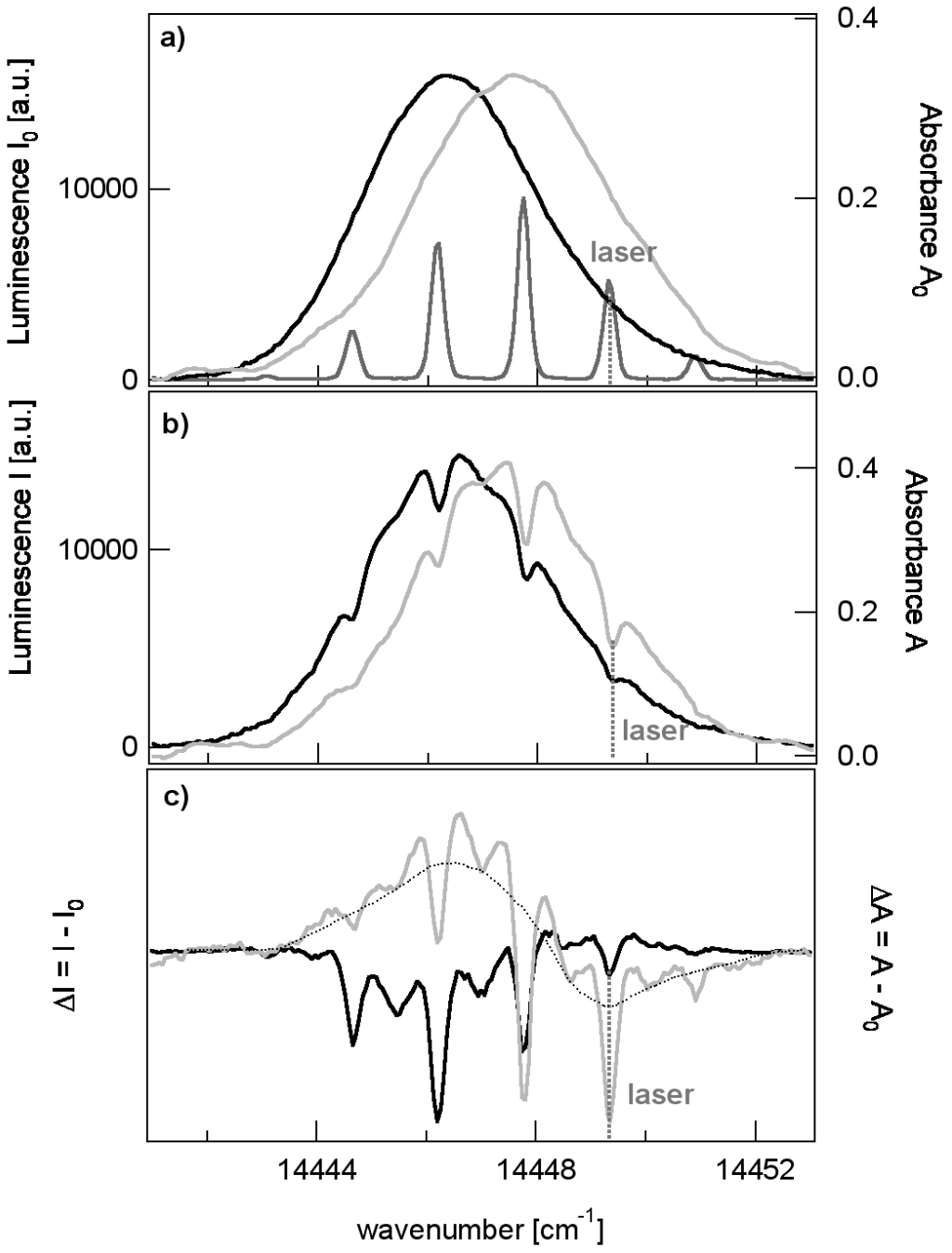

Figure 5.3. a) Absorption (—), non-selectively excited luminescence before hole burning (—) and FLN (—) spectrum of the R_1 transition at of Cr^{3+} in $NaMg[Al_{0.8}Cr_{0.2}(ox)_3]\cdot 9(H_2O/D_2O)$ at 1.4 K. The FLN spectrum is obtained with selective excitation at 14449.3 cm^{-1}, that is within the R_1 absorption. b) Non-selectively excited luminescence (—) and absorption (—) spectrum after hole burning at 14449.3 cm^{-1}. c) Difference luminescence (—) and absorption (—) spectra before and after hole burning at 14449.3 cm^{-1}.

Figure 5.3b shows the non-selectively excited luminescence and absorption spectrum of the R_1 line after irradiation during 40 min at 14449.3 cm^{-1} and 5 mW/mm^2 of the more concentrated sample. It is evident that the irradiation has burnt persistent holes, not only at the laser energy and the satellites at ±D from the resonant line, but for all peaks of the multi-line pattern of the corresponding FLN spectrum.

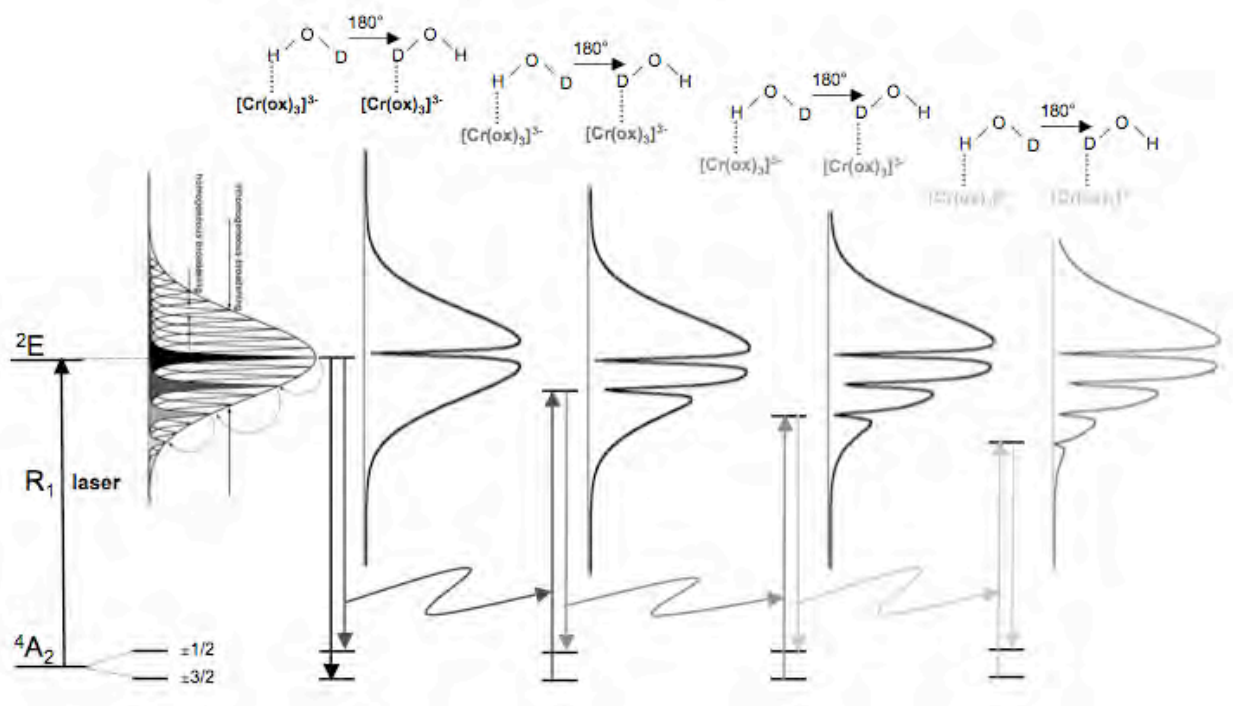

Figure 5.4. Scheme for the persistent hole burning induced by non-radiative resonant energy transfer within the R_1 line of Cr^{3+} in $NaMg[Al_{0.8}Cr_{0.2}(ox)_3]\cdot 9(H_2O/D_2O)$.

In order to enhance the holes visually, Figure 5.3c shows the difference luminescence spectrum $\Delta I = I - I_0$ of the luminescence before (I_0) and after (I) irradiation at 14449.3 cm^{-1} as well as the corresponding difference absorption spectrum $\Delta A = A - A_0$. The intensity distribution of the actual holes closely follows the intensity distribution of the peaks in the FLN spectrum indicating that they are indeed burnt by the resonant energy transfer and not by emission and reabsorption. However, the guide for the eye on the difference absorbance spectrum in Figure 5.3c shows that there are two different types of photoproduct from the hole burning. On both sides of each hole rise well-known selective photoproducts that are directly related to the holes burnt by resonant energy transfer. However, there are non-selective, randomly distributed photo products that manifest as a broad band growing

at lower energies comparing to the excitation energy. This other type of photoproduct can be related to the holes burnt by phonon assisted energy transfer.

5.4 Conclusions

As shown by Riesen et al. in $NaMg[Al_{1-x}Cr_x(ox)_3]\cdot 9(H_2O/D_2O)$ efficient persistent holes burning is due to the deuteration effect, the photoinduced HOD → DOH flip of hydrogen bonded water molecules being responsible for the shift in absorption energy of the selectively excited chromophores. With 20% concentration of Cr^{3+} in $NaMg[Al(ox)_3]\cdot 9(H_2O/D_2O)$, the resonant energy migration within the R_1 line of Cr^{3+} is efficient and the FLN spectrum manifest as a multi line pattern with 6 members. In this letter we showed that it is possible to combine both phenomena and burn not only persistent resonant and side holes, but also energy transfer induced holes. We also showed that there are two types of photoproducts resulting from the energy transfer induced holes. The first are the photoproducts that selectively rise on both sides of the hole and are directly related to the resonant energy transfer. The other type of photoproducts are the non-selective ones that rise as a broad band at lower energies comparing to the excitation and those are related to the holes burnt by phonon assisted energy transfer.

References

[1] H. Riesen, Coord. Chem. Rev. 250 (2006) 1737.

[2] R. Jankowiak, J.M. Hayes, G.J. Small, Chem. Rev. 93 (1993) 1471.

[3] K. Holliday, N.B. Manson, J. Phys. Condens. Matter 1 (1989) 1339.

[4] R.J. Reeves, R.M. Macfarlane, J. Opt. Soc. Am. B 9 (1992) 763.

[5] M.L. Lewis, H. Riesen, Phys. Chem. Comm 26 (2001) 1.

[6] R.A. Bernheim, E.F. Reichenbecher, J. Chem. Phys. 51 (1969) 996.

[7] Y. Kawasaki, L.S. Forster, J. Chem. Phys. 50 (1969) 1010.

[8] T. Schönherr, J. Spanier, H.H. Schmidtke, J. Phys. Chem. 93 (1989) 5969.

[9] M.L. Lewis, H. Riesen, J. Phys. Chem. A 106 (2002) 8039.

[10] H. Riesen, J.L. Hughes, Chem. Phys. Lett. 372 (2003) 563.

[11] H. Riesen, A.D. Rae, Dalton Trans. (2008) 4717.

[12] M.E. von Arx, V.S. Langford, U. Oetliker, A. Hauser, J. Phys. Chem. A 106 (2002) 7099.

[13] A. Hauser, M.E. von Arx, V.S. Langford, U. Oetliker, S. Kairouani, A. Pillonnet, Top. Curr. Chem. 241 (2004) 65.

[14] M. Milos, S. Kairouani, S. Rabaste, A. Hauser, Coord. Chem. Rev. 252 (2008) 2540.

[15] T.S. Piper, R.L. Carlin, J. Chem. Phys. 35 (1961) 1809.

[16] S. Lahiry, R. Kakkar, Chem. Phys. Lett. 88 (1982) 499.

[17] J.L. Hughes, H. Riesen, J. Phys. Chem. A 107 (2003) 35.

6. The effect of external pressure on the excitation energy transfer from $[Cr(ox)_3]^{3-}$ to $[Cr(bpy)_3]^{3+}$ in $[Rh_{1-x}Cr_x(bpy)_3][NaM_{1-y}Cr_y(ox)_3]ClO_4$

ChemPhysChem, accepted for publication, ***2010****.*

Mia Milos, Prodipta Pal, Andreas Hauser*

Contents

Abstract

Resonant excitation energy transfer from $[Cr(ox)_3]^{3-}$ to $[Cr(bpy)_3]^{3+}$ in the doped 3D oxalate networks $[Rh_{1-x}Cr_x(bpy)_3][NaM^{III}_{1-y}Cr_y(ox)_3]ClO_4$ (ox = $C_2O_4^-$, bpy = 2,2'-bipyridine, M = Al, Rh) is due to two types of interaction, namely super exchange coupling and electric dipole-dipole interaction. The energy transfer probability for both mechanisms is proportional to the spectral overlap of the $^2E \rightarrow {}^4A_2$ emission of the $[Cr(ox)_3]^{3-}$ donor and the $^4A_2 \rightarrow {}^2T_1$ absorption of the $[Cr(bpy)_3]^{3+}$ acceptor. The spin-flip transitions of (pseudo-)octahedral Cr^{3+} are known to shift to lower energy with increasing pressure. Because the shift rates of the two transitions in question differ, the spectral overlap between the donor emission and the acceptor absorption is a function of applied pressure. For $[Rh_{1-x}Cr_x(bpy)_3][NaM_{1-y}Cr_y(ox)_3]ClO_4$ the spectral overlap is thus substantially reduced on increasing pressure from 0 to 2.5 GPa. As a result, the energy transfer probability decreases with increasing pressure as evidenced by a decrease in the relative emission intensity from the $[Cr(bpy)_3]^{3+}$ acceptor.

6.1 Introduction

Excitation energy transfer between a donor and an acceptor is an important photophysical process. During the past decades, it has been applied in several fields. In biochemistry, the so-called FRET, is used for analysing conformational substates of biological macromolecules and for relating their structure to the function [1,2]. Moreover, FRET is used to follow molecular dynamics in live cells. Excitation energy transfer has been studied in conjugated organic materials in order to improve optoelectronic devices [3]. Recently, research has become focused on solar cells, where excitation energy transfer plays a very important role for light harvesting [4]. In all cases, investigations down to the single molecule level are needed in order to arrive at a correct description of energy transfer mechanisms in often heterogeneous and disordered environments. External pressure is a versatile tool to tune the relative energies of the different excited states of coordination compounds of transition metal ion [5-7]. Thus Grindberg and Suchocki [8] have recently reviewed the effect of pressure on the electronic structure of $3d^3$ transition metal ions, notably of Cr^{3+} and Mn^{4+} in oxide lattices, and Shen et al. [9] studied the effect of external pressure on the excitation energy transfer from Cr^{3+} to Tm^{3+} co-doped into $Y_3Al_5O_{12}$. Three principal contributions to the overall energy transfer from different electronic states of Cr^{3+} were thus identified, namely from the electronic origins of the ^2E state at low temperature, from thermally activated transfer from the anti-Stokes sidebands of the ^2E state, and from the thermally activated $^4T_2$ state at higher temperatures.

In the Cr^{3+} co-doped three-dimensional oxalate networks of composition $[Rh_{1-x}Cr_x(bpy)_3][NaAl_{1-y}Cr_y(ox)_3]ClO_4$ (ox = $C_2O_4^-$, bpy = 2,2'-bipyridine), resonant excitation energy transfer from $[Cr(ox)_3]^{3-}$ to the encapsulated $[Cr(bpy)_3]^{3+}$ was observed in steady state and in time-resolved luminescence experiments, involving the $^2E \rightarrow {}^4A_2$ emission of $[Cr(ox)_3]^{3-}$ and the $^4A_2 \rightarrow {}^2T_1$ absorption of $[Cr(bpy)_3]^{3+}$ [10]. At a donor doping level of y = 1% and an acceptor doping level of x = 2.5%, its quantum efficiency η_{ET} was found to be 25%. Two mechanisms for this energy transfer were identified: a) A rapid process due to super-exchange coupling between $[Cr(ox)_3]^{3-}$ and $[Cr(bpy)_3]^{3+}$ within the first neighbour shell, with a corresponding transfer rate constant larger than 10^6 s^{-1}, contributing 70% to the total energy transfer. b) A slower

process due to electric dipole–dipole interaction between $[Cr(ox)_3]^{3-}$ and $[Cr(bpy)_3]^{3+}$ at longer distances for those donors which have no acceptors in the nearest neighbour shell contributing the remaining 30% to the total energy transfer. The latter process follows the Förster energy transfer relation with a critical radius of approximately 11 Å. In the comparatively lightly doped systems, that is $x \leq 2.5\%$, the corresponding energy transfer rate constant was found to vary between 10^1 and 10^2 s^{-1} depending on the occupancy of the coordination shell and thus the concentration of $[Cr(bpy)_3]^{3+}$ around a given $[Cr(ox)_3]^{3-}$ [10].

The probability for resonant excitation energy transfer is proportional to the spectral overlap integral between the normalised emission of the donor and the absorption of the acceptor independent on the type of interaction at the origin of the process [11]. The exchange interaction depends upon direct overlap of the electronic wave functions of the donor and the acceptor and thus falls off exponentially with increasing value of R_{DA} [12]. On the other hand, the dipole–dipole interaction is proportional to the oscillator strengths of the donor emission and the acceptor absorption and falls off as the inverse power of three of the donor-acceptor distance R_{DA} [13]. For the donor-acceptor pair under consideration, the spectral overlap is provided by the sharp electronic origins of the $^2E \rightarrow {}^4A_2$ spin-flip emission of $[Cr(ox)_3]^{3-}$ and the $^4A_2 \rightarrow {}^2T_1$ spin-flip absorption of $[Cr(bpy)_3]^{3+}$.

Under external pressure, electronic absorption bands shift in energy. With respect to dd transitions, external pressure has two effects: the reduction in metal-ligand bond length results in an increase in ligand-field strength and a reduction in electron-electron repulsion due to an increasing electron delocalisation onto the ligands (nephelauxetic effect [14]). For spin-allowed transitions involving the promotion of an electron from the t_{2g} to the e_g shell, the increase in ligand-field strength is dominant and spin-allowed dd transitions inevitably shift to higher energy with increasing pressure. For spin-flip transitions, that is, transitions within the same electronic configuration, the nephelauxetic effect dominates and thus these generally shift to lower energies [7].

In the present paper we report the shift rates for the spin-flip transitions of $[Cr(ox)_3]^{3-}$ and $[Cr(bpy)_3]^{3+}$ in high pressure experiments. As the two shift rates differ considerably, the spectral overlap between the respective donor and acceptor

transitions becomes a function of external pressure, and therefore external pressure directly influences the quantum efficiency of the resonant energy transfer.

6.2 Results and Discussion

6.2.1 Absorption and Luminescence spectroscopy

Mixed crystals of $[Rh_{1-x}Cr_x(bpy)_3][NaM^{III}_{1-y}Cr_y(ox)_3]ClO_4$, M = Rh, Al, were synthesised as described in the experimental section. The effective concentrations of $[Cr(bpy)_3]^{3+}$ and $[Cr(ox)_3]^{3-}$ were estimated from the concentrations of the solutions from which they were grown according to the work of von Arx et al. [10]. Thus, for the present study, the concentrations of $[Cr(bpy)_3]^{3+}$ and $[Cr(ox)_3]^{3-}$ are approximately x = 3.5 mole% and y = 1 mole%, respectively. Comparatively low doping levels are used in order to avoid energy migration within the ^2E states of both $[Cr(bpy)_3]^{3+}$ and $[Cr(ox)_3]^{3-}$ [10,15]. The corresponding neat compounds $[Cr(bpy)_3][NaAl(ox)_3]ClO_4$, $[Cr(bpy)_3][NaRh(ox)_3]ClO_4$ and $[Rh(bpy)_3][NaCr(ox)_3]ClO_4$ serve as reference compounds. Figure 6.1 shows the single crystal absorption spectra of the former two together with the absorption and the emission spectrum of the latter following excitation at 532 nm at 10 K in the region of the low-lying $^4A_2 \rightarrow {}^2E$ and $^4A_2 \rightarrow {}^2T_1$ transitions. The absorption of $[Cr(bpy)_3]^{3+}$ includes the zero-field split R_1 and R_2 lines of the $^4A_2 \rightarrow {}^2E$ transition and the structured $^4A_2 \rightarrow {}^2T_1$ transition. Both are spin-flip transitions with most of the intensity in the electronic origins. For $[Cr(bpy)_3][NaAl(ox)_3]ClO_4$, the R_1 and R_2 lines are respectively at 13685.3 cm^{-1} and 13701.5 cm^{-1} and the $^4A_2 \rightarrow {}^2T_1$ transition is centred at 14349 cm^{-1} with a total width of about 85 cm^{-1} (all values in air). For $[Cr(bpy)_3][NaRh(ox)_3]ClO_4$, the R_1 and R_2 lines are respectively at 13714.3 cm^{-1} and 13729.9 cm^{-1} and the $^4A_2 \rightarrow {}^2T_1$ transition is centred at 14376.0 cm^{-1}. The difference in energy for corresponding transitions of around 29 cm^{-1} between the two lattices is not surprising since the chemical pressure has an important influence on the nephelauxetic effect [16].

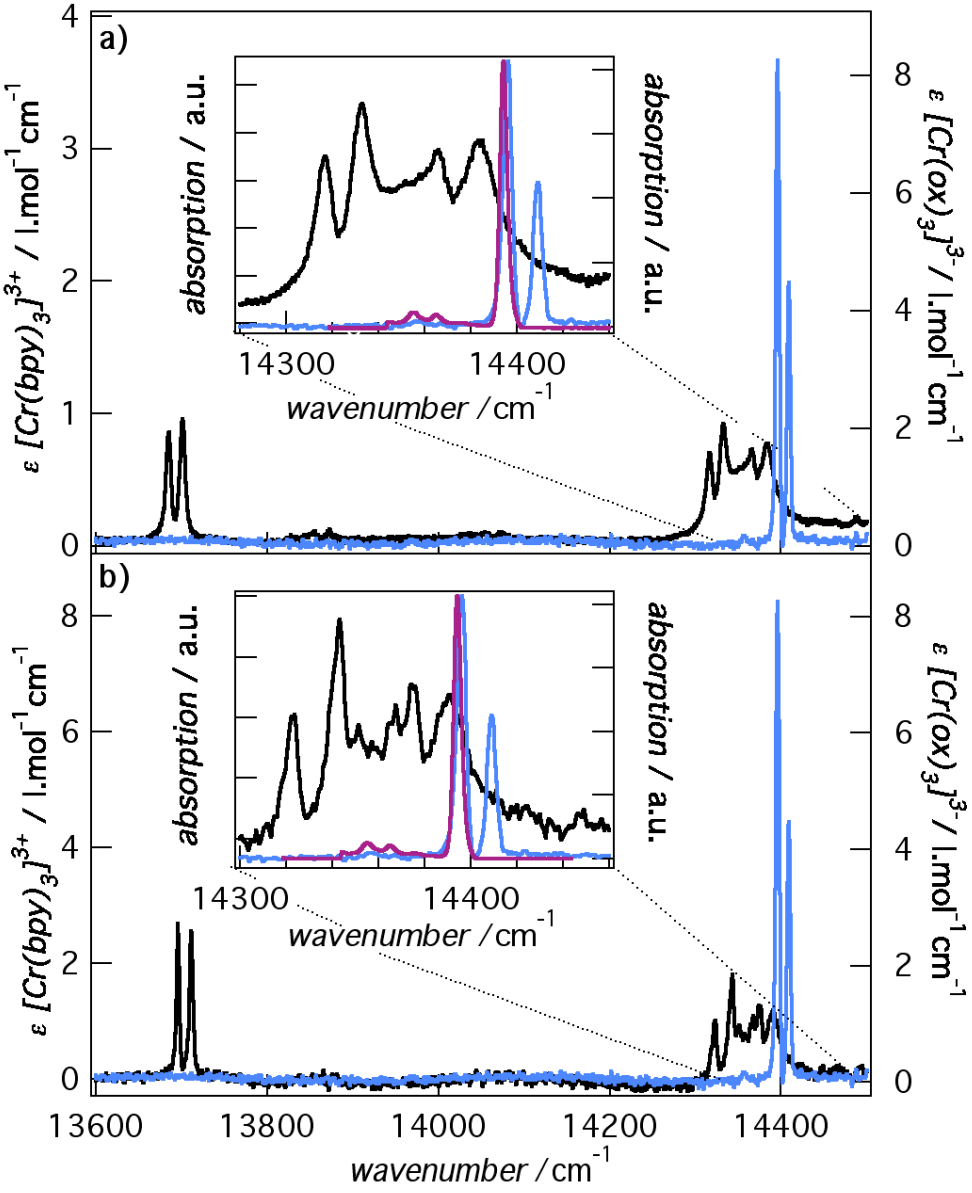

Figure 6.1. Single crystal absorption spectra of a) $[Cr(bpy)_3][NaAl(ox)_3]ClO_4$ and b) $[Cr(bpy)_3][NaRh(ox)_3]ClO_4$ at 10 K (black lines. The absorptions spectrum of $[Rh(bpy)_3][NaCr(ox)_3]ClO_4$ is included in both panels (blue lines). The insets show the region of the $^4A_2 \rightarrow {}^2T_1$ transition of $[Cr(bpy)_3][NaM(ox)_3]ClO_4$, M = Al, Rh, and the $^4A_2 \rightarrow {}^2E$ transition of $[Rh(bpy)_3][NaCr(ox)_3]$ on enlarged scales and include the $^2E \rightarrow {}^4A_2$ luminescence of$[Rh(bpy)_3][NaCr(ox)_3]$ at 1.4 K (red line).

The ionic radius of Al^{3+} is considerably smaller than the one of Rh^{3+} [17]. Consequently, the cavity provided by the oxalate network in which the tris-bipyridine complex is encapsulated, is smaller in the former. A smaller cavity increases the nephelauxetic effect as a result of the shorter Cr-N bond length and an increasing π-

interaction between the oxalate and the bipyridine ligands [16]. As a result, the $[Cr(bpy)_3]^{3+}$ absorptions in the cavities of $[Cr(bpy)_3][NaAl(ox)_3]ClO_4$ are shifted to lower energies compared to the $[Cr(bpy)_3][NaRh(ox)_3]ClO_4$ cavities. The absorption and emission spectrum of neat $[Rh(bpy)_3][NaCr(ox)_3]ClO_4$ consist of the spin-forbidden $^4A_2 \rightarrow {}^2E$ transition, whose R_1 and R_2 lines are centred at 14396.3 cm^{-1} and 14409.0 cm^{-1}. In the emission spectrum recorded at 1.4 K included in the insets of Figure 6.1, the R_1 line dominates.

6.2.2 High-pressure experiments

Figure 6.2 shows luminescence spectra of $[Rh_{1-x}Cr_x(bpy)_3][NaM_{1-y}Cr_y(ox)_3]ClO_4$ (M^{III} = Al^{3+}, Rh^{3+}, x = 0.035, y = 0.01) at different pressures and at 10 K with excitation at 532 nm. The displayed spectra are normalised to the integrated intensity of the R lines of $[Cr(ox)_3]^{3-}$. Irradiation at 532 nm exclusively creates $[Cr(ox)_3]^{3-}$ in its ^2E state via selective excitation into the $^4A_2 \rightarrow {}^4T_2$ band followed by fast intersystem crossing [18]. Despite this, the luminescence spectrum of the co-doped system consists of the $^2E \rightarrow {}^4A_2$ emissions of both $[Cr(ox)_3]^{3-}$ and $[Cr(bpy)_3]^{3+}$ as a result of the resonant energy transfer from the ^2E state of $[Cr(ox)_3]^{3-}$ to the $^2T_1$ state of $[Cr(bpy)_3]^{3+}$ followed by rapid internal conversion. The total quantum efficiency of the energy transfer can be calculated via the relative intensity of the donor emission according to

$$\eta_{ET}^{tot} = \frac{I_A}{I_A + I_D} \qquad (1)$$

In Equation (1), I_A and I_D are the integrated acceptor and donor emission intensities, and intrinsic emission quantum efficiencies of both donor and acceptor of unity are assumed at 10 K [13]. At zero external pressure, the quantum efficiencies are 28% for M = Al and 41% for M = Rh. These values are in line with acceptor concentrations between 3 and 4 mole% [10]. If anything, the acceptor concentration in the Rh sample is slightly larger than in the Al sample.

With increasing pressure both the $[Cr(ox)_3]^{3-}$ and the $[Cr(bpy)_3]^{3+}$ emissions shift to lower energies. The pressure shift of the $[Cr(ox)_3]^{3-}$ R_1 emission shown in Figure 6.3 has been determined previously and is -26 cm^{-1}/GPa [16]. In the present study, the shift of this emission, precisely determined by fitting a Gaussian line shape function,

serves as reference for pressure determination. Figure 6.3 also shows the shift of the R_1 emission of $[Cr(bpy)_3]^{3+}$ as a function of pressure as determined from the spectra of Figure 6.2. With -61 and -79 cm^{-1}/GPa for M = Rh and Al, respectively, the shift rate is 2.5 to 3 times larger than for $[Cr(ox)_3]^{3-}$. This is due to the stronger π interaction of the metal t_{2g}-orbitals with the ligand π orbitals in the case of bipyridine as compared to the oxalate [19,20], making the nephelauxetic effect and its increase with increasing pressure stronger for the tris-bipyridine complex.

The emission spectra in Figure 6.2 show that with increasing pressure the R_1 lines of both species broaden to some extent. This is due to the fact that the compounds under consideration are relatively soft compared to say doped oxides such as ruby ($Al_2O_3:Cr^{3+}$) [21,22] and thus suffer more from inhomogeneous broadening than these. In fact from this pressure induced broadening and the pressure shift, a pressure distribution of 5% around the central value can be estimated. Indeed this broadening is about an substantially larger than for ruby under the same conditions, but then the shift rate of 7.4 $cm^{-1}GPa^{-1}$ for ruby is also substantially smaller.

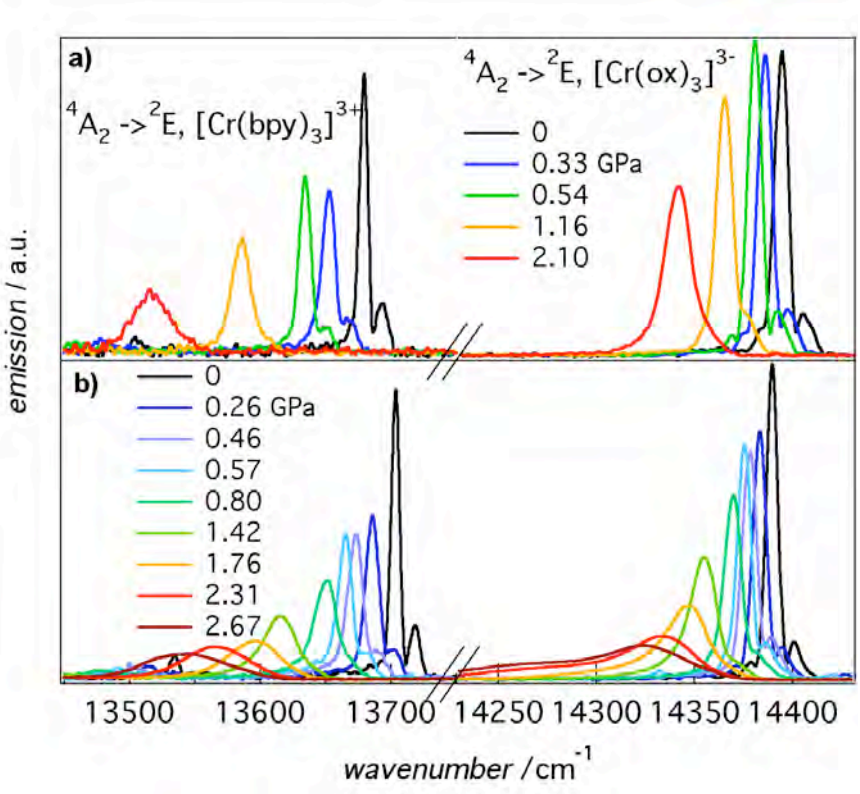

Figure 6.2. Luminescence spectra of $[Rh_{1-x}Cr_x(bpy)_3][NaM_{1-y}Cr_y(ox)_3]ClO_4$, a) $M^{III} = Al^{3+}$, b) $M^{III} = Rh^{3+}$, x = 0.035, y = 0.01 at different pressures, excitation wave length 532 nm.

In addition to the shifts and the broadening, the relative emission intensities of the two bands originating from the two chromophores vary as a function of pressure. This is demonstrated by Figure 6.4a showing the relative emission intensity of the acceptor emission for both systems studied as a function of applied pressure corresponding to directly to the energy transfer quantum efficiency. For both there is a net decrease in the relative intensity from the acceptor, thus it can be concluded that the quantum efficiency of the excitation energy transfer from $[Cr(ox)_3]^{3-}$ to the encapsulated $[Cr(bpy)_3]^{3+}$ decreases with increasing pressure.

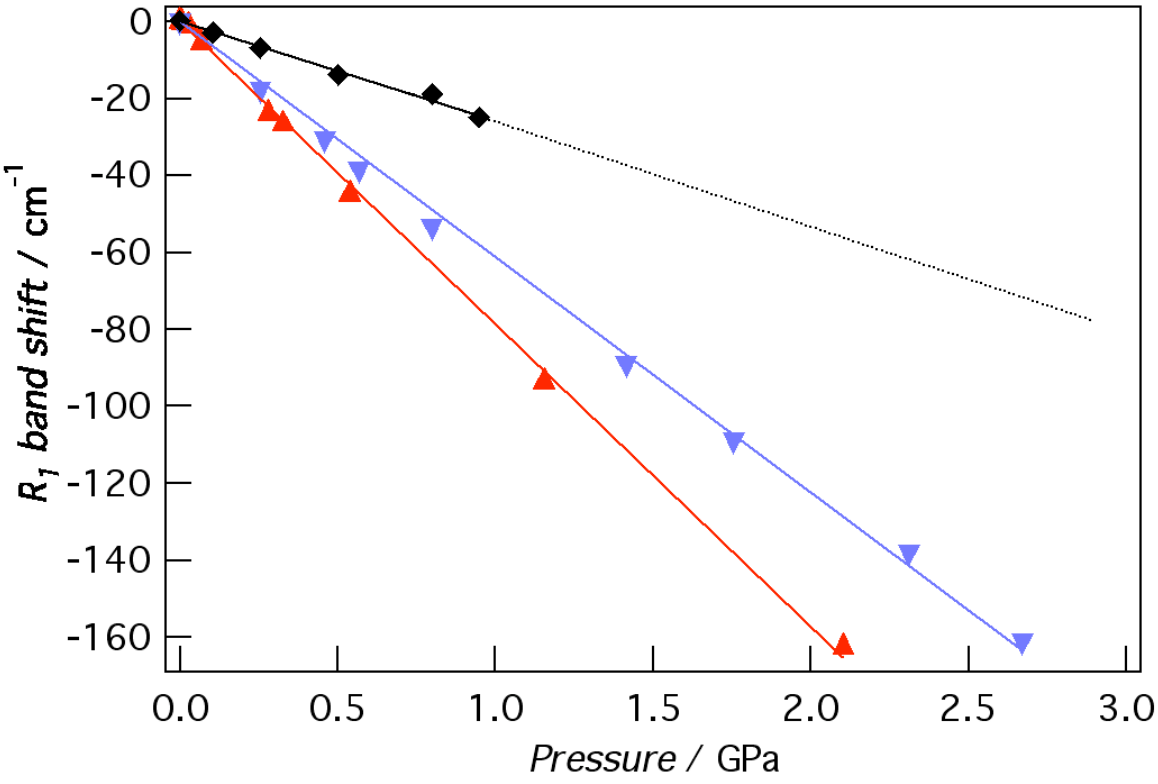

Figure 6.3. Shift of the luminescence of the R_1 lines of $[Cr(bpy)_3]^{3+}$ in $[Rh_{1-x}Cr_x(bpy)_3][NaM_{1-y}Cr_y(ox)_3]ClO_4$, M = Al (▲), Rh (▼), x = 0.035, y = 0.01 at 10 K, and of $[Cr(ox)_3]^{3-}$ in $[Ru(bpy)_3][NaCr(ox)_3]$ (◆) from ref [16].

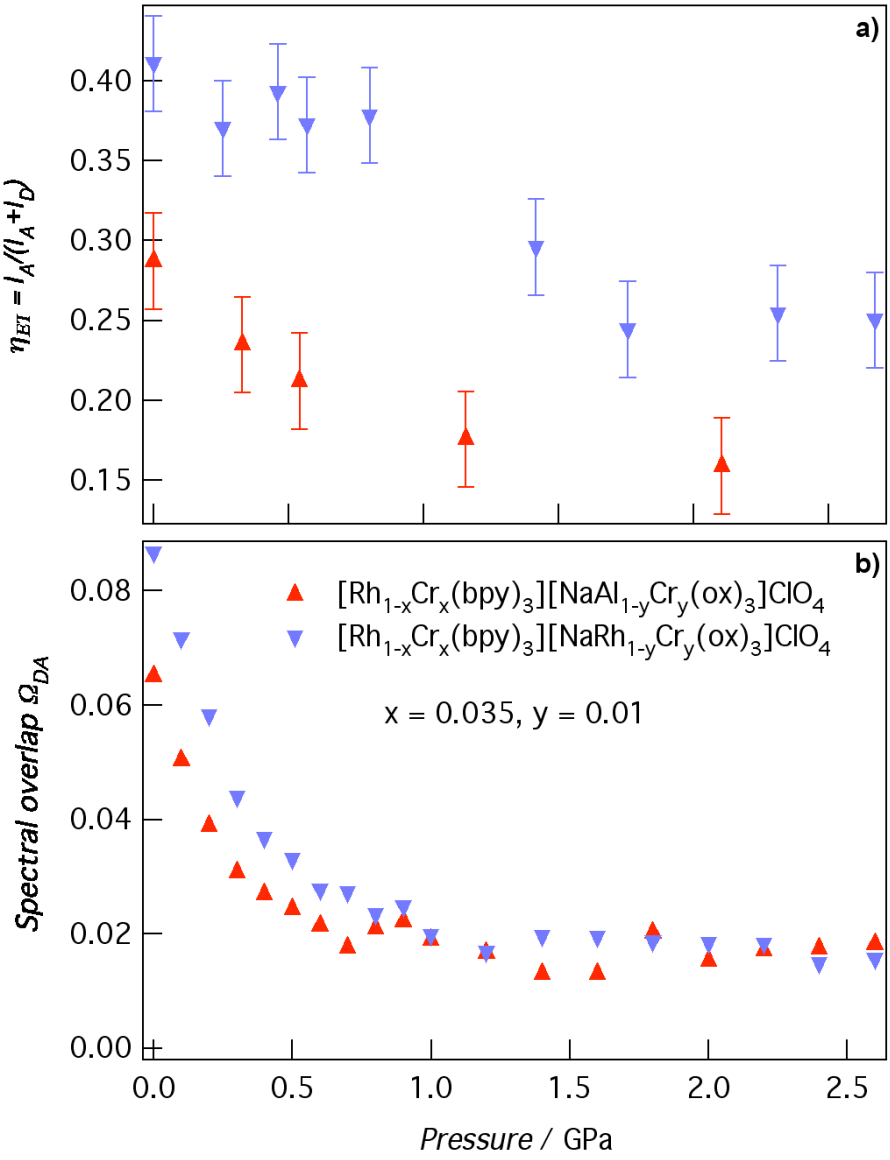

Figure 6.4. a) Energy transfer quantum efficiency and b) spectral overlap between the $^2E \rightarrow {}^4A_2$ emission of $[Cr(ox)_3]^{3-}$ and the $^4A_2 \rightarrow {}^2T_1$ absorption of spectra of $[Cr(bpy)_3]^{3+}$ in $[Rh_{1-x}Cr_x(bpy)_3][NaM_{1-y}Cr_y(ox)_3]ClO_4$, x = 0.035, y = 0.01 as a function of pressure, M = Al, Rh.

6.2.3 Resonant Energy Transfer under pressure

As mentioned above, excitation energy transfer in the co-doped oxalate networks from $[Cr(ox)_3]^{3-}$ to the encapsulated $[Cr(bpy)_3]^{3+}$ is a resonant process and has two contributions: a) a fast one that is due to super-exchange coupling (Dexter mechanism [12]) depending on the direct overlap of the electronic wave functions of the donor and the acceptor for those donors which happen to have an acceptor in

their nearest neighbour shell, and b) a slower one that is due to the electric dipole-dipole interaction (Förster energy transfer [23]) to acceptors at longer distances for the others.[10] The probability for a resonant energy transfer process from the initially excited donor D* to the acceptor A is given by Equation (2) for both types of interaction.[24]

$$w_{DA} = \frac{2\pi}{\hbar}\left|\langle DA^*|H'|D^*A\rangle\right|^2 \Omega_{DA} \qquad (2)$$

The energy transfer probability based on super-exchange coupling and dipole-dipole interaction are both proportional to the spectral overlap integral Ω_{DA} between the donor emission and the acceptor absorption, that is, the integral of the product of the normalised line shape functions of the donor emission, g_D, and the acceptor absorption, g_A, given by Equation (3).

$$\Omega_{DA} = \int g_A(\tilde{\nu}) g_D(\tilde{\nu}) d\tilde{\nu} \qquad (3)$$

Whereas the emission spectra for both donor and acceptor in the co-doped system are readily available, it is not possible to measure the absorption spectra of the doped samples because of the low concentrations. In order to obtain the overlap integral according to Equation (3), hypothetical absorption spectra of the acceptor in $[Rh_{1-x}Cr_x(bpy)_3][NaM^{III}(ox)_3]ClO_4$ with x = 0.035, M = Al, Rh are generated by shifting the absorption spectrum of the respective neat compounds $[Cr(bpy)_3][NaM^{III}(ox)_3]ClO_4$ so as to make their R_1 absorptions of $[Cr(bpy)_3]^{3+}$ coincide with the corresponding R_1 emissions of the doped compounds. This procedure implicitly assumes that the $^2E \rightarrow {}^2T_1$ energy difference is roughly the same for all systems studied, an assumption, which is to some extent substantiated by the spectra of the neat compounds shown in Figure 6.1. We estimate a maximum error in the resulting position of the $^2T_1$ energy of less than 5 cm^{-1}. The resulting extrapolated spectra for the doped systems in the region of the $^4A_2 \rightarrow {}^2T_1$ absorption of $[Cr(bpy)_3]^{3+}$ together with the experimental $^2E \rightarrow {}^4A_2$ emission of $[Cr(ox)_3]^{3-}$ at 10 K are shown in Figure 6.5, both for ambient pressure and at higher pressure.

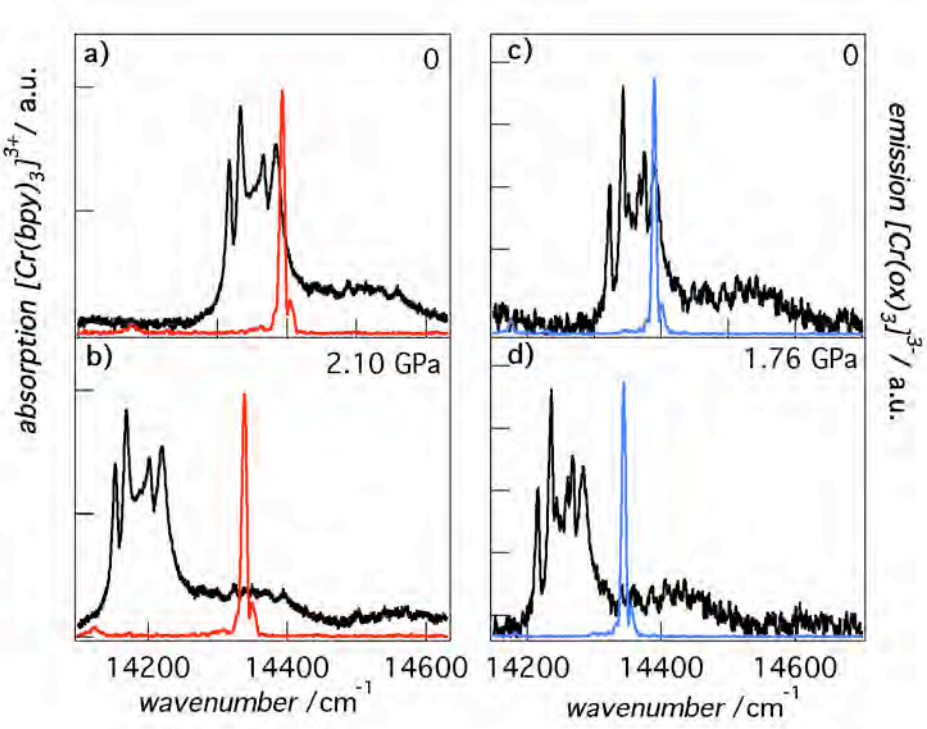

Figure 6.5. Extrapolated $^4A_2 \rightarrow {}^2T_1$ absorption of $[Cr(bpy)_3]^{3+}$ and experimental $^2E \rightarrow {}^4A_2$ emission of $[Cr(ox)_3]^{3-}$ at 10 K in $[Rh_{1-x}Cr_x(bpy)_3][NaAl_{1-y}Cr_y(ox)_3]ClO_4$ at two different pressures, a) 0 GPa and b) 2.10 GPa and in $[Rh_{1-x}Cr_x(bpy)_3][NaRh_{1-y}Cr_y(ox)_3]ClO_4$ at c) 0 GPa and d) 1.76 GPa. With increasing pressure and since the shifts rates of the two transitions are not the same, the spectral overlap integral Ω_{DA} changes.

The latter assumes that the pressure shift of the $^4A_2 \rightarrow {}^2T_1$ transition of $[Cr(bpy)_3]^{3+}$ is close to the one for the corresponding R lines. From these spectra, together with the experimentally determined shift rate of the respective R lines, the spectral overlap integral as a function of pressure shown in Figure 6.4b can be computed. Because of the quite different pressure shift rates of the two chromophores, the overlap integral shows quite a strong dependence on pressure. For M = Al, it decreases monotonously to around 30% of its initial value at higher pressure. For M = Rh, the value of the overlap integral at ambient pressure is a little larger and following the same general behaviour and levelling off at the same value as for M = Al, which is at around 20% of the maximum value. The error introduced by the inhomogeneous broadening with increasing pressure is negligible.

Qualitatively, the decrease in the energy transfer quantum efficiency as a function of pressure (Figure 6.4a) follows the decrease in the spectral overlap integral. However this decrease is only from 28% to 16% for the Al compound and from 41% to 25% for

the Rh compound. At a first glance this is far from the factors of 3 and 5 in the reduction of the overlap integral. In order to understand this, it must be remembered that the energy transfer rate constant of the super-exchange coupling is $k_{ET}^{ex} > 10^6$ s^{-1}, while the energy transfer rate constant of the electric dipole–dipole interaction k_{ET}^{dd} is much slower and is of the order of magnitude of the intrinsic decay rate of the donor $k_{int}^{D} = 770$ s^{-1}. The reduction of the spectral overlap integral decreases both rate constants by the same factor, but as k_{ET}^{ex} is several orders of magnitude larger than k_{int}^{D}, a reduction by a factor of 3 to 5 has no influence on the super-exchange contribution to the quantum efficiency, as k_{ET}^{ex} is still much larger than k_{int}^{D}. For the dipole-dipole contribution describing the energy transfer for donors with no acceptors in the nearest neighbour shell, this is different. As k_{ET}^{dd} is on the order the intrinsic decay rate constant of the donor, its decrease with decreasing spectral overlap directly results in a decrease of the dipole–dipole contribution to the energy transfer.

For the Al system, the dipole–dipole interaction contributes 30% to the total quantum efficiency [10], or a maximum of 9% to the experimentally determined value of 28% for the present system. The observed reduction of 12% is slightly higher than but within experimental accuracy of the expected 9% for suppressing the dipole–dipole contribution.

For the Rh system, the experimentally determined total energy transfer efficiency is 41%. This is somewhat larger than for the Al system and is due to a combination of two possible sources: a) the acceptor doping level is somewhat larger than the nominal 3.5%, b) the dipole–dipole contribution at zero ambient pressure is larger than for the Al system because of the larger spectral overlap. The fact that at high pressure the energy transfer quantum efficiency levels off at 25% indicates that indeed the acceptor concentration is somewhat higher. However, the reduction of the quantum efficiency by 16% instead of the expected 12% when taking the Al system as reference also indicates that the initial dipole–dipole contribution is higher.

6.3 Conclusions

The effect of pressure on energy transfer between $[Cr(ox)_3]^{3-}$ and $[Cr(bpy)_3]^{3+}$ in $[Rh_{1-x}Cr_x(bpy)_3][NaM^{III}_{1-y}Cr_y(ox)_3]ClO_4$, M = Rh, Al have been studied. The shift rates are -26 cm^{-1}/GPa for the ^2E state of $[Cr(ox)_3]^{3-}$ and -61 and -79 cm^{-1}/GPa for the $^2T_1$ state of $[Cr(bpy)_3]^{3+}$ with M^{III} = Rh and Al, respectively. Consequently, with increasing pressure, the spectral overlap integral to which the energy transfer probability is proportional, decreases. The energy transfer in these compounds has two contributions. The quantum efficiency of the fast contribution due to super-exchange interaction is not notably affected by the decrease of the corresponding energy transfer rate. In contrast, for the slow contribution based on electric dipole-dipole interaction, the quantum efficiency is strongly affected by the decrease of the spectral overlap and corresponding decrease of the energy transfer rate. The above results clearly demonstrate the power of pressure experiments in the elucidation of the mechanism of excitation energy transfer processes between sharp line emitters and absorbers. In the present case it clearly identifies the process in question as a resonant process, rather than a phonon-assisted one. The principle can be applied to any sharp line donor-acceptor pair with direct spectral overlap, offering for instance a way to tune upconversion efficiencies in transition metal ion [25] and co-doped lanthanide containing systems.

6.4 Experimental Section

The starting materials $K_3Rh(ox)_3•4.5H_2O$, $K_3Cr(ox)_3•3H_2O$, $K_3Al(ox)_3•xH2O$, $[Rh(bpy)_3](ClO_4)_3•3H_2O$, $[Cr(bpy)_3](ClO_4)_2HbpyClO_4$, and NaCl were either used as purchased or prepared according to standard procedures. The three dimensional oxalate networks with composition $[Rh_{1-x}Cr_x(bpy)_3][NaM^{III}_{1-y}Cr_y(ox)_3]ClO_4$ (x = 0.035, y = 0.01, M^{III} = Al^{3+}, Rh^{3+}) and the neat compounds $[Cr(bpy)_3][NaM^{III}(ox)_3]ClO_4$ and $[Rh(bpy)_3][NaCr(ox)_3]ClO_4$ were synthesised according to the general literature method of Decurtins et al. [26]. For this, stoichiometric mixtures of 10^{-2} M aqueous solutions of the starting materials except for NaCl, for which the concentration was $2x10^{-2}$ M, were prepared. Single crystals of the compounds in the form of perfect

tetrahedra of 0.5 mm edge were obtained by slow evaporation of the solutions stored at 5 °C in a refrigerator. For the doped system, the relative volumes of the solutions to be mixed were calculated such as to obtain the desired doping concentration of Cr^{3+} complexes following von Arx et al. in such a way that 7 mole% of $[Cr(bpy)_3]^{3+}$ and 1 mole% of $[Cr(ox)_3]^{3-}$ in solution result in x = 0.035 and y = 0.01 in the solid [10]. Electronic absorption spectra were obtained on single crystals using a Fourier-transform spectrometer equipped for measuring in the infrared and visible spectral range (Bruker IFS66/S). The absorption spectra were collected at a spectral resolution of 0.5 cm^{-1}. For absorption measurements crystals were mounted on copper apertures, placed in a closed cycle cryostat (Oxford Instruments CCC1204), and collected at 10 K in an atmosphere of He exchange gas. The thickness of the crystals was measured with an optical microscope and varies from 110 µm to 285 µm depending on the sample.

Luminescence measurements were performed at 10 K using the same closed cycle cryostat and the FT spectrometer as for the absorption measurements. High pressures were achieved using a diamond anvil cell (MiniDAC of D'Anvils Ltd.). The sample chamber consisted of a hole with a diameter of 200-250 µm drilled into a pre-indented metal gasket. A small single crystal of the co-doped $[Rh_{1-x}Cr_x(bpy)_3][NaM^{III}_{1-y}Cr_y(ox)_3]ClO_4$ was placed in the sample chamber. The pressure was calibrated with the R_1 ($^4A_2 \rightarrow {}^2E$) transition of $[Cr(ox)]^{3-}$. Silicon oil, polydimethylsiloxane trimethylsiloxyl terminated, was used as the pressure-transmitting medium. The crystals were excited at 532 nm (<10 mW) using a DPSS LASER (ILEE VA-I-N-532) in order to selectively excite the $[Cr(ox)_3]^{3-}$. The shift rate of the R_1 ($^4A_2 \rightarrow {}^2E$) transition of $[Cr(ox)]^{3-}$ was determined previously at -26 cm^{-1}/GPa. The exact position of the R_1 luminescence band of $[Cr(ox)_3]^{3-}$ was determined with a Gaussian fit, and using the above shift rate, the pressure within the DAC was established for each experiment.

Acknowledgements

The authors thank the Swiss National Science Foundation (grant number 200020-125175) for funding, and N. Amstutz for her help in the preparation of the samples.

References

[1] E.A. Bykova, J. Zheng: Spectra FRET: A Fluorescence Resonance Energy Transfer Method in Live Cells, Springer, New York, 2007.

[2] B. Ananthanarayanan, Q. Ni, J. Zhang, Biophysical Tools for Biologists, Vol 2: In Vivo Techniques 89 (2008) 37.

[3] F. Laquai, Y.S. Park, J.J. Kim, T. Basche, Macromol. Rap. Comm. 30 (2009) 1203.

[4] M. Grätzel, Nature 414 (2001) 338.

[5] J.K. Grey, I.S. Butler, Coord. Chem. Rev. 219 (2001) 713.

[6] H.G. Drickamer, C.W. Frank: Electronic Transitions and the High Pressure Chemistry and Physics of Solids, Chapman and Hall, New York, 1973.

[7] K.L. Bray, Top. Curr. Chem. 213 (2001) 1.

[8] M. Grinberg, A. Suchocki, J. Lumin. 125 (2007) 97.

[9] Y.R. Shen, T. Riedener, K.L. Bray, Phys. Rev. B 61 (2000) 11460.

[10] V.S. Langford, M.E. von Arx, A. Hauser, J. Phys. Chem. A 103 (1999) 7161.

[11] E.I. Solomon, A.B.P. Lever: Inorganic electronic structure and spectroscopy, John Wiley & Sons, New York, 1999.

[12] D.L. Dexter, J. Chem. Phys. 21 (1953) 836.

[13] A. Hauser, M.E. von Arx, V.S. Langford, U. Oetliker, S. Kairouani, A. Pillonnet, Top. Curr. Chem. 241 (2004) 65.

[14] C.K. Jørgensen, Discuss. Farad. Soc (1958) 110.

[15] M. Milos, S. Kairouani, S. Rabaste, A. Hauser, Coord. Chem. Rev. 252 (2008) 2540.

[16] M. Milos, A. Hauser, Inorg. Chem. 49 (2010) 3402.

[17] J.E. Huheey, A.E. Keiter, R.L. Keiter: Chimie inorganique, De Boeck Université, 1996.

[18] M.E. von Arx, V.S. Langford, U. Oetliker, A. Hauser, J. Phys. Chem. A 106 (2002) 7099.

[19] M. Atanasov, T. Schönherr, Inorg. Chem. 29 (1990) 4545.

[20] M.A. Atanasov, T. Schönherr, H.H. Schmidtke, Theoretica Chimica Acta 71 (1987) 59.

[21] K. Nakano, Y. Akahama, Y. Ohishi, H. Kawamura, Japanese Journal of Applied Physics Part 1-Regular Papers Short Notes & Review Papers 39 (2000) 1249.

[22] K. Syassen, High Pressure Res 28 (2008) 75.

[23] T. Förster, Annalen Der Physik 2 (1948) 55.

[24] B. Henderson, G.F. Imbusch: Optical Spectroscopy of inorganic solids, Clarendon Press, Oxford, 1989.

[25] O.S. Wenger, G.M. Salley, H.U. Gudel, J. Phys. Chem. B 106 (2002) 10082.

[26] S. Decurtins, H.W. Schmalle, R. Pellaux, P. Schneuwly, A. Hauser, Inorg. Chem. 35 (1996) 1451.

7. A model for spectral diffusion induced by resonant energy migration applied to the $^4A_2 \rightarrow {}^2E$ transition of Cr^{3+} in $[Cr(ox)_3]^{3-}$ (ox = $C_2O_4^{2-}$)

*Published in Journal of Luminescence, 129, **2009**, 1901.*

Mia Milos, Andreas Hauser*

Content

Abstract

In the 3D oxalate networks $[NaCr(ox)_3][Rh(bpy)_3]ClO_4$ and $[NaCr(ox)_3][Ru(bpy)_3]$ (ox = oxalate, bpy = 2,2'-bipyridine) three different types of energy migration within the $^4A_2 \rightarrow {}^2E$ transition can be identified. One is a resonant process between spectral members spaced by the ground-state zero-field splitting (ZFS). This leads to the sequential appearance of additional sharp lines spaced by the ground-state ZFS in the Fluorescence Line Narrowing spectrum across the inhomogeneous line. The second one is a quasi-resonant process between spectral neighbours and manifests itself by rapid spectral diffusion. The third one is the well-known phonon-assisted process setting in at higher temperature.

7.1 Introduction

Excitation energy transfer between a donor and an acceptor and energy migration among identical chromophores play an important role in many areas of physics, chemistry and biology [1-3]. The $^4A_2 \rightarrow {}^2E$ spin-flip transition of Cr^{3+} in an octahedral or nearly octahedral environment is instrumental for an in depth understanding of the parameters governing the latter [4, 5]. The three-dimensional oxalate networks $[NaCr(ox)_3][Ru(bpy)_3]$ and $[NaCr(ox)_3][Rh(bpy)_3]ClO_4$ [6], with their high chromophore concentrations and insignificant exchange interactions between chromophores, have several advantages for their study compared to ruby and other doped systems [5, 7, 8]. In fact, they allow a clear distinction between different mechanisms for energy migration as depicted in Figure 7.1 [9]. Fluorescence Line Narrowing spectroscopy (FLN) showed that at cryogenic temperatures, where phonon-assisted energy migration is negligible, two different types of resonant energy migration may take place. One is a resonant process between spectral members spaced by the ground-state zero-field splitting (ZFS). This leads to the sequential appearance of additional sharp lines spaced by the ground-state ZFS in the FLN spectrum across the inhomogeneous line [10]. The second one is a quasi-resonant process between spectral neighbours and manifests itself by rapid spectral diffusion [9]. The third one is the well-known phonon-assisted process setting in at higher temperature. In the following, we will first develop a simple model for spectral diffusion resulting from energy migration, and then go on to discuss experimental results obtained on the above-mentioned oxalate networks.

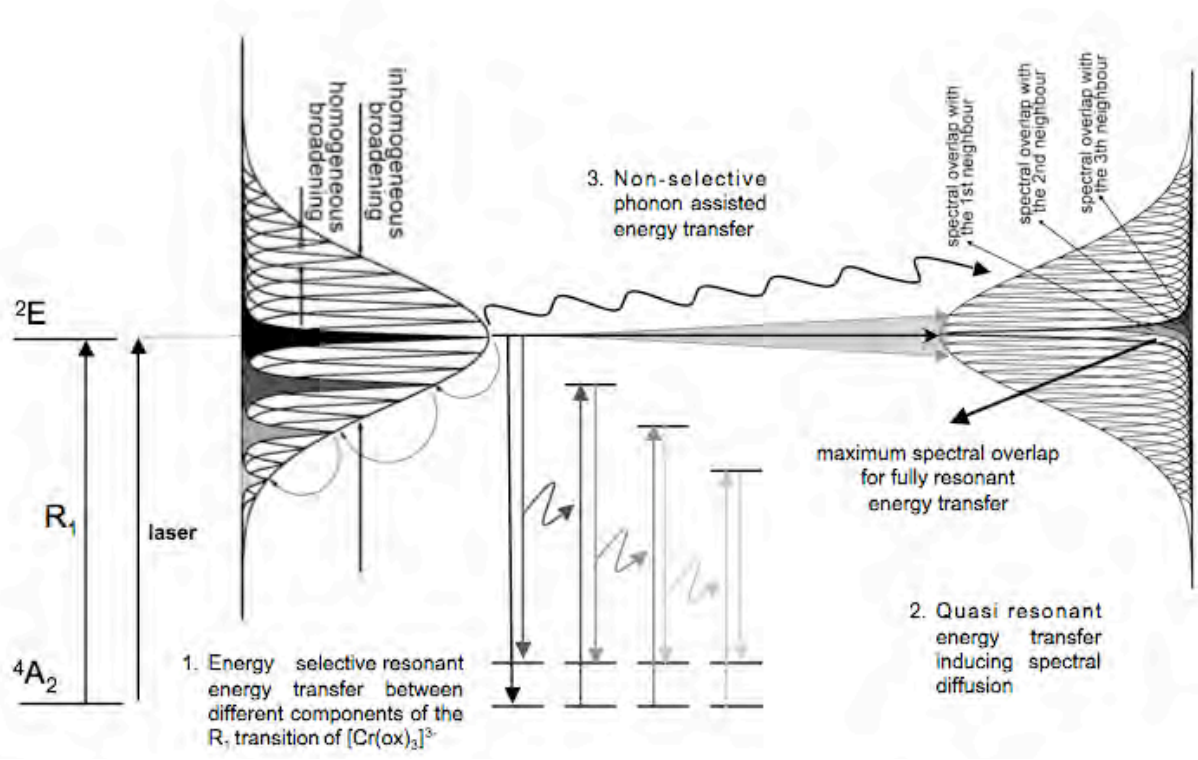

Figure 7.1. Schematic presentation of the three mechanisms for energy migration at high chromophore concentrations. 1. Resonant energy transfer between different components of the ground state. 2. Quasi-resonant energy migration between spectral neighbours resulting in spectral diffusion around the resonant line. 3. Non-energy selective phonon-assisted energy migration at elevated temperature [9].

7.2 Spectral diffusion, the model

At low temperatures the homogeneous line width Γ_{hom} of an electron origin is often much smaller than the inhomogeneous line width $\Gamma_{inh.}$ For the above-mentioned fully concentrated oxalate networks Γ_{hom} is typically 0.02 cm^{-1} (600 MHz) at 1.5 K, whereas Γ_{inh} varies from 1 to 4 cm^{-1} depending upon the exact composition [9]. At low temperatures, where phonon assisted processes are frozen, resonant and quasi-resonant energy migration may still occur because of the high concentration of chromophores. In the absence of exchange interactions, these processes are based on electric dipole–electric dipole interaction between the respective transition dipole moments [11]. The probability for an energy transfer process is given by

$$w_{DA} = \frac{1}{\tau_D}\left(\frac{R_c}{R_{DA}}\right)^6 \tag{7.1}$$

with the critical radius [12]

$$R_c = \left(Const \times \frac{\kappa^2 f_A \Omega_{DA} \eta_D^r}{\tilde{\nu}_{DA}^4}\right)^{1/6} \tag{7.2}$$

At which w_{DA} is equal to the intrinsic decay $k_D = \tau_D^{-1}$. In Equation (7.2), f_A is the dimensionless oscillator strength of the acceptor transition, η_D^r is the luminescence quantum efficiency of the donor transition, $\tilde{\nu}_{DA}$ is the mean energy at which the transfer takes place, κ^2 is a geometrical factor, which averaged over all possible orientations takes on a value of 2/3, *Const* regroups fundamental quantities and takes on a value of ~10^{31} for $\tilde{\nu}_{DA}$ in cm^{-1} and R_c in Å. The spectral overlap integral of the normalised line shape functions of the donor emission, g_D, and the acceptor absorption, g_A, is given by

$$\Omega_{DA} = \int g_A(\tilde{\nu}) g_D(\tilde{\nu}) d\tilde{\nu} \tag{7.3}$$

For energy migration, this has to be taken between the two homogeneous lines either fully resonant for chromophores with exactly the same central frequency, or quasi-resonant with partial spectral overlap for spectral neighbours as shown in Figure 7.1. For two Lorentzian lines of equal width centred at $\tilde{\nu}_D$ and $\tilde{\nu}_A$, respectively, the overlap integral is given by [13]

$$\Omega_{DA} = \frac{1}{\pi} \frac{\Gamma_{hom}}{\Gamma_{hom}^2 + \left(\tilde{\nu}_D - \tilde{\nu}_A\right)^2} \tag{7.4}$$

For the fully resonant case, this simplifies to $\Omega_{DA} = 1/\pi\Gamma_{hom}$. For Γ_{hom} ≈ 0.02 cm^{-1}, this results in a maximum value of Ω_{DA} ≈ 16 cm and of R_c ≈ 34 Å [9]. The mean number of chromophores, n_m, resonant within one homogeneous line width with a donor at the centre of the inhomogeneous distribution within a sphere of radius R_c is given by

$$n_m = \frac{2\Gamma_{hom}}{\Gamma_{inh}} N_{tot} \cdot \frac{4\pi}{3} R_c^3 \quad \sim \quad \frac{\sqrt{\Gamma_{hom}}}{\Gamma_{inh}} \tag{7.5}$$

For Γ_{inh} ≈ 1 cm^{-1}, n_m can be estimated to be > 6, for Γ_{inh} ≈ 4 cm^{-1} it falls to < 2 [9]. Thus at a narrow enough inhomogeneous line width, $\Sigma w_{DA} >> k_D$, where the sum includes all potential acceptors for a given donor.

For computational purposes the continuous distribution of chromophores in the inhomogeneous distribution is divided into n closely spaced discrete sets. In principle, each donor has a different environment of potential acceptors and therefore a different energy transfer probability to members of the sets with which it has non-negligible spectral overlap. For simplicity, an average energy transfer rate constant is assumed, in which case the population of the excited state in set i following pulsed excitation into set i_0 is given by *n* coupled differential equations

$$\frac{dN_{ei}}{dt} = -\left(k_D + k_{ET}\sum_j \Omega_{i,j}N_{gj}\right)N_{ei} + k_{ET}\sum_j \Omega_{j,i}N_{gi}N_{ej} \qquad i = 1, 2, ..., n \qquad (7.6)$$

N_{ei} is the number of centres of the i^{th} set in the excited state, N_{gi} are the corresponding ground state populations, k_{ET} is related to the energy transfer probability, and the $\Omega_{i,j}$ describe all possible spectral overlap integrals according to Equation (7.4). For weak excitation $N_{ei} << N_{gi}$, the N_{gi} are constant and are given by the inhomogeneous Gaussian distribution function. In this case, the set of differential equations becomes linear and can be solved numerically for $N_{ei}(t)$ using the starting condition that at t = 0, $N_{ei\neq i_0} = 0$ and $N_{ei_0} = N_0$. Finally, the evolution of the band shape can be calculated by the weighted sum of Lorentzians

$$f(\tilde{\nu},t) = \sum_i \frac{1}{\pi}\frac{\Gamma_{hom}/2}{(\tilde{\nu}-\tilde{\nu}_i)^2 + (\Gamma_{hom}/2)^2} N_{ei}(t) \qquad (7.7)$$

Figure 7.2a shows the calculated evolution of the band profile and Figure 7.2b the full width at half maximum as a function of delay following pulsed excitation at the centre of the inhomogeneous distribution. For the sample calculation, Γ_{inh} = 1.0 cm^{-1}, Γ_{hom} = 0.02 cm^{-1}, k_D = 700 s^{-1}, and k_{ET} was set to such a value that the maximum value of Σw_{DA} at the centre of the distribution is 10^5 s^{-1}. Evidently, the band broadens quickly, initially keeping its Lorentzian shape, but as the width becomes larger, it first evolves into a Voigt profile and finally ends in the Gaussian profile of the inhomogeneous distribution. The decomposition into Lorentzian and the Gaussian contributions to the profile is included in Figure 7.2b.

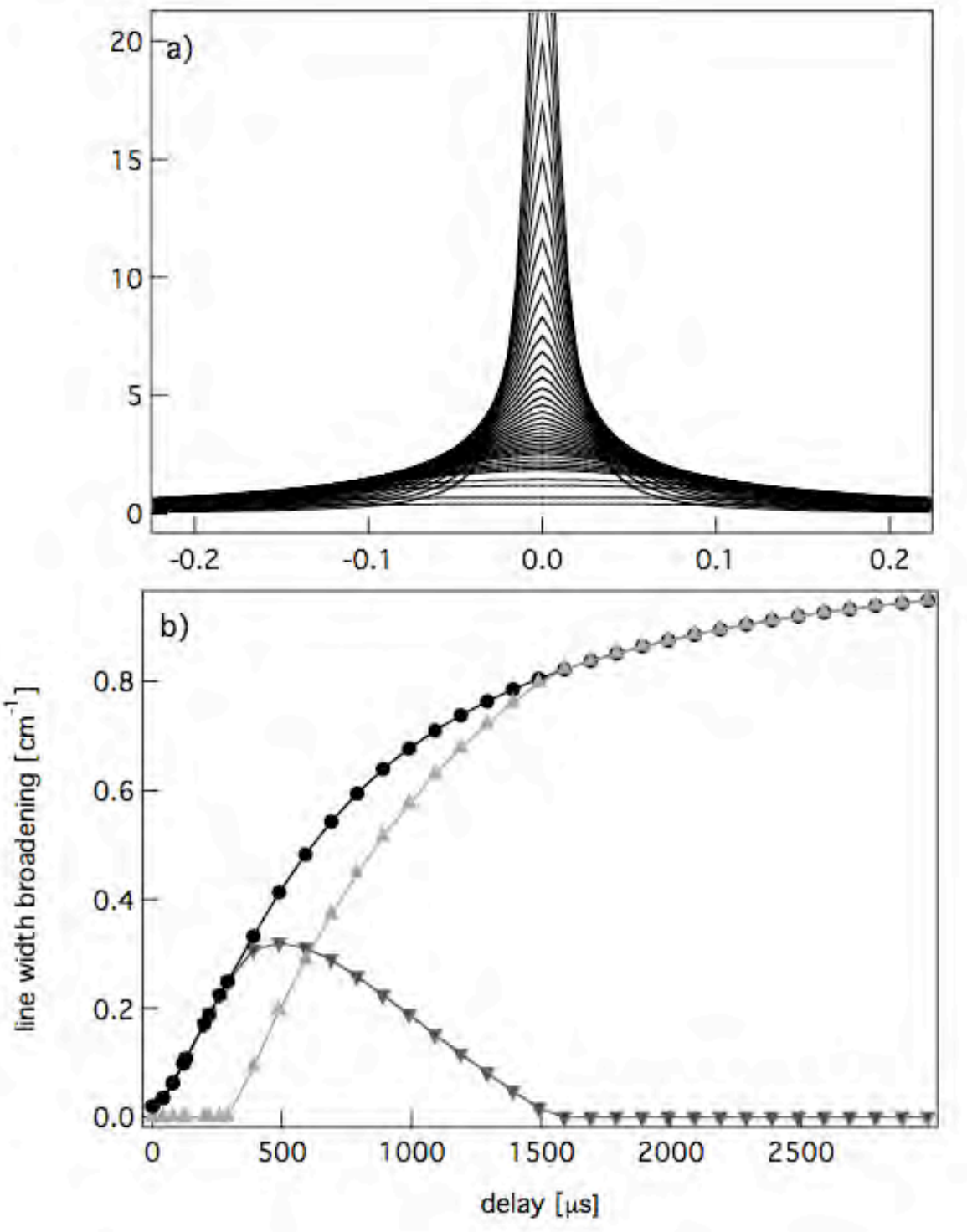

Figure 7.2. a) Evolution of the emission band shape as function of delay following laser excitation through spectral diffusion due to energy migration, b) Full width at half maximum and decomposition into Lorentzian and Gaussian contribution.

7.3 Energy Migration within the ^2E state of Cr^{3+}

Figure 7.3a shows time-resolved FLN spectra for $[NaCr(ox)_3][Ru(bpy)_3]$ at 1.4 K for irradiation into the maximum of the lower energy component of the R_1 line of the $^4A_2 \rightarrow {}^2E$ transition. At the shortest delay the spectrum consists of the normal three lines spaced by the ground-state ZFS of 1.3 cm^{-1} also observed for dilute systems in the absence of energy migration [14, 15]. But already at comparatively short delays, the three lines broaden out rapidly and additional satellite lines appear on both sides also spaced by the ground state ZFS. The latter are due to energy transfer involving the transitions to the upper level of the ground state of the donor and from the lower level of the acceptor such that within the inhomogeneous distribution the two have the same energy, and vice versa. The rapid broadening, as displayed in Figure 7.4 is due to quasi-resonant transfer between spectral neighbours within the inhomogeneous band as described above. That this is really the case is borne out by comparison with the FLN spectra of $[NaCr(ox)_3][Rh(bpy)_3](ClO_4)_2$ at 1.4 K shown in Figure 7.3b and 7.3c. The difference between the two compounds lies in the inhomogeneous widths, which are 1.1 cm^{-1} for the former and 4.2 cm^{-1} for the latter. Thus for the latter the concentration of resonant and quasi-resonant species is considerably smaller and therefore the temporal broadening of the lines in the FLN spectra does not much exceed the spectral resolution of 0.25 cm^{-1} of the detection system. However, as more multiples of the ZFS of 1.3 cm^{-1} can be accommodated within the inhomogeneous width of 4.2 cm^{-1}, the number of satellites appearing with a spacing of the ZFS is larger. The fact that no inhomogeneous background appears at longer delays also proves that the phonon-assisted process is frozen at 1.5 K. At 3.2 K, however, the phonon-assisted process becomes important as shown for $[NaCr(ox)_3][Rh(bpy)_3](ClO_4)_2$ in Figure 7.3c. The signature of the phonon-assisted process is clearly very different from the spectral diffusion observed for the system with the narrower inhomogeneous distribution of Figure 7.3a.

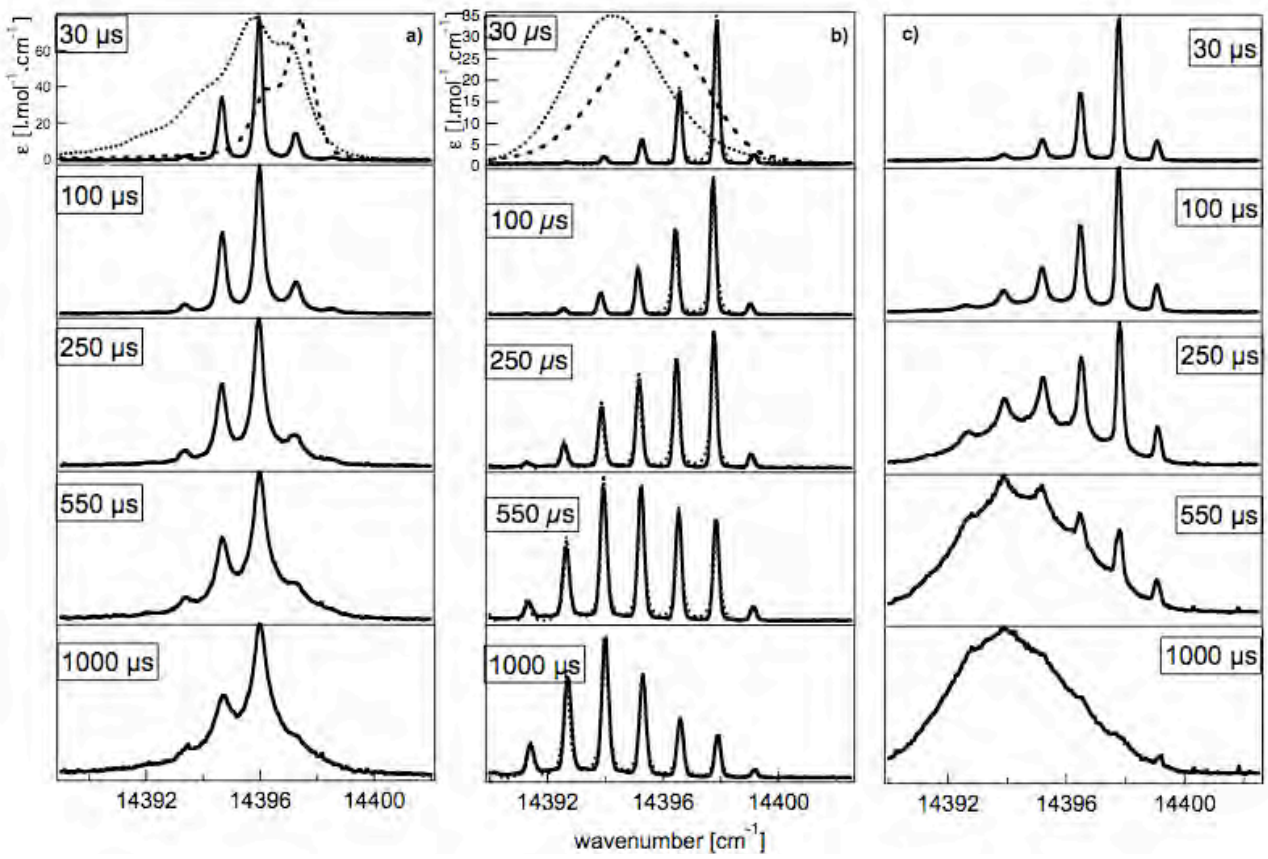

Figure 7.3. a) Time dependant FLN spectra of $[NaCr(ox)_3][Ru(bpy)_3]$ at 1.4 K after excitation into the R1 line of the $^4A_2 \rightarrow ^2E$ transition at 14396.0 cm^{-1}. b) Time dependant FLN spectra of $[NaCr(ox)_3][Rh(bpy)_3](ClO_4)_2$ at 1.4 K after excitation at 14397.8 cm^{-1}, and c) at 3.2 K. The absorption and non-selective luminescence spectra are included for comparison.

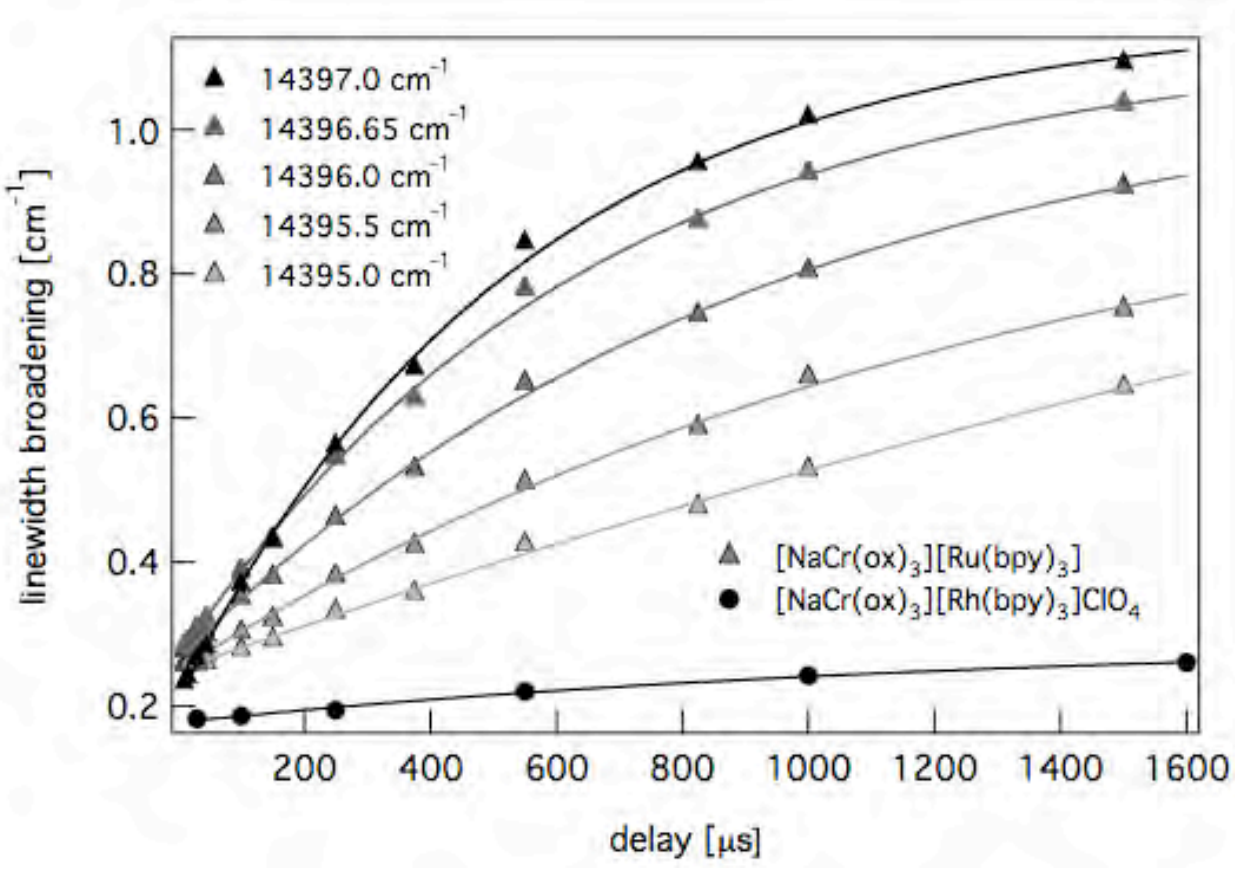

Figure 7.4. Evolution of the observed bandwidth of the individual sharp lines as function of time following pusled excitation for $[NaCr(ox)_3][Ru(bpy)_3]$ (▲)at different wavelengths across the inhomogeneous distribution and for (●) $[NaCr(ox)_3][Rh(bpy)_3](ClO_4)_2$, T = 1.4 K.

7.4 Conclusions

Three different energy migration processes have been clearly distinguished by FLN spectroscopy in three dimensional oxalate network compounds. $[NaCr(ox)_3][Ru(bpy)_3]$ having a 4 times smaller inhomogeneous line width than $[NaCr(ox)_3][Rh(bpy)_3]ClO_4$, has more resonant chromophores inside the critical sphere than the latter provided the homogeneous line widths are the same. This has consequences for the rate of resonant energy migration in those compounds, making it considerably faster in the case of $[NaCr(ox)_3][Ru(bpy)_3]$. With a simple model based on Förster's electric dipole-dipole energy transfer and taking into account all the possible spectral overlap integrals that one chromophore can have with its spectral neighbours, it is possible to

simulate the spectral diffusion in accordance with experimental observation. Fitting the time evolution of the band with a Voigt profile, one notes that the line shape evolves from a Lorentzian function at short delays to a Gaussian distribution limited by the inhomogeneous line width. A key parameter in the model is the homogeneous line width. Thus the question is whether the homogeneous line widths are the same for the two slightly different compounds. In order to clarify this further experiments will include transient spectral hole burning on $[NaCr(ox)_3][Ru(bpy)_3]ClO_4$ and $[NaCr(ox)_3][Ru(bpy)_3]$ as well as $[NaCr(ox)_3][Zn(bpy)_3]$.

Acknowledgements

We thank the Swiss National Science Foundation for financial support of this work.

References

[1] Fejer, M. M., H. Injeyan, and U. Keller, eds. *Advanced solid state lasers, in*. in: OSA Trends in Optics and Photonics, vol. 26. Vol. 26. (1999), Optical Society of America: Washington.

[2] Justel, T., H. Nikol, and C. Ronda, Angew. Chem., International Edition, 37 (1998), 3084.

[3] Gratzel, M., Nature (London, United Kingdom), 414 (2001), 338.

[4] Decurtins, S., et al., Inorg. Chem., 35 (1996), 1451.

[5] Imbusch, G. F., Phys. Rev., 152 (1967), 326.

[6] Decurtins, S., et al., JACS, 116 (1994), 9521.

[7] Basun, S. A., R. S. Meltzer, and G. F. Imbusch, J. Lumin., 125 (2007), 31.

[8] Hasan, Z., S. T. Keany, and N. B. Manson, J. Phys. C: Solid State Physics, 19 (1986), 6381.

[9] Milos, M., et al., Coord. Chem. Rev., (2008),

[10] Hauser, A., et al., Top. Curr. Chem., 241 (2004), 65.

[11] Forster, T., Ann. Physik [6 Folge], 2 (1948), 55.

[12] Henderson, B. and G. F. Imbusch, Clarendon Press, Oxford, (1989),

[13] Di Bartolo, B. and X. Chen, eds. Advances in Energy Transfer Processes. (2001), World Scientific: New Jersey.

[14] Von Arx, M. E., et al., Phys. Rev. B: Condensed Matter, 54 (1996), 15800.

[15] Hauser, A., et al., Chem. Phys. Lett., 261 (1996), 313.

8. Spectral diffusion in the $^4A_2 \rightarrow {}^2E$ transition of octahedral Cr^{3+} in $[NaCr(ox)_3][M^{II}(bpy)_3]$, $M^{II} = Ru^{II}$, Zn^{II}, and $[NaCr(ox)_3][M^{III}(bpy)_3]ClO_4$, $M^{III} = Rh^{III}$

Contents

8.1 Introduction

The $^4A_2(t_{2g}^3) \rightarrow {}^2E(t_{2g}^3)$ transition is at the origin of the strong red ruby ($Al_2O_3:Cr^{3+}$) emission, ruby being the active medium in the first laser ever constructed. The transition is due to the Cr^{3+} ion sitting in a strong octahedral field with $[CrO_6]$ coordination. It's a so-called spin-flip transition with all the intensity concentrated in the electronic origin making the bandwidth very narrow since the Huang-Rhys factor is close to zero. Due to the combined effects of the trigonal distortion (low symmetry field) and spin-orbit coupling, the zero-field splitting (ZFS) in both states appears. In ruby, the ZFS of the ^2E state is 29 cm^{-1} [1], and can be observed by conventional absorption and luminescence spectroscopy. The luminescence of ruby manifests itself with two sharp but intense lines, called R_1 and R_2 line due to the luminescence from the zero-field split components of the ^2E state. At higher doping levels, there are some additional bands due to nearest-neighbour exchange couplings. Those lines are commonly called N lines [2,3].

In the three-dimensional oxalate networks such as $[M^{II}(bpy)_3][NaCr(ox)_3]$ or $[M^{III}(bpy)_3][NaCr(ox)_3]ClO_4$, the Cr^{3+} ions are, similarly to ruby, sitting in a strong octahedral field of $[CrO_6]$ coordination. However, all Cr^{3+} ions are in well defined positions spaced by the two oxalate ligands with a Na^+ ion in between. Thus, the super-exchange interaction between chromium ions is negligible. The luminescence and absorption spectra of Cr^{3+} in those compounds also have two very narrow bands, corresponding to R_1 and R_2 lines. However, no N lines are observed.

In previous work [4-6] it has been shown that in $[Rh(bpy)_3][NaCr(ox)_3]ClO_4$ comparatively efficient energy migration within the R_1 line of Cr^{3+} occurs. At elevated temperatures this migration is phonon-assisted. Below 4.2 K, the phonon-assisted process is frozen in, but the energy migration persists to well below that temperature as resonant process, which manifests itself in a series of sharp lines across the inhomogeneous line width spaced by the ZFS of the ground state [5]. In a preliminary study we reported spectral diffusion of the individual sharp lines as due to quasi-resonant energy transfer in the related compound $[Ru(bpy)_3][NaCr(ox)_3]$ [4]. In this paper we compare the photophysical properties and in particular the spectral diffusion of the R_1 line of Cr^{3+} in three different compounds, namely

$[Rh(bpy)_3][NaCr(ox)_3]ClO_4$, $[Ru(bpy)_3][NaCr(ox)_3]$, and $[Zn(bpy)_3][NaCr(ox)_3]$. In Figure 8.1 the absorption and the luminescence spectra of the three compounds in the region of the R_1 line are shown. As a result of different ionic radii of the metals, the nephelauxetic effect experienced by the Cr^{3+} ions varies slightly between the three lattices [7]. This manifests itself by the relative shifts of the R_1 absorption and emission bands. Furthermore, the inhomogeneous line width of the $^4A_2 \rightarrow {}^2E$ transition varies from one compound to the other. The inhomogeneous broadening is due to the local defects around each chromium ion. Consequently, the absorbed light from the $^4A_2 \rightarrow {}^2E$ transition of each chromium ion does not have exactly the same energy, but there is a Gaussian distribution of all possible energies. The line width for $[Rh(bpy)_3][NaCr(ox)_3]ClO_4$ is significantly larger than for the other two compounds. The width is 4.4 cm^{-1} [4], which is still very narrow compared to other types of d-d transitions and all types of charge transfer transitions, but with respect to $[Zn(bpy)_3][NaCr(ox)_3]$ and $[Ru(bpy)_3][NaCr(ox)_3]$, having respectively line widths of less than 2 cm^{-1} and less than 1 cm^{-1}, the difference is significant. As will be discussed below, this difference, thought to be due to disorder of the ClO_4^- ions, is at the origin of very different rates of all the energy migration processes that occur within the R_1 line of Cr^{3+}. The fact that the corresponding bands in the emission spectra are shifted to lower energies with respect to the absorption bands, gives a first indication that energy migration is indeed an efficient process.

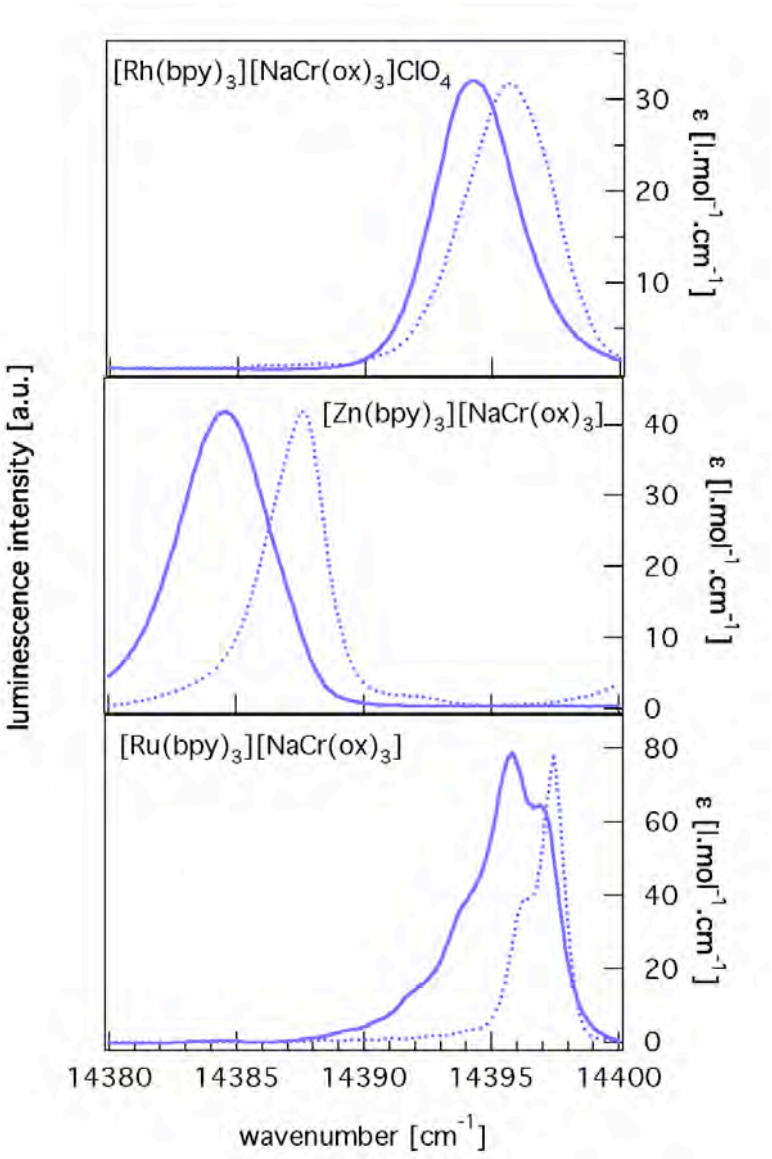

Figure 8.1. Absorption and luminescence spectra in the region of the R_1 line of $[Rh(bpy)_3][NaCr(ox)_3]ClO_4$, $[Ru(bpy)_3][NaCr(ox)_3]$, and $[Zn(bpy)_3][NaCr(ox)_3]$.

8.2 Experimental Section

The stoichiometric compounds $[Ru(bpy)_3][NaCr(ox)_3]$, $[Zn(bpy)_3][NaCr(ox)_3]$, and $[Rh(bpy)_3][NaCr(ox)_3]ClO_4$ were prepared according to the literature method of Decurtins and coworkers [8]. Accordingly, 10^{-2} M aqueous solutions of $K_3Cr(ox)_3{\cdot}3H_2O$, $[Ru(bpy)_3]Cl_2{\cdot}6H_2O$, $[Zn(bpy)_3]Cl_2{\cdot}6H_2O$ and NaCl were prepared. To obtain the compounds, 20 ml of the $K_3Cr(ox)_3$ and NaCl solutions were added to the

same volumes of $[Zn(bpy)_3]^{2+}$ or $[Ru(bpy)_3]^{2+}$ or $[Rh(bpy)_3]^{3+}$ solutions, respectively. Single crystals of the stoichiometric compounds in the form of perfect tetrahedra of 0.5 mm edge were grown by slow evaporation of the solutions stored at 5 °C in a refrigerator. Electronic absorption spectra were recorded on single crystals using a Fourier-transform spectrometer equipped for measuring in the infrared and visible spectral range (Bruker IFS66/S). The absorption spectra were collected at a spectral resolution of 0.5 cm^{-1}. For absorption measurements crystals with one corner of the tetrahedron polished down to a thickness of ~60 µm were mounted on copper apertures, placed in a closed cycle cryostat (Oxford Instruments CCC1204), and collected at 10 K in He exchange gas. For non-selective luminescence spectra as well as for the fluorescence line narrowing spectra, the samples were cooled to 1.4 K in a helium bath cryostat (Cryo Industries). For non-selective luminescence spectra samples were excited at 532 nm, that is into the $^4A_2 \rightarrow {}^4T_2$ transition of Cr^{3+}, from an intracavity frequency doubled Nd:YAG laser (ILEE VA-I-N-532). FLN spectra were obtained by selective excitation using a Ti:Sapphire laser (Coherent 699) at around 14450 cm^{-1}, that is within the R_1 electronic origin of Cr^{3+}. The collected emission was dispersed and analysed using a double monochromator (SPEX 1403) and detected with a CCD camera (Roper Instruments), giving a spectral resolution of about 0.20 cm^{-1}. For a detailed description of the FLN set-up see Chapter 2.

8.3 Results and Discussion

8.3.1 $[Rh(bpy)_3][NaCr(ox)_3]ClO_4$

Resonant and phonon-assisted energy migration within the $^4A_2 \rightarrow {}^2E$ transition of $[Cr(ox)_3]^{3-}$ in $[Rh(bpy)_3][NaCr(ox)_3]ClO_4$ have been well established [4-6]. At 1.4 K the phonon-assisted energy transfer is negligible because lattice vibrations are frozen at this temperature. Thus, at 1.4 K, one observes exclusively resonant energy transfer that occurs between the zero field split components within the inhomogeneous absorption band of $[Rh(bpy)_3][NaCr(ox)_3]ClO_4$. The two different energy migration mechanisms are nicely distinguished by FLN spectroscopy. The resonant energy

migration manifests itself as a multi-line pattern with members spaced by the ZFS of the ground state, while the phonon-assisted energy transfer manifests itself as a non-selective growing of the inhomogeneous band with increasing temperature shifted to the red wing of the absorption band. Figure 8.2 shows absorption and non-selective luminescence of the R_1 line of $[Cr(ox)_3]^{3-}$, as well as the steady state FLN spectra at 1.4 K for different excitation energies within the absorption band. The absorption band is centred at 14395.5 cm^{-1} and the inhomogeneous line width of the absorption band is about 4.4 cm^{-1}. The steady state FLN spectra were recorded with excitation energies of 14392.0, 14394.0, 14395.5, 14396.0, 14397.0, and 14399.0 cm^{-1}, respectively. Up to 8 members of the multi-line pattern spaced by the ground-state ZFS of 1.3 cm^{-1} can be easily discerned. The resonant line corresponds to the luminescence coming from the direct excitation, while the other lines have their origin in the energy that is transferred from the initially excited subset of chromophores via resonant energy transfer involving the upper component of the ground state for the donor and the lower component for the acceptor which happen to be resonant within the inhomogeneous width of the R_1 line. If one focuses on the intensities of the resonant line for different excitations, it can clearly be seen that for the red wing excitation, the resonant line is the most intense, whereas with excitation wavelengths towards the blue wing of the absorption band, the most intense lines are the ones resulting from the resonant energy transfer. At 1.4 K, the energy migration thus results in an overall shift of the emission to lower energies. More precisely, by increasing the excitation energy within the absorption band towards the absorption maximum, we increase the concentration of resonant chromophores. The energy transfer rate depends on the concentration of the resonant chromophores. The higher the concentration of the resonant chromophores, the faster is the energy transfer rate. For excitation in the blue wing of the absorption there is a bottleneck effect as the initially excited set of chromophores sees only a low concentration of resonant acceptors. But once the energy has migrated into the maximum of the inhomogeneous distribution, the energy migration becomes faster again. Figure 8.3 shows time-resolved FLN spectra. The excitation energy is 14395.5 cm^{-1}, that is, at the maximum of the absorption band. Several observations can be made. With increased delay time between the excitation step and the acquisition step, the energy

migrates toward the lower members of the multi-line pattern in subsequent steps. Thus, after 1000 µs delay between excitation and acquisition, the energy is mainly concentrated at 2.6 cm^{-1}, that is, 2D lower in energy compared to the original excitation energy. An interesting point to be mentioned is the fact that there is not a significant difference between the three spectra recorded after 1000, 1500 and 2000 µs delay, except a global decrease in the intensity of the resonant as well as the other lines. This can be explained by the fact that after 1000 µs delay, the thermal equilibrium is established between the excited chromophores via energy transfer. Of particular importance for the present discussion, is the fact that no apparent broadening of the individual members of the multi-line pattern can be noticed. Throughout, the observed line width is essentially given by the spectral resolution of 0.22 cm^{-1} of the experimental set-up.

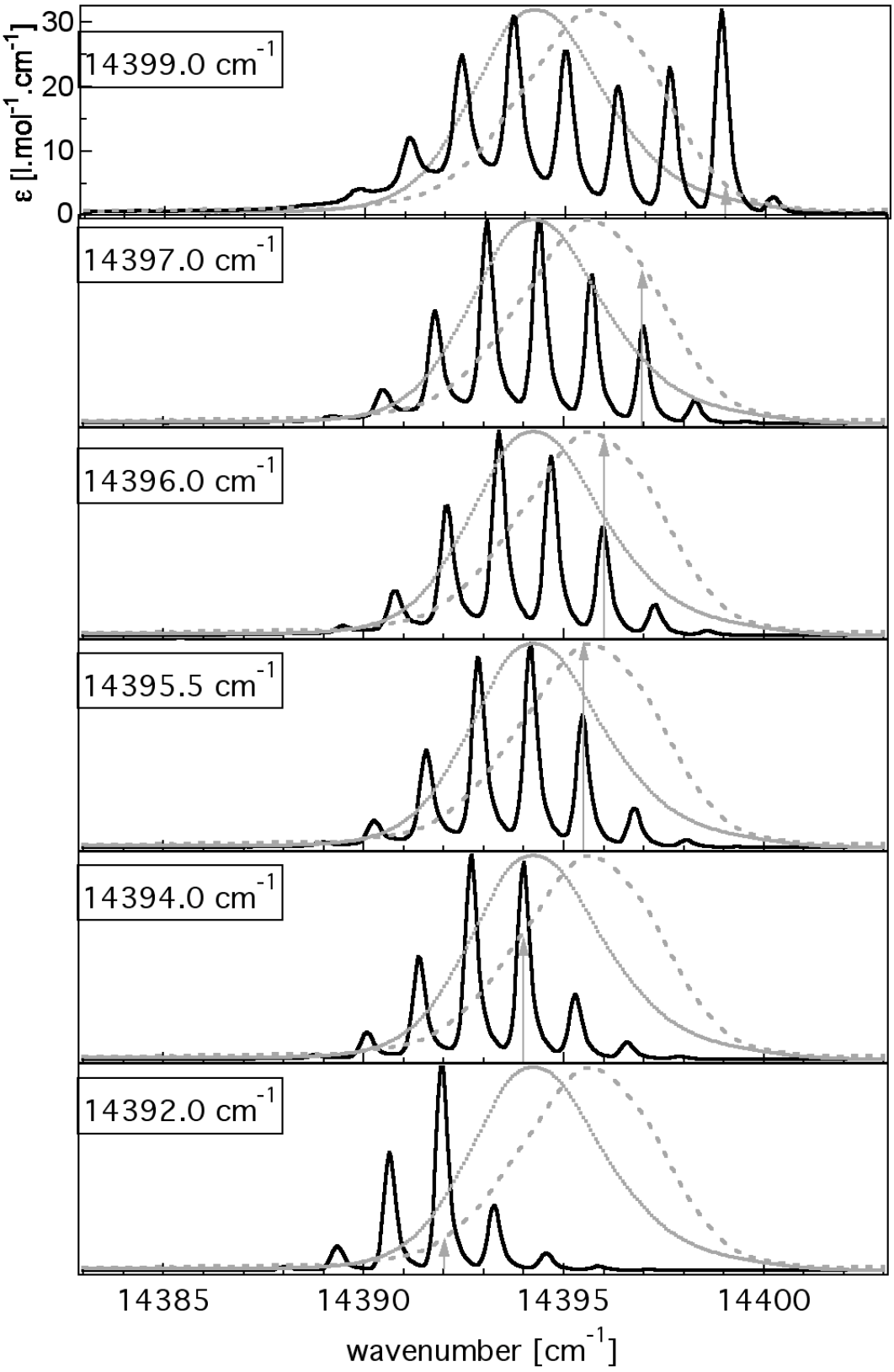

Figure 8.2. Absorption, luminescence and steady state FLN spectra at different excitation energies of $[Rh(bpy)_3][NaCr(ox)_3]ClO_4$.

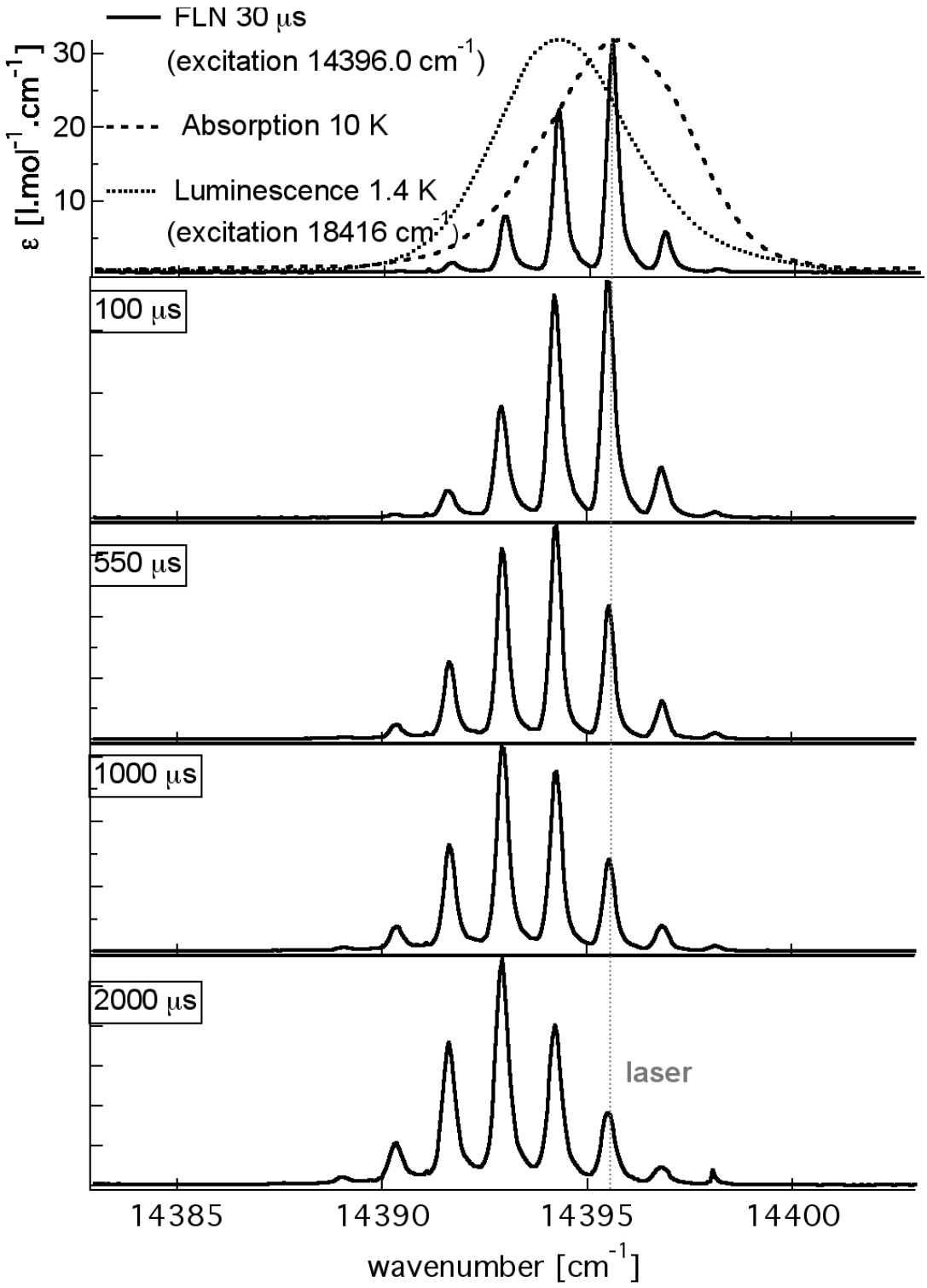

Figure 8.3. Time-resolved FLN spectra following a 14395.5 cm^{-1} excitation within the inhomogeneous line width of $[Rh(bpy)_3][NaCr(ox)_3]ClO_4$.

8.3.2 $[Ru(bpy)_3][NaCr(ox)_3]$

The energy migration within the $[Cr(ox)_3]^{3-}$ R_1 line in $[Ru(bpy)_3][NaCr(ox)_3]$ has been studied and we published recently a review indicating three different types of energy transfer that can be observed in this compound [4]. Beside the phonon-assisted and the resonant energy transfer between zero-field split members within the inhomogeneously broadened band already observed in $[Rh(bpy)_3][NaCr(ox)_3]ClO_4$, in $[Ru(bpy)_3][NaCr(ox)_3]$ one can distinguish a quasi-resonant energy transfer, that is, between the same components within the multi-line pattern. In an FLN spectrum this gives rise to spectral diffusion of the initially sharp lines. It is dominant for small inhomogeneous distributions, which result in a higher concentration of species resonant within one homogeneous line width. In this chapter, so far unpublished experimental results on the energy migration dependent on excitation energy in $[Ru(bpy)_3][NaCr(ox)_3]$ will be discussed. Figure 8.4 shows absorption and luminescence of the R_1 line of $[Cr(ox)_3]^{3-}$, as well as the steady state FLN spectra at 1.4 K for different excitation energies within the absorption band. The absorption band is centred at 14397.0 cm^{-1}, and the inhomogeneous line width of the absorption band is about 1.1 cm^{-1}. The ZFS of the ground state manifests itself as a shoulder in the absorption band. The steady state FLN spectra were performed at 14395.1, 14395.5, 14396.0, 14396.4, 14397.0, and 14398.0 cm^{-1}. Overall, we can distinguish 6 members of the multi-line pattern spaced by the ZFS of the ground state. As for $[Rh(bpy)_3][NaCr(ox)_3]ClO_4$, the most intense line is the resonant one for red wing excitations, and for blue wing excitations, lines at lower energy fed by energy transfer become more intense. However, there is a marked difference between the steady state FLN spectra of $[Rh(bpy)_3][NaCr(ox)_3]ClO_4$ and $[Ru(bpy)_3][NaCr(ox)_3]$. In $[Ru(bpy)_3][NaCr(ox)_3]$, the members of the multi-line pattern show strong spectral diffusion, such that for blue wing excitation, the selectivity of the excited chromophores by energy transfer is almost lost and the FLN spectrum at 14398.0 cm^{-1} excitation almost overlap with the non-selective luminescence spectrum. This spectral diffusion is attributed to quasi-resonant energy transfer. Figure 8.5 shows time-resolved FLN spectra with the excitation at the maximum of the inhomogeneous absorption band. From these spectra it is evident that each individual line broadens

as the delay between excitation and recording the spectrum is increased. This is in contrast to non-energy selective phonon-assisted energy migration, which results simply in a growing in of the inhomogeneous background. Thus as mentioned above, the fast spectral diffusion is indeed due to quasi-resonant energy transfer. The time resolved FLN spectra can be fitted with a sum of 6 Lorentzian functions by fixing the same line width for all the members of the multi-line pattern for a given delay. Although the shape of the individual lines is not expected to stay Lorentzian and neither is the spectral response function of the detection system Lorentzian, the overall fit is good and one can extract a reasonable value of the effective line width for all the excitation energies and plot them as a function of the delay between the excitation and the acquisition of the spectra. Figure 8.8a shows the plot of the effective line width as a function of the delay. One can clearly see that the line width broadens faster with increasing excitation energy. An important point to be mentioned is that the line width reaches a plateau with increasing delay time between excitation and acquisition, and the limiting value of the broadening leads to the inhomogeneous line width.

As mentioned above, the resonant energy transfer rate depends on the concentration of the initially excited resonant chromophores. Thus it is expected to be faster in the present system as compared to $[Rh(bpy)_3][NaCr(ox)_3]ClO_4$ because of the smaller inhomogeneous line width. In a preliminary paper [9], we developed a model for spectral diffusion based on Förster type energy transfer with electric dipole-dipole interactions. However, instead of including only the chromophores that are fully resonant with each other but separated by the ZFS of the ground state for calculating the spectral overlap integral, one should also include all the chromophores whose absorption overlaps only partially with the emission of the initially excited chromophore. This model is discussed in detail in Section 8.4.

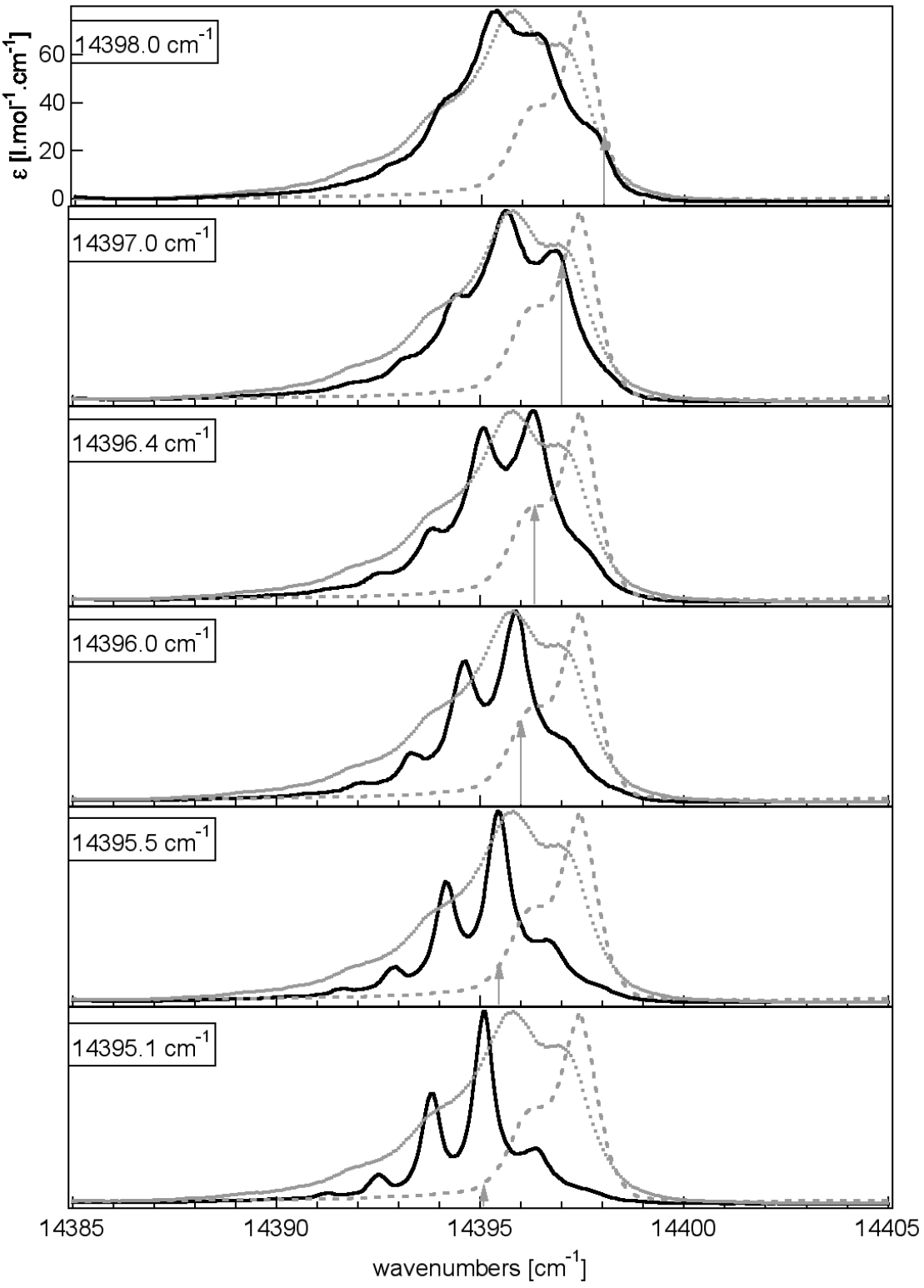

Figure 8.4. Absorption, luminescence and steady state FLN spectra at different excitation energies of $[Ru(bpy)_3][NaCr(ox)_3]$.

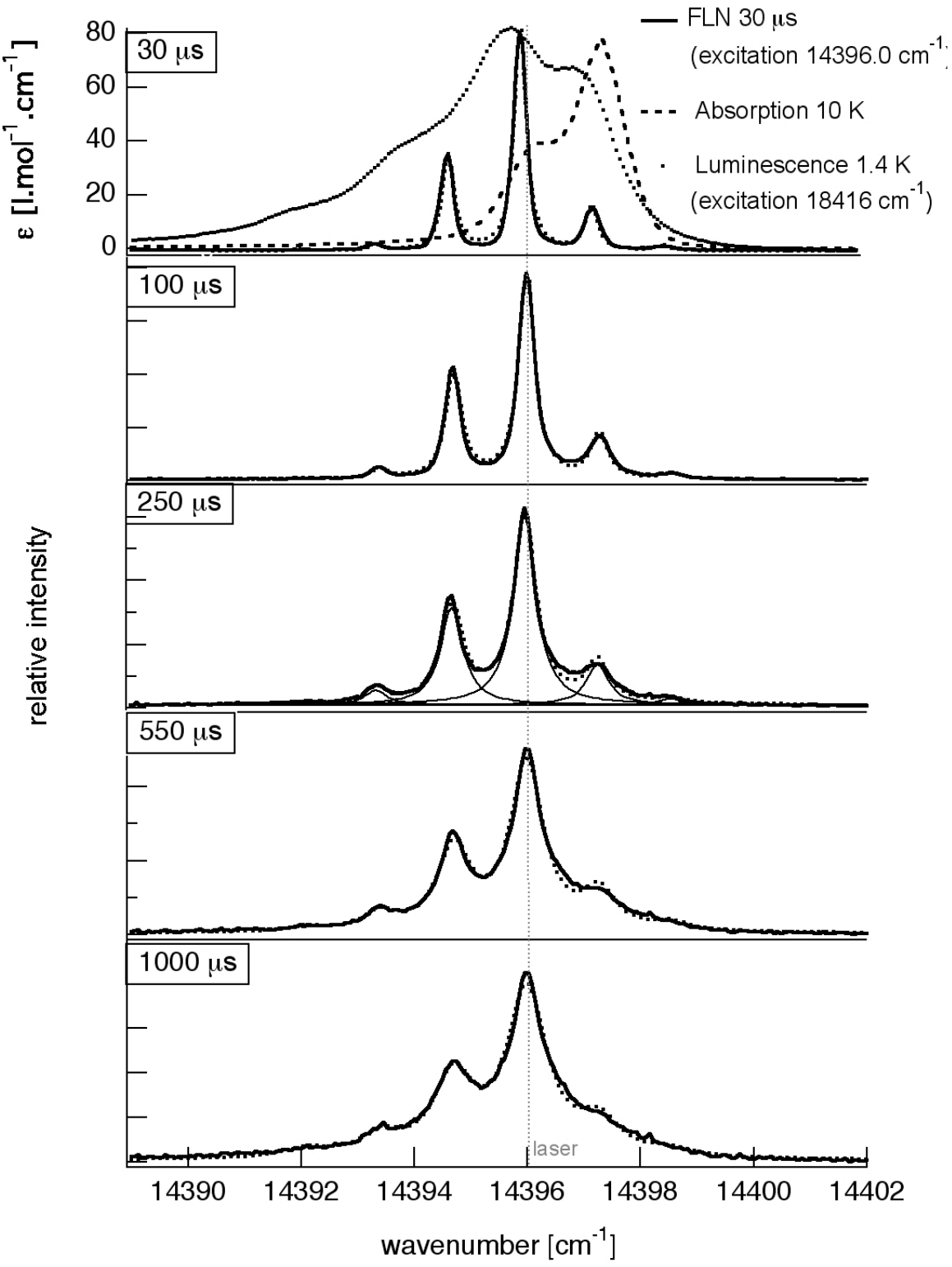

Figure 8.5. Time-resolved FLN spectra following a 14396.0 cm^{-1} excitation within the inhomogeneous line width of $[Ru(bpy)_3][NaCr(ox)_3]$.

8.3.3 $[Zn(bpy)_3][NaCr(ox)_3]$

Figure 8.6 shows the absorption and luminescence spectra of the R_1 line as well as the steady state FLN spectra at 1.4 K for different excitation energies within the absorption spectrum of $[Cr(ox)_3]^{3-}$ in $[Zn(bpy)_3][NaCr(ox)_3]$. The absorption transition is centred at 14387.5 cm^{-1} and the inhomogeneous line width of the absorption transition is about 2.0 cm^{-1}. The ZFS of the ground state is not resolved. The steady state FLN spectra were recorded with excitation energies of 14381.0, 14383.1, 14385.1, 14386.9, 14388.1, 14389.1 and 14391.0 cm^{-1}. We can barely distinguish 5 members of the multi-line pattern spaced by the ZFS at very low excitation energies. $[Zn(bpy)_3][NaCr(ox)_3]$ is very similar to $[Ru(bpy)_3][NaCr(ox)_3]$, at 1.4 K one can observe both resonant and quasi-resonant energy transfer. However, it seems that in spite of the somewhat larger inhomogeneous absorption line width, all the energy transfer processes are faster in $[Zn(bpy)_3][NaCr(ox)_3]$ compared to $[Ru(bpy)_3][NaCr(ox)_3]$. Indeed, in Figure 8.7, showing the time-resolved FLN spectra for irradiation at the centre of the absorption, one can see that spectral diffusion is much faster. Already for a delay of 825 µs, the spectral diffusion reaches its limit, that is the inhomogeneous line width of the absorption band.

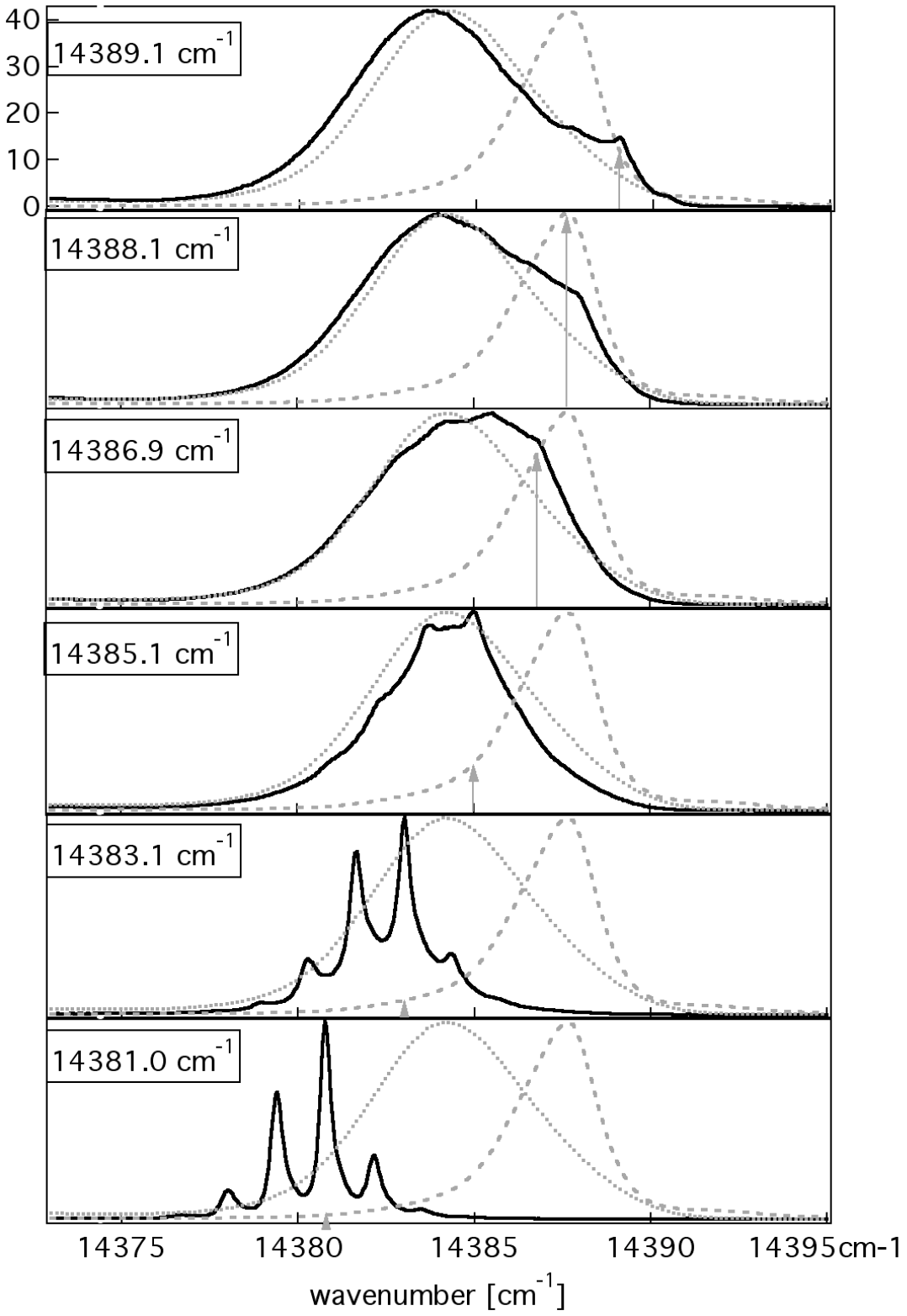

Figure 8.6. Absorption, luminescence and steady state FLN spectra at different excitation energies of $[Zn(bpy)_3][NaCr(ox)_3]$.

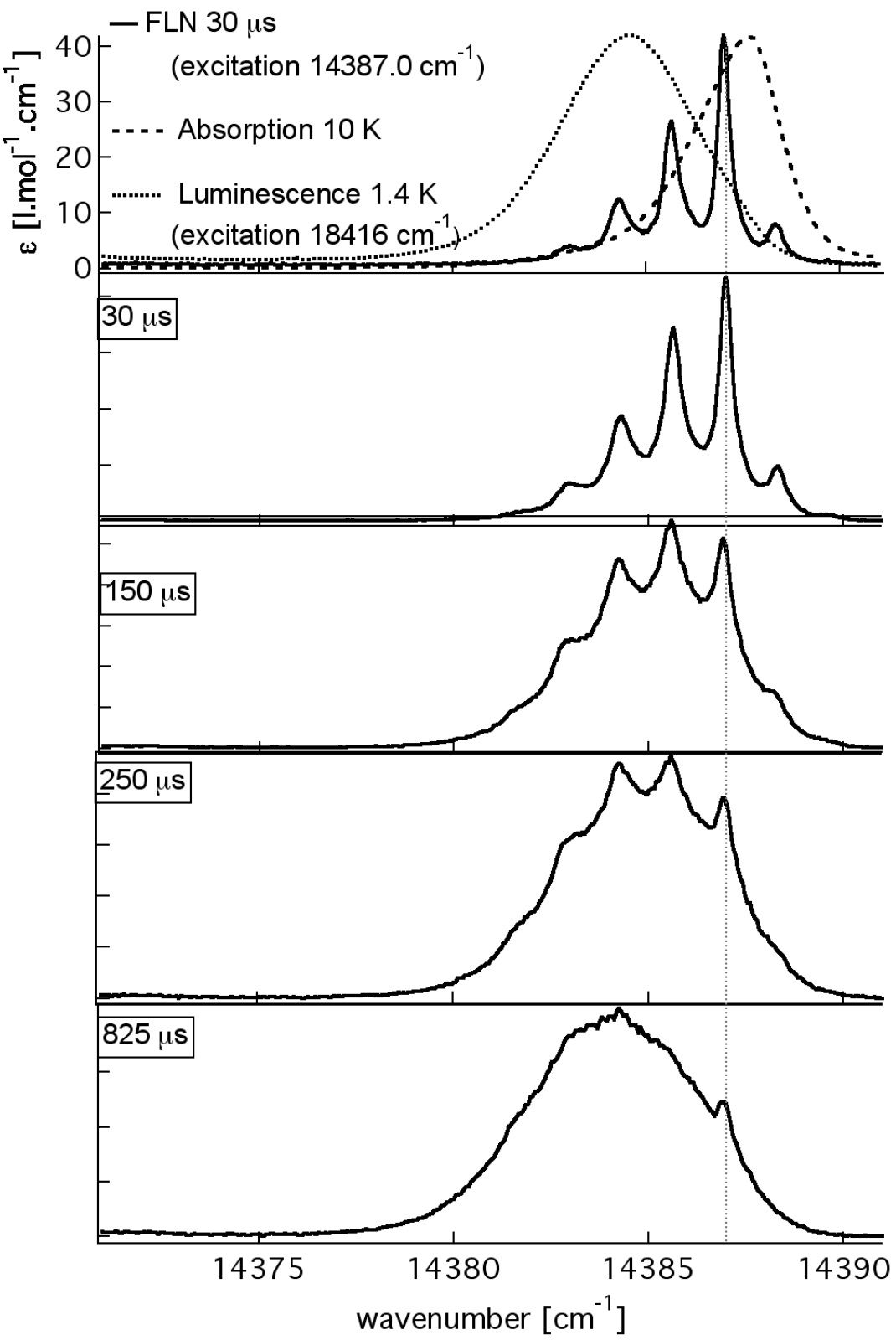

Figure 8.7. Time-resolved FLN spectra following a 14387.0 cm^{-1} excitation within the inhomogeneous line width of $[Zn(bpy)_3][NaCr(ox)_3]$.

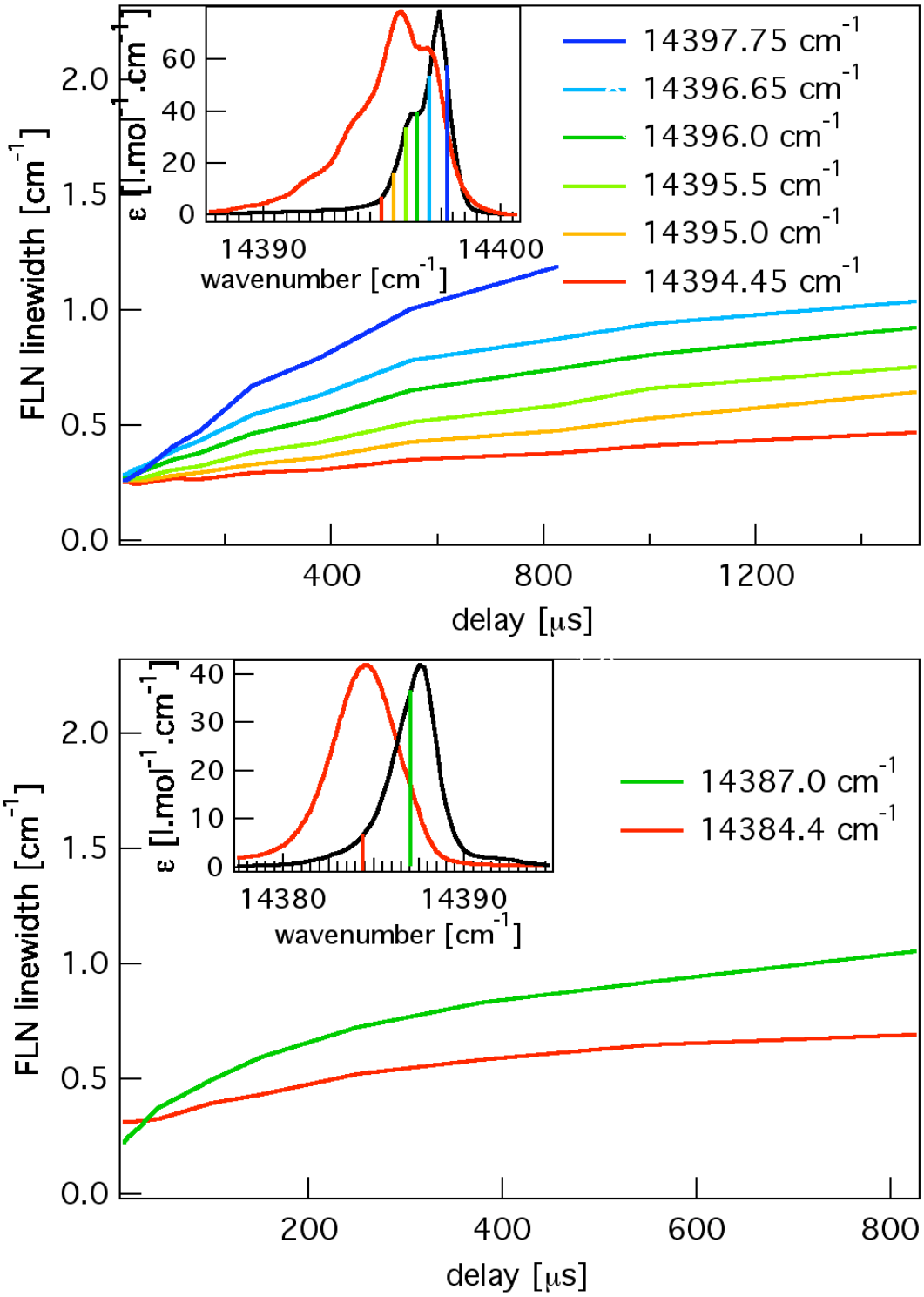

Figure 8.8. Time evolution of the effective line width in the time-resolved FLN experiments at 1.4 K at different excitation energies of a) $[Ru(bpy)_3][NaCr(ox)_3]$, b) $[Zn(bpy)_3][NaCr(ox)_3]$. The insets show the positions within the absorption bands where the excitation occurs for $[Ru(bpy)_3][NaCr(ox)_3]$ and $[Zn(bpy)_3][NaCr(ox)_3]$, respectively.

8.4 Model for Spectral Diffusion in $[Cr(ox)_3]^{3-}$

The spectral diffusion of the individual sharp line is modelled in a simplified model taking into account a single transition (see Figure 8.9). The initial parameters are the inhomogeneous line width, Γ_{inh}, the homogeneous line width, Γ_{hom}, the intrinsic radiative rate constant, k_0, the energy transfer rate constant, k_{ET}, and the resolution step for approximating the continuous inhomogeneous distribution as a sum of Lorentzians, δ.

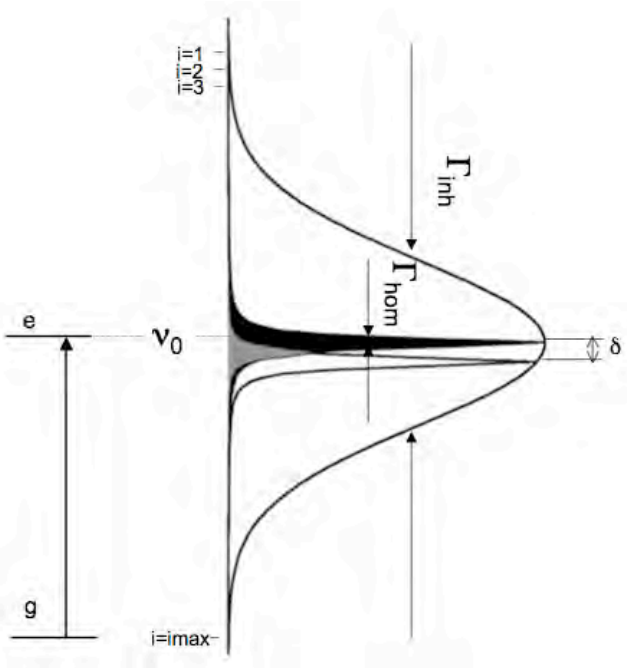

Figure 8.9. Schematic representation of the model for spectral diffusion with the parameters involved.

The total concentration of each set of chromophores, N_{0i} is defined with a normalised Gaussian distribution for a given line width.

$$g(\nu) = \frac{1}{\sqrt{2\pi}\sigma} e^{-\frac{(\nu-\nu_0)^2}{2\sigma^2}} \qquad (1)$$

With $\Gamma_{inh} = 2\sigma\sqrt{2\ln 2} = 2.35\sigma$. The N_{0i} correspond to a vector $\boldsymbol{N_0}$ that has *imax* members, where *imax* is chosen according to *imax* = a*Integer[Γ_{inh}/δ)] + 1, with a = 3 in order to cover the Gaussian distribution out to $\pm 3.5\sigma$. At any time, the populations

of the ground state and excited state of a given set, N_{gi} and N_{ei}, respectively, are related by

$$N_{0i} = N_{gi} + N_{ei} \tag{2}$$

and correspond likewise to vectors $\boldsymbol{N_g}$ and $\boldsymbol{N_e}$ of lengths *imax.*

At t = 0, the excited state populations of all sets except for the one at the excitation wavelength are set to zero. In the limit of the small laser intensities and the short excitation times used in the experiment, the excited state population of the initially excited set of chromophores is taken as 1% of the corresponding value of N_{0i}.

Assuming an average bimolecular rate constant for the energy transfer from a set of chromophores to another, the time evolution of the excited state population can be described by a set of differential equations.

$$\frac{dN_{ei}}{dt} = -\left(k_0 + k_{ET}\sum_j \Omega_{i,j} N_{gj}\right) N_{ei} + k_{ET}\sum_j \Omega_{j,i} N_{gi} N_{ej} \qquad \text{i = 1, 2, ..., imax} \tag{3}$$

Where, k_0 is the intrinsic deactivation rate constant, k_{ET} is the average value of the energy transfer rate constant for a hypothetical spectral overlap integral of unity, N_{ei} is the population of the excited state of a given site, and ΣN_{ej} is the sum of populations in the excited states, N_{gi} is the ground state population of the given state and N_{gj} are the ground state populations of the other sites within the Gaussian distribution. In the limit of weak excitation, the ground state populations can be set equal to the total concentrations, that is $N_{gj} \approx N_{0j}$. Finally $\Omega_{i,j}$ is the spectral overlap integral between the Lorentzian line shapes of two sites i,j.

$$\Omega_{i,j} = \frac{1}{\pi} \cdot \left(\frac{\Gamma_{hom}}{\Gamma_{hom}{}^2 + \left(\delta \cdot (i-j)\right)^2} \right) \qquad \text{i, j = 1, 2, …, imax} \tag{4}$$

For resolving this set of coupled differential equations, we proceed according to a well-established method. It is possible to decompose the set of differential equations, by creating a matrix ***M***

$$\begin{pmatrix} dN_{e1}/dt \\ dN_{e2}/dt \\ dN_{e3}/dt \\ \dots \\ dN_{ei}/dt \end{pmatrix} = \begin{pmatrix} -(k_0 + k_{ET} \cdot \sum_j \Omega_{1,j} \cdot N_{01}) & k_{ET} \cdot \Omega_{1,2} \cdot N_{01} & k_{ET} \cdot \Omega_{1,3} \cdot N_{01} & \dots & k_{ET} \cdot \Omega_{1,j} \cdot N_{01} \\ k_{ET} \cdot \Omega_{2,1} \cdot N_{02} & -(k_0 + k_{ET} \cdot \sum_j \Omega_{2,j} \cdot N_{02}) & k_{ET} \cdot \Omega_{2,3} \cdot N_{02} & \dots & k_{ET} \cdot \Omega_{2,j} \cdot N_{02} \\ k_{ET} \cdot \Omega_{3,1} \cdot N_{03} & k_{ET} \cdot \Omega_{3,2} \cdot N_{03} & -(k_0 + k_{ET} \cdot \sum_j \Omega_{3,j} \cdot N_{03}) & \dots & k_{ET} \cdot \Omega_{3,j} \cdot N_{03} \\ \dots & \dots & \dots & \dots & \dots \\ k_{ET} \cdot \Omega_{i,1} \cdot N_{0i} & k_{ET} \cdot \Omega_{i,2} \cdot N_{0i} & k_{ET} \cdot \Omega_{i,3} \cdot N_{0i} & \dots & -(k_0 + k_{ET} \cdot \sum_j \Omega_{i,j} \cdot N_{0i}) \end{pmatrix} \cdot \begin{pmatrix} N_{e1} \\ N_{e2} \\ N_{e3} \\ \dots \\ N_{ei} \end{pmatrix}$$

$$d\mathbf{N_e}/dt = \mathbf{M}\mathbf{N_e} \qquad (5)$$

This matrix ***M*** represents the set of coupled differential equations. It includes the spectral overlap that is a function of the homogeneous line width, and it includes the population of the ground state for each set of chromophores under a Gaussian distribution, which in the limit of low excitation intensities is equal to the total concentration. The procedure consists in finding eigenvalues and eigenvectors of the matrix ***M***. The matrix ***M*** and the diagonal matrix $\mathbf{\Lambda}$ with the eigenvalues λ_i of M are related by a similarity transformation $\mathbf{P\Lambda P^{-1}} = \mathbf{M}$, where ***P*** is the matrix containing the eigenvectors in the rows. This step decouples the differential equations. Solutions of the decoupled differential equations are $U_i = U_{0i} \exp(\lambda_i t)$, where U_{0i} includes the initial conditions and the λ_i are the eigenvalues. The corresponding vector $\mathbf{U_0}$ is obtained with $\mathbf{U_0} = \mathbf{P^{-1}N_{e0}}$, where $\mathbf{N_{e0}}$ is the excited state population vector at t = 0. Finally we re-couple the solutions with the following operation $\mathbf{N_e} = \mathbf{PU}$. $\mathbf{N_e}$ corresponds to a vector with *imax* members, and each member is a sum of time dependant exponential equations. Each member represents one subset of chromophores. With this sum, it is possible to calculate at a given time the population of each subset of chromophores, N_{ei}(t).

The resulting line shape is a sum of all the Lorentzian functions with the amplitude N_{ei} (t), and the time evolution of this curve according to the result of differential equations correspond to the modelled spectral diffusion.

$$f(x) = \sum_{i=1}^{i\,max} N_{ei} \cdot \frac{\frac{\Gamma_{hom}}{2\pi}}{\left(x - \delta \cdot \left(i - \frac{i\,max+1}{2}\right)\right)^2 + \frac{\Gamma_{hom}{}^2}{4}} \qquad \text{i= 1, 2, …, imax} \qquad (6)$$

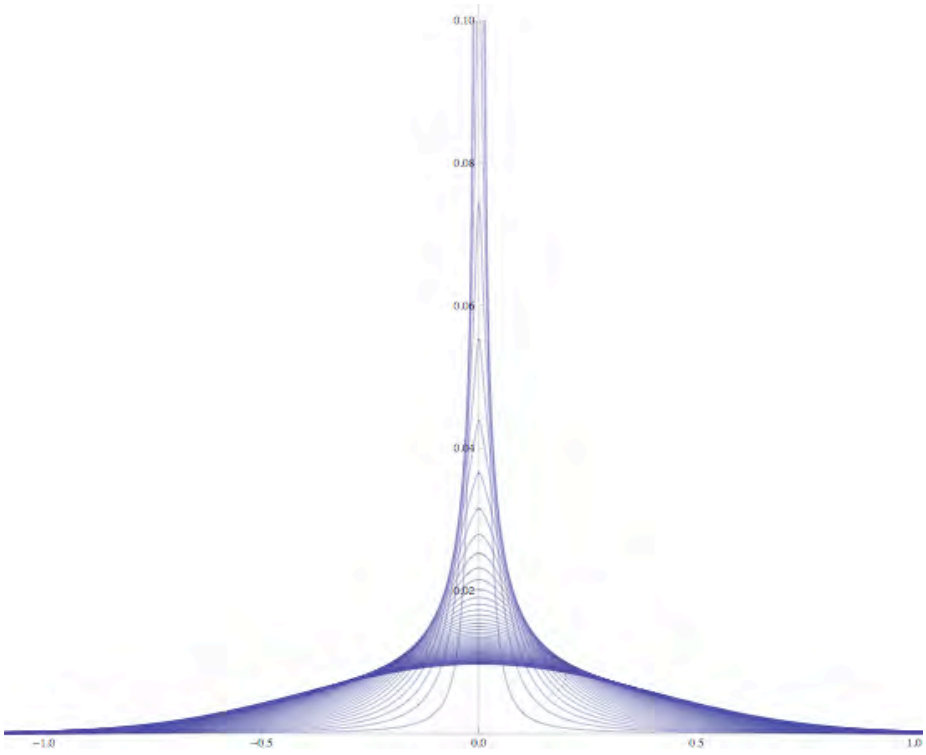

Figure 8.10. Spectral Diffusion according to the model with initial parameters Γ_{inh} = 1 cm^{-1}, Γ_{hom} = 0.02 cm^{-1}, δ = 0.005 cm^{-1}, k_0 = 770 s^{-1}, k_{ET} = 100 cm^{-1}. The waveforms are normalised to the area.

Figure 8.10 shows the calculated line shapes for spectral diffusion with the model values Γ_{inh} = 1 cm^{-1}, Γ_{hom} = 0.02 cm^{-1}, δ = 0.005 cm^{-1}, k_0 = 770 s^{-1}, k_{ET} = 100 s^{-1}. Rather than show the effective waveforms, which have decreasing intensity because of the intrinsic decay, the waveforms in Figure 8.10 are shown normalised to the area. The spectral diffusion as modelled here, leads the effective waveform from a Lorentzian line shape function to a Gaussian line shape function. Indeed, the limiting value for the broadening is the inhomogeneous line width.

Figures 8.11 and 8.12 show the influence of the various parameters on evolution of the line width as function of delay. In Figure 8.11a the influence of the homogeneous line width on the spectral diffusion according to the above model is shown. The inhomogeneous line width, the resolution step, the intrinsic deactivation rate and the effective energy transfer rate constant are kept constant, Γ_{inh} = 1 cm^{-1}, δ = 0.005 cm^{-1}, k_0 = 770 s^{-1}, k_{ET} = 100 s^{-1}, while the value of the homogeneous line width changes from 0.01 to 0.06 cm^{-1}. From Figure 8.11a, one can clearly see that when the homogeneous line width is increased, the spectral diffusion rate increases, however,

always reaching the plateau, that is, the inhomogeneous line width. On the other hand, Figure 8.11b shows the influence of the inhomogeneous line width on spectral diffusion. In this case the homogeneous line width, the resolution step, the intrinsic deactivation rate and the effective energy transfer rate are kept constant, Γ_{hom} = 0.02 cm^{-1}, δ = 0.005 cm^{-1}, k_0 = 770 s^{-1}, k_{ET} = 100 s^{-1}, and the evolution of the effective line width is calculated for Γ_{inh} = 1, 2, and 4 cm^{-1}. The larger the inhomogeneous line width, the longer is the time for spectral diffusion to reach the plateau. The energy transfer processes for larger inhomogeneous line width are slower, because the concentration of resonant or quasi-resonant species is lower. Figure 8.12a shows the influence of the k_{ET} on spectral diffusion. As expected, when k_{ET} is increased, spectral diffusion is faster, showing directly that spectral diffusion is related to the energy transfer. On the other hand, Figure 8.12b shows the influence of the excitation energy within the inhomogeneous band on spectral diffusion. In the present two-state model, the evolution is symmetrical, that is, it is the same for a given deviation from the central frequency whether to higher or to lower energy. This is in contrast to the resonant energy transfer involving the two components of the zero-field split ground state, for which the evolution among the members tends towards a Boltzman distribution. Interestingly, the expected observed line width becomes larger than the inhomogeneous line width for excitation into the wings of the inhomogeneous absorption. The reason for this becomes clear upon inspection of Figure 8.13. For irradiation into the wing of the inhomogeneous distribution, the evolution of the spectrum is not symmetrical but strongly skewed and remains biased towards the wing of the excitation.

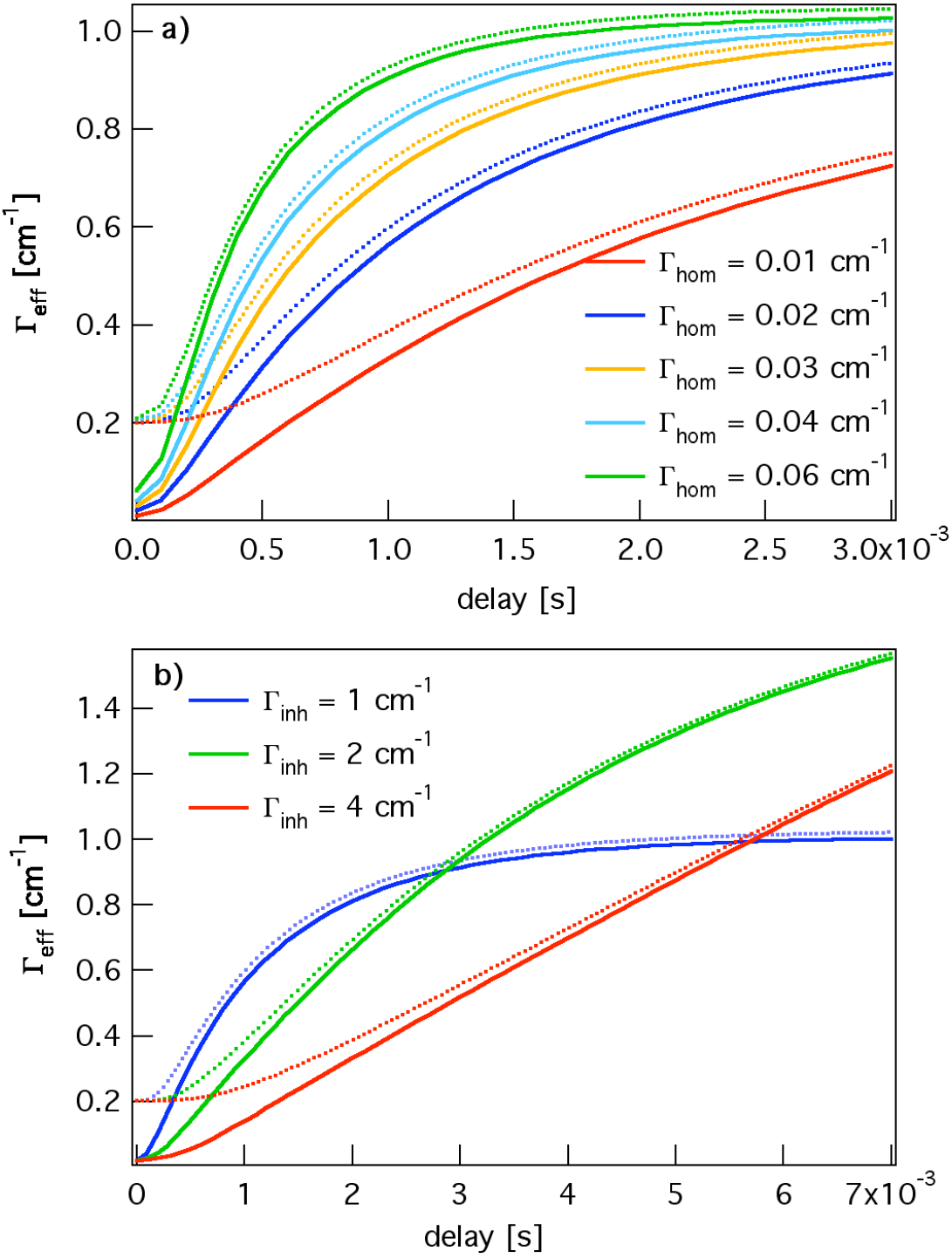

Figure 8.11. Time evolution of the effective line width when a) the homogeneous line width is increased from 0.01 to 0.06 cm^{-1} and Γ_{inh} = 1 cm^{-1}, δ = 0.005 cm^{-1}, k_0 = 770 s^{-1}, k_{ET} = 100 s^{-1}, and b) for inhomogeneous line widths Γ_{inh} = 1, 2, and 4 cm^{-1}, while Γ_{hom} = 0.02 cm^{-1}, δ = 0.005 cm^{-1}, k_0 = 770 s^{-1}, k_{ET} = 100 s^{-1} are kept constant. The dotted lines give the effective evolution when an experimental resolution of the experimental set-up of 0.2 cm^{-1} is taken into account.

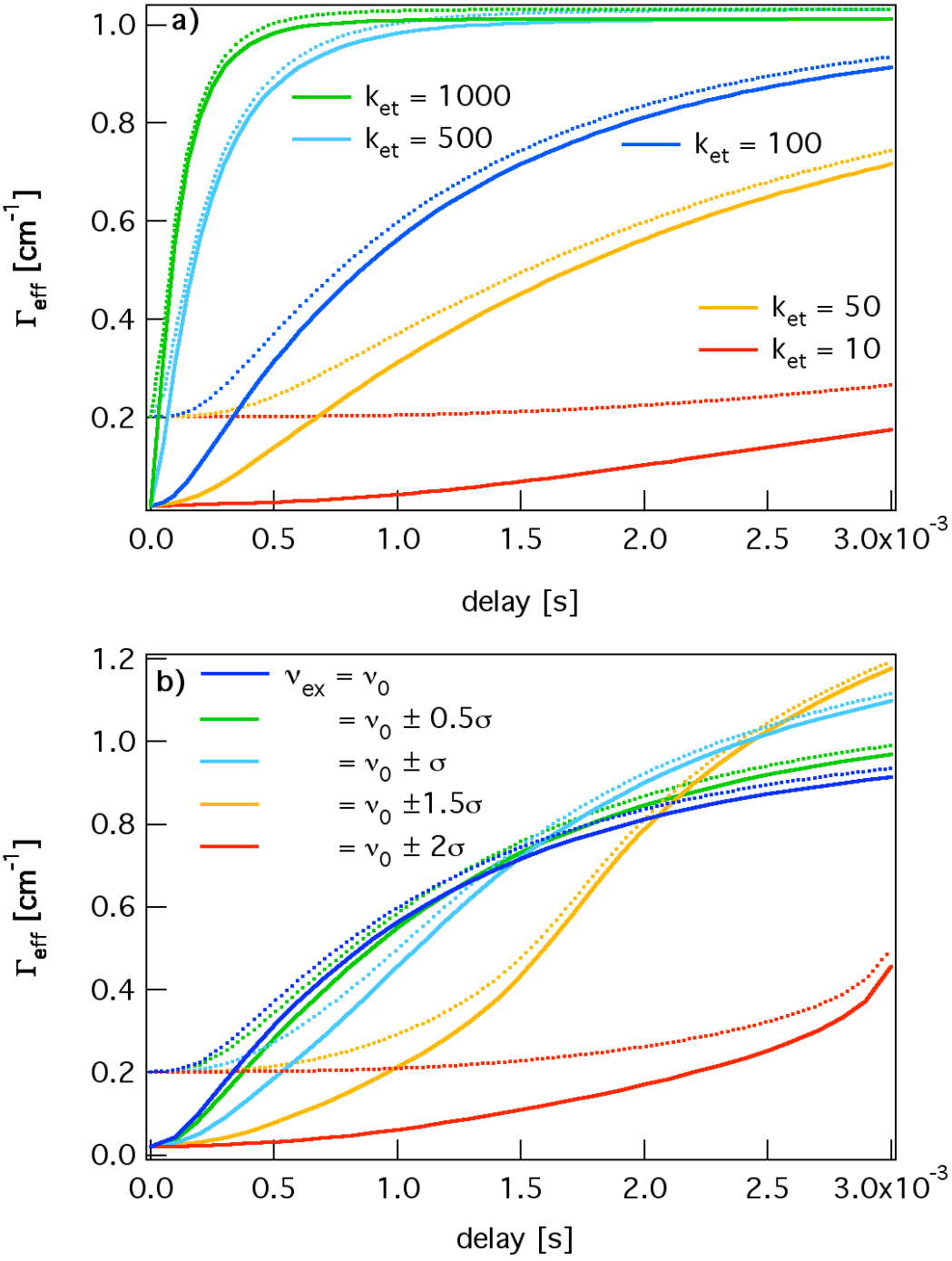

Figure 8.12. Time evolution of the effective line width when a) k_{ET} is increased from 10 to 1000 s^{-1} and Γ_{inh} = 1 cm^{-1}, Γ_{hom} = 0.02 cm^{-1}, δ = 0.005 cm^{-1}, k_0 = 770 s^{-1}, and b) for different excitation within the inhomogeneous band while keeping Γ_{inh} = 1 cm^{-1}, Γ_{hom} = 0.02 cm^{-1}, δ = 0.005 cm^{-1}, k_0 = 770 s^{-1}, k_{ET} = 100 s^{-1} constant. The dotted lines give the effective evolution when an experimental resolution of the experimental set-up of 0.2 cm^{-1} is taken into account.

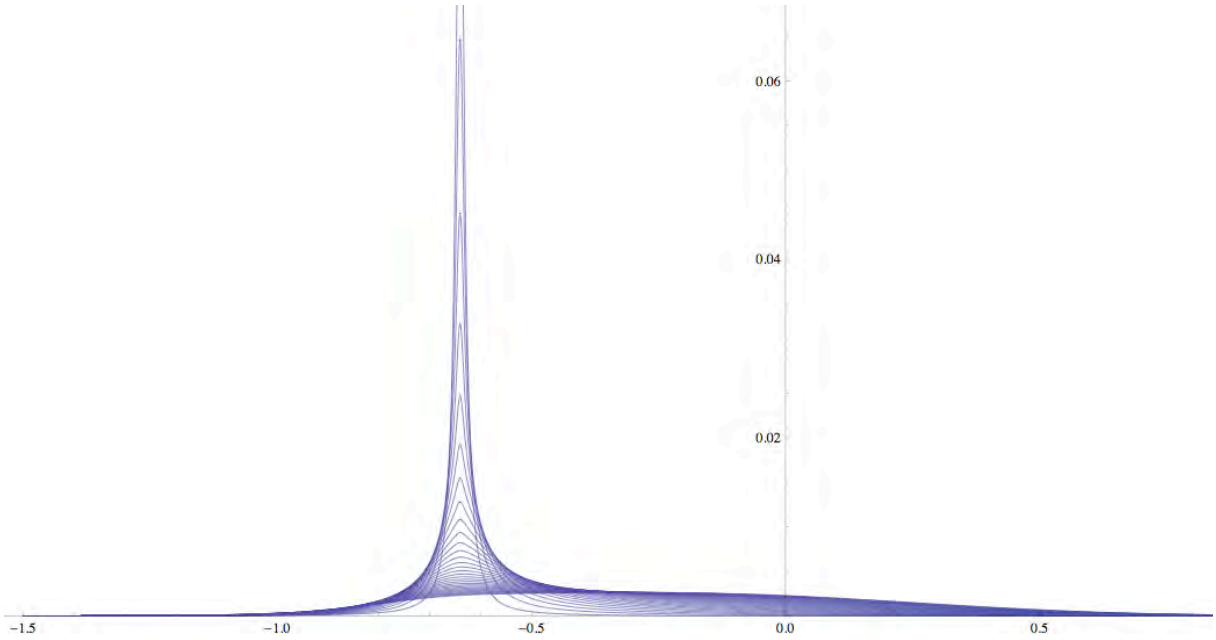

Figure 8.13. Spectral Diffusion according to the model with initial parameters Γ_{inh} = 1 cm^{-1}, Γ_{hom} = 0.02 cm^{-1}, δ = 0.005 cm^{-1}, k_0 = 770 s^{-1}, k_{ET} = 100 cm^{-1} and with excitation at N_{00}-1.5σ. The waveforms are normalised to the area.

8.5 Discussion and Conclusions

For direct comparison, Figure 8.14 shows the time evolution of the effective line width for the three compounds $[Rh(bpy)_3][NaCr(ox)_3]ClO_4$, $[Ru(bpy)_3][NaCr(ox)_3]$, and $[Zn(bpy)_3][NaCr(ox)_3]$ for irradiation just on the low-energy side of the absorption maximum. This corresponds to maximum excitation from the upper M_s = ±1/2 component [10] of the ground state. As expected, the R_1 line of $[Cr(ox)_3]^{3-}$ in the compound with the largest inhomogeneous distribution of Γ_{inh} = 4.4 cm^{-1}, that is $[Rh(bpy)_3][NaCr(ox)_3]ClO_4$, shows the slowest spectral diffusion. Within the time interval of 1.6 ms the observed line width increases from the experimental resolution of 0.20 cm^{-1} to 0.28 cm^{-1}. In agreement with the model curves, the spectral diffusion of the compound with the smallest inhomogeneous line width, namely $[Ru(bpy)_3][NaCr(ox)_3]$ with Γ_{inh} = 1.0 cm^{-1}, is considerably faster. Indeed, this acceleration is also semi-quantitatively correct by direct comparison with model waveforms shown in Figure 8.11b, thus confirming that the spectral diffusion is related to the concentration of the resonant chromophores in the critical sphere, and

that the larger is the inhomogeneous line width, the smaller is the concentration of the resonant chromophores. However, the R_1 line of $[Cr(ox)_3]^{3-}$ in $[Zn(bpy)_3][NaCr(ox)_3]$ shows an unexpected behaviour. In spite of the larger inhomogeneous line width compared to $[Ru(bpy)_3][NaCr(ox)_3]$, the spectral diffusion rate is apparently much faster than for the latter. This could be due to a variation in the other crucial parameter of the model, namely the homogeneous line width. According to reference [4] a comparatively large homogeneous line width results in smaller critical radius for resonant energy transfer, but at the same time this is offset by an increase in the concentration of the resonant chromophores. The latter is dominant such that for larger homogeneous line width the energy migration becomes more efficient. For $[Rh(bpy)_3][NaCr(ox)_3]ClO_4$ the upper limit for the homogeneous line width has been determined by transient spectral hole burning to be 600 MHz or 0.02 cm^{-1}. This value is essentially given by spin-spin relaxation [11], and there is no obvious reason as to why this should vary within the series of compounds.

A more likely hypothesis is that in $[Zn(bpy)_3][NaCr(ox)_3]$, local disorder creates different lattice sites and therefore a rather large distribution in the value of the ground state ZFS. In Figure 8.6 there is indeed a shoulder on the red wing of the absorption band of $[Zn(bpy)_3][NaCr(ox)_3]$. Via energy migration involving the M_s = ±1/2 component of the donor and M_s = ±3/2 component of the acceptor and vice versa, this results in much faster loss of the narrowing than predicted by the simplified model.

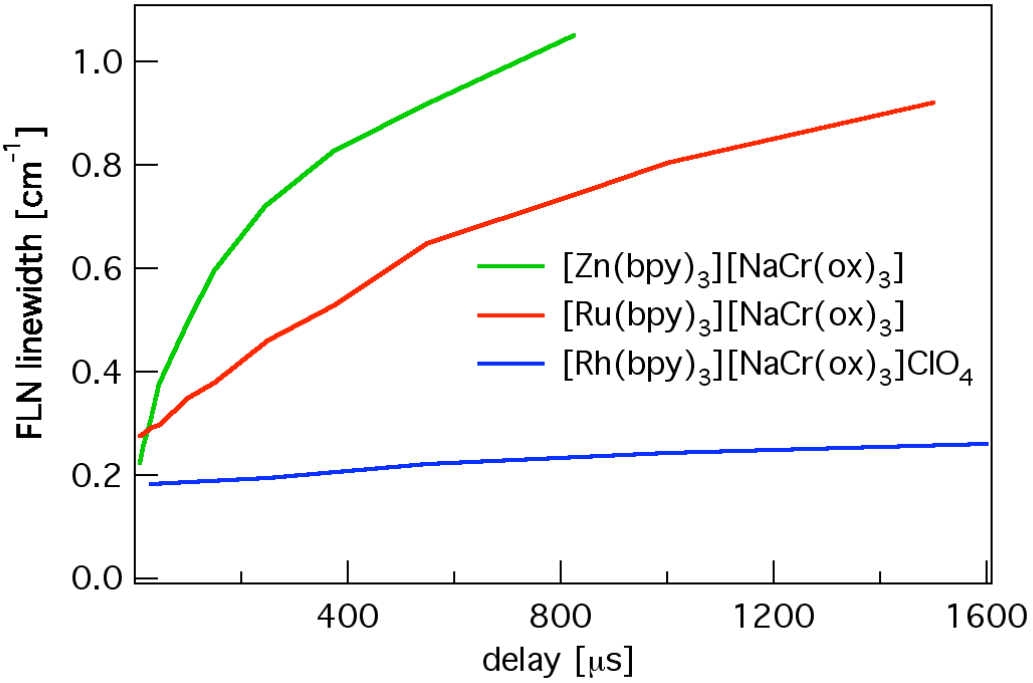

Figure 8.14. Experimental time evolution of the effective FLN line width of $[Rh(bpy)_3][NaCr(ox)_3]ClO_4$ with 14397.8 cm^{-1} excitation, $[Ru(bpy)_3][NaCr(ox)_3]$ with 14396.0 cm^{-1} excitation, and $[Zn(bpy)_3][NaCr(ox)_3]$ with 14387.0 cm^{-1} excitation, having inhomogeneous line widths 4.4 cm^{-1}, less than 1 cm^{-1}, and less than 2 cm^{-1}, respectively.

Furthermore, the simplified two state model developed in this chapter shows a symmetrical evolution of the spectral diffusion with regard to the excitation around the maximum of the inhomogeneous distribution. However, experimentally, we do not observe a symmetrical behaviour. The spectral diffusion is enhanced for excitation the blue wing. This is due to the fact that the two state model doesn't take into account the ±1/2 and ±3/2 levels of the ground state. However, for excitation in the blue wing of the absorption band, both levels are excited simultaneously thus accelerating the energy transfer processes and consequently the spectral diffusion.

In conclusion, for irradiation in the red wing of the inhomogeneous absorption, where the transition from the ±1/2 level if the ground state is dominant the simplified model performs satisfactorily, but for irradiation at higher energies it has to be extended to include the cross-relaxation process resulting in the multi-line pattern. Likewise, the homogeneous line width for all three compounds will have to be determined in order to verify the hypothesis of equal homogeneous line widths for all three.

References

[1] S. Geschwin, G.E. Devlin, R.L. Cohen, S.R. Chinn, Phys. Rev. 137 (1965) 1087.

[2] A. Monteil, E. Duval, J. Phys. C 12 (1979) L415.

[3] R.C. Powell, B. Dibartolo, B. Birang, C.S. Naiman, J. Appl. Phys. 37 (1966) 4973.

[4] M. Milos, S. Kairouani, S. Rabaste, A. Hauser, Coord. Chem. Rev. 252 (2008) 2540.

[5] A. Hauser, M.E. von Arx, V.S. Langford, U. Oetliker, S. Kairouani, A. Pillonnet, Top. Curr. Chem. 241 (2004) 65.

[6] M.E. von Arx, V.S. Langford, U. Oetliker, A. Hauser, J. Phys. Chem. A 106 (2002) 7099.

[7] C.K. Jørgensen, Discuss. Farad. Soc (1958) 110.

[8] S. Decurtins, H.W. Schmalle, R. Pellaux, P. Schneuwly, A. Hauser, Inorg. Chem. 35 (1996) 1451.

[9] M. Milos, A. Hauser, J. Lumin. 129 (2009) 1901.

[10] J.L. Hughes, H. Riesen, J. Phys. Chem. A 107 (2003) 35.

[11] H. Riesen, Coord. Chem. Rev. 250 (2006) 1737.

9. General Conclusions

The chromium tris-oxalate networks are model systems for investigating luminescence properties and energy transfer processes both as energy migration within the ^2E state and in combination with specific donors and acceptors. In this thesis, some prominent photophysical properties of $[Cr(ox)_3]^{3-}$ have been studied, and in particular the influence of the chemical environment, external pressure and electro-magnetic radiation have been investigated.

Energy migration occurs within the ^2E state of $[Cr(ox)_3]^{3-}$, more specifically within the R_1 line at low temperatures, both as resonant and as phonon-assisted processes. The rate of the resonant processes is related to the concentration of chromophores resonant within a homogeneous line width. This is highest at the centre of the inhomogeneous distribution. For larger inhomogeneous line widths, the mean number of resonant chromophores within the critical radius is smaller than for small inhomogeneous widths, resulting in smaller resonant energy transfer rates. For instance, the R_1 line of $[Cr(ox)_3]^{3-}$ in $[Rh(bpy)_3][NaCr(ox)_3]ClO_4$ has an inhomogeneous line width of 4.4 cm^{-1} and the resonant energy transfer processes are almost an order of magnitude slower compared to $[Ru(bpy)_3][NaCr(ox)_3]$ having an inhomogeneous line width of the R_1 line of approximately 1 cm^{-1}. In the latter compound, thanks to the enhanced resonant processes, it is possible to distinguish a quasi-resonant energy transfer process in addition to the resonant energy transfer involving different components of the ground state on donor and acceptor, which gives rise to a characteristic multi-line pattern, and the phonon-assisted energy transfer at elevated temperatures. The quasi-resonant energy transfer occurs between the same subset of chromophores in FLN experiments, and manifests itself as a spectral diffusion of the lines from the multi-line pattern. The spectral diffusion of the individual sharp line is modelled in a simplified model taking into account a single transition. The parameters involved in the model are the inhomogeneous line width, Γ_{inh}, the homogeneous line width, Γ_{hom}, the intrinsic radiative rate constant, k_0, the energy transfer rate constant, k_{ET}, and the resolution step for approximating the continuous inhomogeneous distribution as a sum of Lorentzians, δ. The model

describes, with differential equations, the time dependence of the single excited state, which is related to all the other chromophores within the inhomogeneous line width through spectral overlap.

In the series of mixed crystals with composition $[Zn_{1-x}Ru_x(bpy)_3][NaCr(ox)_3]$, distinct sites are created for each Cr^{3+} ion. The relation between the geometric and electronic structure of Cr^{3+} in the three-dimensional oxalate network lattices is established. The specific sites arise according to the distribution of the four closest M^{2+} positions around a given Cr^{3+} ion. Thus, five specific sites are resolved spectroscopically. Replacing Zn^{2+} ions with Ru^{2+} ions in the three-dimensional oxalate networks, the Cr-O bond length is shortened and the π-π interaction are decreased. Thus, the Racah parameters and the nephelauxetic effect change inducing modifications in photophysical properties of $[Cr(ox)_3]^{3-}$. We developed a simple model that nicely fits the absorption spectra of the mixed crystal series. The population of each site can be modeled with a statistical binomial distribution, while the energy of the ^2E transition of each site and its dependence on the $[Ru(bpy)_3]^{2+}$ mole fraction can be modeled with reference to high-pressure experiments on the neat $[Ru(bpy)_3][NaCr(ox)_3]$ compound. The importance of π-π interactions in the second coordination shell even for the photophysical properties of involving metal centered d-d transitions is pointed out.

We showed that it is possible to burn not only persistent resonant and side holes, but also energy transfer induced holes in $NaMg[Al_{1-x}Cr_x(ox)_3]\cdot 9(H_2O/D_2O)$. In this compound, the efficient persistent hole burning is due to the deuteration effect, the photoinduced HOD $\rightarrow$ DOH flip of hydrogen bonded water molecules being responsible for the shift in absorption energy of the selectively excited chromophores. With 20% concentration of Cr^{3+} in $NaMg[Al(ox)_3]\cdot 9(H_2O/D_2O)$, the resonant energy migration within the R_1 line of Cr^{3+} is efficient and the FLN spectrum manifests itself as a multi-line pattern with 6 members. By combining efficient energy migration and persistent hole burning in this compound we succeeded in burning spectral side holes by resonant energy transfer.

Finally, we studied the effect of pressure on energy transfer between $[Cr(ox)_3]^{3-}$ and $[Cr(bpy)_3]^{3+}$ in $[Rh_{1-x}Cr_x(bpy)_3][NaM^{III}_{1-y}Cr_y(ox)_3]ClO_4$, M = Rh, Al. With increasing pressure, the spectral overlap integral to which the energy transfer probability is proportional, decreases. This is due to different shift rates that are -26 cm^{-1}/GPa for

the ^2E state of $[Cr(ox)_3]^{3-}$ and -61 and -79 cm^{-1}/GPa for the $^2T_1$ state of $[Cr(bpy)_3]^{3+}$ with M^{III} = Rh and Al, respectively. The energy transfer in these compounds has two contributions, the fast super-exchange contribution and the slower contribution based on electric dipole-dipole interaction. The effect of pressure on both contributions is different, demonstrating the power of pressure experiments in the elucidation of the mechanism of excitation energy transfer processes between sharp line emitters and absorbers. The principle can be applied to any sharp line donor-acceptor pair with direct spectral overlap, offering for instance a way to tune up conversion efficiencies in transition metal ion and co-doped lanthanide containing systems.